



University  
of Glasgow

Rex, Charlotte Lucy (2024) *Isotope reconstructions of East Asian Monsoon behaviour across Glacial Terminations I and II from Lake Suigetsu, Japan (IAP2-18-54)*. PhD thesis.

<http://theses.gla.ac.uk/84032/>

Copyright and moral rights for this work are retained by the author

A copy can be downloaded for personal non-commercial research or study, without prior permission or charge

This work cannot be reproduced or quoted extensively from without first obtaining permission in writing from the author

The content must not be changed in any way or sold commercially in any format or medium without the formal permission of the author

When referring to this work, full bibliographic details including the author, title, awarding institution and date of the thesis must be given

Enlighten: Theses

<https://theses.gla.ac.uk/>  
[research-enlighten@glasgow.ac.uk](mailto:research-enlighten@glasgow.ac.uk)

**Isotope reconstructions of East Asian Monsoon  
behaviour across Glacial Terminations I and II from  
Lake Suigetsu, Japan**

**(IAP2-18-54)**

Charlotte Lucy Rex

BSc(Hons) Chemistry and Earth Sciences, MSc(Res) Polar and Alpine Change

Submitted in fulfilment of the requirements for the Degree of  
Doctor of Philosophy

Scottish Universities Environmental Research Centre  
& School of Geographical and Earth Sciences

College of Science and Engineering

University of Glasgow

October 2023

This thesis is dedicated to my grandparents,  
Julia Rex, Charles Rex, Juliet Evans, and Ronald Evans.

Or as they are known to me,  
Nanny, Pumpy, Old Granny, and Grandad Evans.

# Declaration of Originality

Name: Charlotte Lucy Rex

Registration Number: xxxxxxxx

The contents of this thesis are the result of research carried out at the University of Glasgow between October 2019 and October 2023, under the supervision of Dr Richard Staff (primary; University of Glasgow), Prof Jaime Toney (University of Glasgow), Prof Melanie Leng (British Geological Survey) and Dr Emma Pearson (Newcastle University).

I certify that the thesis presented here for examination for a PhD degree of the University of Glasgow is solely my own work other than where I have clearly indicated that it is the work of others (in which case the extent of any work carried out jointly by me and any other person is clearly identified in it) and that the thesis has not been edited by a third party beyond what is permitted by the University's PGR Code of Practice.

The copyright of this thesis rests with the author. No quotation from it is permitted without full acknowledgement.

I declare that the thesis does not include work forming part of a thesis presented successfully for another degree.

I declare that this thesis has been produced in accordance with the University of Glasgow's Code of Good Practice in Research.

I acknowledge that if any issues are raised regarding good research practice based on review of the thesis, the examination may be postponed pending the outcome of any investigation of the issues.

I confirm that Chapter 2 was jointly authored with J.J. Tyler, K. Nagaya, R.A. Staff, M.J. Leng, K. Yamada, I. Kitaba, J. Kitagawa, H. Kojima and T. Nakagawa and I contributed 80 % of this work.

I confirm that Chapter 3 was jointly authored with R.A. Staff, M.J. Leng, J.L. Toney, E.J. Pearson, J.J. Tyler, G.E.A. Swann, J.H. Lacey, M. Saito-Kato and T. Nakagawa and I contributed 80 % of this work.

I confirm that Chapter 4 was jointly authored with R.A. Staff, J.L. Toney, E.J. Pearson, A. Francke, M. Saito-Kato and T. Nakagawa and I contributed 80 % of this work.

I confirm that Chapter 5 was jointly authored with R.A. Staff, D.C.W. Sanderson, A.J. Cresswell, M.H. Marshall, M. Hyodo, D. Horiuchi, R. Tada and T. Nakagawa and I contributed 80 % of this work.

Signature:

Date: 06/10/2023

## Abstract

Understanding the response of the East Asian Monsoon to rising temperatures is crucial in light of recent anthropogenic climate change and the vulnerability of East Asia to future climatic hazards. However, East Asian Monsoon dynamics during warming periods in the late Quaternary are poorly understood, particularly on decadal to millennial timescales. Significant sources of this uncertainty are the spatially and temporally heterogeneous responses of the East Asian Monsoon to submillennial temperature fluctuations. The conflicting patterns observed in available reconstructions of East Asian Monsoon strength suggest that the teleconnections acting during these intervals were complex. Understanding the behaviours of the East Asian Monsoon by accounting for links to remote climatic perturbations allows for a more holistic understanding of deglacial climate changes.

A means of tackling this ambiguity is by contributing well-dated, high-resolution records of East Asian Monsoon evolution spanning Glacial Terminations I and II (which typify accessible, contrasting examples of rapid global warming) to the growing network of reconstructions from across the region. The aim of this thesis is to deconvolve East Asian Monsoon evolution during the last two glacial terminations by utilising the unique hydrological distribution of East Asian Monsoon precipitation over Japan to reconstruct both seasonal modes of the system (i.e., the East Asian Winter Monsoon and East Asian Summer Monsoon). This aim is met by the construction of isotope-based, season-specific East Asian Monsoon records across Glacial Terminations I and II using materials from the Lake Suigetsu sediment cores.

This thesis is comprised of four interconnected research papers, preceded by an introduction and succeeded by a summary of findings, discussion of relevance, suggestions for future work and conclusions. In the first research paper, we utilise extended contemporary monitoring of the stable isotope composition of precipitation, river water and lake water in the Lake Suigetsu catchment to understand the factors affecting these variables and aid robust interpretation of isotope-based proxy reconstructions from the Lake Suigetsu sediment cores. Our results show that the composition of precipitation was influenced by the dual East Asian Monsoon system, and that these signals were then transferred to the

lake system where they were combined with secondary local influences on lake water composition. Based on our knowledge of late Quaternary catchment dynamics, these observations suggest that the palaeo-isotope composition of Lake Suigetsu was closely related to the East Asian Monsoon.

In the second research paper, we examine the influence of remote climatic processes on the East Asian Winter Monsoon and East Asian Summer Monsoon in Japan during Glacial Termination I by reconstructing trends in the strength of each seasonal mode. This is achieved using oxygen isotope analysis of diatom silica and compound-specific hydrogen isotope analysis of n-alkanoic acids from the Lake Suigetsu sediment cores. Our results support distinctive seasonal behaviours of the East Asian Monsoon during Glacial Termination I, with evidence for East Asian Winter Monsoon weakening and East Asian Summer Monsoon strengthening. The East Asian Summer Monsoon also exhibited variations in strength which were synchronous with Antarctic temperature fluctuations after 16,000 years ago, which supports a temporally restricted climatic link between Japan and the Southern Hemisphere at this time.

In the third research paper, we reconstruct the East Asian Summer Monsoon in Japan during Glacial Termination II, and contrast the findings to those from Glacial Termination I. The reconstruction presented in this chapter, which is based on compound-specific hydrogen isotope analysis of n-alkanoic acids, provides evidence for early East Asian Summer Monsoon strengthening followed by a gradual weakening phase with submillennial-scale variability. Comparison of this record to others derived from mainland China supports the assertion that East Asian Summer Monsoon behaviours during Glacial Termination II were spatially heterogeneous. Additionally, the different evolutions of the East Asian Summer Monsoon during Glacial Terminations I and II indicate that the system operated distinctively under contrasting boundary conditions, although the new reconstructions from Japan were consistently more closely linked with Southern Hemisphere (Antarctic) temperatures than Northern Hemisphere (Greenlandic) temperatures during both intervals.

The fourth research paper was motivated by a lack of an absolute chronology for the oldest (pre-50,000 years ago) parts of the Lake Suigetsu sediment cores (which includes Glacial Termination II). In this paper, we appraise the

luminescence characteristics of the cores using rapid profiling techniques. These are employed across four key time periods in order to assess the application of these methods for the detection of local and environmental shifts, and to assess the suitability of the core materials for luminescence dating. We show that the luminescence characteristics of the cores were susceptible to a range of environmental perturbations, best illustrating local changes by using high-resolution contiguous sampling. The feasibility of future luminescence dating is supported by quantifiable luminescence signals, and first order approximate ages suggest that blue light optically stimulated luminescence dating of feldspar provides the most accurate and most practical assessment of burial age. This technique should be the subject of dating efforts in pursuit of refinements to the Suigetsu core chronology before 50,000 years ago.

The findings of this thesis contribute to our collective knowledge of East Asian Monsoon behaviours during glacial terminations. Critically, they represent a geographical expansion of the regional high-resolution record network to include Japan. The value of this process is demonstrated by the decoupled evolutions of each seasonal mode during Glacial Termination I, and a remote link between Antarctic temperatures and East Asian Summer Monsoon evolution in Japan during Glacial Terminations I and II, which were hitherto unconstrained by high resolution analysis. These findings acknowledge and begin to rationalise spatial and temporal heterogeneities in East Asian Monsoon behaviours by comparison to other records. This work highlights the complexity of the East Asian Monsoon, and the value of long records from contrasting deglacial periods for a better comprehension of this system in the context of anthropogenic climate change.

# Table of Contents

|   |          |
|---|----------|
| List of Tables.....   | xii      |
| List of Figures.....  | xiii     |
| Acknowledgements .....  | xiv      |
| Definitions and Abbreviations .....   | xviii    |
| <b>Chapter 1 Introduction .....</b>   | <b>1</b> |
| 1.1 Monsoon Systems.....  | 1        |
| 1.2 The East Asian Monsoon.....   | 3        |
| 1.2.1 Overview .....  | 3        |
| 1.2.2 Drivers .....   | 5        |
| 1.2.3 Significance .....  | 7        |
| 1.3 Thesis Rationale.....   | 8        |
| 1.3.1 The Palaeo–East Asian Monsoon .....   | 8        |
| 1.3.2 Challenges and Uncertainties .....  | 9        |
| 1.3.3 East Asian Monsoon Reconstructions from Japan .....   | 11       |
| 1.3.4 Thesis Aims.....  | 12       |
| 1.4 Lake Suigetsu, Japan .....  | 13       |
| 1.4.1 Setting .....   | 13       |
| 1.4.2 Climate .....   | 15       |
| 1.4.3 Coring Campaigns .....  | 17       |
| 1.4.4 Chronological Control .....   | 21       |
| 1.4.5 Palaeoenvironmental Investigation .....   | 23       |
| 1.5 Thesis Structure .....  | 24       |
| 1.5.1 The Contemporary Stable Isotope Hydrology of Lake Suigetsu and Surrounding Catchment (Japan) and its Implications for Sediment Derived Palaeoclimate Records (Chapter 2)..... | 25       |
| 1.5.2 Insights into Deglacial East Asian Monsoon Seasonality and Inter–Regional Teleconnections from Lake Suigetsu, Japan (Chapter 3) ....  | 26       |
| 1.5.3 Novel Observations of East Asian Summer Monsoon Evolution During Glacial Termination II from Lake Suigetsu, Japan (Chapter 4).....  | 26       |
| 1.5.4 Controls on Luminescence Signals in Lake Sediment Cores: a Study from Lake Suigetsu, Japan (Chapter 5) .....  | 27       |
| 1.5.5 Summary and Future Work (Chapter 6).....  | 27       |
| 1.5.6 Conclusions (Chapter 7).....  | 27       |
| 1.6 Introduction to Principal Thesis Techniques .....   | 28       |
| 1.6.1 Stable Isotopes .....   | 28       |
| 1.6.2 Water Isotope Analysis .....  | 31       |
| 1.6.3 Diatom Isotope Analysis.....  | 31       |
| 1.6.4 Alkyl Lipid Concentration and Isotope Analysis .....  | 33       |

|                  |   |            |
|------------------|---|------------|
| 1.6.5            | Luminescence Dating and Profiling.....  | 34         |
| <b>Chapter 2</b> | <b>The Contemporary Stable Isotope Hydrology of Lake Suigetsu and Surrounding Catchment (Japan) and its Implications for Sediment-Derived Palaeoclimate Records .....</b> | <b>37</b>  |
| 2.1              | Abstract.....   | 39         |
| 2.2              | Keywords .....  | 39         |
| 2.3              | Introduction.....   | 39         |
| 2.4              | Study Site.....   | 43         |
| 2.4.1            | Hydrology.....  | 43         |
| 2.4.2            | Climate .....   | 45         |
| 2.5              | Materials and Methods .....   | 46         |
| 2.5.1            | Sampling Methods.....   | 46         |
| 2.5.2            | Analytical Methods.....   | 48         |
| 2.6              | Results and Interpretation.....   | 50         |
| 2.6.1            | Precipitation $\delta^{18}\text{O}$ and $\delta^2\text{H}$ .....  | 50         |
| 2.6.2            | Precipitation d-excess .....  | 54         |
| 2.6.3            | Quantity-Weighted Composition .....   | 55         |
| 2.6.4            | Temperature and Amount Effects .....  | 56         |
| 2.6.5            | Comparison to Tokyo .....   | 58         |
| 2.6.6            | Catchment Effects .....   | 59         |
| 2.6.7            | River and Lake Water d-excess .....   | 62         |
| 2.6.8            | River and Lake Water $\delta^{18}\text{O}$ and $\delta^2\text{H}$ .....   | 63         |
| 2.6.9            | Vertical Profiles of Lake Water Isotopes in Lake Suigetsu.....  | 65         |
| 2.7              | Discussion .....  | 67         |
| 2.8              | Conclusions.....  | 72         |
| <b>Chapter 3</b> | <b>Insights into Deglacial East Asian Monsoon Seasonality and Inter-Regional Teleconnections from Lake Suigetsu, Japan .....</b>  | <b>74</b>  |
| 3.1              | Abstract.....   | 76         |
| 3.2              | Introduction.....   | 76         |
| 3.3              | Materials and Methods .....   | 81         |
| 3.3.1            | Core Materials .....  | 81         |
| 3.3.2            | $\delta^{18}\text{O}_{\text{diatom}}$ Analysis .....  | 83         |
| 3.3.3            | $\delta^2\text{H}_{\text{acid}}$ Analysis.....  | 86         |
| 3.4              | Results .....   | 89         |
| 3.4.1            | Observations at Lake Suigetsu .....   | 89         |
| 3.4.2            | Proxy Drivers.....  | 94         |
| 3.4.3            | EAM Evolution in Japan During TI.....   | 98         |
| 3.5              | Discussion .....  | 102        |
| <b>Chapter 4</b> | <b>Novel Observations of East Asian Summer Monsoon Evolution During Glacial Termination II from Lake Suigetsu, Japan.....</b>   | <b>107</b> |

|   |   |            |
|---|---|------------|
| 4.1   | Abstract.....   | 109        |
| 4.2   | Highlights.....   | 110        |
| 4.3   | Keywords .....  | 110        |
| 4.4   | Introduction.....   | 110        |
| 4.5   | Study Site.....   | 115        |
| 4.6   | Materials and Methods .....                                 | 117        |
| 4.6.1   | Core Materials .....  | 117        |
| 4.6.2   | Sample Preparation.....                                     | 119        |
| 4.6.3   | GC-MS and GC-FID Analysis .....                             | 120        |
| 4.6.4   | GC-IRMS Analysis.....                                       | 122        |
| 4.7   | Results .....   | 123        |
| 4.7.1   | Lipid Concentration and Index Variations .....              | 123        |
| 4.7.2   | Catchment Evolution .....                                   | 126        |
| 4.7.3   | $\delta^2\text{H}_{\text{acid}}$ Variations .....           | 127        |
| 4.7.4   | Signal Interpretation .....                                 | 129        |
| 4.7.5   | EASM Evolution .....  | 131        |
| 4.8   | Discussion .....  | 133        |
| 4.8.1   | A Note on Chronological Alignment .....                     | 133        |
| 4.8.2   | Comparison to Continental EASM Records.....                 | 134        |
| 4.8.3   | Contrasting EASM Evolution in Japan During TI and TII ..... | 136        |
| 4.8.4   | Climate Forcing.....  | 138        |
| 4.8.5   | Submillennial Variability .....                             | 140        |
| 4.8.6   | Future Work.....  | 141        |
| 4.9   | Conclusions.....  | 141        |
| <b>Chapter 5 Controls on Luminescence Signals in Lake Sediment Cores: a Study from Lake Suigetsu, Japan .....</b> |   | <b>144</b> |
| 5.1   | Abstract.....   | 146        |
| 5.2   | Highlights.....   | 146        |
| 5.3   | Keywords .....  | 146        |
| 5.4   | Introduction.....   | 147        |
| 5.5   | Regional Setting .....                                      | 149        |
| 5.6   | Materials and Methods .....                                 | 150        |
| 5.6.1   | Core Materials .....  | 150        |
| 5.6.2   | Sample Analysis .....                                       | 151        |
| 5.7   | Results and Interpretation.....                             | 154        |
| 5.7.1   | Time Period 1, the Last 500 Years .....                     | 154        |
| 5.7.2   | Time Period 2, the Laschamp Excursion.....                  | 157        |
| 5.7.3   | Time Period 3, the Varve Limit .....                        | 159        |
| 5.7.4   | Time Period 4, Termination II.....                          | 161        |

|   |   |            |
|---|---|------------|
| 5.7.5   | Estimated Dose Rates .....  | 162        |
| 5.8   | Discussion .....  | 165        |
| 5.8.1   | Luminescence Characteristics and Environmental Change .....   | 165        |
| 5.8.2   | Assessment of Dating Potential .....  | 166        |
| 5.9   | Conclusions.....  | 167        |
| <b>Chapter 6 Summary and Future Work.....</b> |   | <b>169</b> |
| 6.1   | Summary of Findings.....  | 169        |
| 6.1.1   | The Contemporary Stable Isotope Hydrology of Lake Suigetsu and Surrounding Catchment (Japan) and its Implications for Sediment-Derived Palaeoclimate Records (Chapter 2)..... | 169        |
| 6.1.2   | Insights into Deglacial East Asian Monsoon Seasonality and Inter-Regional Teleconnections from Lake Suigetsu, Japan (Chapter 3) ...   | 171        |
| 6.1.3   | Novel Observations of East Asian Summer Monsoon Evolution During Glacial Termination II from Lake Suigetsu, Japan (Chapter 4) .....   | 173        |
| 6.1.4   | Controls on Luminescence Signals in Lake Sediment Cores: a Study from Lake Suigetsu, Japan (Chapter 5) .....  | 174        |
| 6.2   | Response to Thesis Aims and Objectives .....  | 176        |
| 6.3   | Relevance of Findings .....   | 179        |
| 6.4   | Directions for Future Research .....  | 182        |
| 6.4.1   | Contemporary Stable Isotope Monitoring.....   | 182        |
| 6.4.2   | Applications of Luminescence Techniques to Lake Sediment Cores  | 182        |
| 6.4.3   | East Asian Monsoon Behaviours .....   | 183        |
| <b>Chapter 7 Conclusions .....</b>            |   | <b>186</b> |
| <b>Appendices. ....</b>                       |   | <b>191</b> |
|   | Appendix 1 – Publications.....  | 191        |
| <b>References. ....</b>                       |   | <b>213</b> |

## List of Tables

|  |     |
|--|-----|
| Table 1.1 Physical characteristics of the modern Five Lakes of Mikata. ....                  | 17  |
| Table 2.1 Sampling locations.....  | 47  |
| Table 2.2 Results of the precipitation isotope regression analysis.....                      | 57  |
| Table 5.1 Results of the ICP-MS and ICP-OES analysis and water content<br>calculations. .... | 161 |
| Table 5.2 Results of the microdosimetry calculations. ....                                   | 164 |

## List of Figures

|   |     |
|---|-----|
| Figure 1.1 Key monsoon regions across the globe. ....   | 2   |
| Figure 1.2 The seasonal modes of the East Asian Monsoon system. ....  | 4   |
| Figure 1.3 Location and setting of Lake Suigetsu and the Five Lakes of Mikata. ....   | 16  |
| Figure 1.4 Climate at the Five Lakes of Mikata. ....  | 17  |
| Figure 1.5 Core image showing presence of annual laminations (varves). ....   | 18  |
| Figure 1.6 Photograph of the coring rig during the SG12 campaign. ....  | 19  |
| Figure 1.7 Core photographs of the SG06 archive. ....   | 20  |
| Figure 1.8 The idealised varve structure. ....  | 20  |
| Figure 1.9 Summary of the structure of this thesis. ....  | 25  |
| Figure 2.1 Map of the Five Lakes of Mikata catchment. ....  | 42  |
| Figure 2.2 Climate at the Five Lakes of Mikata. ....  | 46  |
| Figure 2.3 Precipitation $\delta^{18}\text{O}$ and $\delta^2\text{H}$ at Wakasa and Tokyo. ....   | 51  |
| Figure 2.4 Variations in $\delta_{\text{precipitation}}$ with time. ....  | 52  |
| Figure 2.5 HYSPLIT back trajectory model results. ....  | 53  |
| Figure 2.6 Precipitation $\delta^{18}\text{O}$ and $\delta^2\text{H}$ at Tokyo, 2013. ....  | 59  |
| Figure 2.7 Surface water $\delta^{18}\text{O}$ and $\delta^2\text{H}$ . ....  | 60  |
| Figure 2.8 Variations in $\delta_{\text{river}}$ and $\delta_{\text{lake}}$ with time. ....   | 61  |
| Figure 2.9 Variations in Suigetsu $\delta_{\text{lake}}$ with depth. ....   | 66  |
| Figure 3.1 Lake Suigetsu and other key sites. ....  | 79  |
| Figure 3.2 Diatom SEM Imagery. ....   | 84  |
| Figure 3.3 Chromatogram of the n-alkanoic acid fraction of Sample 6B. ....  | 88  |
| Figure 3.4 Proxy changes at Lake Suigetsu during Termination I. ....  | 91  |
| Figure 3.5 Proxy weights, abundances and concentrations. ....   | 93  |
| Figure 3.6 Comparison of Lake Suigetsu bulk $\delta^{18}\text{O}_{\text{diatom}}$ and Lake Suigetsu diatom taxonomic counts. ....                                 | 97  |
| Figure 3.7 Changing EASM influence on $\delta^2\text{H}_{\text{acid}}$ at Lake Suigetsu. ....   | 98  |
| Figure 3.8 EAM evolution at Lake Suigetsu during Termination I with contextual global benchmark records. ....   | 101 |
| Figure 4.1 The differences between the climatic sequences of TI and TII. ....   | 113 |
| Figure 4.2 The location of Lake Suigetsu and the Five Lakes of Mikata. ....   | 116 |
| Figure 4.3 Example GC-FID A2 fraction chromatograms. ....   | 121 |
| Figure 4.4 Example GC-FID N1 fraction chromatogram. ....  | 121 |
| Figure 4.5 Evidence for catchment evolution at Lake Suigetsu during Glacial Termination II. ....  | 125 |
| Figure 4.6 $\delta^2\text{H}$ derived from the $\text{C}_{26}$ , $\text{C}_{28}$ and $\text{C}_{30}$ n-alkanoic acid homologues during TII at Lake Suigetsu. .... | 128 |
| Figure 4.7 $\delta^2\text{H}_{\text{C}_{30}\text{acid}}$ and pollen-derived temperature evolution during TII at Lake Suigetsu. ....                               | 132 |
| Figure 4.8 Records of EASM strength between 134 and 124 ka BP and location indicators. ....   | 135 |
| Figure 4.9 Comparison of records from Greenland (Gr), Lake Suigetsu (SG) and Antarctica (Ant) during TI and TII. ....   | 137 |
| Figure 5.1 Location of Lake Suigetsu. ....  | 149 |
| Figure 5.2 Lab profiling measurement schemes. ....  | 153 |
| Figure 5.3 Results of the POSL and lab profiling analysis of Time Period 1. ....  | 156 |
| Figure 5.4 Results of the POSL and lab profiling analysis of Time Period 2. ....  | 158 |
| Figure 5.5 Results of the POSL and lab profiling analysis of Time Period 3. ....  | 160 |
| Figure 5.6 Results of the POSL and lab profiling analysis of Time Period 4. ....  | 163 |

## Acknowledgements

I would like to begin by thanking my exceptional primary supervisor, Dr Richard Staff, because without his support I simply wouldn't have a thesis. Richard, thank you for believing in me, for encouraging me and for being such a legendary *sensei*. You have salvaged this process more times than I think you know about, and you have embodied collegiality, integrity and kindness every step of the way. Thank you for always being my personal cheerleader, on-call Suigetsu expert and grammar police (this is the only section I wouldn't let you read in advance, so I am sorry for the inevitable typos). I will always be grateful for the opportunity to be your “dodgy first pancake” of a PhD student. ATB (beach umbrella emoji).

To my extended supervisory team: Prof Jaime Toney, Prof Mel Leng and Dr Emma Pearson, thank you for your support, assistance, and encouragement throughout this process. I will always be grateful for your contributions to shaping my project and keeping me on track through the ups and downs. To Jaime, thank you for being so generous with your endless knowledge; to Mel, thank you for always being the voice of reason, especially with reviewer comments; and to Emma, thank you for your valuable insights and feedback. To my “unofficial” supervisors, Dr Jon Tyler and Prof David Sanderson, thank you for going above and beyond and always making time to help me when I needed it. Both of you made sure that my research kept moving during even the darkest times of the Covid-19 pandemic, and for that I will always be immensely grateful.

I would also like to extend my endless gratitude to the whole Suigetsu research group for being the greatest collaborators that a PhD student could hope for. To Prof Takeshi Nakagawa, for pioneering this entire project; the Suigetsu legacy is truly a reflection of your leadership and dedication. I hope I did you proud. To the Japan team: Prof Ikuko Kitaba, Dr Kei Yamada, Dr Junko Kitagawa, Dr Kazu Nagaya, and Aki Yamasaki, thank you for your support, ideas and insights, as well as your generosity in hosting us during our visits to Wakasa. I wish to express special thanks to Kazu for conducting the two years of modern isotope sampling, which was a truly mammoth effort involving the addition of a rainfall sampler to his front garden. I hope the excuse to use your fancy camera

equipment made the experience a lot more fun. To the Australia team: Dr Alex Francke and (soon to be Dr) Vanessa Nowinski, I am so grateful for the opportunity to work with you both. Thank you for your assistance and advice throughout; Alex, for pioneering the updated >50ka chronology, and Vanessa, for your sound advice and expert LevelFinder usage in Japan.

At the University of Glasgow, I would like to thank Ali Salik for his technical support, Dr Alan Cresswell for his excellent training and for handling the HF when it scared me senseless, and others at SUERC (Dr Derek Fabel, Dr Valerie Olive and Dr Lorna Carmichael) and GES (Dr Mark Wildman) for their assistance with equipment and lab time, and valuable advice on this journey. At the British Geological Survey, I would like to thank Dr Jack Lacey for imparting his incomparable knowledge of the fluorination line and Carol Arrowsmith for patiently analysing the modern water samples for us. At the University of Nottingham, I would like to thank Prof George Swann for his kindness and patience in helping me with my XRF analysis, as well sharing his expert knowledge of diatom mass balance calculations. At the University of Hokkaido, I would like to thank Dr Osamu Seki for saving my final chapter by performing the isotope analyses on my Glacial Termination II biomarker samples – your generosity at the eleventh hour gave me faith in the scientific community again.

I would also like to acknowledge the endless support and encouragement of the professional services staff at the University of Glasgow, who have enriched my PhD experience beyond measure. To the College of Science and Engineering Graduate School, in particular Heather Lambie, for always championing me and providing me with countless opportunities for personal and professional growth, and to the Researcher Development team, especially Dr Joanna Royle and Dr Kay Guccione, for their unparalleled mentorship and the internship experience of a lifetime. You are the unsung heroes of my time in Glasgow and honestly the reason I stuck around for so long, and I cannot thank you enough for showing me the value of my skills and the meaning of teamwork.

To the organisations and funding bodies who assisted financially with the contents of this PhD thesis, thank you for your support. These include the NERC IAPETUS2 Doctoral Training Partnership, the National Environmental Isotope Facility (NEIF), the British Geological Survey British University Funding Initiative

(BGS BUFI), the School of Geographical and Earth Sciences (GES), the Scottish Alliance for Geoscience, Environment and Society (SAGES) and the Quaternary Research Association (QRA).

To my family and friends, thank you for believing in me even in the darkest of times. Special thanks must go to my mum, Joanna Rex, who despite having declared herself “out of her depth” during my undergraduate dissertation, always made time to check my use of tenses and as a result now knows a great deal about how rainy it was in Japan a long time ago. Thank you for the endless supply of love and chocolate. To my dad, Trevor Rex, thank you for the support and for always being willing to drive my stuff from one end of the country to the other. To the most iconic STEM gurlies: Dr Áine O'Brien, Dr Ellen Macdonald and (soon to be Dr) Charlotte Slaymark, thank you for your sage advice and impeccable taste in GIFs. To Emily and Charlotte Staff: thank you for always being so enthusiastic about my diatoms and for causing constant havoc in the background of my supervisory meetings. To Jo, Mark and Philip Chitty: thank you for your support and kindness, and for facilitating my obsession with highland cows in the name of morale. To my fellow Cecilians, especially Tilly Bird, Ross Burns, Lucy Docherty, Mhairi McCormack, Kirsty Arnott and Bee Regan: the opportunity to slay with you on a biweekly basis kept me sane. And to my besties, Kaylee McHale and Helen Lankester: thank you for being there with me from beginning to end.

My final “thank you” goes to James Chitty, for being the kindest and most wonderful partner that a PhD student could hope for. There hasn't been a time during my PhD where I haven't appreciated your support, reassurance, and wisdom. Thank you for being there to commiserate my disasters and celebrate my achievements with me. I wouldn't have wanted anyone else by my side throughout this process, especially whilst writing my thesis, when you never failed to make me laugh and reminded me regularly why I wasn't doing a corporate job. I will always look forward to telling you every single detail of my day over a substantial amount of garlic bread and an episode of *Modern Family*. Here's to a lifetime as Team Awesome.

## 七転び八起き

“Fall down seven times, stand up eight”

## Definitions and Abbreviations

Common definitions and abbreviations used throughout this thesis are given below and defined at first usage in Chapters 1–5. SI units, element symbols and chemical names are not included here but standard nomenclature is used throughout (e.g., “Gy yr<sup>-1</sup>” Grays per year; “Ti” titanium; “HCl” hydrochloric acid).

|                 |  |
|-----------------|--|
| ‰               | per mille; parts per thousand  |
| 1-φ             | Relative (radiation dose) attenuation fraction; proportion of external dose absorbed by a matrix   |
| Ar–Ar           | Argon–argon dating; used for determining the age of a variety of geological materials, including tephra  |
| A(N)01–1cm      | Depth code for the Suigetsu core, whereby “A” denotes the borehole, “01” denotes the core section, “(N)” denotes the half of the longitudinally cut core and “1cm” denotes the depth down-core (as identified in the core photographs taken immediately after core extraction) |
| ACL             | Average Chain Length (of n-alkanes); subscripts denote specific chain lengths, e.g., ACL <sub>15–33</sub> is the concentration-weighted ACL of n-alkanes containing between 15 and 33 carbon atoms   |
| ACR             | Antarctic Cold Reversal; late glacial stade in Antarctica  |
| AD              | Anno Domini (where AD 1 = 1949 yr BP)  |
| AMOC            | Atlantic Meridional Overturning Circulation  |
| AO              | Arctic Oscillation   |
| BA              | Bølling–Allerød Interstade; late glacial interstade in the North Atlantic  |
| BECS            | Biomarkers for Environmental and Climate Science; University of Glasgow laboratory facility  |
| BFC             | Diatomite standard from Shasta County California; isotope standard for diatoms   |
| cal BP          | Calibrated radiocarbon years before AD 1950  |
| Composite Depth | Depth from bottom of the lake for the Suigetsu sediment cores as defined by the “master core”; created from aligning core sections from different boreholes  |
| CPI             | Carbon Preference Index (of n-alkanes); indicator of the concentration dominance of odd or even chain lengths within a sample of n-alkanes; subscripts denote specific chain lengths, e.g., CPI <sub>27–32</sub> includes n-alkanes containing between 27 and 32 carbon atoms  |
| CWProxy         | Continuous Wave Proxy; measurement scheme used in POSL analysis  |
| C <sub>XX</sub> | Alkyl lipid homologue with XX carbon atoms; e.g., the C <sub>30</sub> n-alkanoic acid contains 30 carbon atoms   |
| D <sub>e</sub>  | Equivalent dose; a quantification of the total dose received by a sample since the last bleaching event  |
| d-excess        | Second order stable isotope parameter derived from δ <sup>18</sup> O and δ <sup>2</sup> H  |

|                    |  |
|--------------------|--|
| DFO–2006 timescale | Dome Fuji ice core timescale (2006 version)  |
| $D_R$              | Dose rate; a quantification of the amounts of naturally occurring ionizing radiation at a site   |
| EAM                | East Asian Monsoon   |
| EASM               | East Asian Summer Monsoon  |
| EAWM               | East Asian Winter Monsoon  |
| EDC3 timescale     | EPICA Dome C timescale (2007 version)  |
| $ED_e$             | Estimated Equivalent Dose; sensitivity–corrected net luminescence signal   |
| $ED_R$             | Estimated Dose Rate  |
| EI                 | Electron Impact; method used to ionise and fragment substances in GC–MS  |
| ENSO               | El Niño/Southern Oscillation   |
| EPICA Dome C       | European Project for Ice Coring in Antarctica Dome C; extraction location of the EPICA Dome C ice core   |
| Event Free Depth   | Composite depth of the Suigetsu cores with all instantaneous events >5mm removed; used for age–depth modelling   |
| FAMEs              | Fatty Acid Methyl Esters   |
| $F_w$              | Water absorption factor; proportion of external radiation dose absorbed by water in a matrix   |
| GC                 | Gas chromatography; used for separating substances in a mixture  |
| GC–FID             | Gas chromatography – flame ionisation detector; used for the separation and detection of organic substances in a mixture   |
| GC–IRMS            | Gas chromatography – isotope ratio mass spectrometer (also known as GC–py–IRMS or GC–TE–IRMS when connected via a furnace); used to measure the isotope composition of components in a mixture |
| GC–MS              | Gas chromatography – mass spectrometer; used for the separation, detection and identification of substances in a mixture   |
| GICC05 timescale   | Greenland Ice Core Chronology timescale (2005 version)   |
| GISP               | Greenland Ice Sheet Precipitation; isotope standard for water  |
| GMWL               | Global Meteoric Water Line; describes the global annual average relationship between $\delta^{18}O$ and $\delta^2H$  |
| GRIP               | Greenland Ice Core Project   |
| GS/GI              | Greenland Stade/Greenland Interstade   |
| GSSP               | Global Boundary Stratotype Section and Point; international stratigraphic boundary denoting an interval of geological time   |
| H1/H11             | Heinrich Event 1/Heinrich Event 11   |
| ICP–MS             | Inductively Coupled Plasma – Mass Spectrometry; used for elemental analysis  |
| ICP–OES            | Inductively Coupled Plasma – Optical Emission Spectrometry; used for elemental analysis  |
| IntCal             | International radiocarbon calibration curve; iterations include IntCal13 (2013 version) and IntCal20 (2020 version)  |
| IntCal20 yr BP     | Years before AD 1950, calibrated using the IntCal20 radiocarbon calibration curve; used interchangeably with “cal BP” unless specified   |

|              |  |
|--------------|--|
| Interstade   | Short term (millennial-scale) period of warmer temperatures (also known as “interstadial conditions”)  |
| IR           | Infrared   |
| IRMS         | Isotope Ratio Mass Spectrometer; used to determine the isotope composition of a sample   |
| IRSL         | Infrared Stimulated Luminescence   |
| ITCZ         | Inter-Tropical Convergence Zone  |
| ITRAX        | XRF core scanner   |
| J            | Natural remanent magnetisation   |
| ka BP        | Thousand years before AD 1950; generally referring to a non-radiocarbon-derived age, but calculated relative to the radiocarbon chronological datum of AD 1950 |
| ka           | Thousand years   |
| LGM          | Last Glacial Maximum   |
| LL-channel   | Sediment core subsampling equipment; similar to a U-channel  |
| MAAT         | Mean Annual Air Temperature  |
| Marine20     | International marine radiocarbon calibration curve, 2020 version   |
| MCS          | In-house carbonate standard for the British Geological   |
| Survey       |  |
| MIS X        | Marine Isotope Stage X; e.g., Marine Isotope Stage 1, MIS1   |
| MS           | Mass Spectrometer  |
| MSD          | Mass Spectrometer Detector   |
| MTCO         | Mean Temperature of the Coldest month; typically derived from pollen analysis  |
| MTWA         | Mean Temperature of the Warmest month; typically derived from pollen analysis  |
| OSL          | Optically Stimulated Luminescence  |
| PDO          | Pacific Decadal Oscillation  |
| PIRSL        | Portable Infrared Stimulated Luminescence  |
| PIRSLnet     | Net Portable Infrared Stimulated Luminescence signal (total minus background)  |
| PMF          | Polymineral Fine fraction of a sediment sample   |
| PMF-blue     | Blue light stimulated luminescence signal from the fine grained polymineral fraction of a sediment sample  |
| PMF-IR       | Infrared stimulated luminescence signal from the fine grained polymineral fraction of a sediment sample  |
| POSL         | Portable Optically Stimulated Luminescence   |
| POSLnet      | Net Portable Optically Stimulated Luminescence signal (total minus background)   |
| QF           | Quartz Fine fraction of a sediment sample  |
| QF-blue      | Blue light stimulated luminescence signal from the fine grained quartz-dominated fraction of a sediment sample   |
| RSL          | Relative Sea Level   |
| SEM          | Scanning Electron Microscope   |
| Sens         | Dose sensitivity of a sediment sample  |
| SG timescale | Current (2023) version of the pre-50 ka BP (i.e., non-radiocarbon) Suigetsu core age-depth model timescale   |
| SG06_2012    | Preliminary timescale associated with the SG06 core, 2012 version; subsequently updated to the IntCal20 timescale  |
| SGXX         | Specific Suigetsu sediment core; e.g., SG06; extracted in 2006   |

|                                     |   |
|-------------------------------------|---|
| SLAP(2)                             | Standard Light Antarctic Precipitation; “2” denotes second standard version; isotope standard for water   |
| Stade                               | Short term (millennial-scale) period of colder temperatures (also known as “stadial conditions”)  |
| SST                                 | Sea Surface Temperature   |
| TAF                                 | Total Acid Fraction (of lipids), consisting of A1 and A2 (n-alkanoic acid) fractions  |
| TAR                                 | Terrestrial to Aquatic Ratio (of n-alkanes); measure of the concentration of long-chained (terrestrial) to short-chained (aquatic) n-alkanes  |
| TI                                  | Glacial Termination I; the transition from MIS 2 to MIS 1   |
| TII                                 | Glacial Termination II; the transition from MIS 6 to MIS 5e   |
| TL                                  | Thermoluminescence  |
| TLE                                 | Total Lipid Extract; isolated from a sample by accelerated solvent extraction   |
| TN                                  | Total Nitrogen content  |
| TNF                                 | Total Neutral Fraction (of lipids), consisting of N1 (n-alkanes), N2, N3 and N4 fractions   |
| TOC                                 | Total Organic Carbon content  |
| U-Th                                | Uranium-thorium dating; used for determining the age of carbonates  |
| U-Th timescale                      | Timescale based on uranium-thorium dating; common timescale for speleothem records  |
| Varve                               | A deposit of sediment which has accumulated during the course of a year; annual sediment layer; may be comprised of seasonal sub-layers   |
| VPDB                                | Vienna Pee Dee Belemnite; isotope standard for carbonates   |
| VSMOW(2)                            | Vienna Standard Mean Ocean Water; “2” denotes second standard version; isotope standard for water   |
| WAIS Divide                         | West Antarctic Ice Sheet Divide; extraction location of the WAIS Divide ice core  |
| WD2014 timescale                    | WAIS Divide ice core timescale (2014 version)   |
| XGT                                 | X-ray fluorescence analytical microscope; used for elemental analysis   |
| <sup>x</sup> H                      | Isotope of hydrogen (x = 1 or 2 in the context of this thesis)  |
| <sup>x</sup> O                      | Isotope of oxygen (x = 16 or 18 in the content of this thesis)  |
| XRF                                 | X-Ray Fluorescence; used for elemental analysis   |
| YD                                  | Younger Dryas Stade; late glacial stadial in the North Atlantic   |
| yr BP                               | Years before AD 1950; generally referring to a non-radiocarbon-derived age, but calculated relative to the radiocarbon chronological datum of AD 1950   |
| δ                                   | Delta notation; used when stable isotope compositions are presented relative to the composition of a standard material ( $\delta = ((\text{sample} - \text{standard})/\text{standard}) * 1000$ ); units ‰ |
| δ <sup>13</sup> C                   | Measure of the ratio of stable carbon isotopes <sup>13</sup> C and <sup>12</sup> C in a sample  |
| δ <sup>13</sup> C <sub>diatom</sub> | Carbon isotope composition of diatom silica   |
| δ <sup>13</sup> C <sub>org</sub>    | Carbon isotope composition of organic matter  |
| δ <sup>15</sup> N                   | Measure of the ratio of stable nitrogen isotopes <sup>15</sup> N and <sup>14</sup> N in a sample  |
| δ <sup>15</sup> N <sub>diatom</sub> | Nitrogen isotope composition of diatom silica   |

|  |  |
|--|--|
| $\delta^{18}\text{O}$                        | Measure of the ratio of stable oxygen isotopes $^{18}\text{O}$ and $^{16}\text{O}$ in a sample                                     |
| $\delta^{18}\text{O}_{\text{diatom}}$        | Oxygen isotope composition of aquatic diatom silica  |
| $\delta^{18}\text{O}_{\text{ice}}$           | Oxygen isotope composition of ice  |
| $\delta^{18}\text{O}_{\text{lake}}$          | Oxygen isotope composition of lake water   |
| $\delta^{18}\text{O}_{\text{precipitation}}$ | Oxygen isotope composition of precipitation  |
| $\delta^{18}\text{O}_{\text{speleothem}}$    | Oxygen isotope composition of speleothem calcite   |
| $\delta^2\text{H}$                           | Measure of the ratio of stable hydrogen isotopes $^2\text{H}$ and $^1\text{H}$ in a sample   |
| $\delta^2\text{H}_{\text{acid}}$             | Compound-specific hydrogen isotope composition of n-alkanoic acids   |
| $\delta^2\text{H}_{\text{CXXacid}}$          | Compound-specific hydrogen isotope composition of n-alkanoic acids with XX carbon atoms; e.g., $\delta^2\text{H}_{\text{C30acid}}$ |
| $\delta^2\text{H}_{\text{lake}}$             | Hydrogen isotope composition of lake water   |
| $\delta^2\text{H}_{\text{precipitation}}$    | Hydrogen isotope composition of precipitation  |
| $\delta^{30}\text{Si}$                       | Measure of the ratio of stable silicon isotopes $^{30}\text{Si}$ and $^{28}\text{Si}$ in a sample                                  |
| $\delta^{30}\text{Si}_{\text{diatom}}$       | Silicon isotope composition of diatom silica   |
| $\delta_{\text{lake}}$                       | Isotope composition of lake water; collective term for $\delta^{18}\text{O}$ , $\delta^2\text{H}$ and d-excess of lake water       |
| $\delta_{\text{precipitation}}$              | Isotope composition of precipitation; collective term for $\delta^{18}\text{O}$ , $\delta^2\text{H}$ and d-excess of precipitation |
| $\delta_{\text{river}}$                      | Isotope composition of river water; collective term for $\delta^{18}\text{O}$ , $\delta^2\text{H}$ and d-excess of river water     |
| $\Delta T$                                   | Temperature change   |
| $\varphi$                                    | Absorbed dose fraction; proportion of internal dose absorbed by the grains in a matrix   |
| $\chi$                                       | Low-field magnetic susceptibility  |

# Chapter 1 Introduction

This chapter provides context for the research presented in this thesis, the focus of which is reconstructing East Asian Monsoon behaviours in Japan across Glacial Terminations I and II using isotope-based proxies derived from the Lake Suigetsu sediment cores. Section 1.1 introduces monsoon systems, their characteristics and locations. The East Asian Monsoon is then highlighted in Section 1.2, which describes the seasonal configurations of this system, the range of drivers acting on different timescales, and the significance of the East Asian Monsoon for the vast population living under its influence. Section 1.3 provides the rationale for this thesis by highlighting the value of palaeo-East Asian Monsoon reconstructions, the limitations of current records and the potential of records from Japan, before introducing the specific aim and objectives of this research. Key contextual information regarding Lake Suigetsu and its surrounding catchment is provided in Section 1.4, including a description of the geographical setting, local climate, previous coring campaigns, core chronological control and existing palaeoenvironmental studies. The structure of the thesis, including a summary of each of the chapters, is given in Section 1.5. Section 1.6 introduces stable isotopes and the techniques employed in this thesis, providing background information for non-specialists.

## 1.1 Monsoon Systems

Monsoons are highly dynamic energetic systems associated with semi-annually reversing prevailing winds and form a key component of the global climate system (Webster *et al.*, 1998; Wang *et al.*, 2012; Chen *et al.*, 2019). Earth's major monsoon systems (Figure 1.1) can be thought of as both regionally confined with individual features, and components of a unified “global monsoon”, which operates under the influence of common drivers (Mohtadi *et al.*, 2016; Geen *et al.*, 2020). A traditional view of monsoon systems posits that they are large scale “sea-breezes”, driven by the thermal contrast between land and ocean, which generates a strong low-level atmospheric pressure gradient and surface-propagating winds (Kitoh, 2017). During summer the direction of monsoonal winds is from ocean to land before reversing during winter and flowing from land to ocean (Overpeck *et al.*, 1996; Sanyal and Sinha, 2010). More recently, this perspective has been challenged, and some tropical

monsoons are now sometimes thought of as operationally closer to convergence zones (eddy driven) than sea-breezes (thermally driven) (Geen *et al.*, 2020). Regardless of their ultimate driver, the strong seasonality of each monsoon system is underpinned by semi-annually reversing regional pressure gradients, and it is this behaviour which defines the summer and winter modes of each monsoon system (Webster *et al.*, 1998). Monsoon systems are highly complex, because they exist at the interface of atmospheric and oceanic processes and interact with regional topographic features (Berkelhammer *et al.*, 2010; Geen *et al.*, 2020). Hence, their behaviours are difficult to predict and attract a significant amount of research.

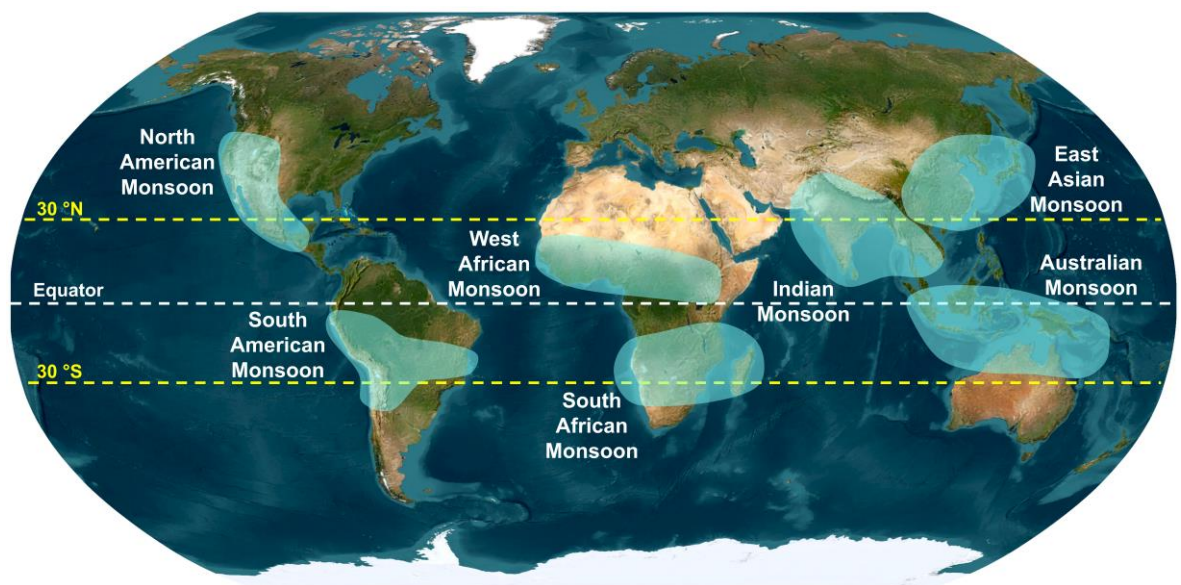


**Figure 1.1 Key monsoon regions across the globe.** Figure adapted from Dominguez *et al.*, 2020. Basemap is World Imagery from Esri (2023a) with a Robinson projection (scale 1:81,435,618).

Monsoons are fundamentally the propagation of winds across the surface, but such winds can interact with water sources and topography to generate precipitation; these processes are unique to the geographic setting of each specific monsoon system, however the direction of the prevailing winds normally results in a precipitation-bearing summer monsoon which originates in the oceanic domain and a dry winter monsoon which originates in the terrestrial domain (Wang *et al.*, 1999; Sanyal and Sinha, 2010). Indeed, in many monsoon regions, this summer precipitation is intense and forms a significant proportion of annual freshwater delivery (Sandeep *et al.*, 2017). The heavy precipitation which accompanies summer monsoon regimes across the globe is perhaps the

defining characteristic of a monsoonal climate, and hence descriptions of the monsoon are increasingly becoming focussed on evolving precipitation patterns (both in terms of temporal and spatial distribution), rather than the underlying behaviour of the prevailing winds (Kitoh, 2017).

## 1.2 The East Asian Monsoon

### 1.2.1 Overview

The East Asian Monsoon (EAM) is an eminent example of a highly seasonal monsoon system, consisting of East Asian Summer Monsoon (EASM) and East Asian Winter Monsoon (EAWM) modes (Figure 1.2). Both the EASM and EAWM are distinctive components of climate across vast areas of China, Korea and Japan (He *et al.*, 2017b; Chen *et al.*, 2019). The EAM is unusual because it is at least partially subtropical, in contrast to most monsoon systems which exist within the confines of the tropics (Figure 1.1; Liu *et al.*, 2013; Geen *et al.*, 2020). As such, the region can exhibit four seasons within a single year, although the EASM and EAWM are still highly dominant features (Yihui and Chan, 2005). Some authors consider the EAM a hybrid of tropical and subtropical monsoons (Yihui and Chan, 2005), meaning that the behaviour of the EAM system is driven by a combination of processes within and outside of the tropics. Indeed, the EAM is demonstrably controlled by the behaviours of pressure and frontal systems acting in East Asia at different times of the year, but predominantly by the pressure gradient between Continental Asia and the Pacific Ocean.

During boreal summer (June to August), south–easterly EASM winds operate across East Asia, accompanied by high temperatures and heavy precipitation (Lau and Li, 1984; Xu *et al.*, 2013; Chowdary *et al.*, 2019). These winds are brought about by low pressure over south Asia (the Asiatic Low) to the west and high pressure over the mid–latitude Pacific Ocean (the Western Pacific Subtropical High) to the east, which determine the precipitation characteristics of the EASM by channelling moisture–rich air northwards from the Western Pacific Warm Pool (Figure 1.2; Kurita *et al.*, 2015; Xu *et al.*, 2020; Yang *et al.*, 2022). In this region the evaporation rates are high due to elevated sea surface temperatures (Yang *et al.*, 2022). As it propagates across south China, Japan and Korea, EASM precipitation forms a band, known as the EASM front, or “Meiyu” in

China, “Baiu” in Japan and “Changma” in Korea, which delivers intense precipitation between late May and early July (Yang *et al.*, 2022) and weakens as it moves northwards (Geen *et al.*, 2020). The EASM precipitation front dissipates in northern China, but downstream influences of the EASM can be observed up to 55 °N, which includes Mongolia and parts of Russia (Liepe *et al.*, 2015). During the summer months, when the EASM front has propagated northwards, the climate of East Asia can be thought of as dominantly controlled by the Pacific air mass (Nakagawa *et al.*, 2006).

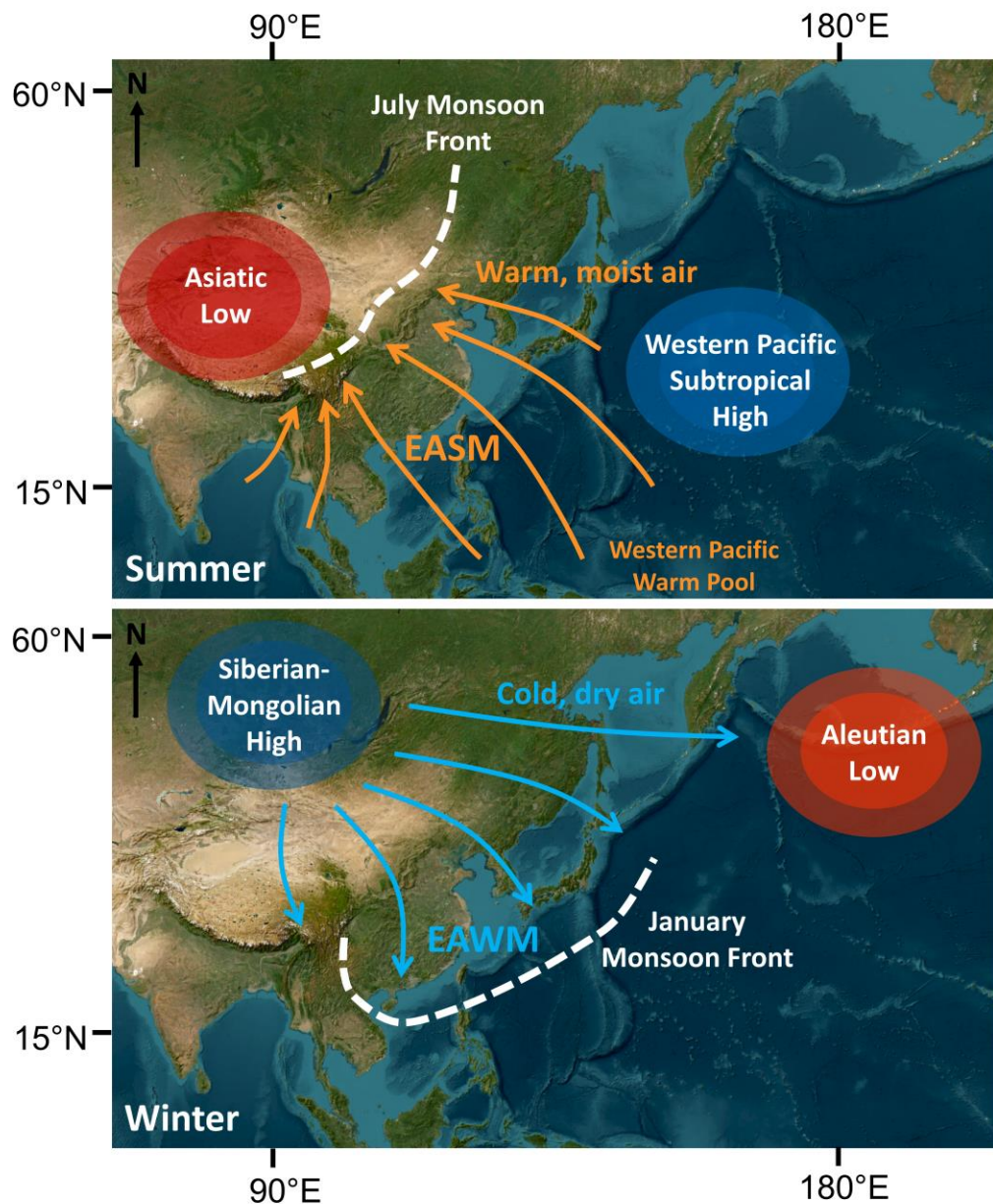


**Figure 1.2 The seasonal modes of the East Asian Monsoon system.** Schematic diagrams showing both EASM and EAWM behaviours across the East Asian Monsoon region. The upper panel shows the key pressure and frontal systems for the EASM, and the lower panel for the EAWM. Arrows show the direction of the prevailing winds. Basemap is a composite World Imagery satellite image from Esri (2023b) with a Mercator projection (scale 1:45,567,224).

During the boreal winter (December to February), the north–westerly EAWM winds dominate East Asia, accompanied by low temperatures and little to no precipitation (Xu *et al.*, 2013; Chowdary *et al.*, 2019; Ma *et al.*, 2020). These winds are directed by high pressure over Siberian Russia (the Siberian–Mongolia High) to the west and low pressure over the north Pacific Ocean (the Aleutian Low) to the east (Figure 1.2; Wang *et al.*, 2012; Ma *et al.*, 2020). Cold and dry conditions are characteristic of much of East Asia during the EAWM, but an exception to this pattern is Japan, which receives heavy snowfall between December and February due to the interaction of EAWM winds with warm surface waters delivered to the Sea of Japan by the Tsushima Current (Gallagher *et al.*, 2015; Amekawa *et al.*, 2021). The maximum extent of EAWM influence is commonly thought of as the South China Sea, however the effect of the EAWM can propagate downstream across the Pacific region and towards the southern hemisphere via interconnected climate systems (Ma *et al.*, 2020). During the winter months, when the EAWM front has propagated southwards, the climate of East Asia can be thought of as dominantly controlled by the continental/Siberian air mass (Nakagawa *et al.*, 2006).

### 1.2.2 Drivers

The EAM is highly dynamic and is controlled by the interconnected behaviour of tropical and extratropical components of the global climate system (Yihui and Chan, 2005; Mohtadi *et al.*, 2016). This results in a vast array of EAM drivers, each of which can influence monsoon winds or precipitation on different timescales. Many of these drivers are related and the propagation of feedbacks can act to amplify or diminish monsoonal change (Webster *et al.*, 1998; Jin *et al.*, 2014; Mohtadi *et al.*, 2016). In many ways, the EAM region can be considered a critical intersection for other regional systems and is demonstrably sensitive to both proximal and remote climatic perturbations, either via common drivers or the propagation of inter–regional teleconnections. As such, it is important to not underestimate the complexity of EAM system behaviour. Drivers act by perturbing one or more elements of the EAM system climate configuration. This includes the pressure and frontal systems described above, as well as components such as Western Pacific Warm Pool evaporation, which contributes to moisture delivery to East Asia during the EASM. Drivers which affect an element common to both the EASM and EAWM will affect both seasonal modes

and drivers which alter an element unique to either summer or winter will only affect one mode. The drivers discussed subsequently are considered in order of the timescales at which they have greatest effect on EAM strength, however some drivers could theoretically act across different timescales if they triggered conditions which persisted for longer or shorter intervals than conventionally observed or reconstructed.

On orbital timescales, EAM strengthening and weakening (both in terms of wind strength and precipitation quantity) is dominantly controlled by fluctuations in Northern Hemisphere insolation which affect the intensity of the land–ocean pressure gradient (Mohtadi *et al.*, 2016; Shi, 2016). This is predominately controlled by the precession of the Earth’s axis with a cyclical period of 23 ka; intervals where the Northern Hemisphere is closer to the Sun increase the amount of insolation reaching the low latitudes and are associated with a stronger EASM (Wang *et al.*, 2008; Thomas *et al.*, 2015). Obliquity cycles (with a cyclical period of 41 ka) also impact on the EAM system but this effect is indirect and predominately driven by changes in cryosphere behaviour; the expansion of Northern Hemisphere ice sheets causes EASM strengthening via strengthening of the Western Pacific Subtropical High and a positional shift of the jet stream (Mohtadi *et al.*, 2016) and EAWM strengthening by decreasing continental temperatures (Chen *et al.*, 2019). Clemens *et al.* (2018) suggested that these effects could be more dominant than precession cycles and that the direct response of monsoon strength to insolation was instead an artefact of speleothem reconstructions, but this is still debated. It is possible that a relationship between EAM strength and atmospheric CO<sub>2</sub> concentration also exists on orbital timescales, however isolation of these effects is difficult to achieve because they coincide with significant changes to insolation and ice cover (Zhang *et al.*, 2013; Mohtadi *et al.*, 2016).

It is on millennial timescales that the coherency of orbital forcing is lost. Under these circumstances EAM strength can become decoupled from insolation and instead the dominant drivers become disturbances in Earth’s atmosphere and ocean circulations (which are often coupled themselves). A key component of these shifts is the expansion and contraction of the meridional (Hadley and Ferrell) and polar atmospheric circulation cells and repositioning of the ITCZ (Wang *et al.*, 2005; Wang *et al.*, 2010; Liang *et al.*, 2020). As such, EAM

behaviour on millennial timescales is affected by the interhemispheric temperature gradient, which controls ITCZ movement (Han *et al.*, 2016; Liang *et al.*, 2020). This rearrangement is further associated with shifting upper tropospheric westerly and polar jets, as well as movement of the lower tropospheric westerlies and trade winds (Chowdary *et al.*, 2019; Ma and Chen, 2021). There is also evidence to support the influence of remote climatic change on EAM strength (teleconnections) via such mechanisms; most notably, changes in the North Atlantic region (relating to the behaviour of the Atlantic Meridional Overturning Circulation (AMOC)) have been suggested to affect the EASM by impacting on both the ITCZ and the westerly jet (e.g., Chiang *et al.*, 2015; Zhang *et al.*, 2019). It has been posited that the westerly jet shifts southwards during periods of AMOC slow-down, which weakens the Western Pacific Subtropical High and reduces EASM strength (Kubota *et al.*, 2019).

On shorter timescales (annual to multidecadal), other atmospheric and oceanic phenomena can also influence EAM strength. This includes both tropical and extratropical oceanic oscillations, such as El Niño/Southern Oscillation (ENSO) and the Pacific Decadal Oscillation (PDO), which affect EASM strength by altering the position and strength of the Western Pacific Subtropical High (Cai and Tian, 2016; Zhang *et al.*, 2019; Xu *et al.*, 2020; Yang *et al.*, 2022), and the Arctic Oscillation (AO), which affects EAWM strength by altering the strength of Siberian High and the polar and subtropical jets (He *et al.*, 2017b). It follows that ENSO can further affect EASM strength by altering sea surface temperatures (and hence the amount of evaporation) in the Western Pacific Warm Pool. The interconnected nature of the Earth's climate system causes other short-term climatic disturbances to affect EAM strength (albeit to different extents). This includes sunspot activity and ejection of sulphates into the atmosphere by volcanic eruptions (Mohtadi *et al.*, 2016).

### 1.2.3 Significance

The EAM influences the hydrology of a vast area (~10 million km<sup>2</sup>) and affects over 1.6 billion people across the region who rely on monsoonal freshwater delivery for agricultural, industrial and domestic purposes (Kitoh, 2017). Understanding the monsoon system is critical because changes to the behaviour of this system can spatially and temporally redistribute this precipitation and

bring about natural hazards such as floods and droughts (Chen *et al.*, 2019), the impact of which is enhanced by the presence of large, densely populated areas within the EAM regime (Webster *et al.*, 1998; Wang *et al.*, 2005; Park *et al.*, 2019). Additionally, this can have adverse effects on regional economies and social development (Lau and Li, 1984; Vuille *et al.*, 2005; Chowdary *et al.*, 2019). Not only this, but the monsoon has important cultural and religious associations (Li *et al.*, 2014), inspires artistic interpretation, and has been associated with social stability on historical timescales (Zhang *et al.*, 2008; Tan *et al.*, 2011). This highlights the multifaceted importance of the EAM and reiterates the necessity of understanding EAM behaviour for future monsoon prediction in a changing climate (Mohtadi *et al.*, 2016; Chen *et al.*, 2019).

## 1.3 Thesis Rationale

### 1.3.1 The Palaeo–East Asian Monsoon

Contemporary climate records lack observational data from the breadth of conditions and duration of time required to fully understand the behaviours of climate systems. As a result, the development of extended palaeoclimate records is an international scientific priority (Mohtadi *et al.*, 2016). Due to the dynamism, complexity, and significance of the EAM, it follows that a network of high-resolution records of EAM behaviour are important for better comprehension of this system. The highest calibre examples of such records (which exemplify the resolution, duration and age control required to thoroughly study EAM behaviours) are from speleothems in China, which provide indications of EASM evolution on orbital and suborbital timescales. Indeed, for many years the “model” EASM record was derived from an oxygen isotope ( $\delta^{18}\text{O}$ ) record from Hulu Cave, eastern China (Wang *et al.*, 2001). This has subsequently been supplemented by other renowned stalagmite  $\delta^{18}\text{O}$  records from across the country, including Sanbao Cave (Wang *et al.*, 2008), Dongge Cave (Yuan *et al.*, 2004) and Linzhu Cave (Zhang *et al.*, 2019), which are often employed in regional composite records of EASM behaviour (e.g., Cheng *et al.*, 2016). Other palaeoclimate archives have also contributed to the regional network of records, including Lake Huguang Maar (Yancheva *et al.*, 2007), the Dahu Peat (Zhong *et al.*, 2011) and ocean cores from the South China and East China Seas (e.g., Wang *et al.*, 1999). Conflicting interpretations from these records have formed the

basis of the evidence for the EAM drivers discussed above in Section 1.2.2, predominantly supporting Northern Hemisphere insolation as the dominant driver on orbital timescales (Wang *et al.*, 2008), with varying influences of atmospheric and oceanic drivers on suborbital timescales. The considerable complexity of the EAM system means that a common approach is to rationalise observations of the system by evoking mechanisms based on evidence, thereby contributing to the collective knowledge of EAM behaviour.

### 1.3.2 Challenges and Uncertainties

Considering the impacts of recent anthropogenically-driven climate change, understanding EAM behaviour during periods of warming is critical. However, East Asian climate variability during such periods remains poorly understood, especially compared to better-constrained climate systems such as the North Atlantic (Duan *et al.*, 2019; Xue *et al.*, 2019). This is the case for the two most recent major warming periods of the Late Pleistocene: the last and penultimate glacial terminations (Termination I (TI), from Marine Isotope Stage 2 (MIS 2) to MIS 1, and Termination II (TII), from MIS 6 to MIS 5e). Glacial terminations are key features of Quaternary climate change which are characterised by the rapid global transition from glacial to interglacial conditions and associated with increasing Northern Hemisphere summer insolation, heightening atmospheric greenhouse gas concentrations, rising sea levels and the decay of northern hemisphere ice sheets (Denton *et al.*, 2010; He *et al.*, 2017b; Duan *et al.*, 2019). TI and TII are ideal intervals for studying EAM evolution with rising global temperatures because they are accessible (in terms of archive preservation) and exemplify contrasting deglacial climate sequences with distinct end member conditions, allowing for consideration of how the EAM behaves under different circumstances.

Generally, EASM strengthening and EAWM weakening are associated with the transition from glacial to interglacial conditions (Gallagher *et al.*, 2018; Zhang *et al.*, 2019); due to the close relationship between EASM strength and Northern Hemisphere summer insolation, some of the most significant and rapid late Quaternary changes in EAM strength occurred during glacial terminations (Yuan *et al.*, 2004; Wang *et al.*, 2008; Cheng *et al.*, 2016). However finer resolution (millennial, centennial and decadal) fluctuations across TI and TII are

inadequately constrained, and mechanisms are largely undefined. Indeed, monsoonal responses to stage–interstage fluctuations during deglacial periods are spatially and temporally heterogeneous, likely resulting from the complex drivers of the EAM and the transient and/or spatially restricted teleconnections operating across the region. For example, there is conflicting evidence for the presence of “Younger Dryas”–type cold reversals (which are typified by North Atlantic climate records) during both transitions (Yoshida and Takeuti, 2009; Hayashi *et al.*, 2010; Shen *et al.*, 2010; Duan *et al.*, 2019; Xue *et al.*, 2019). Current evidence suggests that these North Atlantic–style inversions only occur in EAM records from regions and/or time periods where there was a teleconnection to propagate this signal between the North Atlantic and the EAM region (Yoshida and Takeuti, 2009; Gallagher *et al.*, 2018; Nakagawa *et al.*, 2021).

The uncertainty associated with deglacial EAM behaviours from during T1 and TII is largely due to the lack of long, high resolution, well–dated palaeo–EAM records. As is often the case with palaeoclimate records, there are considerably more records from recent intervals, such as the Holocene, where archive materials are better preserved. Records which span the full transition from glacial to interglacial conditions are relatively rare (Liepe *et al.*, 2015). Furthermore, producing well–constrained age models for many archives is difficult, due to the availability of chronometers (e.g., plant macrofossils for radiocarbon dating, carbonates for uranium–thorium dating, quartz/feldspar for optically stimulated luminescence dating) and the limitations of dating techniques; this is particularly relevant to TII, which is beyond the limit of radiocarbon dating. It is for these reasons that there is a substantial bias towards speleothem records in the EAM region. These are undoubtedly useful; however, they only provide a single EAM proxy ( $\delta^{18}\text{O}$ ), with  $\delta^{13}\text{C}$  interpreted as a proxy for temperature, and  $\delta^{18}\text{O}$  is widely interpreted as a proxy for EASM strength, which results in the other mode, the EAWM, remaining poorly researched. Moreover, it is worth noting that there is conflicting evidence for the drivers of speleothem  $\delta^{18}\text{O}$ , which adds additional uncertainty to our comprehension of EAM dynamics. The limited spatial coverage of speleothem records means that peripheral areas of the EAM region, which are arguably more sensitive to externally–forced change, are critically understudied (Liepe *et al.*, 2015).

### 1.3.3 East Asian Monsoon Reconstructions from Japan

The unique location of Japan within the EAM region results in a rare expression of EAM precipitation as the monsoon front progresses over the country during both summer and winter (Gallagher *et al.*, 2018). The Japanese archipelago is located between two large water bodies; the Sea of Japan to the northwest and the Pacific Ocean to the southeast, and as a result the wind trajectories of both EAM modes pass over a moisture source, become water saturated, and liberate precipitation over Japan (Hayashi *et al.*, 2010). As a result, a semi-annual (winter and summer) precipitation pattern is typical of central Japan, particularly for areas on the Sea of Japan coast, where the balance of EASM and EAWM influences is more equal (Yoshida and Takeuti, 2009; Shen *et al.*, 2010; Sone *et al.*, 2013). More specifically, it is the interaction of cold EAWM winds with warm surface waters from the Tsushima Current in the Sea of Japan which results in heavy snowfall in Japan between December and February, and the interaction of EASM winds with warm surface waters between the Western Pacific Warm Pool and the Pacific coast of Japan which causes heavy rainfall to propagate northwards across the country across June and July (Schmidt *et al.*, 2019). Precipitation is generally reduced in the intervening seasons (spring and autumn) aside from short-term intense rainfall associated with cyclonic typhoon events between August and October (Schlolut *et al.*, 2014). It is this unique hydrological distribution which makes studying past EAM evolution in Japan valuable for our comprehension of both EASM and EAWM modes in isolation, because both are detectable in their own right.

Despite this capacity for valuable EAM reconstructions from Japan, there are significantly fewer available than for the continental EAM region. Indeed, a large proportion of records from the Japanese Islands are derived from either pollen-based reconstructions of climate (Yoshida and Takeuti, 2009; Hayashi *et al.*, 2010; Liepe *et al.*, 2015; Nakagawa *et al.*, 2021) or reconstructions of lake productivity via biological proxies (Ishiwatari *et al.*, 2009; Urabe *et al.*, 2014). Whilst stalagmite reconstructions of EAM behaviour across TI in Japan exist (Sone *et al.*, 2015; Mori *et al.*, 2018; Amekawa *et al.*, 2021), they are in the minority and seldom extend across a full glacial termination. The reconstruction of temperature from pollen data via a modern analogue technique is well established for Japan (Nakagawa *et al.*, 2002; Nakagawa *et al.*, 2021), but the

reconstruction of precipitation is associated with much greater uncertainty, making it harder to accurately obtain an indication of EAM behaviour (Schlölaut *et al.*, 2017). EAM reconstructions based on measures of lake productivity are also inherently flawed, because they commonly make assumptions that lake changes are related to large scale climatic processes, rather than local/catchment behaviours. Furthermore, they assume that this behaviour can be ascribed to a single season, which, given the expression of the EASM and EAWM precipitation in Japan, is highly unlikely. It is for these reasons that efforts to synthesise records of EAM intensity often also omit Japan and the Korean Peninsula, despite the region's potential to offer a wealth of information relating to large scale reorganisation of the monsoon system and its influences (e.g., Wang *et al.*, 2010).

### **1.3.4 Thesis Aims**

This thesis is motivated by significant uncertainty surrounding the behaviour of the EASM and EAWM during periods of warming and the response of EAM strength to rising temperatures. This manifests as spatially and temporally heterogeneous EAM behaviours across glacial terminations as reconstructed by palaeoclimate records, particularly in terms of a monsoonal response to stage–interstage fluctuations. Understanding deglacial monsoon dynamics is critical, given the significant impact of the EAM on East Asia and the vulnerability of this region to extreme weather events related to changes to EAM behaviour in light of anthropogenic climate change. Additionally, the positioning of the EAM and close relationship with other regional climate systems means that an improved comprehension of the dynamics and drivers of the EAM with rising temperatures can contribute to a better understanding of the global climate system as a whole. In many ways, tackling the complexity of the EAM system and its relationship to processes across the globe is crucial for progressing our knowledge of climate behaviours worldwide. A means to achieving this is via a more widespread network of palaeo–EAM records which can probe EAM evolution across a breadth of conditions on long timescales. Of particular interest is EAM behaviour across the last two glacial terminations (TI and TII) because they typify accessible, contrasting examples of rapid global warming. However, besides a small number of records (which are dominantly derived from Chinese speleothems), the vast majority are lacking the temporal coverage, sampling

resolution and high-quality chronological control required to effectively examine deglacial monsoon dynamics across these intervals. An exciting, yet currently untapped, prospect is the development of palaeo-EAM records from Japan, which has a unique hydroclimate that is both dominated by EAM precipitation but also exhibits tangible seasonal expressions of EASM and EAWM behaviour.

The overall aim of this thesis is *to deconvolve East Asian Monsoon evolution in Japan during the last two glacial terminations.*

Subsidiary objectives are:

1. To contribute new records of palaeo-EAM behaviour to the growing regional record network,
2. To consider the response of the EAM to warming temperatures,
3. To deconvolve the different behaviours of the two seasonal modes of the EAM,
4. To determine the persistence of teleconnections and signal transfer into the EAM region,
5. And to rationalise spatial heterogeneities in these behaviours across the region.

This aim and these objectives are met by the construction of EAM records across TI and TII using materials from the Lake Suigetsu sediment cores, a palaeoclimate archive of exceptional quality located in central Japan. The Lake Suigetsu sediment cores are optimised for this research because they comprise materials from both TI and TII in the same archive, are constrained by high-quality chronological control, have significant potential for seasonal-specific multiproxy analysis and preserve conditions within an area which receives a balanced amount of contemporary EASM and EAWM precipitation annually.

## **1.4 Lake Suigetsu, Japan**

### **1.4.1 Setting**

The Five Lakes of Mikata (35° 35' N, 135° 53'E) are a collection of tectonic lakes located near the towns of Wakasa and Mihama on the Sea of Japan coast of

Fukui Prefecture, Honshu Island, Central Japan (Figure 1.3; Shigematsu *et al.*, 1961; Albert *et al.*, 2019; Nakagawa *et al.*, 2021). The lakes are located less than 2 km from the active Mikata fault line, running north–south to the side of the lakes, and have formed via the subsidence of the western side of the fault through time (Schlolaut *et al.*, 2018). The five–lake system consists of Lake Suigetsu, Lake Mikata, Lake Suga, Lake Kugushi and Lake Hiruga. Lake Suigetsu and Lake Suga are closely interconnected by a wide channel with a gentle slope, making Lake Suga effectively a side–basin of Lake Suigetsu (Schlolaut *et al.*, 2014). In the early stages of the lake system, (prior to ~130,000 yr BP), the area was fluvial–lacustrine, and as accommodation space was created by movement of the Mikata fault, the lakes have developed into their current configuration. Lake Suigetsu is surrounded by steep Palaeozoic hillsides for much of its perimeter and has a relatively small direct catchment area (8.3 km<sup>2</sup>) relative to its surface area (4.2 km<sup>2</sup>) (Suzuki *et al.*, 2016; Albert *et al.*, 2019). As a result of anthropogenic activity (discussed further below), the lakes are situated at modern day sea level (McLean *et al.*, 2019).

The main source of freshwater to the lakes is via the Hasu River (~10 km length) to the south (Schlolaut *et al.*, 2014; McLean *et al.*, 2018). In the past, the Hasu River entered Lake Suigetsu via low ground to the east of Lake Suga, but at 39,200 cal BP this channel was shifted in a westerly direction (possibly by tectonic activity) and from this point onwards, freshwater has flowed into Lake Suigetsu via Lake Mikata (Schlolaut *et al.*, 2014). A shallow (< 4 m) sill between the two lakes (the Seto Channel) prevents coarse detrital material from Lake Mikata entering Lake Suigetsu and only fine allochthonous and authigenic material is found in Lake Suigetsu post–39,200 cal BP (Shigematsu *et al.*, 1961; Nakagawa *et al.*, 2012; Schlolaut *et al.*, 2014).

Previously, Lake Suigetsu was persistently freshwater, with an outflow to Wakasa Bay via the Kiyama River, aside from during the Eemian and mid–Holocene global sea level highstands, when evidence from diatom assemblage counts supports saline conditions (Nakagawa *et al.*, 2021). Additionally, saline water incursion into Lake Suigetsu has occurred annually since AD 1664, when the Urami Canal was opened to connect Lake Suigetsu with Lake Kugushi (and thus Wakasa Bay). This was devised to create an outlet for excess water following the AD 1662 Kanbun earthquake, when the bed of the Kiyama River was raised and the

surrounding area flooded (Kawakami *et al.*, 1996; Suzuki *et al.*, 2016). As a result, Lake Suigetsu has been meromictic since AD 1664; the upper mixolimnion (to ~ 8 m depth) is oxic and brackish and the lower monimolimnion is anoxic and saline. In the present day, the lakes have all been artificially connected to each other and all show some degree of salinity (Table 1.1; Section 2.4.1); Lake Mikata is connected to Lake Suga by the Horikiri Channel and Lake Suigetsu is connected to Lake Hiruga by the subterranean Saga Tunnel. Lake Hiruga and Lake Kugushi are then connected directly to Wakasa Bay by the Hiruga Waterway and Hayase River, respectively (Staff, 2011).

### 1.4.2 Climate

The modern-day climate at the Five Lakes of Mikata is temperate and monsoonal, being situated extra-tropically and beneath the seasonally migrating EAM front (Nakagawa *et al.*, 2006). This climate is typical of areas situated on the Sea of Japan coast of Honshu Island. The region experiences four distinct seasons each year (Figure 1.4; Japanese Meteorological Agency). During winter, temperatures are low (January mean = 4.3 °C) and the area experiences large quantities of precipitation in the form of both snowfall and rainfall, delivered to the catchment by the EAWM (winter mean = 233 mm per month). Spring is the driest season of the year, commonly associated with mild temperatures (April mean = 12.6 °C). During the summer months, temperatures are high (July mean = 25.6 °C) and there are significant amounts of rainfall, predominately supplied by the propagation of the Baiu (EASM) front across Japan during July (July mean = 184 mm per month). Autumn is mild once again (October mean = 17.6 °C), and often associated with large quantities of rainfall brought by typhoons, which can pass over the region between August and early October (typhoon season mean = 185 mm per month) (Schlollaut *et al.*, 2014). The dominance of EAWM and EASM precipitation in the region annually suggests that the location of Lake Suigetsu is optimised for reconstructing the behaviour of both seasonal modes of the EAM (Nakagawa *et al.*, 2006; Nakagawa *et al.*, 2012). This quality is enhanced by the relative seasonal balance between summer and winter precipitation, which is improved by the location of the lake on the Sea of Japan coast, which experiences a more direct influence of EAWM precipitation relative to other parts of Japan (Nakagawa *et al.*, 2006; Sone *et al.*, 2013).

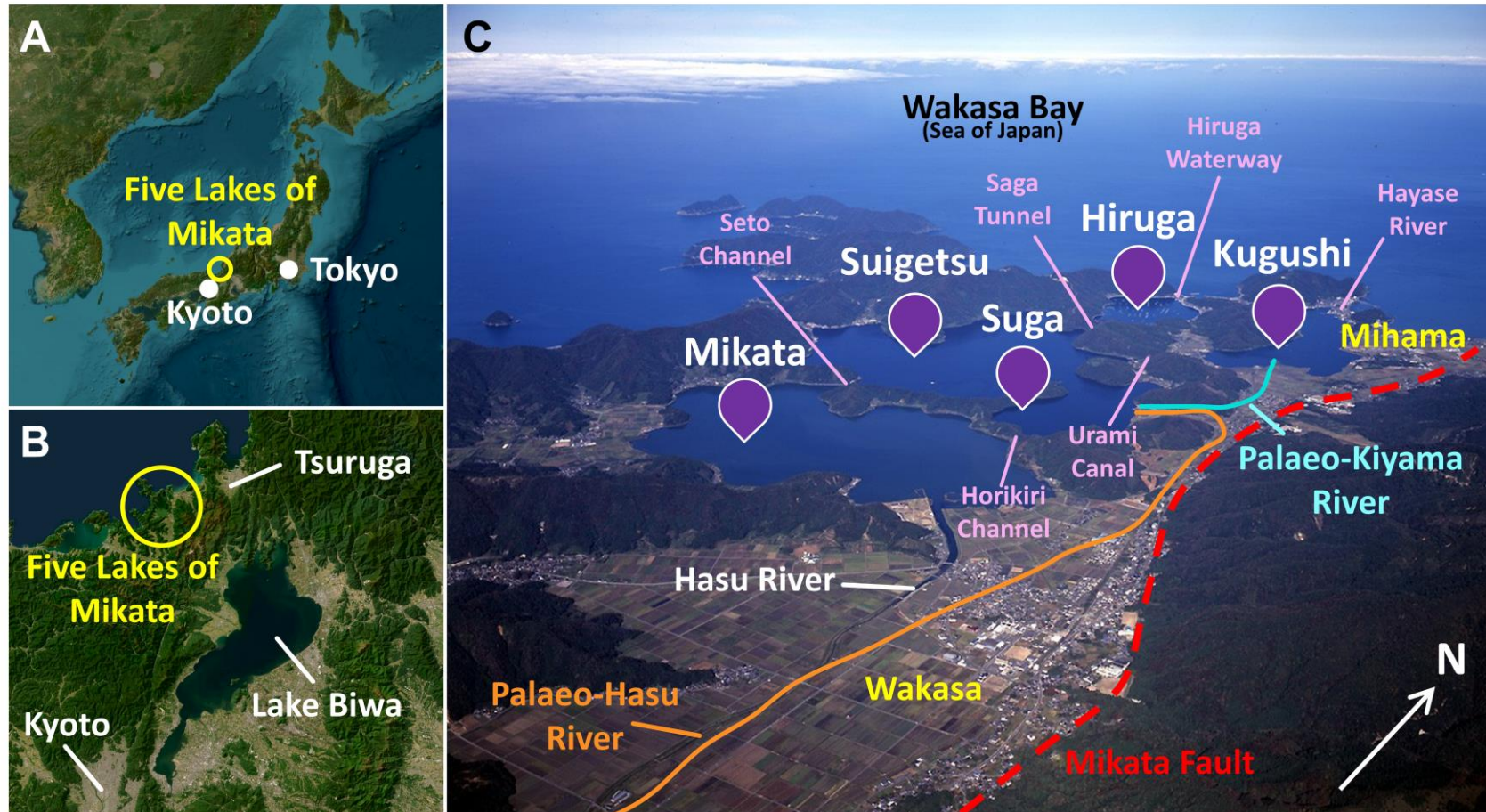


**Figure 1.3 Location and setting of Lake Suigetsu and the Five Lakes of Mikata.** Panel A shows the location of the lakes relative to major Japanese cities on Honshu Island (Basemap is World Imagery from Esri (2023c) with a Compact Miller projection (scale 1:7,851,046)). Panel B shows the location of the lakes relative to Kyoto and Lake Biwa (Basemap is World Imagery from Esri (2023d) with a Compact Miller projection (scale 1:439,079)). Panel C is an aerial photo taken from the southeast (provided by T. Nakagawa) and shows the setting of the lakes, key features of the surrounding area, channels and tunnels connecting the lakes to one another, and the location of the palaeo Hasu and Kiyama rivers.

**Table 1.1 Physical characteristics of the modern Five Lakes of Mikata.** Data from Shigematsu *et al.* (1961). Freshwater is defined as having a salinity of  $<0.5 \text{ g kg}^{-1}$ , brackish water as having a salinity of  $0.5$  to  $10 \text{ g kg}^{-1}$ , and saline water as having a salinity of  $>10 \text{ g kg}^{-1}$ .

| Lake     | Area (km <sup>2</sup> ) | Maximum Depth (m) | Salinity                     |
|----------|-------------------------|-------------------|------------------------------|
| Mikata   | 3.61                    | 5.8               | Fresh to brackish            |
| Suigetsu | 4.20                    | 34.0              | Meromictic – brackish/saline |
| Suga     | 0.82                    | 12.5              | Meromictic – brackish/saline |
| Kugushi  | 1.45                    | 2.5               | Saline                       |
| Hiruga   | 4.16                    | 38.5              | Saline                       |

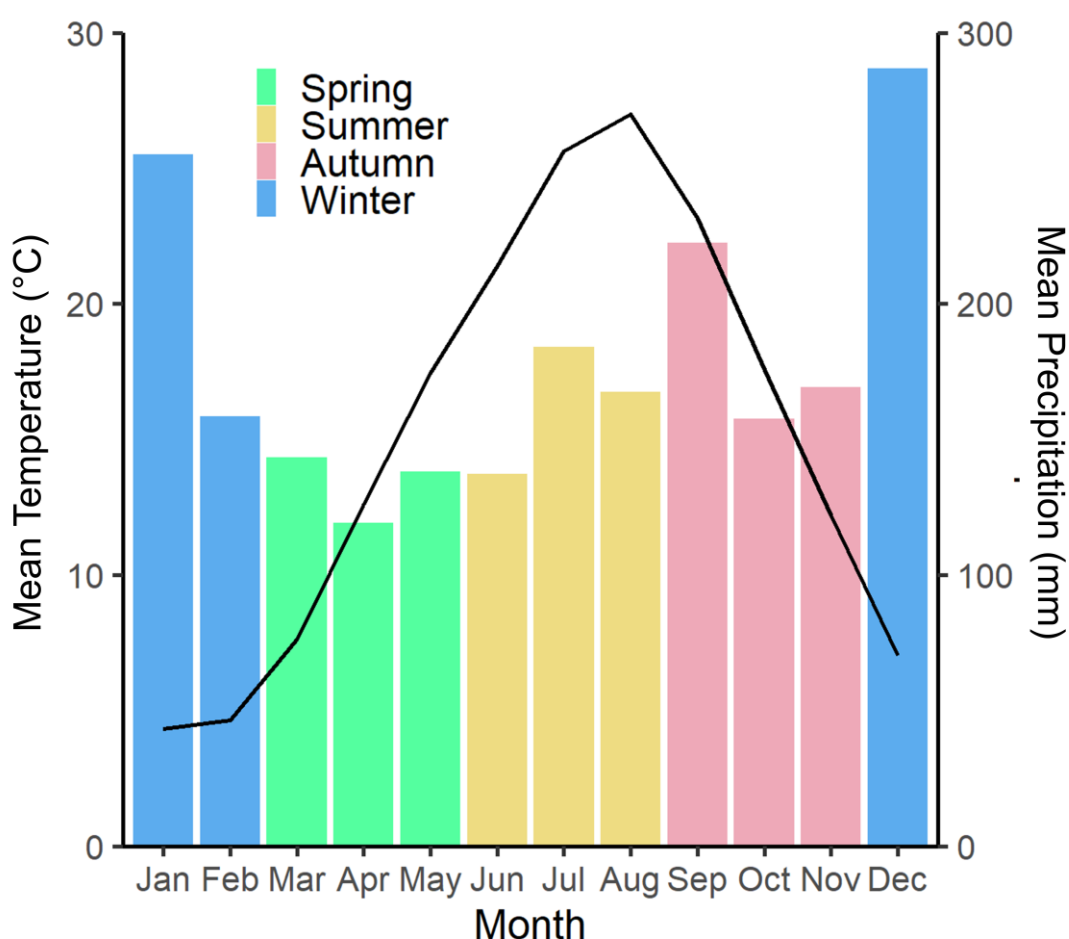


**Figure 1.4 Climate at the Five Lakes of Mikata.** Monthly average temperature (line graph) and precipitation data (bar chart) from the Japanese Meteorological Association Mihama weather station. Observation interval: January 1990 to February 2022.

### 1.4.3 Coring Campaigns

Research relating to Lake Suigetsu has been driven partially by the unique characteristics of Lake Suigetsu in the modern day as a meromictic lake with distinctive chemical profiles (e.g., Matsuyama, 1974; Masuzawa and Kitano,

1982b; Kondo *et al.*, 2014) but principally by the rare characteristics of the sediment underlying the lake itself. Initial deep coring of Lake Suigetsu in 1993 (producing the “SG93” core) revealed the presence of annual laminations (varves) persisting across large sections of sediment depth, caused by pale and dark layers relating to mineral-rich and diatom-rich materials, respectively (Figure 1.5; Kitagawa and Van der Plicht, 1998). This was the first example of varved sediments in Japan and has subsequently inspired over 30 years of Suigetsu-related research across different facets of Quaternary Science. Motivated by this discovery, subsequent deep coring campaigns (Figure 1.6) took place in 2006 (“SG06” core), 2012 (“SG12” core) and 2014 (“SG14” core). Each of these cores consists of overlapping sections (usually between 1–2 m in length) from four parallel boreholes situated ~20 m apart; a “master core” for each was constructed by aligning these overlapping sections via distinctive marker layers (Figure 1.7; Albert *et al.*, 2019). This approach was taken to avoid interruptions in the sedimentation due to material lost during the coring process (between successive core sections; Staff *et al.*, 2010). The most recent (2014) campaign extracted sediments extending as far as the basal gravel layer beneath Lake Suigetsu (McLean *et al.*, 2018).

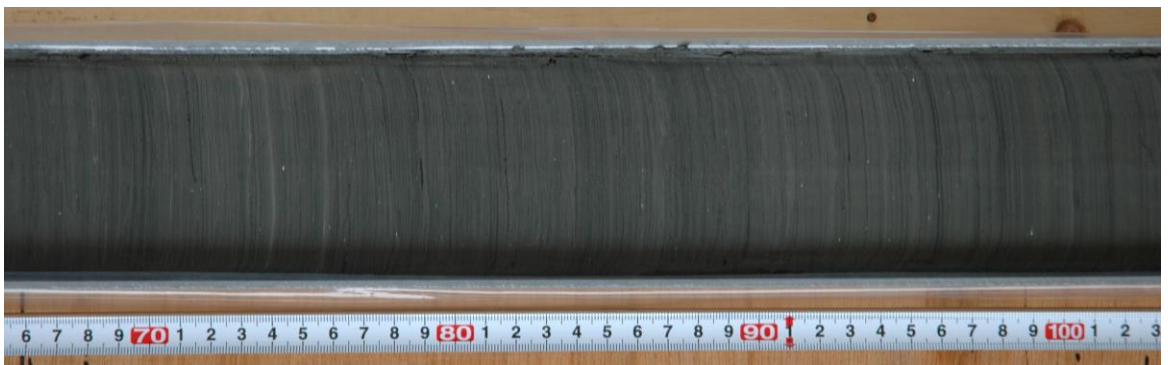


**Figure 1.5 Core image showing presence of annual laminations (varves).** Image shows excellent sediment structure preservation and continuous varving within the SG06 core. Sediments are from core section A(N)17 (~41,000 yr BP) (provided by T. Nakagawa).

The result of these coring campaigns is a palaeoclimate archive of exceptional quality which spans the history of sedimentation at Lake Suigetsu (i.e., from the present day to in excess of 150,000 yr BP (MIS 6)) (Nakagawa *et al.*, 2012; McLean *et al.*, 2018). The preserved sequence, covering >98 m of composite sediment depth, encapsulates two glacial and two full interglacial periods of continuous sedimentation, i.e., there are no stratigraphic gaps (Nakagawa *et al.*,

2021). Within this temporal coverage, the Suigetsu cores contain continuous, countable varves between ~50,000 and ~10,000 yr BP, providing the longest continuously varved record from the Quaternary, and discontinuous varves between ~71,000 and ~50,000 yr BP (Schlolut *et al.*, 2012; Nakagawa *et al.*, 2012; Schlolut *et al.*, 2018). The presence of these varves strongly supports excellent preservation of material from Lake Suigetsu by means of bottom–water anoxia (which prevents bioturbation of sediment), the interception of high–energy hydrological processes by Lake Mikata (Nakagawa *et al.*, 2021), and physical protection by the deep water column and the steep–sided hills that surround the lake (Staff, 2011). A full description of the sedimentary structure of the cores from a microscopic (individual varve; Figure 1.8) to facies level is provided by Schlolut *et al.* (2012) and Schlolut *et al.* (2018).



**Figure 1.6 Photograph of the coring rig during the SG12 campaign.** Image shows the hydro–pressure piston sampler mounted on a floating coring rig (provided by T. Nakagawa).

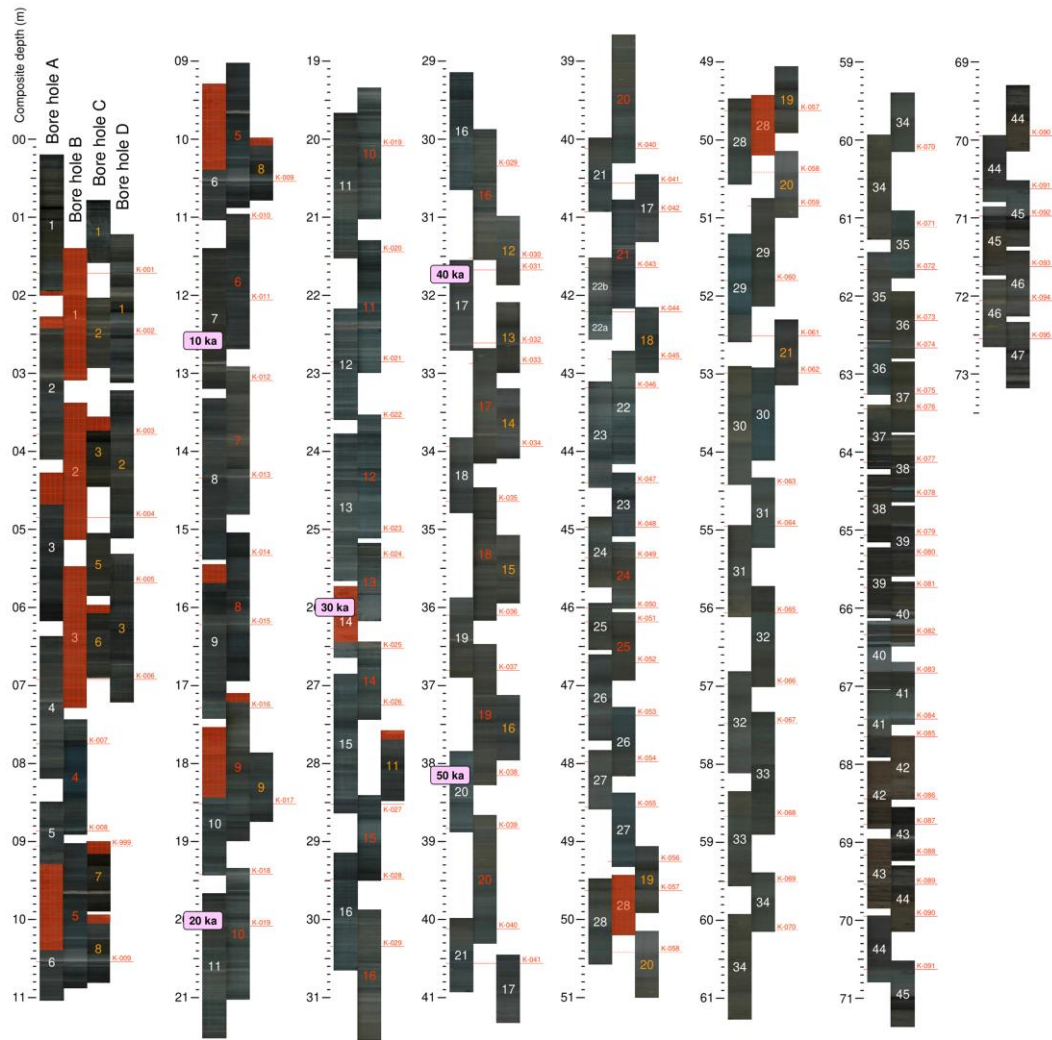


**Figure 1.7 Core photographs of the SG06 archive.** Overlapping core sections showing 73.4 m of continuous sedimentation (i.e., no stratigraphic gaps). Provided by T. Nakagawa and adapted from Nakagawa *et al.* (2012).

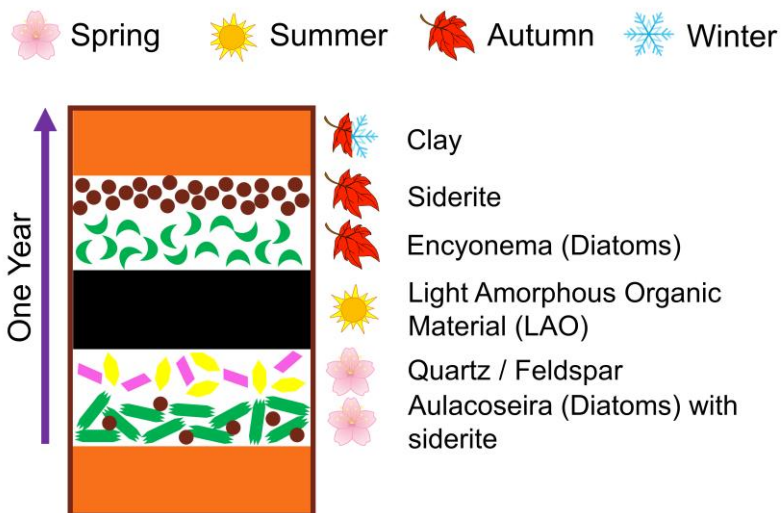


**Figure 1.8 The idealised varve structure.** Seasonal layers expressed in a singular annual layer (varve) within the Suigetsu sediment cores. Adapted from Scholaut *et al.* (2012).

#### 1.4.4 Chronological Control

The current age model for the Suigetsu sediment cores employs Bayesian age–depth modelling using the OxCal software package (Bronk Ramsey, 2009; Bronk Ramsey and Lee, 2013). The age model was constructed using a variety of chronological techniques for different sections of the cores; radiocarbon dating of plant macrofossils, varve counting, use of tephra tie points, and “climatic wiggle matching”. This current iteration was produced based on the SG06 core, because this was the material utilised for the most recent varve count and was a significant focus for radiocarbon dating. However, the chronology can be transferred between cores due to robust sedimentological description of all core sections and alignment of each master core using distinctive marker horizons (McLean *et al.*, 2018). The excellent preservation of material in Lake Suigetsu aids this correlation because there are extremely limited differences between the four deep cores and hence, they are almost identical replicates of each other. Between the base of the core and 50,300 yr BP, age control is given by wiggle matching of the relative abundance of *Cryptomeria* pollen grains in SG06 to the same quantity in Pacific Ocean core MD01–2421, offshore Japan (Oba *et al.*, 2006; Franke *et al.*, in prep). A singular absolute tie point provided by Ar–Ar dating of the Aso–4 volcanic eruption at 86,400 yr BP was incorporated into this wiggle matching process (Albert *et al.*, 2019). MD01–2421 was previously aligned to the Pacific regional benthic stack (Lisiecki and Stern, 2016), which facilitates alignment of the Suigetsu cores to other palaeoclimate archives.

Between 50,300 yr BP and 13,900 yr BP, age control is provided by radiocarbon dating and varve counting. First, a preliminary age scale was generated by combining uncalibrated radiocarbon dates (Bronk Ramsey *et al.*, 2020) with a varve chronology constructed via thin section microscopic varve counts (Schlolut *et al.*, 2012; Schlolut *et al.*, 2018) and interpolation of sections of poor lamination quality (Schlolut, 2018). The radiocarbon dates consist of those directly determined from the SG06 cores (Staff *et al.*, 2011; Bronk Ramsey *et al.*, 2012) and those determined from the SG93 cores and subsequently updated onto the SG06 depth scale (Kitagawa and Van Der Plicht, 2000; Staff *et al.*, 2013). This preliminary age scale was then modelled onto the Hulu Cave radiocarbon dataset to reduce the cumulative varve count uncertainty by taking advantage of the shared structure between the Suigetsu and Hulu datasets

(Bronk Ramsey *et al.*, 2020). The resulting age scale forms the Lake Suigetsu contribution to the IntCal20 radiocarbon calibration curve (Heaton *et al.*, 2020; Reimer *et al.*, 2020). IntCal20 modelling subsequently generated IntCal20 ages for each Suigetsu radiocarbon date. Hence, ages for this interval of the Suigetsu cores are given on the IntCal20 timescale (i.e., IntCal20 yr BP, or cal BP).

Between 13,900 yr BP and the top of the cores, age control is provided by radiocarbon dating, varve counting and dated event layers. An age model was generated by combining uncalibrated radiocarbon dates with four tie points: the Iz-Kt tephra originating from the AD 838 eruption of Kozushima (McLean *et al.*, 2018), the KGP tephra from the ~BC 1200 eruption Kawagodaira (McLean *et al.*, 2018), the B-Tm tephra from the “Millennium Eruption” of Changbaishan (McLean *et al.*, 2016) and the connection of Lake Suigetsu with the Sea of Japan in AD 1664 (Saito-Kato *et al.*, 2013). For the varved sections of this interval, varve counting was used as the depth unit in the OxCal model, and for non-varved sections, “event-free” depth was used as the depth unit. Event-free depth was defined as composite depth with all instantaneous events greater than 5 mm removed (Schlolut *et al.*, 2014; Staff *et al.*, in prep). This construction was then modelled onto the portion of the IntCal20 radiocarbon calibration curve covered by tree ring datasets to generate an age model on the IntCal20 timescale (Staff *et al.*, in prep). The older (>13,900 yr BP) and younger (<13,900 yr BP) radiocarbon-based age models were modelled with equivalent rigidity (linearity) and tied at the depth corresponding to 13,900 yr BP to avoid inconsistencies (Staff *et al.*, in prep). Across the interval 50,300 to 0 yr BP, over 800 radiocarbon dates contribute to the Suigetsu sediment core age model. This high dating density, combined with the contribution of the Suigetsu sediment cores to the IntCal13 and IntCal20 calibration curves (as the only solely atmospheric record beyond the limit of tree rings; Reimer *et al.*, 2014; Reimer *et al.*, 2020), is why the Suigetsu chronology is widely thought of as world leading.

Previous iterations of the age model utilised  $\mu$ XRF (ITRAX) core scanning for varve counting (Marshall *et al.*, 2012), however these results no longer contribute due to varve counting errors across periods of low sedimentation rate (e.g., the last glacial maximum) (Schlolut *et al.*, 2018). Current research is investigating radiocarbon dating of pollen grains from the cores to provide an

even higher density of radiocarbon ages within the 50,300 to 0 yr BP interval (Yamada *et al.*, 2021). High resolution tephra analysis has been conducted for the core, including geochemical identification of numerous eruptions (e.g., Smith *et al.*, 2013; McLean *et al.*, 2016; McLean *et al.*, 2018; Albert *et al.*, 2019), but aside from the ones noted above, these do not contribute to the age model because they do not reduce uncertainty in the radiocarbon dataset. The Suigetsu age model has, however, been utilised to date eruptions from across the region preserved within the cores, e.g., the eruptive history of Aso, Sambe, Changbaishan and Ulleungdo volcanoes (Albert *et al.*, 2018; McLean *et al.*, 2019; McLean *et al.*, 2020).

### 1.4.5 Palaeoenvironmental Investigation

The composition of the Lake Suigetsu sediment cores makes it ideal for multiproxy analysis, and the potential of the cores for reconstructing past environmental change (both locally to the catchment and regionally to East Asia) has been previously identified (Nakagawa *et al.*, 2012). Of particular note is the extensive high-resolution palynological investigation which has been conducted on the Suigetsu cores (e.g., Nakagawa *et al.*, 2003; Yasuda *et al.*, 2004; Nakagawa *et al.*, 2006; Nakagawa *et al.*, 2021). Much of this has focussed on applying a modern analogue technique (Nakagawa *et al.*, 2002) to raw pollen counts to reconstruct both annually-averaged and seasonally-weighted temperature and precipitation, with particular focus on the transition from glacial to interglacial transitions across TI (Nakagawa *et al.*, 2021). It was found that temperatures at Lake Suigetsu exhibited a similar structure to records from the North Atlantic during this interval, including a “late glacial interstade” (“Bølling-Allerød”-type event) and “late glacial stade” (“Younger Dryas”-type event) superimposed on an overall increase in temperature between the Last Glacial Maximum (LGM) and the Holocene (Nakagawa *et al.*, 2021). Whilst the onset of the late glacial stade and the Holocene were synchronous between Japan and the North Atlantic, the transition into the late glacial interstade in Japan occurred ~200 years earlier than the Bølling-Allerød in the North Atlantic, attributed to a sudden northwards movement of the westerly jet occurring asynchronously with AMOC behaviours (Nakagawa *et al.*, 2021). This determination of temperature structure established by pollen species change at Lake Suigetsu was also utilised by Walker *et al.* (2009) in defining the Holocene

onset, and the site was designated as an auxiliary Global Boundary Stratotype Section and Point (GSSP). Precipitation reconstructions based on the pollen dataset, alongside diatom assemblage counts and the aforementioned  $\mu$ XRF elemental composition dataset, were also used to demonstrate a bi-partite structure to the late glacial stage at Lake Suigetsu, with cooling and increasingly wet conditions in the first half, followed by cold and wet conditions in the second (Schlolut *et al.*, 2017). Extension of the high-resolution pollen climate reconstruction for Lake Suigetsu continues to be a priority.

On a more local scale, analysis has been focussed on changes to lake productivity and geochemistry across climatic transitions, including reconstructions of total organic carbon (Pearson *et al.*, 2014), chlorine-specific carbon and nitrogen isotopes (Tyler *et al.*, 2010) and diatom assemblage counts (Kossler *et al.*, 2011). The location of Lake Suigetsu within a region affected by typhoons and adjacent to the Sea of Japan and the Mikata fault line also ideally positions the archive for reconstructions of earthquake, flood and tsunami behaviours (Kawakami *et al.*, 1996; Saito-Kato *et al.*, 2013; Schlolut *et al.*, 2014; Suzuki *et al.*, 2016). More recently, research (including this thesis) has begun to focus on the potential of the Lake Suigetsu sediment cores for reconstruction of EAM behaviour, in light of its location within the climate regime and motivated by the uncertainty associated with precipitation reconstructions generated from the pollen dataset. These studies are utilising isotope-based reconstructions from authigenic sedimentary organic compounds, minerals and fossils to reconstruct EAM evolution. This includes diatoms, pollen grains, alkyl lipids, cellulose, and siderite. Isotope-based reconstructions are of particular interest because they have the potential to provide robust links to hydrological change on a regional scale.

## 1.5 Thesis Structure

This thesis realises the aim and objectives of this work through four interconnected research papers which either have undergone, or are intended for, publication in peer-reviewed journals (presented in Chapters 2–5; Figure 1.9). These research papers are supplemented by a summary and discussion of future work (Chapter 6) and the thesis conclusions (Chapter 7).

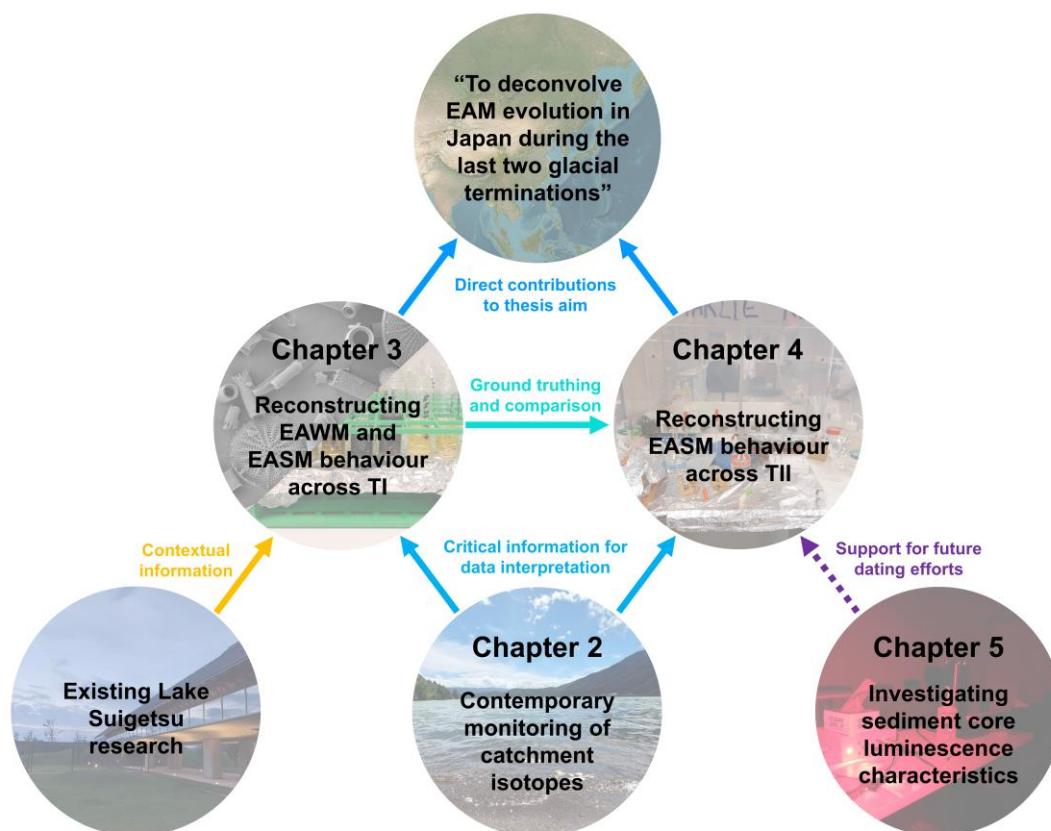


Figure 1.9 Summary of the structure of this thesis.

### 1.5.1 The Contemporary Stable Isotope Hydrology of Lake Suigetsu and Surrounding Catchment (Japan) and its Implications for Sediment Derived Palaeoclimate Records (Chapter 2)

Chapter 2 presents the results of contemporary monitoring of the stable isotope composition ( $\delta^{18}\text{O}$ ,  $\delta^2\text{H}$  and d-excess) of precipitation, river and lake waters within the Five Lakes of Mikata catchment, with a view to evaluating the factors affecting these quantities. This research paper examines signal transfer through the catchment to resolve the influence of precipitation isotope composition on the composition of Lake Suigetsu relative to local effects, and thus determine how isotope signals relating to regional-scale hydrological (i.e., climatic) change are propagated to the isotope composition of sedimentary organic compounds, minerals and fossils. The findings of this chapter facilitate the interpretation of isotope-based proxy reconstructions of past climate from the Lake Suigetsu sediment cores within the context of changes to the EAM. As a result, the outcomes of this research critically underpin Chapter 3 and Chapter 4. This

research paper has been published in *Quaternary Science Advances* (Rex et al., 2024).

### **1.5.2 Insights into Deglacial East Asian Monsoon Seasonality and Inter-Regional Teleconnections from Lake Suigetsu, Japan (Chapter 3)**

Chapter 3 uses materials from the Lake Suigetsu sediment cores to reconstruct the seasonal behaviours of the EAM across the last glacial termination (TI) using two isotope proxy systems: bulk oxygen isotope ratio analysis of diatom silica ( $\delta^{18}\text{O}_{\text{diatom}}$ ) and compound-specific hydrogen isotope ratio analysis of n-alkanoic acids ( $\delta^2\text{H}_{\text{acid}}$ ). EAWM and EASM evolution are examined separately, facilitated by the distinctive seasonality of each proxy. The behaviours of these proxies describe how EAM behaviour relates to increasing global temperatures and how the EAWM and EASM were affected by stade-interstade fluctuations in both the Northern and Southern Hemisphere. These reconstructions also offer the opportunity to study the remote climatic teleconnections acting on each seasonal EAM mode during this interval. These results are supported by observations in Chapter 2 and contribute to the comparison between deglacial monsoon behaviours during Terminations I and II presented in Chapter 4. This research paper has been submitted for publication in *Nature Communications*.

### **1.5.3 Novel Observations of East Asian Summer Monsoon Evolution During Glacial Termination II from Lake Suigetsu, Japan (Chapter 4)**

Chapter 4 reconstructs EASM behaviours across the penultimate glacial termination (TII) using compound-specific hydrogen isotope ratio analysis of n-alkanoic acids ( $\delta^2\text{H}_{\text{acid}}$ ) from the Suigetsu cores. Additional analyses (of n-alkanoic acid and n-alkane concentrations) are used to characterise environmental change at Lake Suigetsu and pinpoint shifts in catchment evolution across this hitherto poorly constrained interval of lake development. The behaviour of  $\delta^2\text{H}_{\text{acid}}$  is compared to other EASM records from across the region to examine the spatial heterogeneities of this system across Termination II. These results are also contrasted with equivalent measures ( $\delta^2\text{H}_{\text{acid}}$  and pollen-derived temperature) from Chapter 3 in order to analyse EASM behaviours across Termination I and Termination II in the context of their distinctive

climatic conditions. Like the results of Chapter 3, the results of this chapter are also strengthened by the findings of Chapter 2. This research paper has been submitted for publication in *Quaternary Science Reviews*.

#### **1.5.4 Controls on Luminescence Signals in Lake Sediment Cores: a Study from Lake Suigetsu, Japan (Chapter 5)**

Chapter 5 examines the luminescence characteristics of four intervals within the Lake Suigetsu sediment cores across the past 140,000 years to investigate the use of luminescence techniques for detecting environmental change. The selected intervals encompass a range of environmental contexts and are all significant on either a local or global scale. Rapid down-core profiling techniques (portable optically stimulated luminescence and laboratory profiling) are used to determine the versatility of such methods for examining environmental change using sediment cores. A secondary aim of this chapter is to assess the potential of the Lake Suigetsu sediments for age determination using Optically Stimulated Luminescence dating. Dating is not performed as part of this thesis, but these results will support future dating efforts and the extension of the existing high-resolution chronology past ~50,000 yr BP, which has particular relevance for EAM reconstructions from Termination II (e.g., Chapter 4). This research paper has been published in *Quaternary Geochronology* (Rex *et al.*, 2022).

#### **1.5.5 Summary and Future Work (Chapter 6)**

Chapter 6 provides a summary of the findings of Chapters 2 – 5, examines the results in the context of the aim and objectives of the thesis, evaluates the relevance and impact of the conclusions, and presents suggestions for further research.

#### **1.5.6 Conclusions (Chapter 7)**

Chapter 7 provides the conclusions of this thesis.

## 1.6 Introduction to Principal Thesis Techniques

### 1.6.1 Stable Isotopes

Stable isotopes are forms of an element with different numbers of neutrons and thus atomic masses. Unlike radioisotopes, stable isotopes do not undergo decay, making them useful for a variety of applications, including tracing the origin, history and interactions of substances (Tiwari *et al.*, 2015; IAEA, 2023). Both hydrogen and oxygen stable isotopes are widely utilised for the investigation and reconstruction of meteorological processes because these are the elements which comprise water (H<sub>2</sub>O). In a single water molecule, it is possible to have different combinations (known as isotopologues) of the naturally occurring hydrogen and oxygen stable isotopes: <sup>1</sup>H (hydrogen), <sup>2</sup>H (deuterium), <sup>16</sup>O (oxygen-16), <sup>17</sup>O (oxygen-17) and <sup>18</sup>O (oxygen-18) (Yoshimura, 2015). <sup>1</sup>H and <sup>16</sup>O are the most abundant, with <sup>1</sup>H accounting for 99.99 % of all hydrogen atoms and <sup>16</sup>O accounting for 99.76 % of all oxygen atoms (Rosman and Taylor, 1998). Absolute measurements of single isotope concentrations within a sample are difficult; hence, isotope compositions are most commonly expressed as a ratio of the rarer to the more abundant isotope in each pair (e.g., <sup>2</sup>H/<sup>1</sup>H) (Tiwari *et al.*, 2015). This ratio is reported relative to a standard of known composition (specific to the type of material being measured) in delta (δ) notation with units of per mille (per mil, parts per thousand, ‰) (Yoshimura, 2015). This allows for comparisons between datasets. For hydrogen and oxygen isotope compositions, the most common international reference materials (standards) are Vienna Standard Mean Ocean Water (VSMOW; for water samples) and Vienna Pee Dee Belemnite (VPDB; for carbonates). Others, such as Standard Light Antarctic Precipitation (SLAP), are sometimes used (Brand *et al.*, 2014).

Using a isotope ratio mass spectrometer (IRMS), the stable hydrogen isotope composition, δ<sup>2</sup>H, of a sample can be calculated by employing Equation 1.1.

$$\delta^{2}\text{H} (\text{‰}) = \left( \frac{\left( \frac{{}^{2}\text{H}}{{}^{1}\text{H}} \right)_{\text{sample}}}{\left( \frac{{}^{2}\text{H}}{{}^{1}\text{H}} \right)_{\text{standard}}} - 1 \right) \times 1000$$

Equation 1.1

Due to the relatively low abundance of  $^{17}\text{O}$ , the  $^{18}\text{O}/^{16}\text{O}$  ratio is the most commonly measured of the oxygen isotope ratios (Delaygue, 2009). Similarly to  $\delta^2\text{H}$ , the stable oxygen isotope composition,  $\delta^{18}\text{O}$ , of a sample can be calculated using Equation 1.2.

$$\delta^{18}\text{O} (\text{‰}) = \left( \frac{\left( \frac{^{18}\text{O}}{^{16}\text{O}} \right)_{\text{sample}}}{\left( \frac{^{18}\text{O}}{^{16}\text{O}} \right)_{\text{standard}}} - 1 \right) \times 1000$$

**Equation 1.2**

Stable isotope compositions are most useful in their ability to indicate processes which show mass-dependent fractionation, or the preferential inclusion or exclusion of one isotope or isotopologue over another due to differences in atomic mass (Dansgaard, 1964; Sauer et al., 2001). Fractionation can occur as a result of equilibrium exchange reactions, which redistribute isotopes with equal rates of forward and reverse transfers, and kinetic exchange reactions, where the rates of each transfer are unequal (Tiwari *et al.*, 2015). Equilibrium fractionation occurs when the substitution of a heavier isotope for a lighter isotope is favourable (Chacko et al., 2001), for example during the condensation of water vapour in rain clouds, whereby the heavier water isotopes ( $^{18}\text{O}$  and  $^2\text{H}$ ) become enriched in the liquid phase whilst the lighter isotopes ( $^{16}\text{O}$  and  $^1\text{H}$ ) remain in the gas phase (Bowen *et al.*, 2019). Some precipitation reactions can also occur in isotopic equilibrium at low temperatures (Tiwari *et al.*, 2015). In addition to equilibrium fractionation, many processes can be affected by kinetic fractionation (Kendall and Caldwell, 1998). Kinetic fractionation occurs when the rate of a chemical or physical process is different for different isotopes (Tiwari *et al.*, 2015). The evaporation of liquid water to form water vapour is associated with kinetic fractionation when the humidity is less than 100 %; during this process, the lighter isotopes become enriched in the gas phase and the heavier isotopes remain in the liquid phase, enhancing the degree of fractionation which would be expected under equilibrium conditions (Kendall and Caldwell, 1998; Bowen *et al.*, 2019). Biological processes are also often associated with kinetic fractionation (Kendall and Caldwell, 1998).

If the isotope composition of a sample of water derived from precipitation is controlled by equilibrium fractionation processes alone, a clear relationship between  $\delta^2\text{H}$  and  $\delta^{18}\text{O}$  is observed. This is defined by the Global Meteoric Water Line (GMWL) (Craig, 1961) which refers to the global average relationship of these isotope ratios in precipitation (Equation 1.3; Voelker et al., 2014). The exact composition of a sample along this line can be controlled by factors such as temperature, latitude and continentality; seasonality is often a notable feature (Jouzel, 2003). Due to the GMWL representing a global average of the  $\delta^2\text{H}$ – $\delta^{18}\text{O}$  relationship, it is possible to see different meteoric water lines (with different relationships between  $\delta^2\text{H}$  and  $\delta^{18}\text{O}$ ) for different regions (Putman *et al.*, 2019). A meteoric water line calculated for a given area is known as a Local Meteoric Water Line (LMWL) and can have a different slope and/or intercept to the GMWL, normally resulting from a difference in temperature and isotope composition range, or kinetic effects (Putman *et al.*, 2019; Lécuyer *et al.*, 2021). LMWLs are typically calculated using linear regression analysis.

$$\delta^2\text{H} = (8 \times \delta^{18}\text{O}) + 10$$

Equation 1.3

If a kinetic fractionation process occurs, such as evaporation, compositions will no longer conform to the GMWL relationship. It is for this reason that areas with a dominant evaporation control (a kinetic process) will be associated with water isotope compositions which lie away from the GMWL (Voelker et al., 2014). Due to the heavier masses of its isotopes, kinetic fractionation has a greater effect on the oxygen isotope composition of water than the hydrogen isotope composition (Bershaw, 2018). Hence, greater enrichment of  $^2\text{H}$  relative to  $^{18}\text{O}$  often results from kinetic fractionation processes. This is known as the “deuterium excess” (“d-excess”, expressed in per mille (‰); Dansgaard, 1964) and represents the offset between the isotope composition of a water sample and the GMWL. D-excess is considered a secondary stable isotope parameter because it is derived from  $\delta^2\text{H}$  and  $\delta^{18}\text{O}$  (Equation 1.4; Bershaw, 2018).

$$\text{d-excess (‰)} = \delta^2\text{H} - (8 \times \delta^{18}\text{O})$$

Equation 1.4

### 1.6.2 Water Isotope Analysis

Isotope analysis of water samples from a range of sources (including, but not limited to, precipitation, river water, lake water and groundwater) within a catchment can provide critical local and regional hydrological information (Wassenaar *et al.*, 2011). This technique is relatively straightforward: samples are obtained and sealed to prevent further fractionation with the air, before the ratio of heavy ( $^{18}\text{O}$  and  $^2\text{H}$ ) to light ( $^{16}\text{O}$  and  $^1\text{H}$ ) oxygen and hydrogen is measured using an isotope ratio mass spectrometer (IRMS) and compared to a standard to yield the stable oxygen ( $\delta^{18}\text{O}$ ) and hydrogen ( $\delta^2\text{H}$ ) isotope composition (Lacey and Jones, 2018). Secondary isotope parameters, such as deuterium excess (d-excess), can then be derived from these measurements (Machavaram and Krishnamurthy, 1995). The complexity of this method is more notable in the interpretation of the resulting dataset, which can be reflective of a range of processes which are unique to the specific study location. For example, the isotope composition of environmental waters can be influenced by both regional climatic processes (such as water source, fractionation along the air mass trajectory and seasonality) and local hydrologic processes (such as evaporation, mixing, and human influences), each of which must be considered during interpretation (Darling, 2004). However, when signals can be identified, this can provide indispensable information regarding how a catchment operates (Benson and White, 1994; Russell and Johnson, 2006; Gibson *et al.*, 2016). By considering any differences between contemporary and past catchment configurations and processes, these findings can provide essential evidence to support the interpretation of palaeo-isotope reconstructions of climatic and environmental change (e.g., Lacey and Jones, 2018).

### 1.6.3 Diatom Isotope Analysis

Diatoms are microscopic single-celled photosynthetic algae with a shell (also known as a frustule) composed of amorphous biogenic silica ( $\text{SiO}_2 \cdot n\text{H}_2\text{O}$ ). In lakes, they grow rapidly (and authigenically) during bloom season(s) each year (Leng and Barker, 2006). They are abundant across a range of lake types (even in low pH waters when carbonate preservation is poor) limited by nutrients, but also other factors including light, temperature and internal competition for resources, and the interactions between all of these (Leng and Barker, 2006;

Smith *et al.*, 2016). It has been estimated that there are over 30,000 species of diatoms globally (Mann and Vanormelingen, 2013), each with a unique, intricate frustule morphology. Different diatom species are adapted to different environmental conditions (e.g., salinity, pH and depth) which designates their classification (Fu *et al.*, 2022). After each diatom bloom, typically between 5 and 20 % of frustules settle out and are preserved in lake sediments (Leng and Barker, 2006), facilitating their use in studies of the past. Not only do species adaptations allow for the reconstruction of environmental conditions based on relative abundances (e.g., Saito-Kato *et al.*, 2013), but isotope analysis of the frustules can be an important tool in understanding palaeoenvironmental and palaeoclimatic change (e.g., Dean *et al.* 2018; Cartier *et al.*, 2019). Elemental isotope compositions, including  $\delta^{30}\text{Si}_{\text{diatom}}$ ,  $\delta^{13}\text{C}_{\text{diatom}}$  and  $\delta^{15}\text{N}_{\text{diatom}}$ , are all used to varying degrees for the reconstruction of nutrient availability and productivity, but the most common analysis performed on diatom frustules is the determination of the oxygen isotope composition ( $\delta^{18}\text{O}_{\text{diatom}}$ ), which reflects a combination of lake water temperature and composition during the bloom season (van Hardenbroek *et al.*, 2018) and hence has the strongest links to past climatic change.

In order to determine  $\delta^{18}\text{O}_{\text{diatom}}$ , samples of near-pure diatom material must first be prepared using a multi-step process of chemical treatment, density separations and filtering (e.g., Morley *et al.*, 2004; Swann and Snelling, 2023). If close to 100 % purification cannot be achieved, then a mass-balance approach must be taken to correct  $\delta^{18}\text{O}_{\text{diatom}}$ , because the measurement process liberates all oxygen from the sample (including that of contaminants; Brewer *et al.*, 2008). Samples are commonly checked for contamination using a combination of light microscopy, scanning electron microscopy, x-ray fluorescence and Fourier-transform infrared spectroscopy. Measurement is usually performed using step-wise fluorination, which removes the outer hydrous layer of each frustule with a stoichiometric deficiency of bromine pentafluoride ( $\text{BrF}_5$ ) before liberation of the remaining structural diatom oxygen with the same reagent, conversion to  $\text{CO}_2$  using graphite, measurement of the ratio of  $^{18}\text{O}$  to  $^{16}\text{O}$  using an IRMS and then comparison to standard materials to yield  $\delta^{18}\text{O}_{\text{diatom}}$  (Swann *et al.*, 2007; Leng and Sloane, 2008). The interpretation of  $\delta^{18}\text{O}_{\text{diatom}}$  records relies on a good understanding of lake seasonality (in order to derive the bloom season(s),

and hence any seasonal weighting of the preserved signals) and can be aided by complementary temperature and/or precipitation reconstructions to deconvolve the major drivers (Leng and Barker, 2006). Often,  $\delta^{18}\text{O}_{\text{diatom}}$  more closely reflects changes to lake and precipitation composition rather than temperature (van Hardenbroek *et al.*, 2018), and there is little to no evidence for disequilibrium effects beyond analytical error (Swann *et al.*, 2007; van Hardenbroek *et al.*, 2018).  $\delta^{18}\text{O}_{\text{diatom}}$  analysis has been employed in a growing number of studies for the reconstruction of hydroclimatic change (e.g., Rozanski *et al.*, 2010; Mackay *et al.*, 2011; Dean *et al.*, 2018; Mesiter *et al.*, in review).

#### 1.6.4 Alkyl Lipid Concentration and Isotope Analysis

Lipids are a broad group of organic compounds which, in the environment, are often derived from a specific source or process and hence are routinely used as “biomarkers” (Sauer *et al.*, 2001; Sachse *et al.*, 2012). Alkyl lipids are the key hydrophobic components of organic tissue and include n-alkanes, n-alcohols, saturated and unsaturated n-alkanoic acids, hydroxy n-alkanoic acids and alkenones (Holtvoeth *et al.*, 2019). A common feature of all of these compound classes are extended alkyl chains. Typically, long chain compounds (containing 26 or more carbon atoms) are a key component of terrestrial plant leaf waxes and short chain compounds (containing 21 or fewer carbon atoms) are derived from aquatic algae, whilst mid-length chain compounds come from submerged macrophytes (Castañeda and Schouten, 2011; Holtvoeth *et al.*, 2019), however the exact source of each homologue can vary on a site-by-site basis. N-alkanes and n-alkanoic acids are generally well preserved in lake sediments; aquatic lipids are preserved following migration through the water column after authigenic formation, and terrestrial lipids are delivered to the lake via wind or water erosion (Castañeda and Schouten, 2011). Lipid preservation, like with all organic matter, is enhanced in lakes with either permanent or seasonal bottom water anoxia (Castañeda and Schouten, 2011). Analysis of the lipid concentration variations (and indices derived from these, such as the Terrestrial to Aquatic Ratio (TAR), Carbon Preference Index (CPI) and Average Chain Length (ACL)) down-core can provide information on productivity, preservation and environmental changes occurring within a lake catchment (Section 4.6.3 and equations therein, Aichner *et al.*, 2018; Zhang *et al.*, 2020). Additionally, an emerging technique is the determination of the hydrogen isotope composition of

specific n-alkane and n-alkanoic acid homologues (i.e., “compound-specific hydrogen isotope analysis”;  $\delta^2\text{H}$ ) for palaeoclimate reconstructions (Holtvoeth *et al.*, 2019). This variable has close links to climatic change.

In order to measure the  $\delta^2\text{H}$  value of a specific alkyl lipid, the total lipid extract (TLE) is initially isolated from the bulk sediment using an accelerated solvent extractor. Each compound class must then be isolated via column chromatography, which exploits the differential adsorption of each type of lipid to a stationary phase in order to separate the mixture into fractions (Plancq *et al.*, 2018). Subsequent columns can then be utilized to perform further clean-ups on each fraction. N-alkanoic acids are methylated (to form fatty acid methyl esters; FAMES) prior to the cleanup column so they can be analysed in this form (Tierney *et al.*, 2022). A gas chromatography – mass spectrometer (GC-MS) is used to identify the compounds present in each fraction, and a gas chromatography – flame ionisation detector (GC-FID) is used to quantify the concentration of each compound (Plancq *et al.*, 2018; García-Alix *et al.*, 2021). A gas chromatography – isotope ratio mass spectrometer (GC-IRMS) connected via a furnace (also known as GC-py-IRMS or GC-TC-IRMS) is used to separate each homologue of the compound class of interest and measure its  $\delta^2\text{H}$  value (Chivall *et al.*, 2012; Tierney *et al.*, 2022). Interpretation of reconstructions based on  $\delta^2\text{H}$  is not always straightforward; the composition of alkyl lipids is highly correlated with the water that the source plant or algae uses during growth, however there are other factors which can disrupt this relationship, including water and air temperature and vegetative change (Sachse *et al.*, 2012; Holtvoeth *et al.*, 2019). Employing complementary proxies, such as pollen analysis, can assist in deconvolving these influences (Holtvoeth *et al.*, 2019). However, both terrestrial- and algal-derived lipids are heavily weighted towards the summer growth season, making signal seasonality less complex than other proxies (Sachse *et al.*, 2012). In particular, hydrogen isotope analysis of n-alkanoic acids ( $\delta^2\text{H}_{\text{acid}}$ ) is increasingly being utilized for hydroclimatic reconstructions (e.g., Aichner *et al.*, 2015; Tierney *et al.*, 2022).

### 1.6.5 Luminescence Dating and Profiling

Luminescence dating is a chronological technique which can be used to determine the burial age of some of Earth’s most common naturally occurring

minerals (Smedley, 2018). This method is key for Quaternary geochronologists, being one of a suite of dating tools which can be employed to produce archive age control (Lian and Roberts, 2006). The technique works following the fundamental principle that upon excitation by ionising radiation (from radioactive minerals, or cosmogenic rays), electrons become trapped in defects in the crystal lattice of a mineral, where they accumulate over time (Wintle, 2008). These electrons can be released (bleached) by stimulation with light, heat or pressure (or a combination of these processes; Smedley, 2018). Bleaching events effectively “reset” the mineral by emptying the electron traps, so it is possible to determine how much time has elapsed since the last natural bleaching event (i.e., the burial age) by bleaching artificially in the laboratory (Lian and Roberts, 2006; Smedley, 2018). When electrons are released from their traps, they return to a recombination centre, which results in the emission of a photon (with equivalent energy to the difference between the energy of the recombination centre and the trap); i.e., this process causes the mineral to luminesce (Wintle and Adamiec, 2017). This phenomenon is commonly observed in a variety of materials, but luminescence dating principally focusses on quartz and some feldspars (Duller, 2008) because these have stable traps and quantifiable signals. If this process is triggered by light exposure, it is known as Optically Stimulated Luminescence (OSL), and if it is triggered by heat exposure, it is known as Thermoluminescence (TL). A special case of OSL which stimulates the sample with infrared light is known as Infrared Stimulated Luminescence (IRSL) (Lian and Roberts, 2006). Burial age can be determined from a sample of purified minerals by comparing the measured luminescence signal (i.e., photon count) to the signals emitted following known quantities of radiation to produce an equivalent dose ( $D_e$ , in grays; Wintle, 2008; Wintle and Adamiec, 2017). This is then divided by a measure of in-situ environmental alpha, beta, gamma and cosmogenic radiation (collectively known as the dose rate,  $D_R$ , in grays per year) to yield an age (Duller, 2008; Wintle and Adamiec, 2017). This process is time-intensive and samples can take on the order of weeks to be fully prepared and measured.

The larger uncertainties sometimes associated with luminescence dating means that other chronological techniques are preferable in some settings, however the abundance of quartz and feldspar globally (Lian and Roberts, 2006), as well as

the potential of the technique to provide accurate measurements of age across the full Quaternary period (0 to 2 million years; Smedley, 2018), makes it a powerful tool, especially in the absence of alternative methods. The application of luminescence dating to beaches and dunes is well established (e.g., Fuchs *et al.*, 2012; Bateman *et al.*, 2020), and recent work has been pushing the frontiers of the technique in order to apply it to more complex settings, including lakes and glacial sediments (Fuchs and Owen, 2008; Gao *et al.*, 2017; Cong *et al.*, 2021). Careful consideration of bleaching histories, sediment re-working and variable palaeo-water contents is required for application of luminescence dating to these environments. In addition to expanding the facility of luminescence dating for providing absolute age control, there has been increasing utilization of luminescence profiling techniques across a range of settings (e.g., Stone *et al.*, 2019; Munyikwa *et al.*, 2021). Profiling techniques employ bulk sediments, or those which have undergone limited preparation, and measure the luminescence signals from that material to identify changes in the local environment and accumulation rate, sometimes by linking absolutely dated tie points (e.g., Kinnaird *et al.*, 2011; Bateman *et al.*, 2015). Common profiling methods are portable OSL (POSL), which measures the luminescence signal via a simple photon count (Sanderson and Murphy, 2010), and laboratory profiling, which calibrates the raw photon counts to those following known doses to provide estimated  $D_e$  ( $ED_e$ ) values (Burbidge *et al.*, 2007).

## Chapter 2 The Contemporary Stable Isotope Hydrology of Lake Suigetsu and Surrounding Catchment (Japan) and its Implications for Sediment-Derived Palaeoclimate Records

Rex, Charlie L.<sup>1</sup>, Tyler, Jonathan J.<sup>2</sup>, Nagaya, Kazuyoshi<sup>3</sup>, Staff, Richard A.<sup>1</sup>, Leng, Melanie J.<sup>4</sup>, Yamada, Keitaro<sup>5</sup>, Kitaba, Ikuko<sup>5</sup>, Kitagawa, Junko<sup>3</sup>, Kojima, Hideaki<sup>6</sup>, Nakagawa, Takeshi<sup>5</sup> (2024). 'The contemporary stable isotope hydrology of Lake Suigetsu and surrounding catchment (Japan) and its implications for sediment derived palaeoclimate records', *Quaternary Science Advances*, 13, article 100145. Available at: <https://doi.org/10.1016/j.qsa.2023.100145>. Submitted (unreviewed) version available on EarthArXiv at: <https://doi.org/10.31223/X53X2D>.

<sup>1</sup>*SUERC, University of Glasgow*

<sup>2</sup>*University of Adelaide*

<sup>3</sup>*Fukui Varve Museum*

<sup>4</sup>*British Geological Survey*

<sup>5</sup>*Ritsumeikan University*

<sup>6</sup>*Wakasa Mikata Jomon Museum*

The text presented here is identical to that of the submitted version and preprint, except for the following:

- The numbering of figures and tables,
- The acknowledgement of the contribution(s) of other authors and individuals where appropriate,
- The integration of the supplementary material into the main text for the benefit of the reader of this thesis,
- Amendments made following the examination of this thesis at the request of the examiners, and
- Amendments made following peer review of this text at the request of the reviewers.

The original formatted publication can be viewed in Appendix 1 – Publications. The publisher (Elsevier) permits inclusion of published articles in full or in part in a thesis for non-commercial purposes.

Authorship Declaration: C.L.R. analysed and interpreted all datasets and wrote the manuscript (first draft, editing and final draft). J.J.T., R.A.S., M.J.L. and T.N. provided feedback, supervision and guidance. K.N. led and performed the 2020–22 water sampling, assisted by K.Y., I.K. and J.K.. The 2011–12 water sampling was performed by H.K. and T. Tanabe. C.L.R., M.J.L., K.N. and K.Y. administered the project. C. Arrowsmith performed the isotope analysis. J. Lacey assisted with the writing of Section 2.5.2 (Analytical Methods). M. Ankor designed and built the rainwater sampler. Y. Miyamoto provided the high-resolution water quality data for the water column of Lake Suigetsu.

Funding: This research was financially supported by an Australian Research Council (ARC) Discovery Project (DP200101768) and a Japan Society for the Promotion of Science (JSPS) KAKENHI Grant (19K20442). C.L.R. was supported by the NERC IAPETUS2 Doctoral Training Partnership.

Accompanying data can be found at

<https://doi.org/10.5525/gla.researchdata.1429>.

## 2.1 Abstract

The Lake Suigetsu sediment cores exemplify a high-quality archive of palaeoclimatic change in East Asia during the past 150 ka. Robust interpretation of stable isotope-based proxy reconstructions from the Suigetsu cores can be aided by a greater understanding of the factors affecting the isotope composition of the lake and how it relates to that of precipitation. Here we use extended contemporary monitoring to establish the factors affecting the stable isotope composition ( $\delta^{18}\text{O}$ ,  $\delta^2\text{H}$  and d-excess) of precipitation, river water and lake water in the catchment surrounding Lake Suigetsu, central Japan. We show that the composition of precipitation is influenced by the dual East Asian Monsoon system, producing minima in  $\delta^{18}\text{O}$  and  $\delta^2\text{H}$  and semi-annually varying d-excess values across the year. These signals are then transferred to the lake system, where they are combined with secondary local influences on lake water composition: homogenisation with existing catchment waters, a catchment transit lag, the interaction with saline water from the nearby Sea of Japan, and evaporative enrichment during summer. Our observations suggest that the palaeo-isotope composition of Lake Suigetsu was closely related to the behaviour of the East Asian Monsoon. We highlight lake stratification and proxy seasonality as critical components of signal interpretation.

## 2.2 Keywords

Stable Isotopes; Precipitation Isotopes; Lake Water Isotopes; East Asian Monsoon; Sediment Cores

## 2.3 Introduction

The Five Lakes of Mikata are a collection of tectonic lakes located in Fukui Prefecture, central Japan, and comprise Lake Mikata, Lake Suigetsu, Lake Suga, Lake Kugushi and Lake Hiruga (Figure 2.1). To-date, much of the Quaternary research undertaken on the lakes has focussed on Lake Suigetsu, the central lake of the system, by virtue of its unique underlying sedimentary sequence. This sequence is exceptionally well-preserved by a deep water column (34 m) and surrounding hills, which hinder wind turbation; bottom water anoxia, which prevents bioturbation; and a shallow connection (the Seto Channel) between

Lake Suigetsu and Lake Mikata (upstream of Lake Suigetsu, Figure 2.1C), which prevents disturbances by high energy events (Nakagawa *et al.*, 2021). A series of previous deep coring campaigns have extracted sediment from Lake Suigetsu to generate a high-quality archive of environmental change (“the Lake Suigetsu sediment cores”) spanning >98 m from the present day to in excess of 150 ka BP (Nakagawa *et al.*, 2012). A distinctive characteristic of the Suigetsu cores is that they contain annual laminations (varves) between ~50 and 10 ka BP, comprising the longest continuously varved record from the Quaternary (Schlolut *et al.*, 2012). The youngest sediments (up to 50.3 ka BP) have been dated to high precision using radiocarbon dating of >800 macrofossils (Staff *et al.*, 2011; Bronk Ramsey *et al.*, 2012; Bronk Ramsey *et al.*, 2020), varve counting using optical microscopy (Schlolut *et al.*, 2012; Schlolut *et al.*, 2018), and analysis of volcanic tephra deposits with independent ages (e.g., Smith *et al.*, 2011; McLean *et al.*, 2016). Between 50.3 ka BP and 13.9 ka BP, Lake Suigetsu contributes the only non-reservoir corrected dataset within the international consensus radiocarbon calibration curve, “IntCal”.

It is this excellent archive preservation and world-leading chronological control which makes multiproxy palaeoenvironmental analyses of the Suigetsu cores an exciting prospect. Indeed, the location of Lake Suigetsu at a lower latitude than other global benchmark records (e.g., the Greenland and Antarctic Ice Cores) makes this archive an avenue for establishing a more holistic global perspective on past climatic change. Additionally, the Japanese archipelago is situated within the East Asian Monsoon (EAM) regime, a critical, yet complex, component of the global climate system for which palaeoclimate reconstructions offer a means to greater understanding. Not only is Japan situated directly beneath the seasonally migrating EAM front, making it sensitive to changes in the EAM system (Jun-Mei *et al.*, 2013; Nakagawa *et al.*, 2012; Gallagher *et al.*, 2018), but unlike continental areas, Japan experiences EAM precipitation semi-annually (twice a year), because both the winter (EAWM) and summer (EASM) prevailing monsoon winds pass over large bodies of water before reaching the Japanese Islands. Therefore, both seasonal modes have tangible hydrological influence over precipitation in Japan, and reconstructions from here have the unique potential to determine the behaviours of both the EAWM and the EASM. In light of this, the Suigetsu cores continue to be the subject of an ever-growing collection of

investigations into climatic change over the last glacial–interglacial cycle (e.g., Schlolaut *et al.*, 2017; Nakagawa *et al.*, 2021), including contributing to the definition of the Holocene onset as an auxiliary stratotype (Walker *et al.*, 2009). An ongoing avenue of research is the development of palaeoclimate reconstructions derived from oxygen and hydrogen isotope compositions of pollen grains, biogenic silica and siderite (all of which are abundant components of the cores), because these offer a means to infer past hydrological change (including links to EAM behaviour).

Robust interpretation of such sedimentary proxies is predicated on a strong understanding of the controls acting on lake isotope composition ( $\delta_{\text{lake}}$ ), which, in the absence of historical datasets, can be achieved by extended contemporary monitoring. Of particular interest is the extent to which variability in the isotope composition of precipitation ( $\delta_{\text{precipitation}}$ , which provides a link to regional–scale hydrological change) is reflected in the isotope composition of river water ( $\delta_{\text{river}}$ ) and  $\delta_{\text{lake}}$  and, in turn, lake sedimentary components; however, this depends strongly on catchment and lake hydrology. Variability in groundwater, river, and in rare cases, marine contributions to the lake water balance can act to dampen and sometimes conceal the isotope composition of recent precipitation (e.g., Seal and Shanks, 1998; Lacey and Jones, 2018). In addition, evaporation of lake waters can strongly modify  $\delta_{\text{lake}}$  compared to inflowing water (Gonfiantini, 1986; Russell and Johnson, 2006; Wassenaar *et al.*, 2011). These concepts are commonly used in modern hydrology (Gibson *et al.*, 2016); for example, during mass balance modelling to determine the surface versus groundwater contribution to Lake Ohrid, south–eastern Europe (Lacey and Jones, 2018) or to consider mass losses due to evaporation, such as for Lake Edward, East Africa (Russell and Johnson, 2006). Monitoring for an extended period (on the order of years) is required in order to fully understand the evolution of  $\delta_{\text{lake}}$ , particularly in regions where the climate is so seasonal. This approach allows for both local influences (such as changing inputs and evaporation) to be identified alongside regional scale climatic shifts.

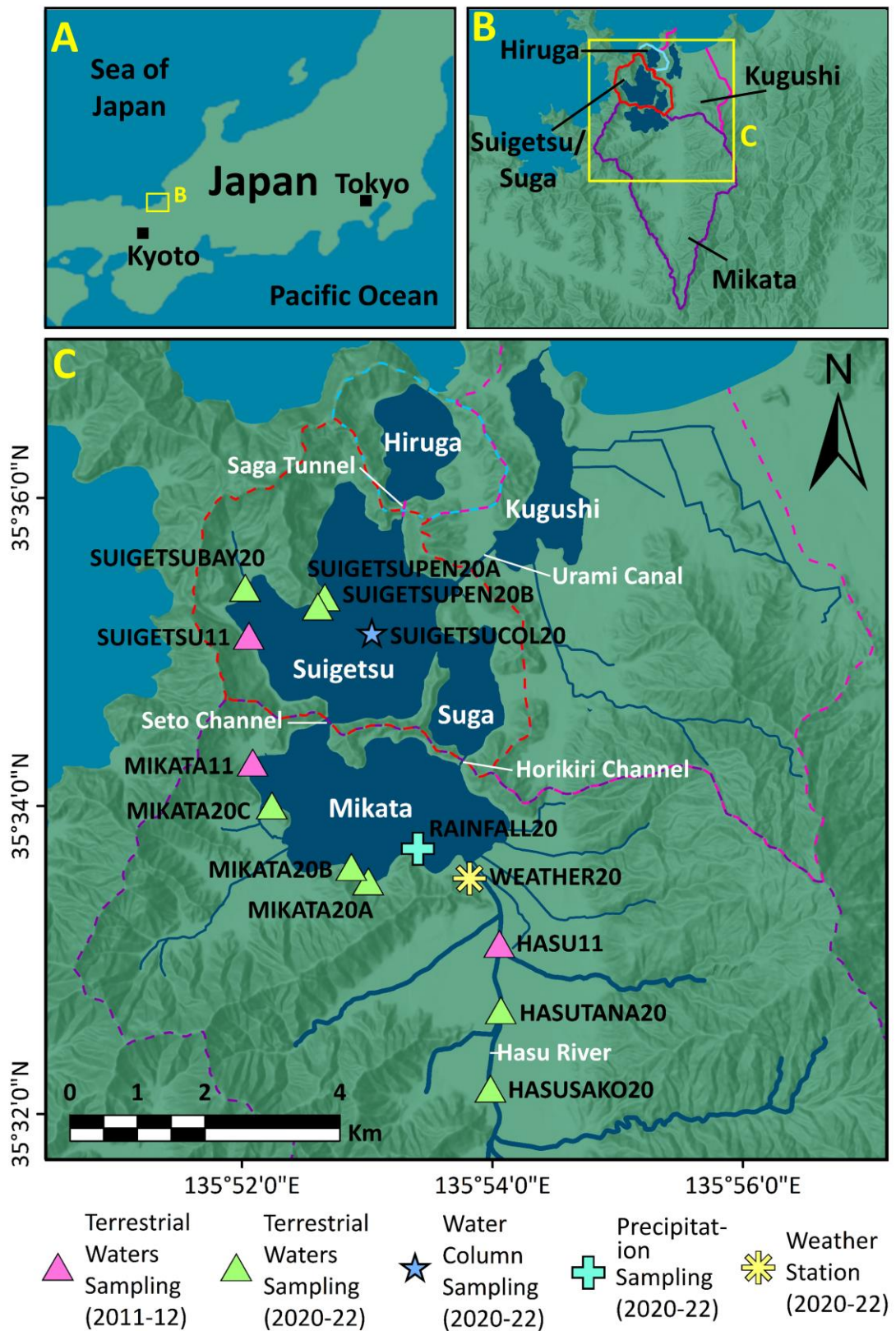


**Figure 2.1 Map of the Five Lakes of Mikata catchment.** Yellow outlines show the extent of subsequent panels in the sequence. Panel A shows the location of the region in relation to major Japanese cities. Panel B shows the catchment area of each lake. Panel C shows the sampling locations for this study, including precipitation sampling, river and lake sampling, and sampling of the Lake Suigetsu water column, as well as the location of the weather station. Full details of locations shown here are available in Table 2.1. Basemaps: custom World Dark Grey Base and World Hillshade from Esri (2022a; 2022b) (scale 1:10,000,000 (A), 1:400,000 (B), 1:67,946 (C)).

In this study we aimed to better understand the controls acting on the isotope composition of water within Lake Suigetsu and its surrounding catchment, in order to facilitate interpretation of isotope-based proxy reconstructions of past climate from the Lake Suigetsu sediment cores. By monitoring  $\delta_{\text{precipitation}}$ ,  $\delta_{\text{river}}$  and  $\delta_{\text{lake}}$  over a total observation period of two years and ten months across 2011–2012 and 2020–2022, we assessed the factors affecting the relationships between these variables. Conceptualising  $\delta_{\text{lake}}$  of Lake Suigetsu is particularly important because whilst the lake and catchment receive high volumes of precipitation annually, there are other controls which could act to alter or obscure this precipitation signal; namely, that expected evaporation rates are high due to a warm summer climate, and in the present day there is some interaction between the lake and the Sea of Japan. Consequently, resolving the relative influence of  $\delta_{\text{precipitation}}$  (and the propagation of  $\delta_{\text{precipitation}}$  signals to  $\delta_{\text{lake}}$ ) is crucial to understanding the major controls over long term  $\delta_{\text{lake}}$  within the context of regional scale hydrological (and thus climatic) change.

## 2.4 Study Site

### 2.4.1 Hydrology

The Five Lakes of Mikata are located adjacent to the towns of Wakasa and Mihama in Fukui Prefecture, Honshu Island, central Japan. The lakes lie to the west of the active Mikata fault line and were formed as the western side of the fault subsided over time (Figure 2.1C; Nakagawa *et al.*, 2012). Over the last ~400 years, the Five Lakes of Mikata catchment has been anthropogenically influenced by the construction of channels and tunnels to connect the lakes. In the present day, the lakes form a route between the freshwater Hasu River and the saline Sea of Japan (Figure 2.1C). Lake Mikata, the southernmost lake, is fed by the Hasu River to the south, has an area of ~3.61 km<sup>2</sup> and a maximum depth of 5.8 m and has the largest discrete catchment area (~50 km<sup>2</sup>; Figure 2.1B). Lake Mikata is connected to Lake Suigetsu via the shallow (~2 m deep) Seto Channel, and to the adjacent Lake Suga via the artificial (<0.5 m deep) Horikiri Channel. Lake Suigetsu, which has an area of ~4.2 km<sup>2</sup> and a maximum depth of 34.0 m, then feeds Lake Hiruga (via the subterranean Saga Tunnel, which was sealed during the observation period) and Lake Kugushi (via the surficial Urami Canal), which both flow directly into the Sea of Japan (Shigematsu *et al.*, 1961;

Figure 2.1C). In the past, prior to the construction of the Horikiri Channel, Saga Tunnel and Urami Canal, Lake Kugushi was a coastal lagoon (part of Wakasa Bay), and Lake Hiruga was not connected to the sea (except during flooding), so four of the five lakes were freshwater (Shigematsu *et al.*, 1961; Masuzawa and Kitano, 1982a). At this time, the outflow from Lake Suigetsu was via Lake Suga (effectively a side basin of Lake Suigetsu), which was connected to Lake Kugushi via a channel (the Kiyama River) through low ground to the east of the lakes.

Principally, water flows in a south-to-north direction through the catchment, driven by the large quantities of precipitation in the region. However, in the present-day, seawater washes back into Lake Suga, Lake Suigetsu and Lake Mikata during high tide in autumn (Kondo and Butani, 2007). As a result, all five lakes now have some degree of marine-derived salinity and observations show that salinity in the lakes increases during the autumnal high tide and then decreases due to continued freshwater input via precipitation and surface runoff during winter. Lake Hiruga and Lake Kugushi are saline, and Lake Mikata is fresh to brackish ( $0\text{--}3\text{ g kg}^{-1}$ ). Lake Suigetsu and Lake Suga are both meromictic (permanently stratified), with an upper mixolimnion (aerobic, brackish to saline water;  $2\text{--}8\text{ g kg}^{-1}$ ) separated from a lower monimolimnion (anaerobic, saline water;  $\sim 13\text{ g kg}^{-1}$ ) by a chemocline at  $\sim 8\text{ m}$  depth (Matsuyama, 1974; Kondo *et al.*, 2000; Kondo and Butani 2007). The mixolimnion exhibits a salinity gradient between the surface (fresh) and the chemocline (saline) (Matsuyama, 1974; Kondo *et al.*, 2000). Mixing in the mixolimnion occurs once each year, during the autumn, resulting in an increase in surface water salinity, a chemocline raised in depth and a steepening of the salinity gradient (Kondo *et al.*, 2000). The chemocline then lowers in depth and a more gradual salinity gradient is re-established during winter. The monimolimnion is a persistent seawater-derived saline layer, confirmed by geochemical analysis (Shigematsu *et al.*, 1961), and has a limited freshwater influence (Matsuyama, 1973). This layer is replenished annually at the autumnal high tide (Kondo and Butani, 2007). It is not known whether this autumn seawater incursion drives mixing in the upper  $\sim 8\text{ m}$  of the water column, or if these two processes are merely coincident, although the latter is suspected. No major long-term increases in salinity have been observed in the monimolimnion in the past 70 years; salinity remained approximately  $12\text{ to }16\text{ g kg}^{-1}$  in the intervals 1951–1966 and 2008–10

(Matsuyama, 1973, Kondo *et al.*, 2014). Complete lake water vertical mixing events are unusual but have been detected (in 1997; Kondo *et al.*, 2000).

The residence time of Lake Suigetsu was calculated to be on the order of ~ 1 year, assuming a total annual precipitation of ~2.3 m (Japan Meteorological Agency, 2022) across a ~60 km<sup>2</sup> catchment (~0.14 km<sup>3</sup> precipitation annually) and then applying this to a simple single box model (surface area of ~4.3 km<sup>2</sup> and ~34 m depth equating to a ~0.15 km<sup>3</sup> volume). However, when considering the evidence for a stable monimolimnion in Lake Suigetsu with a very long residence time (Shigematsu *et al.*, 1961), a two-box model is more appropriate, with water effectively flushing solely through the top ~8 m of the lake (Matsuyama, 1973). In this case, the residence time of the mixolimnion is on the order of ~3 months.

### 2.4.2 Climate

The climate of the Five Lakes of Mikata catchment is temperate with high levels of precipitation. The temperature profile is typical of Japan, with low temperatures in winter (reaching a minimum in January with a mean temperature of 4.3 °C) and high in summer (reaching a maximum in August with a mean temperature of 27.0 °C). The annual distribution of precipitation is more unusual, because a large proportion of the total annual precipitation falls during winter (Figure 2.2). This is unlike much of Japan, where summer is the wettest season. The large quantities of precipitation received in winter are a result of the catchment being located on the Sea of Japan coast, where it receives a significant input of EAWM precipitation annually. This EAWM precipitation falls as both rain and snow and is concentrated in December and January. Spring (March to May) is the driest season of the year, which precedes a second rainy period in early summer which accompanies the EASM. The EASM rainy season is known as the *Tsuyu* or *Baiu*, which occurs at Lake Suigetsu around late June into July, immediately prior to the period of maximum temperature. This is followed by typhoon season from August to September, during which a series of low-pressure systems pass over Japan from the Pacific Ocean to the south, resulting in a third annual period of rain. Winter (EAWM) and summer (EASM) precipitation are the most significant extended (persistent) freshwater inputs to

the catchment; typhoon season precipitation comprises a series of intense isolated precipitation events.

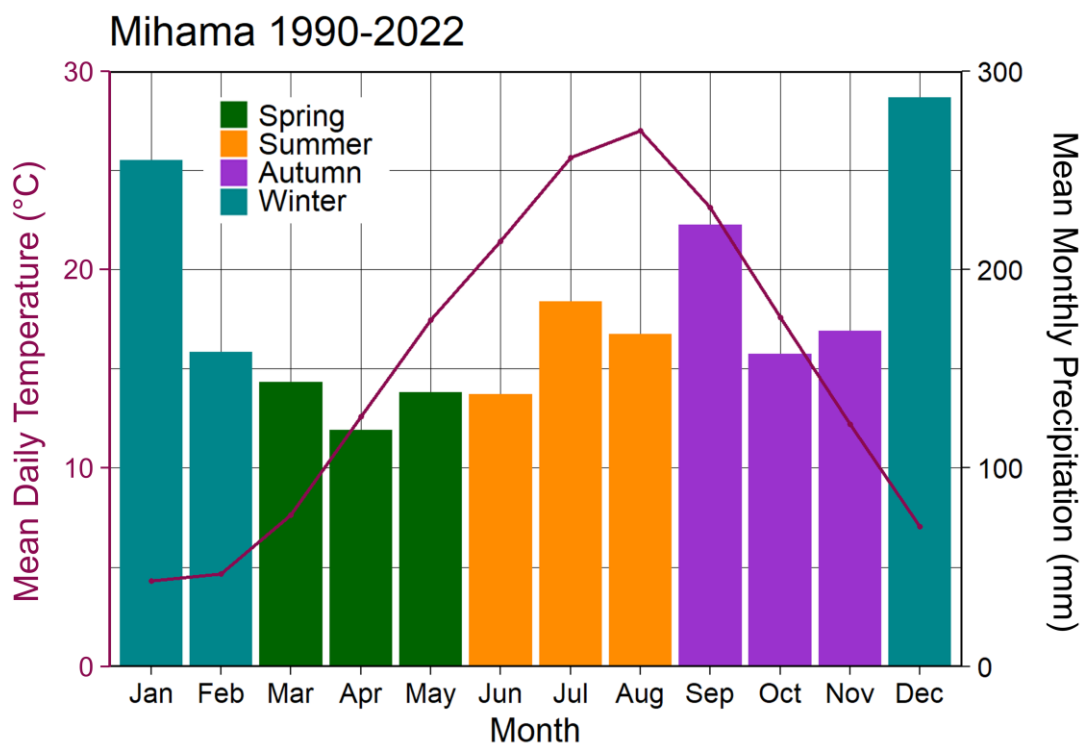


**Figure 2.2 Climate at the Five Lakes of Mikata.** Monthly variations in mean daily temperature (pink curve) and mean total monthly precipitation (bars) at Mihama, adjacent to Lake Kugushi (35°36'00"N 135°55'00"E). Data from the Japan Meteorological Agency, 1<sup>st</sup> January 1990 to 28<sup>th</sup> February 2022.

## 2.5 Materials and Methods

### 2.5.1 Sampling Methods

Samples of lake and river waters ( $n = 463$ ) were taken from the Hasu River, Lake Mikata and Lake Suigetsu (Figure 2.1C) on a weekly basis between 1<sup>st</sup> March 2011 and 3<sup>rd</sup> January 2012 (by H. Kojima and T. Tanabe), and again between 15<sup>th</sup> July 2020 and 29<sup>th</sup> July 2022 (by K. Nagaya). Water was collected by submerging a collection vessel in the top ~50 cm of water before subsampling using a vial leaving no or minimal head space. Precise sampling locations were altered between the 2011/12 and 2020/22 sampling intervals, and during periods of inaccessibility (e.g., due to bridge repairs, snowfall, lake freezing and flooding; Table 2.1). The slight changes in sampling location are unlikely to affect the isotope composition recorded, being within the same water depth range and situated away from lake inputs. If visible algae were present in the water, the

samples were filtered using a 50  $\mu\text{m}$  polyethylene terephthalate (PET) mesh filter. Surface water data from the 2011–2012 observation period do not have the accompanying (precipitation and water column) data described below because this was an extended pilot study focussed on the river and lake waters; however, we have nevertheless included these 2011–2012 data in our analysis because there are subtle differences in these data that contribute to a more comprehensive view of isotope variations in the catchment.

**Table 2.1 Sampling locations.** Details of sampling locations noted in the text and on Figure 2.1, with notes relating to when each location was used.

| Sampling Location                | Coordinates                 | Location Code  | Notes  |
|----------------------------------|-----------------------------|----------------|--|
| Hasu River (2011–12)             | 35° 33'07"N<br>135° 54'03"E | HASU11         |  |
| Mikata (2011–12)                 | 35° 34'18"N<br>135° 52'05"E | MIKATA11       |  |
| Suigetsu (2011–12)               | 35° 34'59"N<br>135° 52'08"E | SUIGETSU11     |  |
| Mikata (2020–22)                 | 35° 33'33"N<br>135° 52'58"E | MIKATA20A      | (Unless inaccessible – usually due to heavy rain and high lake levels) |
| Mikata 2 (2020–22)               | 35° 33'38"N<br>135° 52'49"E | MIKATA20B      | (When Mikata was inaccessible)   |
| Mikata 3 (2020–22)               | 35° 34'01"N<br>135° 52'10"E | MIKATA20C      | (When Mikata and Mikata 2 were inaccessible)                           |
| Hasu River Tana Bridge (2020–22) | 35° 32'40"N<br>135° 54'04"E | HASUTANA20     | (Unless blocked for renovations)                                       |
| Hasu River Sako Bridge (2020–22) | 35° 32'10"N<br>135° 53'59"E | HASUSAKO20     | (When Hasu Tana Bridge was blocked for renovations)                    |
| Suigetsu Peninsula (2020–22)     | 35° 35'17"N<br>135° 52'34"E | SUIGETSUPEN20A | (Until 18 Aug 2020 – moved due to algal growth)                        |
| Suigetsu Peninsula (2020–22)     | 35° 35'22"N<br>135° 52'40"E | SUIGETSUPEN20B | (Since 26 Aug 2020, unless inaccessible – usually due to snow)         |
| Suigetsu Bay (2020–22)           | 35° 35'25"N<br>135° 52'02"E | SUIGETSUBAY20  | (When Suigetsu Peninsula was inaccessible)                             |
| Suigetsu Roadside (2020–22)      | 35° 35'04"N<br>135° 52'05"E | SUIGETSUROAD20 | (Not used as of 05/01/22)  |
| Suigetsu Column (2020–22)        | 35° 35'05"N<br>135° 53'01"E | SUIGETSUCOL20  | (approx. – better described as the centre of the lake)                 |
| Netatmo Weather Station          | 35° 33'32"N<br>135° 53'48"E | WEATHER20      |  |
| Precipitation (2020–22)          | 35° 33'43"N<br>135° 53'25"E | RAINFALL20     |  |

Precipitation samples ( $n = 120$ ) were captured between 13<sup>th</sup> July 2020 and 29<sup>th</sup> July 2022 using a purpose built (3D printed) funnel and glass bottle holder (designed by M. Ankor) in Wakasa (at the location indicated in Figure 2.1C). Silicone oil was added to the collection bottle to prevent evaporation. Water subsamples were taken from the bottle using a Teflon pipette (by K. Nagaya).

Subsamples were taken on an event basis; every day during periods of frequent precipitation, but less often during periods of reduced precipitation. The water was allowed to overflow the sample vial in order to remove the floating silicone oil. Fresh snowfall samples were collected from pristine areas of snow after deposition and melted with silicone oil in a lidded container before being transferred to the collection vial. An automated Netatmo weather station (location also shown in Figure 2.1C) was deployed to provide temperature, humidity, precipitation amount and wind data to accompany the isotope data. Backwards air parcel trajectory analysis was performed for four precipitation events (one representative of each season) using the NOAA Air Resources Laboratory HYSPLIT model (Stein *et al.*, 2015, Rolph *et al.*, 2017). The selected events ended on 27<sup>th</sup> December 2020, 16<sup>th</sup> September 2021, 2<sup>nd</sup> May 2022 and 7<sup>th</sup> July 2022, respectively. Back trajectories were generated for air parcels arriving at the catchment every 12 hours at 1500 m.a.s.l. across a 72-hour window prior to the end of each event.

Water column profiling was conducted ~quarterly on 22<sup>nd</sup> December 2020, 8<sup>th</sup> April 2021, 5<sup>th</sup> August 2021, 17<sup>th</sup> November 2021, 23<sup>rd</sup> April 2022 and 21<sup>st</sup> July 2022 at the approximate centre of Lake Suigetsu (Figure 2.1C) (by K. Nagaya and colleagues). Samples were taken every 2 m between the surface and 10 m depth, every 5 m between 10 m and 30 m depth, and then every 2 m between 30 m and 34 m (n = 70). A sealable van Dorn water sampler was used to prevent mixing of the sample with water at different depths during transit to the surface. A Hydrolab DS5 water quality meter was also used to measure temperature and salinity profiles on each sampling date; higher resolution geochemical data were collected for the December 2020, April 2021, November 2021, April 2022 and July 2022 dates (by Y. Miyamoto). The low-resolution data collected for the August 2021 date (using a TOA-DKK WQC-24 meter) are also shown in Section 2.6.

### 2.5.2 Analytical Methods

Oxygen isotope ( $\delta^{18}\text{O}$ ) measurements were made using an Isoprime 100 mass spectrometer with an Aquaprep dual-inlet system using the  $\text{CO}_2$  equilibration method (by C. Arrowsmith). Subsamples (totalling 200  $\mu\text{l}$ ) were placed in a heated sample tray at 40 °C before the air was evacuated and each exetainer

was flushed with CO<sub>2</sub>. The samples were then left to equilibrate for between 12 (first sample) and 37 (last sample) hours. Any remaining water vapour was then removed on a sample-by-sample basis using a cryogenic water trap, before each sample was expanded into the dual inlet isotope ratio mass spectrometer (IRMS) for analysis. The samples were measured in alternate pulses alongside a reference CO<sub>2</sub> gas, and the integrated values of the sample were compared to the reference gas values to determine the <sup>18</sup>O/<sup>16</sup>O ratio. Two internal laboratory standards (CA-HI and CA-LO) were analysed in each run. The value of these standards has been determined accurately by comparison with international calibration and reference materials (VSMOW2, SLAP2 and GISP). This facilitated the calculation of the <sup>18</sup>O/<sup>16</sup>O ratio of each sample versus VSMOW2, and subsequent expression of the oxygen isotope ratio in delta (δ) units (δ<sup>18</sup>O) in parts per mille (‰). The typical standard deviation is <0.05 ‰.

Hydrogen isotope (δ<sup>2</sup>H) measurements were made in duplicate using a continuous flow, high temperature conversion elemental analyser – IRMS (TC-EA-IRMS) (EuroPyrOH-Isoprime) with liquid autosampler (by C. Arrowsmith). Subsamples (0.5 μl) were injected into a heated septa-sealed port at 160 °C and converted to water vapour. The vapourised sample was then flushed through a chromium-packed reactor at 980 °C by the helium carrier gas, which reduced the water to hydrogen gas. A reference hydrogen gas pulse was introduced to the IRMS prior to the gas pulse from each sample. The sample peaks were then integrated and corrected for the H<sub>3</sub><sup>+</sup> contribution before comparison to the reference gas to yield the <sup>2</sup>H/<sup>1</sup>H ratio. Each sample was measured five times. As with the oxygen isotope measurements, the samples were then compared to measurements of CA-HI and CA-LO to calculate the <sup>2</sup>H/<sup>1</sup>H ratio of each sample versus VSMOW2, and expression of the hydrogen isotope ratio in delta units as for the oxygen isotopes. The typical standard deviation is <0.5 ‰.

The aforementioned δ<sup>18</sup>O and δ<sup>2</sup>H measurements were then used to calculate deuterium excess (d-excess; Equation 2.1), a second-order parameter which can be considered as a measure of deviation from the Global Meteoric Water Line (GMWL, which has a gradient of 8). This occurs when there is a greater amount of <sup>2</sup>H relative to <sup>18</sup>O, caused by diffusive fractionation during evaporation of water molecules (Bershaw, 2018).

$$d\text{-excess} = \delta^2\text{H} - (8 \times \delta^{18}\text{O})$$

Equation 2.1

## 2.6 Results and Interpretation

### 2.6.1 Precipitation $\delta^{18}\text{O}$ and $\delta^2\text{H}$

Values of  $\delta^{18}\text{O}$  for the precipitation at Wakasa (July 2020 to July 2022) ranged from  $-13.2\text{‰}$  to  $-2.4\text{‰}$ , with a mean value of  $-7.0\text{‰}$  and standard deviation of  $1.6\text{‰}$  (Figure 2.3A).  $\delta^2\text{H}$  values ranged from  $-96.4\text{‰}$  to  $2.3\text{‰}$ , with a mean of  $-39.1\text{‰}$  and standard deviation of  $11.9\text{‰}$ . Figure 2.3A shows only small seasonal differences in  $\delta^{18}\text{O}$  and  $\delta^2\text{H}$  because there was considerable intra-seasonal variability and overlap. Throughout the study period,  $\delta^{18}\text{O}$  and  $\delta^2\text{H}$  were associated with rapid high amplitude fluctuations with time (Figure 2.4); however, winter and summer minima were observed when the data were considered on a monthly basis; likely due to greater quantities of precipitation (Figure 2.2) during these seasons (discussed in Section 2.6.4). This trend was clearest in the  $\delta^{18}\text{O}$  values, but a summer minimum was also observed in the  $\delta^2\text{H}$  values (Figure 2.4); the winter minimum likely obscured by high d-excess values (described in Section 542.6.2). Back trajectory analysis of four precipitation events from across our sampling period indicates that air parcels arriving at the catchment predominately originated over Continental Asia during the winter, in the oceanic domain (Pacific Ocean, Philippine Sea and East China Sea) during summer, and a mixture of the two during the spring and autumn (Figure 2.5).

These trajectories, which ultimately reflect the operation of the EAM as dual EAWM and EASM modes, highlight the influence of the EAM on the climate of Japan, and can explain the lack of distinctive seasonal precipitation  $\delta^{18}\text{O}$  and  $\delta^2\text{H}$  trends at Wakasa. EAWM and EASM precipitation over Japan generally have very similar compositions (Taniguchi *et al.*, 2000; Uemura *et al.*, 2012) in direct contrast to Continental Asia, where EAWM and EASM precipitation exhibit distinct compositions due to continental ( $\delta^{18}\text{O}_{\text{precipitation}} \sim -4\text{‰}$ ) versus oceanic sources ( $\delta^{18}\text{O}_{\text{precipitation}} \sim -10\text{‰}$ ), and hence vary seasonally (Araguas-Araguas *et al.*, 1998). EAWM air masses originate in central Asia and Siberia and are predominately cold and dry, and hence whilst distillation and moisture recycling

earlier in the trajectory is possible, the isotope signal of EAWM precipitation over Japan is dominated by the interaction of this air mass with the Sea of Japan. The evaporation from the Sea of Japan in winter has a light isotope signal ( $\delta^{18}\text{O} \sim -8 \text{ ‰}$ ; Uemura *et al.*, 2012) and the transport distance is short (on the order of  $<1000 \text{ km}$ ), so this signal is retained in winter precipitation  $\delta^{18}\text{O}$  and  $\delta^2\text{H}$  (i.e., little further depletion of the heavier isotopes occurs during transport). Conversely, EASM air masses originate over the Pacific Ocean and track towards the Japanese archipelago via the Philippine Sea and East China Sea (the trajectory ultimately determined by the positioning of the Western Pacific Subtropical High (Xu *et al.*, 2020; Figure 2.5). Evaporation from this oceanic domain has a range of isotope compositions (from  $\delta^{18}\text{O} \sim -4 \text{ ‰}$  in the Western Pacific Warm Pool to  $\delta^{18}\text{O} \sim -8 \text{ ‰}$  in the East China Sea; Uemura *et al.*, 2012); however, the distance from the sources with a heavier isotope signal to Japan is greater, such that overall depletion of the heavier isotopes during transport acts to minimise differences between proximal and distal sources. As such, EASM  $\delta^{18}\text{O}$  and  $\delta^2\text{H}$  is low, as with the EAWM.

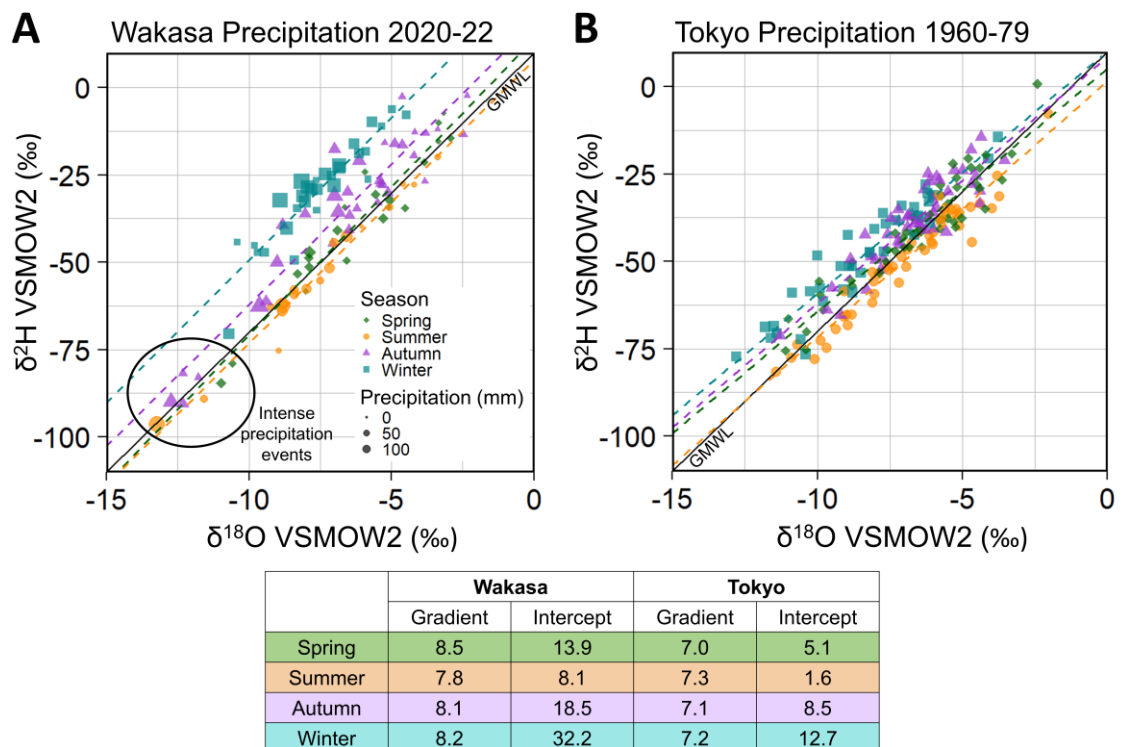


**Figure 2.3 Precipitation  $\delta^{18}\text{O}$  and  $\delta^2\text{H}$  at Wakasa and Tokyo.** A comparison of isotopes in precipitation at (A) Wakasa 2020–22 (event basis, Sea of Japan Coast) and (B) Tokyo 1960–79 (monthly averages, Pacific Ocean Coast). Linear regression local meteoric water lines for each season are shown and numerically described in the table. Black diagonal lines represent the Global Meteoric Water Line (GMWL). The points plotted for the composition of Wakasa are scaled by

quantity of precipitation (as calculated from the Wakasa weather station; WEATHER20 in Figure 2.1). Seasons are defined as: Spring (Mar–May), Summer (Jun–Aug), Autumn (Sep–Nov), Winter (Dec–Feb). d-excess is higher for points above the GMWL. Samples were collected by K. Nagaya and analysed by C. Arrowsmith.

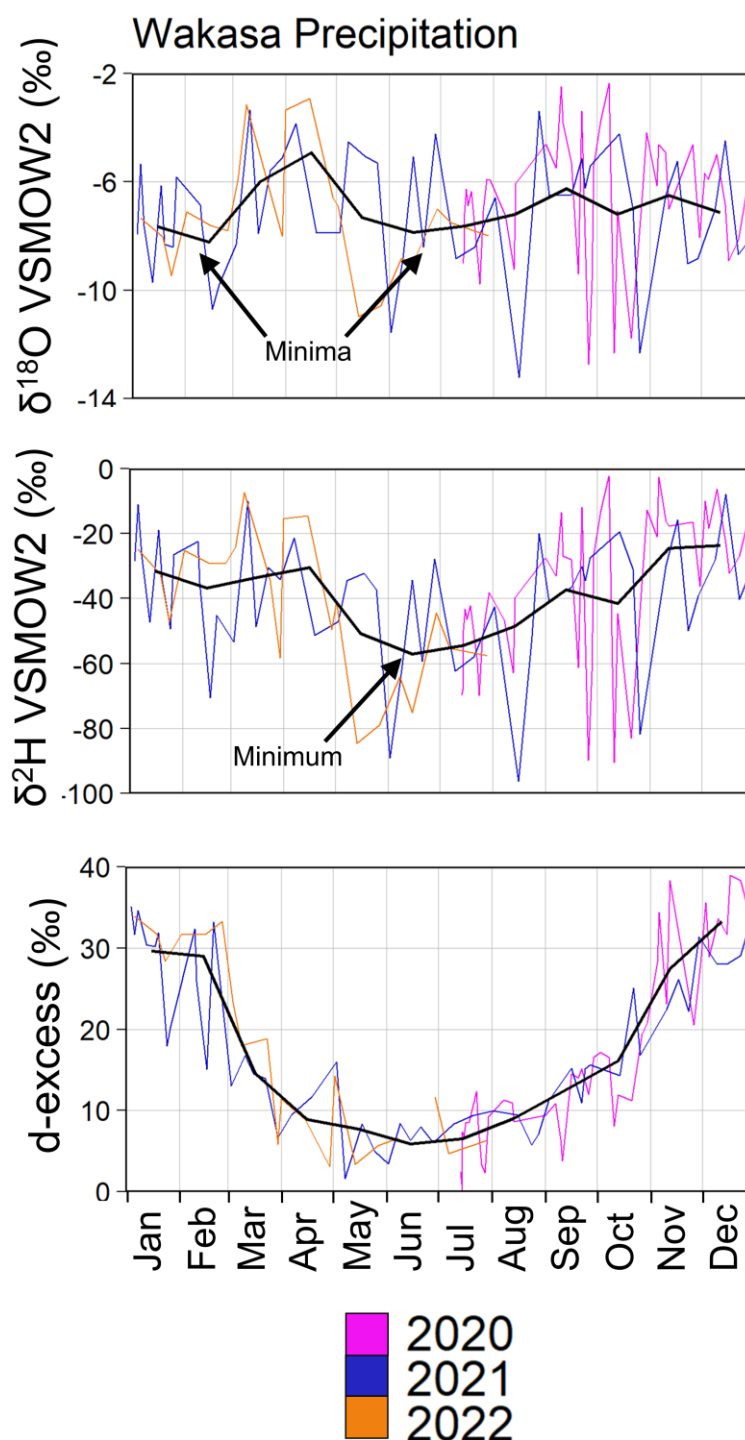


**Figure 2.4 Variations in  $\delta_{\text{precipitation}}$  with time.**  $\delta^{18}\text{O}$ ,  $\delta^2\text{H}$  and d-excess values from precipitation at Wakasa from across the study period (colour lines). Black lines represent monthly averages of each dataset. Samples were collected by K. Nagaya and analysed by C. Arrowsmith.

This similarity in the isotope composition of precipitation from each end member trajectory likely results in the limited seasonality that we observed at Wakasa. The air parcel trajectories during spring and autumn exhibited mixed behaviour, and we suggest that this lack of strong prevailing wind direction and a mixture of vapour sources during these intermediate seasons produced precipitation with a similar composition to the EAM months, although we suspect that the spring and autumn values were slightly higher due to relatively reduced quantities of precipitation during these seasons (discussed further in Section 2.6.4). Intra-seasonal variability was likely due to subtle differences in the airmass trajectories associated with each precipitation event.

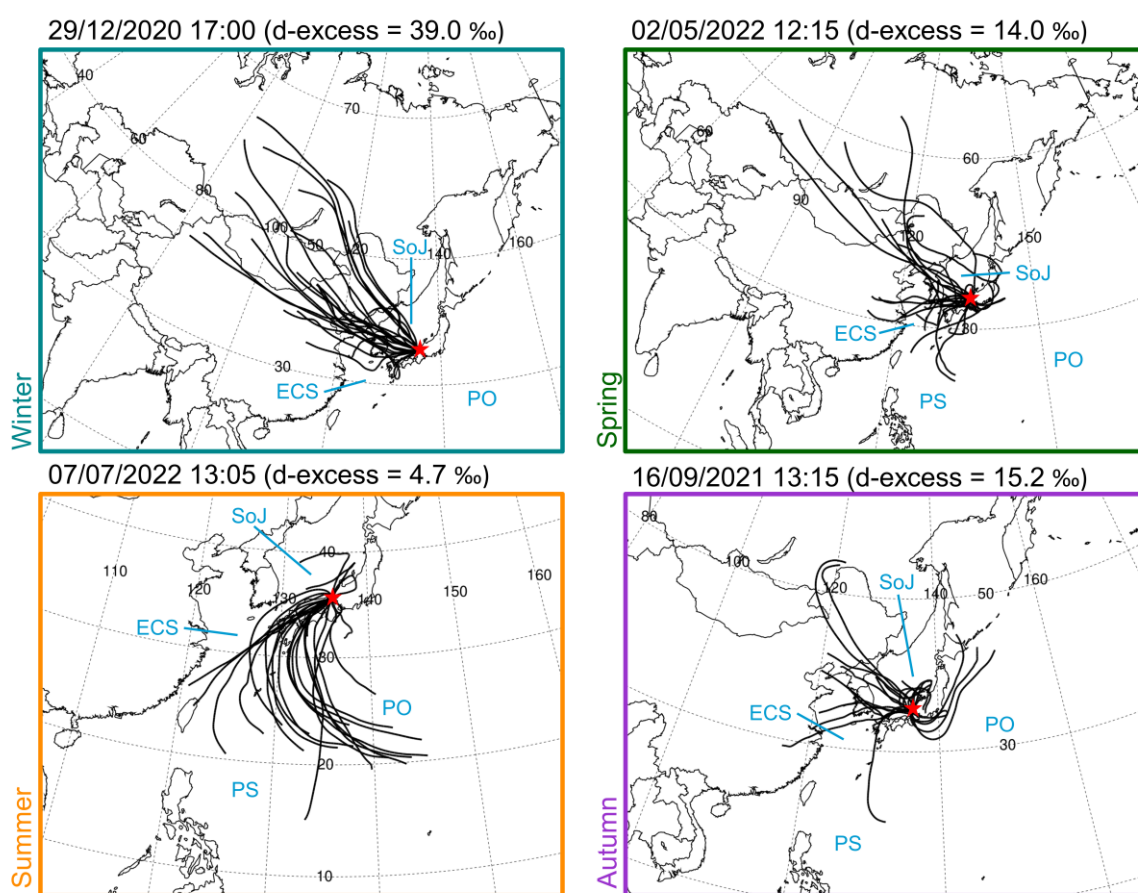


**Figure 2.5 HYSPLIT back trajectory model results.** HYSPLIT back trajectory model results for four rainfall events across the 2020–22 rainfall study period. Events were selected to cover a range of  $d$ -excess values which are typical of each of the four seasons. Dates and times indicate the end of each sampling interval. Red stars indicate the position of the catchment; backtrace analysis was performed to the exact position of the precipitation sampler (RAINFALL20 in Figure 2.1). Surrounding seas and oceans are labelled as follows: SoJ = Sea of Japan, ECS = East China Sea, PS = Philippine Sea, PO = Pacific Ocean.

Very low  $\delta^{18}\text{O}$  and  $\delta^2\text{H}$  values (in the  $\delta^{18}\text{O}$  range of  $-13.2$  ‰ to  $-11.0$  ‰) were uncommon at Wakasa; however, a minor cluster of precipitation events was

nevertheless associated with such values (Figure 2.3A). The majority of these datapoints represent precipitation from August to October (Figure 2.4) and include rains from Tropical Storm Dolphin (2020). Given the seasonality of such events, a simple explanation could be that this precipitation was derived from tropical storms (typhoons), which are associated with  $\delta^{18}\text{O}$  values up to 6 ‰ lower than other summer precipitation events, driven by strong fractionation processes in heavy cyclonic precipitation (Lawrence and Gedzelman, 1996; Fudeyasu *et al.*, 2008; Li *et al.*, 2010; Jackisch *et al.*, 2022). However, it is worth noting that precipitation from earlier months of the year also occasionally exhibited these values, and other typhoon events did not. Instead, we posit that these compositions were associated more generally with intense precipitation events. Whilst they do not universally correspond to periods with large quantities of precipitation, this does not preclude a relationship with intense precipitation events because our analysis considered only the total amount of precipitation which fell in the collection period, not the intensity. Not all typhoon events result in intense precipitation at Wakasa due to its location, and many typhoons are associated with high wind speeds alone; hence, some were not associated with very low isotope values during the study period.

### 2.6.2 Precipitation d-excess

In contrast to the  $\delta^{18}\text{O}$  and  $\delta^2\text{H}$  datasets, we observed very clear high-amplitude seasonal patterns in precipitation d-excess, which exhibited an average value of 17.1 ‰ and range of 35.6 ‰ across the entire dataset (Figure 2.3A). The values for summer precipitation fell broadly along the GMWL, whereas winter precipitation consistently expressed higher d-excess values, offset yet parallel to the GMWL (Figure 2.3A). The autumn and spring d-excess values exhibited intermediate values with some overlap with summer and winter, particularly so for the autumn. Regression lines between  $\delta^{18}\text{O}$  and  $\delta^2\text{H}$  applied to each season had similar gradients (-8), with minor differences due to the relatively limited amount of data across a narrow range. The difference in intercept between the summer and winter regression lines was 24.1 ‰ (equating to a difference in seasonally averaged d-excess of 23.5 ‰).

Collective observations of d-excess at sites across Japan suggest that this variable shows this distinct pattern regardless of location (Uemura *et al.*, 2012;

Hasegawa *et al.*, 2014; Ichiyanagi and Tanoue, 2016). High values of d-excess in winter precipitation and low values in summer precipitation can be attributed to contrasting relative humidity values in the precipitation source regions, which overprints the d-excess of the source water itself (Xia *et al.*, 2018; Uemura *et al.*, 2012). Due to cooler sea surface temperatures (and thus low relative humidity) over the Sea of Japan during the winter, we suggest that winter (EAWM) precipitation exhibits higher d-excess values relative to summer (EASM) precipitation, which originates from the oceanic domain during the summer where relative humidity is high (Araguas-Araguas *et al.*, 1998; Kurita *et al.*, 2015). Relative humidity can affect d-excess via multiple mechanisms, but in the low latitudes the dominant control is the amount of raindrop re-evaporation, and in the mid latitudes oceanic evaporation conditions show greater significance (Xia *et al.*, 2022). The gradual transition of influence between these contrasting extremes suggests that there were no abrupt shifts or interfaces between systems at play in this region during spring or autumn and instead, hydrologically, Japan transitioned gradually between the influence of the EAWM and EASM operational modes; supported by the back trajectory analysis (Figure 2.5).

### 2.6.3 Quantity-Weighted Composition

The largest precipitation events during our study interval occurred during winter and, to a lesser extent, during the late summer and early autumn (Figure 2.3A), which is in line with the long-term climate data from nearby Mihama (Figure 2.2). The largest winter events exhibited higher d-excess values, whilst the largest late summer/early autumn events showed low  $\delta^{18}\text{O}$  and  $\delta^2\text{H}$  values (as discussed above). This has important implications for the introduction of precipitation to the catchment; most notably, this indicates that the largest contribution to the catchment on an annual basis is that of a mid-range isotope composition (with high d-excess), with a secondary component having low  $\delta^{18}\text{O}$  and  $\delta^2\text{H}$  values (with low d-excess). When weighted by precipitation amount, the annual mean  $\delta^{18}\text{O}$  was  $-7.4\text{‰}$ , the annual mean  $\delta^2\text{H}$  was  $-39.7\text{‰}$  and the annual mean d-excess was  $19.8\text{‰}$ , which lies between the winter and autumn regression lines. A caveat to this is that the values used to calculate precipitation amount for this analysis were measured by the Netatmo weather station, which did not contain a heating element, so the quantity of

precipitation may be underestimated for snowfall events and hence the precipitation-weighted annual mean  $\delta^{18}\text{O}$  and  $\delta^2\text{H}$  values may lie closer to the winter average. Snowfall events are likely to be amongst the smallest winter precipitation events in Figure 2.3A, however, the relatively tight grouping of winter values suggests that the difference between snowfall and rainfall isotope values was not particularly marked across the observation period.

#### 2.6.4 Temperature and Amount Effects

Least-squares linear regression was performed using the precipitation  $\delta^{18}\text{O}$  and  $\delta^2\text{H}$  values to provide an indication of the influence of a “temperature effect” or precipitation “amount effect”. The isotope data were compared to the average temperature and the total precipitation amount (square root transformed) during each collection period, as measured by the Netatmo weather station (position indicated in Figure 2.1C). These analyses were conducted using monthly average  $\delta^{18}\text{O}$  and  $\delta^2\text{H}$  values (to reduce the influence of noise) and then repeated using datapoints from each season in isolation, and the full results are presented in Table 2.2. All of the calculated  $R^2$  values were low (0.00 – 0.34), suggesting that neither temperature nor precipitation amount explained a large proportion of variability in precipitation  $\delta^{18}\text{O}$  or  $\delta^2\text{H}$ . Our findings are in line with other studies, which have suggested that local meteorological parameters are not as prominent as source region and transport effects on precipitation isotopes in Japan (e.g., Hasegawa *et al.*, 2014; Ichiyangi *et al.*, 2016); however, others have found that they can retain moderate influence on a local scale (Ichiyangi and Tanoue, 2016). Our  $R^2$  values are similar to those presented by Ichiyangi and Tanoue (2016), who found that the  $\delta^{18}\text{O}$  of precipitation in Fukui City, ~60 km from Lake Suigetsu, showed weak to no correlation with either temperature ( $R^2 = 0.02$ ) or precipitation amount ( $R^2 = 0.14$ ).

Analysing the data by season allows for changes in more dominant influences (e.g., opposing precipitation sources) to be minimised, and thus any obscured temperature and amount effects to be more easily identified. Indeed, this method reveals a stronger relationship between precipitation amount and isotope composition in spring, summer and autumn (but no relationship to temperature during those seasons). This suggests that there was a small amount effect acting on isotopes in precipitation at Wakasa, but no observable

temperature effect on event-based timescales. Conversely, winter precipitation isotopes were very weakly correlated with temperature ( $R^2(\delta^{18}\text{O}) = 0.18$ ) and not correlated with precipitation amount ( $R^2(\delta^{18}\text{O}) = 0.00$ ). However, as previously mentioned, the Netatmo weather station did not contain a heating element and hence snowfall amount was underestimated. Hence, we posit that there may have been a small amount effect influencing precipitation isotopes during winter, in line with other seasons, but this was not accounted for by our methods. This analysis suggests that the amount effect was a second-order control on isotopes in precipitation at Wakasa but was obscured by seasonality. Indeed, our dataset provides further qualitative evidence for such an amount effect because we observed minima in precipitation  $\delta^{18}\text{O}$  and  $\delta^2\text{H}$  coinciding with the periods of greatest precipitation amount (excluding the winter  $\delta^2\text{H}$  minimum, observed by high d-excess values) and attributed very low  $\delta^{18}\text{O}$  and  $\delta^2\text{H}$  values to intense precipitation events. It might be expected that a clearer relationship would be observed between precipitation  $\delta^{18}\text{O}$  and  $\delta^2\text{H}$  and the integrated amount of precipitation from across the entire transport pathway (as proposed by Uemura *et al.* (2012)). A lack of any temperature effect was not unexpected, because it has been posited that temperature effects merely explain spatial, not temporal, differences in precipitation isotope composition (Ichiyanagi *et al.*, 2016).

**Table 2.2 Results of the precipitation isotope regression analysis.** Coefficients of determination ( $R^2$ ) between  $\delta^{18}\text{O}$  and  $\delta^2\text{H}$  in precipitation, square root transformed total precipitation during the collection period, and average temperature during the collection period. Least-squares linear regression slopes and intercepts are also provided.

|                                     | Total Precipitation (square root transformed) |       |           | Average Temperature |       |           |
|-------------------------------------|---|-------|-----------|---------------------|-------|-----------|
|                                     | $R^2$   | Slope | Intercept | $R^2$               | Slope | Intercept |
| $\delta^{18}\text{O}$ (all data)    | 0.18  | -0.38 | -4.94     | 0.01                | 0.03  | -7.39     |
| $\delta^2\text{H}$ (all data)       | 0.06  | -2.06 | -25.45    | 0.09                | -0.81 | -25.73    |
| $\delta^{18}\text{O}$ (spring only) | 0.18  | -0.47 | -3.91     | 0.07                | -0.15 | -4.32     |
| $\delta^2\text{H}$ (spring only)    | 0.19  | -4.31 | -17.64    | 0.23                | -2.37 | -9.17     |
| $\delta^{18}\text{O}$ (summer only) | 0.34  | -0.45 | -5.31     | 0.07                | 0.20  | -12.71    |
| $\delta^2\text{H}$ (summer only)    | 0.26  | -3.3  | -37.55    | 0.12                | 2.18  | -109.30   |
| $\delta^{18}\text{O}$ (autumn only) | 0.30  | -0.64 | -3.44     | 0.06                | 0.12  | -8.89     |
| $\delta^2\text{H}$ (autumn only)    | 0.20  | -4.49 | -12.54    | 0.00                | -0.24 | -30.32    |

|                                     |      |       |        |      |      |       |
|-------------------------------------|------|-------|--------|------|------|-------|
| $\delta^{18}\text{O}$ (winter only) | 0.00 | -0.04 | -7.33  | 0.18 | 0.26 | -8.97 |
| $\delta^2\text{H}$ (winter only)    | 0.00 | 1.13  | -35.72 | 0.04 | 1.13 | 35.72 |

## 2.6.5 Comparison to Tokyo

The isotope composition of precipitation at Wakasa and the nearest GNIP station at Tokyo (350 km to the east) was very similar, albeit with some key disparities (Figure 2.3B). The same seasonal patterns in d-excess were observed at both locations, with the summer and winter values acting as end members, and intermediate spring and autumn values. However, compared to Wakasa, the seasonal difference at Tokyo was much less distinct, and the difference between the summer and winter regression line intercept was only 11.1 ‰ (reflecting a difference in seasonally averaged d-excess of 13.0 ‰). This is most likely due to a smaller relative influence of EAWM precipitation (which is associated with the highest d-excess values); Wakasa is located on the Sea of Japan coast, where there is a strong EAWM (and thus Sea of Japan) influence, and Tokyo is located on the Pacific coast, where these influences are significantly weaker. Instead, winter precipitation at Tokyo generally falls in short duration events that result from recycled local water. The local meteoric water line gradients were also shallower and more consistent at Tokyo across the seasons; however, this is likely to be the result of a larger dataset from Tokyo which captured values over a longer timescale. It is important to note that these datasets do not have the same resolution or cover the same period (the Wakasa precipitation dataset is on an event-basis over 2020–22, and the Tokyo precipitation dataset is monthly from 1961–79); however, the same trends are observed when the Wakasa precipitation data is considered at a monthly resolution, and also in comparison to event-based data from Tokyo from 2013 (Figure 2.6; Ichiyanagi and Tanoue, 2016). The similarities between these data and the longer term monthly GNIP data (Figure 2.3) show that the differences observed between precipitation isotopes in Wakasa and Tokyo cannot be attributed to differences in climate between 1960–79 and the present day. The data presented from 2013 are more scattered than the Tokyo GNIP data (likely a result of a short sampling period) but retain the same summer and winter end members which closely overlap due to similar d-excess values (Figure 2.6). Furthermore, these data demonstrate

that considering monthly averages, rather than shorter-term (event based) values simply removes excess scatter from the dataset and does not eliminate seasonal patterns. Hence, the comparisons made between the Wakasa precipitation data and the Tokyo GNIP data are reasonable.

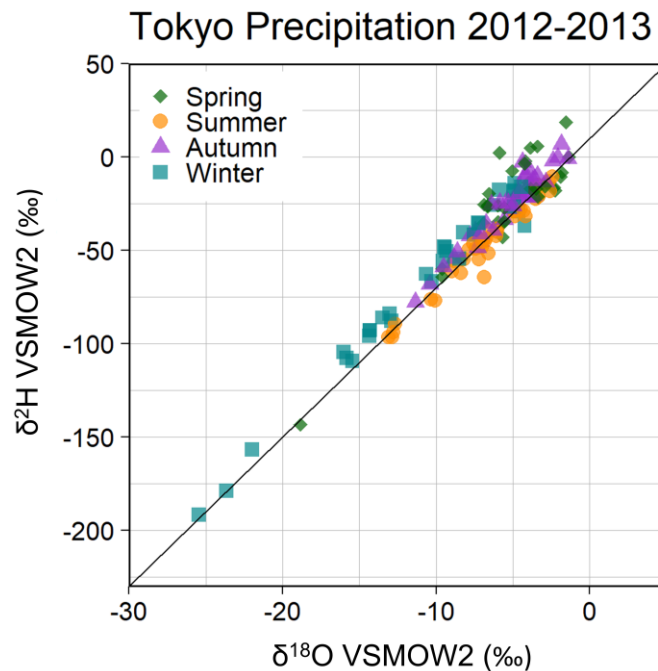


**Figure 2.6 Precipitation  $\delta^{18}\text{O}$  and  $\delta^2\text{H}$  at Tokyo, 2013.** Isotopes in precipitation for Tokyo, 2013, based on event-based sampling in Arakawa and Meguro districts, Tokyo Prefecture (Ichiyanagi and Tanoue, 2016). Similarities between this dataset and the equivalent Tokyo dataset in Figure 2.3B demonstrate the robustness of comparison between the Tokyo GNIP dataset and the isotopes in precipitation at Wakasa (this study).

### 2.6.6 Catchment Effects

The seasonal patterns in Hasu River  $\delta_{\text{river}}$  and Lake Mikata and Lake Suigetsu surface  $\delta_{\text{lake}}$  paralleled those of  $\delta_{\text{precipitation}}$ , showing that the precipitation signals were transferred to the catchment, although there is evidence for some internal modification (Figure 2.7). All three locations (the Hasu River, Lake Mikata and Lake Suigetsu) exhibit a smaller range of  $\delta^{18}\text{O}$  and  $\delta^2\text{H}$  values than precipitation, and hence plot as a tighter grouping of points (range( $\delta^{18}\text{O}$ ) =  $-9.5$  to  $-4.5$  ‰,  $1\sigma(\delta^{18}\text{O}) = 1.0$  ‰ for river and lake water (Figure 2.7A) versus  $-13.0$  to  $-2.5$  ‰ and  $2.3$  ‰ respectively for precipitation (Figure 2.3A)), which indicates homogenisation of precipitation inputs with existing catchment waters (likely both surficial water and groundwater). Whilst the isotope composition of groundwater was not quantified as part of this study, and hence remains an

unknown input to the lake system, we posit that groundwater composition was merely a slower average of precipitation composition; otherwise, lake water  $\delta^{18}\text{O}$  and  $\delta^2\text{H}$  would be offset to that of precipitation. We also observed that in-catchment homogenisation attenuated the effect of peripheral values and thus there was a limited influence of isolated events (including the aforementioned intense precipitation events with very low  $\delta^{18}\text{O}$  and  $\delta^2\text{H}$  values) on the lake system. Instead, prolonged precipitation modes were the more dominant control. Despite annually averaged precipitation being strongly weighted to winter, signals from all four seasons were detectable in the river and lakes (discussed further in Section 2.6.7).

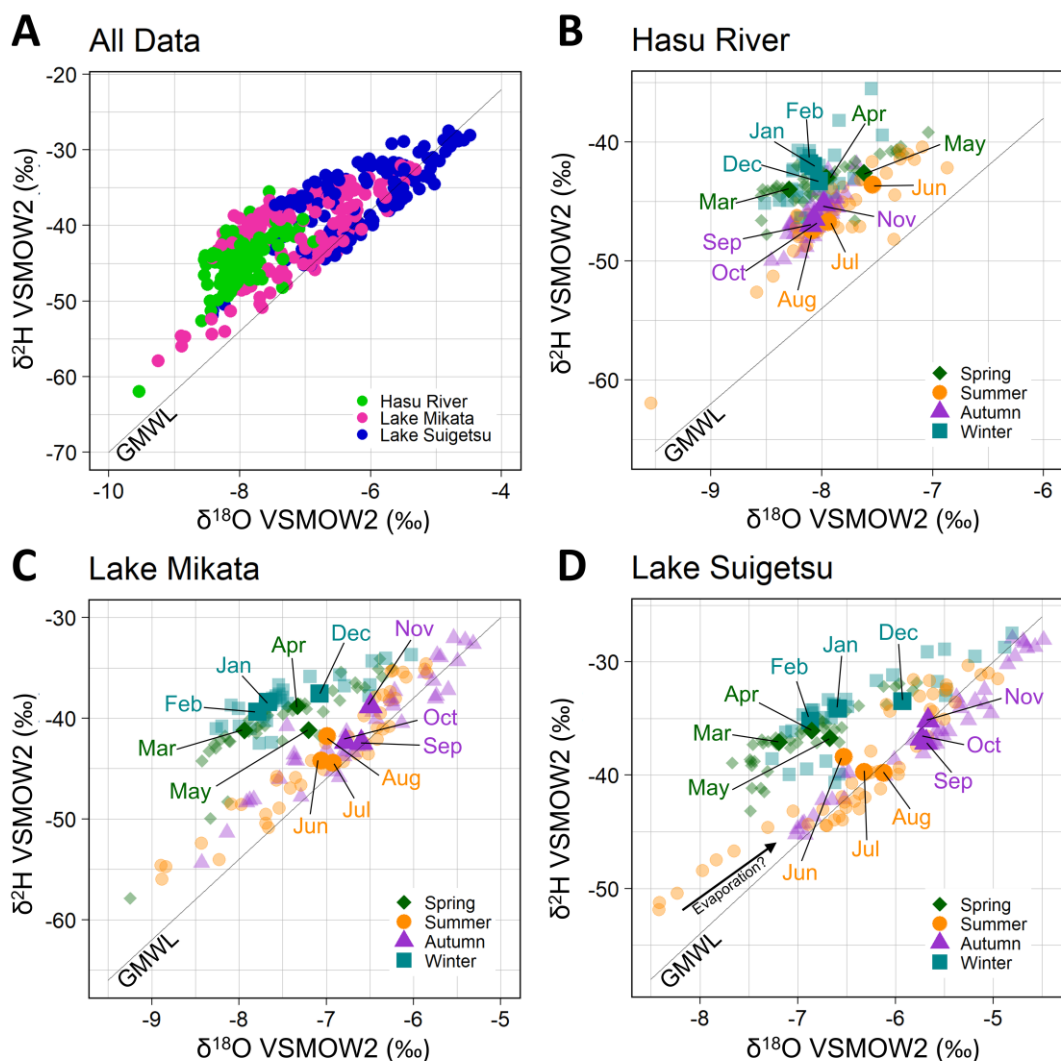


**Figure 2.7 Surface water  $\delta^{18}\text{O}$  and  $\delta^2\text{H}$ .** The isotope composition of surface waters from the Hasu River, Lake Mikata and Lake Suigetsu. Panel A shows differences in composition between parts of the catchment, with colour corresponding to location. Subsequent panels show seasonal variations in composition at (B) the Hasu River, (C) Lake Mikata and (D) Lake Suigetsu. In B–D, monthly averages are shown as opaque symbols and labelled, whilst underlying data points are shown as transparent symbols. Points in B–D are colour-coded by season as in Figure 2.3. Samples were collected by K. Nagaya and analysed by C. Arrowsmith.

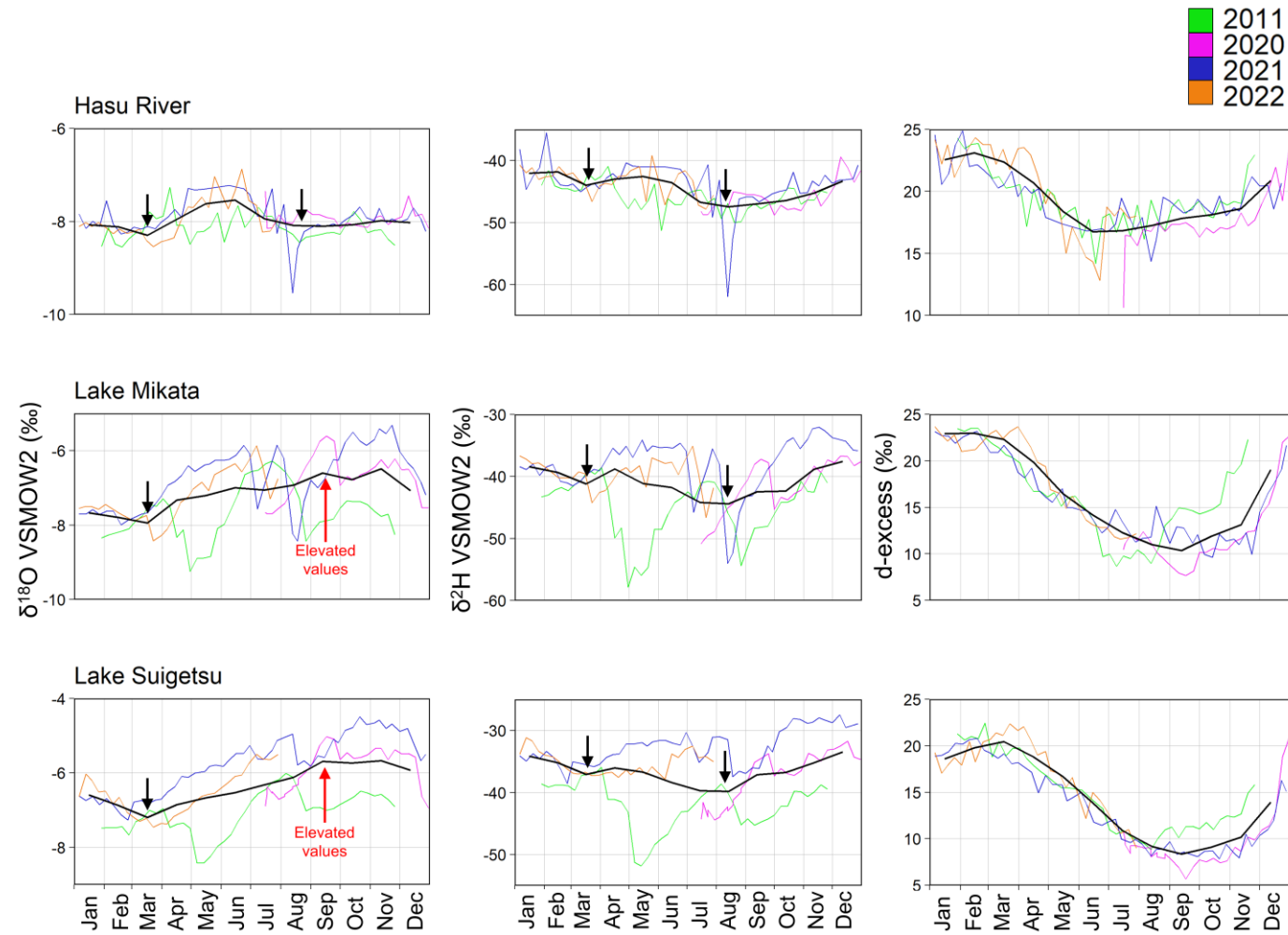


**Figure 2.8 Variations in  $\delta_{\text{river}}$  and  $\delta_{\text{lake}}$  with time.**  $\delta^{18}\text{O}$ ,  $\delta^2\text{H}$  and d-excess values from the Hasu River, Lake Mikata and Lake Suigetsu from across the study period (colour lines). Black lines represent monthly averages of each dataset. Vertical scales are non-equivalent to best represent the shape of the data for each location. Samples were collected by K. Nagaya and analysed by C. Arrowsmith

The evolution of  $\delta^{18}\text{O}$  and  $\delta^2\text{H}$  as water moves through the catchment from the Hasu River to Lake Mikata and then to Lake Suigetsu, also reveals some interesting patterns (Figure 2.7A). The Hasu River exhibits a very tight grouping ( $1\sigma(\delta^{18}\text{O}) = 0.36 \text{ ‰}$ ) of low isotope ratios (mean( $\delta^{18}\text{O}$ ) =  $-7.98 \text{ ‰}$ ). Isotope values then increased, parallel to the GMWL, as the water moved through to Lake Mikata (mean( $\delta^{18}\text{O}$ ) =  $-7.13 \text{ ‰}$ ,  $1\sigma(\delta^{18}\text{O}) = 0.83 \text{ ‰}$ ) and then to Lake Suigetsu (mean( $\delta^{18}\text{O}$ ) =  $-6.32 \text{ ‰}$ ,  $1\sigma(\delta^{18}\text{O}) = 0.85 \text{ ‰}$ ). This suggests some mixing with seawater (which has higher  $\delta^{18}\text{O}$  and  $\delta^2\text{H}$ ) in the lakes, with a greater departure in values for Lake Suigetsu, which is the most saline of the three locations (2 to  $14 \text{ g kg}^{-1}$ ; discussed further in Section 2.6.9). Comparatively, the compositions of Lake Mikata and Lake Suigetsu also covered a greater range than the Hasu River. Prior to this study, it was assumed that the Hasu River was the primary input to the lakes, however the differences in the range of their isotope compositions suggests that there was an additional overland (responsive) flow component feeding the lake system and that the river received a substantial groundwater input, producing a more homogenised isotope signal (Figure 2.7B). Despite this, the river still reflected the seasonality of precipitation composition, and whilst monthly average composition values for the Hasu River exhibited smaller variations than Lake Mikata and Lake Suigetsu, the signals from the river maintained coincident timing with these parts of the catchment (Figure 2.8). These observations suggest that the Hasu River had both direct and groundwater influences on its isotope composition, but we cannot rule out the possibility that weekly sampling of the river did not fully capture the most extreme isotope values here, due to the rate of river flow relative to the sampling resolution and the large catchment area.

### 2.6.7 River and Lake Water d-excess

Despite the signal homogenisation, seasonal variations in river and lake water d-excess were very similar to precipitation d-excess, with clear differences observed across the year (Figure 2.7B, Figure 2.7C and Figure 2.7D) which can be interpreted in line with the precipitation signals. This offers the most convincing evidence that  $\delta_{\text{precipitation}}$  signals are detectable in  $\delta_{\text{lake}}$ . However, the difference between lake water (Figure 2.8) and precipitation d-excess seasonality (Figure 2.4) highlights a major modification of the precipitation signals delivered to the catchment. The seasonal extremes observed in the lakes fell during spring (high

d-excess) and autumn (low d-excess; Figure 2.8), in contrast to the winter and summer extremes observed in precipitation d-excess (Figure 2.4). This indicates a lag of ~1–3 months between an input of precipitation and detection of this signal in lake water composition, which we attribute to the average time taken for the water to transit through the catchment. Incidentally, this interval is equivalent to the residence time of the mixolimnion, providing support for our estimation that every three months the upper ~8m of the water column is replaced with precipitation from three months previously. A comparison of Lake Suigetsu d-excess to Wakasa precipitation d-excess suggests that the transit lag was proportional to the amount of precipitation and was longer (two to three months) for the drier summer months and shorter (one to two months) during the wetter winter months. A shorter winter lag compared to summer contrasts with what might be expected for a season associated with the accumulation of snow in the catchment (which can persist on high ground for weeks at a time) and the delayed release of snowmelt to the lakes. This appears to suggest that either the snowmelt lag was negligible compared to catchment transit time, possibly because only precipitation falling on the highest ground in the catchment was delayed, or that there was still sufficient winter rainfall or rapidly melting snow to cause a response in the lake and river water within one to two months.

### **2.6.8 River and Lake Water $\delta^{18}\text{O}$ and $\delta^2\text{H}$**

The river and lake water  $\delta^{18}\text{O}$  and  $\delta^2\text{H}$  values were also very similar to precipitation, exhibiting intra-seasonal variability with major overlap (Figure 2.7B, Figure 2.7C and Figure 2.7D). The Hasu River showed  $\delta^{18}\text{O}$  minima in spring and late summer, a  $\delta^2\text{H}$  minimum in late summer and slight downward inflection in  $\delta^2\text{H}$  during spring, which were reflected in both the raw datasets and in the monthly averages (Figure 2.8). Lake Mikata and Lake Suigetsu showed greater inter- and intra-annual differences than the Hasu River, but monthly averaged data from these parts of the catchment also exhibited minima in  $\delta^{18}\text{O}$  in the spring and  $\delta^2\text{H}$  in the late summer, as well as a downward inflection in  $\delta^2\text{H}$  during the spring (Figure 2.8). We relate these minima to winter (EAWM) precipitation and summer (EASM) precipitation, as detailed above in relation to precipitation  $\delta^{18}\text{O}$  and  $\delta^2\text{H}$ ; importantly, accounting for the aforementioned transit lag. However, unlike precipitation  $\delta^{18}\text{O}$ , lake  $\delta^{18}\text{O}$  lacked a minimum

coinciding with summer (EASM) water entering the lake; instead, there were elevated  $\delta^{18}\text{O}$  values in the autumn in Lake Suigetsu (and to a lesser extent, Lake Mikata). The autumnal  $\delta^{18}\text{O}$  peak (based on monthly averages) in Lake Suigetsu was approximately 3 ‰ greater than the  $\delta^{18}\text{O}$  of summer precipitation. We attribute this trend to a combination of lake water mixing and saline water incursion, which brings saline water with high  $\delta^{18}\text{O}$  and  $\delta^2\text{H}$  values to the surface, causing elevated lake isotope values in autumn (discussed in Section 2.6.9) and a small amount of summer evaporative enrichment. We might also expect to see this trend in  $\delta^2\text{H}$ , given our proposed mechanisms, however this was not observed, likely as an artefact of a relatively small spring  $\delta^2\text{H}$  inflection (due to high d-excess values).

Besides these elevated values of lake water  $\delta^{18}\text{O}$  in summer and autumn, there is very limited evidence for an evaporation effect on the composition of lake water; a subset of summer values in each lake expressed a  $\delta^{18}\text{O}$  versus  $\delta^2\text{H}$  relationship with a reduced slope (similar to a local evaporation line), however this was restricted to the data collected in 2011 and was not present in the 2020–2022 data (Figure 2.7C and Figure 2.7D). Additionally, the  $\delta^{18}\text{O}$  versus  $\delta^2\text{H}$  slope for other seasons did not suggest evaporation effects. This highlights the potential for inter-annual variability in the influence of evaporation on lake water isotopes, but demonstrates that this effect was a secondary one and affected summer  $\delta^{18}\text{O}$  and  $\delta^2\text{H}$  alone. We posit that the enhanced evaporation in summer 2011 was due to lower relative humidity. Relative humidity data was not available from the local Mihama weather station, but the nearest data from Tsuruga, 14 km to the northeast shows that relative humidity in 2011 was on average 5 % lower than summer 2021 (Japanese Meteorological Agency, 2023). Whilst Tsuruga experiences subtly different weather conditions, it is reasonable to compare these locations on seasonal timescales.

As well as this evaporation trend,  $\delta_{\text{lake}}$  in 2011 showed some discrepancies relative to the 2020–2022 interval (the data from which were broadly consistent). The data from 2011 showed a distinctive trend (a minimum in  $\delta^{18}\text{O}$  and  $\delta^2\text{H}$  in May, and an earlier increase in d-excess in the autumn). Because these trends were not observed for the Hasu River, they can be attributed to within-lake processes; however, there is no comparable precipitation isotope data available for this period in order to further interrogate this interpretation.

Data from the local Mihama weather station shows intense precipitation during May 2011 (448 mm), which could have resulted in a significant direct input of low  $\delta^{18}\text{O}$  and  $\delta^2\text{H}$  water into Lake Mikata and Lake Suigetsu during this month; however, with available data this remains speculative. Overall high precipitation amounts in 2011, and hence a shorter residence time, might also explain the earlier increase in lake d-excess in autumn 2011 compared to the 2020–2022 observation period.

### 2.6.9 Vertical Profiles of Lake Water Isotopes in Lake Suigetsu

The ~quarterly depth profiling of Lake Suigetsu shows seasonal variations in the mixolimnion (above the chemocline), but compositions were consistent and homogenous in the monimolimnion year-round (Figure 2.9). In the monimolimnion, temperature and salinity were consistently at  $\sim 16\text{ }^\circ\text{C}$  and  $\sim 14\text{ g kg}^{-1}$ , respectively. Above the chemocline, the water temperature was highest in the summer and lowest in the winter. A salinity minimum was observed during the spring and maximum during the autumn, with summer and winter exhibiting intermediate values. These observations are in agreement with the findings of Kondo *et al.* (2000), which presented long term monitoring of changes in temperature and salinity with depth at Lake Suigetsu. Throughout the sampling period the monimolimnion waters had higher  $\delta^{18}\text{O}$  and  $\delta^2\text{H}$  values relative to the mixolimnion and showed no variation with depth between  $\sim 8\text{ m}$  and the lake bottom at 34 m. The d-excess values in the monimolimnion were also invariant and generally lower than the mixolimnion. In the mixolimnion, the  $\delta^{18}\text{O}$ ,  $\delta^2\text{H}$  and d-excess values showed smooth gradients between the chemocline and the surface, which suggests that the shape of each depth profile was driven by the difference between deepwater and surficial  $\delta_{\text{lake}}$ . The d-excess depth profiles in Figure 2.9 matched the seasonal fluctuations discussed above, with the highest values in spring and lowest values in autumn.

The  $\delta^{18}\text{O}$ ,  $\delta^2\text{H}$  and d-excess profiles did not show any correlation with temperature and hence lake water temperature is unlikely to have been a controlling factor. However, there was an increase in salinity,  $\delta^{18}\text{O}$  and  $\delta^2\text{H}$  through summer and autumn which suggests common drivers. We theorise that this trend was a result of saline water incursion and mixolimnion mixing during autumn (evidenced by Kondo *et al.*, 2020). Summer evaporation could have

enhanced this effect via the enrichment of heavier isotopes at the surface and by increasing the relative concentration of dissolved ions. There is evidence for a combination of these effects at play, because both the summer (August) and winter (November) profiles exhibited raised surface  $\delta^{18}\text{O}$  and  $\delta^2\text{H}$  values (Figure 2.9); however, the evidence for evaporation trends in the surface water samples (discussed above) was limited to 2011, so we suggest that in most years evaporation was less influential than mixing. These effects explain the absence of a late summer  $\delta^{18}\text{O}$  minimum in Lake Mikata and Lake Suigetsu (in contrast to precipitation  $\delta^{18}\text{O}$ ) and elevated autumn values (discussed above; Figure 2.8). D-excess did not appear to change majorly in autumn; possibly due to the overwhelming influence of seasonality, but most likely because the d-excess values at the surface and in the saline deep water were similar during the autumn. Hence, any amount of incursion or mixing would not result in a change in d-excess at the surface.

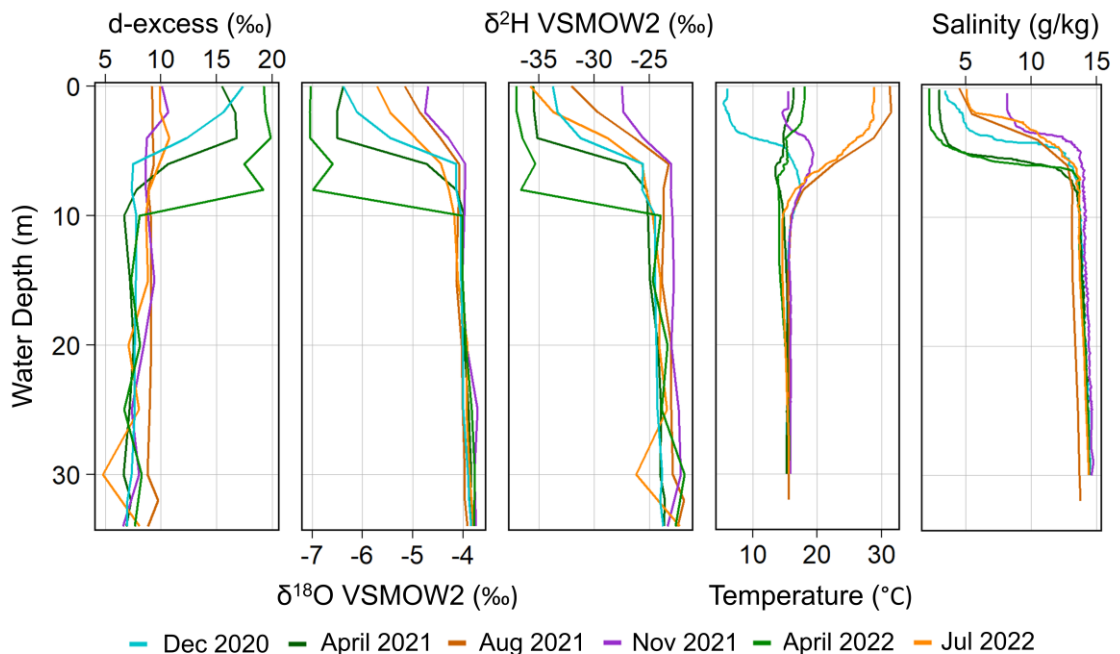


**Figure 2.9 Variations in Suigetsu  $\delta_{\text{lake}}$  with depth.** d-excess,  $\delta^{18}\text{O}$ ,  $\delta^2\text{H}$ , temperature and salinity profiles across the study interval. Data were collected (approximately quarterly) on 22<sup>nd</sup> December 2020, 8<sup>th</sup> April 2021, 5<sup>th</sup> August 2021, 17<sup>th</sup> November 2021, 23<sup>rd</sup> April 2022, and 21<sup>st</sup> July 2022. Samples were collected by K. Nagaya and analysed by C. Arrowsmith. Temperature and salinity data were provided by Y. Miyamoto.

The combined influence of saline water incursion, mixing and evaporation did not persist through the entirety of the year; evidence from the surface water isotopes indicates that evaporation was limited to the summer, and extended

monitoring by Kondo *et al.* (2000) suggested that mixolimnion mixing was temporally constrained to autumn. Our observations suggest that heavy winter precipitation delivered to the catchment regenerated the freshwater mixolimnion in Lake Suigetsu and effectively “reset” the effects described above, producing the minima in  $\delta^{18}\text{O}$  and  $\delta^2\text{H}$  in the surface waters (Figure 2.8) and reinstating the relationship between precipitation and lake  $\delta^{18}\text{O}$  and  $\delta^2\text{H}$ . However, since the surface waters of Lake Suigetsu retain some salinity year-round, the influence of saline water is never zero, merely diminished in relation to the effect of precipitation inputs. We observed an increase in  $\delta^{18}\text{O}$  and  $\delta^2\text{H}$  of the surface waters from the freshwater Hasu River to the fresh-brackish Lake Mikata and then to the brackish-saline Lake Suigetsu (Figure 2.7), which was likely due to increasing quantities of Sea of Japan-derived waters (with higher isotope compositions). The composition of Lake Suigetsu showed the greatest departure from the Hasu River composition during autumn, but there was still  $\sim 1$  ‰ difference in  $\delta^{18}\text{O}$  during spring between the locations which can be attributed to this non-zero salinity. Lake Mikata existed between the compositions of Lake Suigetsu and the Hasu River because it is a shallower water body with no persistent saline deepwater but does experience a small degree of saline water incursion during autumn (Kondo *et al.*, unpublished data) and possibly some evaporation.

## 2.7 Discussion

The key motivation of this study was to understand the major controls of  $\delta_{\text{river}}$  and  $\delta_{\text{lake}}$  within the Five Lakes of Mikata catchment and hence direct future interpretation of isotope-based palaeoclimate proxies from the Lake Suigetsu sediment cores. Our results show that a dominant control of Lake Suigetsu  $\delta_{\text{lake}}$  (as well as Lake Mikata  $\delta_{\text{lake}}$ ) was the isotope composition of precipitation, and whilst there were internal catchment processes (homogenisation, a transit lag, seawater influences and evaporation) that affected the composition of river and lakes, for the most part (excluding autumn) these did not obscure the  $\delta_{\text{precipitation}}$  signals, or prevent their detection in  $\delta_{\text{lake}}$ . Indeed, the predominant effect of the signal homogenisation was to limit the effect of  $\delta_{\text{precipitation}}$  dataset noise on  $\delta_{\text{lake}}$ . In order to better understand the propagation of  $\delta_{\text{precipitation}}$  signals to  $\delta_{\text{lake}}$  across the span of the Suigetsu cores, it is important to consider the ways in which the current lake configuration is non-analogous to the past.

Our observations also indicate that evaporation effects were not particularly influential during the study period (with the strongest evidence limited to a single year) and were limited to the summer months. This would be expected to be the case for much of the interval covered by the Suigetsu cores, given that, aside from the Eemian, our monitoring period existed at the upper limit of temperatures experienced at the Five Lakes of Mikata for the last 150 ka. Whilst it is important to consider that evaporation is not singularly related to air temperature, but rather a range of interconnected physical processes, Lake Suigetsu receives large quantities of precipitation annually which limits the impact of evaporation on  $\delta_{\text{lake}}$  (Vystavna *et al.*, 2021). It follows that evaporation is not likely to have been a major driver of  $\delta_{\text{lake}}$  across the history of Lake Suigetsu sedimentation, as long as the region was not significantly more arid in the past, but should still be considered when interpreting proxies of summer  $\delta_{\text{lake}}$ .

Marine influences are also negligible from a palaeo-isotope perspective. In the modern day, saline water incursions and mixing of surface lake water with low  $\delta^{18}\text{O}$  and  $\delta^2\text{H}$  deepwater originating from the Sea of Japan had a demonstrable effect on lake  $\delta^{18}\text{O}$  and  $\delta^2\text{H}$  in the autumn months. However, the connection between Lake Suigetsu and the Sea of Japan is anthropogenic and there were no marine influences on the lakes for most of the late Pleistocene (exceptions being at  $\sim 7$  ka during a highstand in the Sea of Japan, and during the Eemian global highstand) as corroborated by diatom assemblage counts of freshwater versus brackish-tolerant species (Saito-Kato *et al.*, in prep). Aside from these intervals, we predict that  $\delta_{\text{lake}}$  was not affected by seawater, either via saline water incursions or mixing. There is evidence for stratification in the past (deepwater anoxia is supported by varve preservation, and surface water oxygenation is supported by aquatic productivity); however, we would not expect to see the same stark difference in isotope compositions above and below the palaeo-chemocline as the present-day chemocline because the deepwater and surficial waters would have had the same meteoric source. As a result, there would be no influence of the Sea of Japan to Lake Suigetsu outside of these periods and the elevated autumn  $\delta^{18}\text{O}$  and  $\delta^2\text{H}$  values that partially obscure the summer precipitation  $\delta^{18}\text{O}$  minima would not be observed. Hence, in the intervals where Lake Suigetsu was a freshwater lake, we would expect  $\delta_{\text{precipitation}}$

and  $\delta_{\text{lake}}$  to be more closely aligned, and no offset between the Hasu River, Lake Mikata and Lake Suigetsu.

However, persistence of this stratification regime, evidenced by the preservation of varves that required basal water anoxia, suggests that the mechanistic elements of signal homogenisation (muting the seasonal precipitation signal in the surface water and homogenising the deepwater) and seasonal lags in the surface water were still active during this time, although subject to some variability. As a result, on longer timescales, palaeoclimate proxies that record deepwater conditions (e.g., isotopes of siderite ( $\text{FeCO}_3$ ), abundant in Lake Suigetsu) would record an averaged  $\delta_{\text{precipitation}}$  signal, possibly over a number of years (accounting for other fractionation processes involved in signal capture by the proxy system). Conversely, palaeoclimate proxies that record surface water conditions (e.g., diatoms and other algae) will record seasonally lagged  $\delta_{\text{precipitation}}$ ; i.e., spring-weighted proxies will capture winter  $\delta_{\text{precipitation}}$ , and so forth. This relationship is of course subject to variations in the lag time (which, if lengthened, could cause greater overlap of seasonal signals) and differences in climate, which could alter the timing of delivery to the lakes. During glacial intervals, pollen reconstructed temperature for the coldest month is consistently below  $0^\circ\text{C}$ , suggesting that the limited snowmelt lag in the present day would be more prominent. Additionally, the lakes were likely frozen on the surface for much of the winter. Overall, this would be expected to have stalled the movement of water through the catchment and extend the transit lag between delivery of winter (EAWM) precipitation and detection in the lake into the spring season. Under these circumstances, palaeoclimate proxies that capture the spring  $\delta_{\text{lake}}$ , such as spring blooming diatoms, would capture winter (EAWM)  $\delta_{\text{precipitation}}$  (arguably with even greater certainty than the present day). Proxies that capture summer  $\delta_{\text{lake}}$ , such as algal biomarkers would, by contrast, capture a mix between winter, spring and summer  $\delta_{\text{precipitation}}$  because these would enter the lake in quicker succession (although spring precipitation quantities are very small in comparison to winter and summer, and hence are unlikely to have a significant effect). Autumn  $\delta_{\text{lake}}$ -capturing proxies, such as autumn blooming diatoms, would still predominately capture summer (EASM)  $\delta_{\text{precipitation}}$  composition. Terrestrial proxies (e.g.,  $\delta^{18}\text{O}$  of pollen grains and  $\delta^2\text{H}$  of long-chained n-alkanes and n-alkanoic acids) would be unaffected by changes

to the transit lag as they capture soil pore water rather than lake water and would be expected to more closely reflect changing  $\delta_{\text{precipitation}}$ .

Having established that the dominant driver of  $\delta_{\text{lake}}$  is  $\delta_{\text{precipitation}}$ , it is prudent to consider what could affect this quantity in the past. We anticipate that palaeo-EAM precipitation from both seasonal modes was a dominant influence on  $\delta_{\text{precipitation}}$  delivered to the catchment because winter and summer are associated with large quantities of precipitation (and hence  $\delta_{\text{precipitation}}$  will be weighted towards the composition of the EAWM and EASM). Additionally, whilst autumn (predominately typhoon) precipitation provides a third period of rain annually, and we observe the influence of intense precipitation events on  $\delta^{18}\text{O}$  and  $\delta^2\text{H}$  of precipitation, these signals were not detected in the lakes. For this reason, we anticipate that unless typhoon frequency was significantly greater in the past, the tendency of  $\delta_{\text{lake}}$  to reflect only extended seasonal precipitation events (i.e., the EAM) will limit the influence of typhoon precipitation, even if it is recorded in  $\delta_{\text{precipitation}}$ . It is not unreasonable, therefore, to exclude the typhoon season influence on  $\delta_{\text{precipitation}}$ , and consider  $\delta_{\text{precipitation}}$  at Wakasa to be most closely linked with EAM behaviour. Importantly, the influence of both EAWM and EASM components were observed at the catchment, establishing that the area is a sensitive location – even optimised, especially relative to Tokyo – for studying both components of the EAM. This is particularly useful given the skew in existing palaeoclimate reconstructions towards the summer months.

However, our findings were consistent with others from central Japan (e.g., Taniguchi *et al.*, 2000), which note that for contemporary isotopes there is no major difference in  $\delta^{18}\text{O}$  and  $\delta^2\text{H}$  between EAWM and EASM precipitation. As such, it is important to note that unlike Continental Asia, annually integrated  $\delta^{18}\text{O}$  and  $\delta^2\text{H}$  do not reflect the changing relative input of EAWM and EASM precipitation, because their compositions are so alike. Isotope composition averaged on multiannual timescales will not reflect the balance between these systems unless either one of EAWM or EASM changes in strength and the other remains stable, or one increases in strength and the other decreases concurrently. These changes in behaviour can be caused by different climatic regimes (such as glacial periods) or across climatic transitions. Under such conditions, the changing strength of the EAWM and EASM would be expected to impact on both the annually averaged deep  $\delta_{\text{lake}}$  and the seasonally-lagged

surface water  $\delta_{\text{lake}}$ ; the former by affecting the balance between the two seasonal modes, and the latter by affecting either EAWM or EASM  $\delta_{\text{precipitation}}$ . Under these circumstances, EAWM and EASM  $\delta_{\text{precipitation}}$  would diverge, and hence terrestrial and surface water palaeoclimate proxy seasonality becomes extremely important for interpretation. It is therefore vital to know which composition (winter-weighted, summer-weighted or mixed) is captured by each palaeoclimate proxy before interpreting the signal, accounting also for changes to the lag time.

Our observations are restricted to the study interval, and hence provide limited contributions to the interpretation of long-term drivers of  $\delta^{18}\text{O}$  and  $\delta^2\text{H}$  associated with EAM behaviour, however this remains an important component of palaeoclimate proxy interpretation. EAM rainfall  $\delta_{\text{precipitation}}$  tends to respond inversely to monsoon strength, due to a combination of preferential rainout of the heavier isotopes, enhanced by increased quantities of precipitation and increased cloud top height with a stronger monsoonal convection, which is associated with low condensation temperatures (Cai and Tian, 2016). Our results show that the amount effect does not have a strong relationship within the catchment in the modern day; however, that does not preclude a relationship to monsoon intensity; Uemura *et al.* (2012) noted a limited influence of local precipitation amount on  $\delta^{18}\text{O}$  in Okinawa (Southern Japan), but that the precipitation amount integrated over the full transport pathway was significant. Furthermore, the Fukugaguchi stalagmite record (Itoigawa, central Japan) shows a strong relationship of  $\delta^{18}\text{O}$  to EAWM precipitation amount despite modern  $\delta_{\text{precipitation}}$  showing a statistically weak relationship to precipitation amount (Sone *et al.*, 2013). Other factors which could contribute to the overall signal are changes at source: composition, temperature and relative humidity (e.g., Amekawa *et al.*, 2021), and, in the EASM mode, the positioning of the EAM front (Kurita *et al.*, 2015). Furthermore, the prevalence of sea ice during glacial periods, particularly in the relatively isolated Sea of Japan, might be expected to limit evaporation despite changes to EAWM strength. Hence, it is vital to consider how EAM  $\delta_{\text{precipitation}}$  was controlled by the evolution of the climate of the region as a whole and how this affected  $\delta_{\text{precipitation}}$  at Wakasa.

Finally, the clearest seasonal signal derived from the catchment was undoubtedly that of d-excess, and this was the only isotope parameter which

demonstrated the ability to distinguish precipitation from different seasons. Not only this, but the transfer of the d-excess signal from precipitation to lake was clearer than for  $\delta^{18}\text{O}$  and  $\delta^2\text{H}$ , possibly due to the amplitude of seasonal changes and the limited influence of other competing controls. However, it is much more difficult to calculate d-excess using palaeo-isotope reconstructions, because it requires the combination of temporally and spatially equivalent  $\delta^{18}\text{O}$  and  $\delta^2\text{H}$  values. If compatible palaeoclimate proxy records are produced and d-excess calculation becomes possible, this should be a consideration for future research based on the excellent seasonal distinctions observed in this variable and its potential as a powerful proxy of past monsoon dynamics.

## 2.8 Conclusions

Understanding the relationship between climate variability, the isotope composition of precipitation and the transfer of precipitation isotope signals into lake waters is essential to support the interpretation of past climates using isotope-based proxies derived from lake sediments. Using contemporary monitoring of the isotope composition of precipitation ( $\delta_{\text{precipitation}}$ ), river water ( $\delta_{\text{river}}$ ) and lake water ( $\delta_{\text{lake}}$ ) across the Five Lakes of Mikata catchment, Japan, we assessed the factors affecting  $\delta_{\text{lake}}$ , with a particular focus on Lake Suigetsu. Precipitation  $\delta^{18}\text{O}$  and  $\delta^2\text{H}$  exhibited only small seasonal differences across the year due to the similar compositions of winter (EAWM) and summer (EASM) precipitation, which act as end members with opposing trajectories. Precipitation d-excess, by contrast, clearly demarcated the different seasonal influences due to different evaporation conditions at the moisture sources of the EAWM (Sea of Japan) and EASM (Pacific Ocean domain), with a gradual shift between the two during the spring and autumn. The difference between winter and summer d-excess was enhanced by the location of the catchment. There was limited statistical evidence to support a temperature effect over precipitation  $\delta^{18}\text{O}$  or  $\delta^2\text{H}$ ; however, when considering the data on a seasonal basis, there was some evidence to support a local amount effect, with minima in monthly averaged  $\delta^{18}\text{O}$  and  $\delta^2\text{H}$  during the wettest (EAM) seasons of the year.

We found that  $\delta_{\text{lake}}$  and  $\delta_{\text{precipitation}}$  were directly related, although the spread of values of  $\delta_{\text{lake}}$  was more limited due to in-catchment homogenisation. Despite this, compositional patterns were preserved, and it was still possible to detect

seasonal trends in  $\delta_{\text{lake}}$ , which paralleled those of  $\delta_{\text{precipitation}}$  and were attributed to the same causes. A two to three-month transit lag between  $\delta_{\text{precipitation}}$  and  $\delta_{\text{lake}}$  was observed and the length of this lag related to the quantity of precipitation. The influence of isolated precipitation events on  $\delta_{\text{lake}}$  (including typhoons) was negligible in comparison to significant extended freshwater inputs to the catchment from the East Asian Monsoon. The incursion of saline water from the Sea of Japan and autumnal mixing resulted in elevated  $\delta^{18}\text{O}$  and  $\delta^2\text{H}$  values in the lakes during late summer and autumn (obscuring the  $\delta^{18}\text{O}$  minimum equated to the EASM) and caused a greater effect for Lake Suigetsu than Lake Mikata. This was possibly combined with summer evaporation effects, although evidence for the influence of evaporation varied between years. The large influx of winter precipitation to the catchment re-established the relationship between  $\delta_{\text{lake}}$  and  $\delta_{\text{precipitation}}$  which extended from winter to early summer. Deep water composition in Lake Suigetsu was stable and homogenous across the study period.

These results will facilitate interpretation of palaeoclimate reconstructions derived from oxygen and hydrogen isotope analysis of the Lake Suigetsu sediment cores. It is expected that  $\delta_{\text{precipitation}}$  (and thus  $\delta_{\text{lake}}$ ) will be closely related to East Asian Summer Monsoon and East Asian Winter Monsoon  $\delta_{\text{precipitation}}$  fluctuations across the ~150 ka of the late Quaternary covered by the Suigetsu cores. The seasonal patterns in  $\delta_{\text{lake}}$  could be altered under different climatic regimes by large scale drivers (such as monsoon strength and balance of seasonal precipitation), along with the influence of local factors, including the transit lag. However, not all of the factors affecting  $\delta_{\text{lake}}$  observed during this contemporary monitoring will be significant on longer timescales. The incursion of sea water is a consequence of anthropogenic catchment alteration and, as such, is not expected to have affected the lake water isotope hydrology prior to the last ~400 years. Evaporation is also expected to have minimal effects on down-core  $\delta_{\text{lake}}$  reconstructions which are limited to the summer months. Robust interpretation is predicated on sound understanding of proxy seasonality and whether the proxy captures surficial or deepwater  $\delta_{\text{lake}}$ .

## Chapter 3 Insights into Deglacial East Asian Monsoon Seasonality and Inter-Regional Teleconnections from Lake Suigetsu, Japan

Rex, Charlie L.<sup>1,2</sup>, Staff, Richard A.<sup>1</sup>, Leng, Melanie J.<sup>3</sup>, Toney, Jaime L.<sup>2</sup>, Pearson, Emma J.<sup>4</sup>, Tyler, Jonathan J.<sup>5</sup>, Swann, George E.A.<sup>6</sup>, Lacey, Jack H.<sup>3</sup>, Saito-Kato, Megumi<sup>7</sup>, Nakagawa, Takeshi<sup>8</sup> (unpublished). 'Insights into deglacial East Asian Monsoon seasonality and inter-regional teleconnections from Lake Suigetsu, Japan'. Submitted to: *Nature Communications*. Available on EarthArXiv at: <https://doi.org/10.31223/X56Q3N>.

<sup>1</sup>*SUERC, University of Glasgow*

<sup>2</sup>*GES, University of Glasgow*

<sup>3</sup>*British Geological Survey*

<sup>4</sup>*Newcastle University*

<sup>5</sup>*University of Adelaide*

<sup>6</sup>*University of Nottingham*

<sup>7</sup>*National Museum of Nature and Science, Japan*

<sup>8</sup>*Ritsumeikan University*

The text presented here is identical to that of the preprint, except for the following:

- The numbering of figures,
- The reordering of sections to be consistent with other chapters,
- The acknowledgement of the contribution(s) of other authors and individuals where appropriate,
- The integration of the supplementary material into the main text for the benefit of the reader of this thesis, and
- Amendments made following the examination of this thesis at the request of the examiners.

The text presented here and the preprint are an updated version of the original journal submission and differ from the original submission in the following ways:

- Revisions were made to the original submitted version in response to the first round of reviewer comments (major revision and resubmission requested), and
- Some small grammatical changes were made to the original version to improve the writing and to be consistent with other chapters.

Authorship Declaration: C.L.R. designed the study, performed the core sampling, prepared and analysed the  $\delta^{18}\text{O}_{\text{diatom}}$  and  $\delta^2\text{H}_{\text{acid}}$  samples, corrected and interpreted the resulting datasets, and wrote the manuscript (first draft, editing and final draft). R.A.S. assisted with the core sampling and interpretation. R.A.S., M.J.L., J.L.T., E.P. and T.N. provided feedback, supervision and guidance. J.H.L. assisted with performing the  $\delta^{18}\text{O}_{\text{diatom}}$  analysis. M.A. Salik assisted with performing the  $\delta^2\text{H}_{\text{acid}}$  analysis. G.E.A.S. assisted with the mass balance corrections on the  $\delta^{18}\text{O}_{\text{diatom}}$  dataset. J.J.T. provided the total organic carbon dataset (Figure 3.5). M.S-K. provided the diatom species abundance (including %*Aulacoseira*) datasets (Figure 3.5, Figure 3.6). T.N. provided the pollen-derived temperature datasets (Figure 3.4, Figure 3.8) and access to core materials. A. Lacinska assisted with the scanning electron microscope (SEM) analysis and captured the images of the diatom samples (Figure 3.2). M. Wildman provided access to microscope facilities.

Funding: This research was financially supported by a National Environmental Isotope Facility (NEIF) grant (2308). C.L.R. was supported by the NERC IAPETUS2 Doctoral Training Partnership and the British Geological Survey (BGS) British University Funding Initiative (BUFI).

Accompanying data can be found at

<http://doi.org/10.5525/gla.researchdata.1439>.

### 3.1 Abstract

The past evolution of the East Asian Monsoon (EAM) was affected by remote climate processes. However, there is uncertainty surrounding these teleconnections and their impact on each seasonal EAM mode during periods of rapid global change. Here we use the unique biannual precipitation patterns of central Japan to reconstruct winter and summer EAM evolution during the last glacial termination (22,000 – 10,000 cal BP). Oxygen isotope analysis of diatoms and hydrogen isotope analysis of n-alkanoic acids from the Lake Suigetsu sediment cores show that in Japan the winter EAM weakened and the summer EAM strengthened with deglaciation. Only the summer mode exhibited variations coeval with stage-interstage fluctuations. A relationship between the summer EAM and Antarctic temperature post-16,000 cal BP supports a remote link to the Southern Hemisphere. These trends were different to continental EAM records and highlight the value of broadening the geographical range of reconstructions to rationalise system heterogeneities.

### 3.2 Introduction

The East Asian Monsoon (EAM) region is located at a point of convergence of multiple, globally interconnected climatic systems, with the palaeo-EAM system demonstrably affected by remote surface and atmospheric processes on centennial to millennial timescales. This is most eminently exemplified by the teleconnection between summer EAM strength and North Atlantic temperature during the late Pleistocene; first evidenced by the relationship between the Hulu Cave stalagmite and Greenland ice core oxygen isotope ( $\delta^{18}\text{O}$ ) records (Wang *et al.*, 2001; Zhang *et al.*, 2019) and subsequently corroborated by studies from across the region (Herzschuh, 2006; Liu *et al.*, 2022). This relationship is thought to have been driven by the influence of Atlantic Meridional Overturning Circulation (AMOC) on the position of the Intertropical Convergence Zone (ITCZ) (Zhang *et al.*, 2019). However, other reconstructions of EAM strength have noted an inverse relationship to Antarctic temperatures in this interval (Han *et al.*, 2016; Zhang *et al.*, 2016) and, as a result, the view of teleconnections acting on the EAM region has expanded to consider links to other climate systems, including Antarctica and the Pacific Ocean.

The behaviour of the EAM during the last glacial termination (TI; 22,000 to 10,000 cal BP) is an ideal focus for characterising the changing seasonality of this system and the persistence of these teleconnections. As a global transition, TI exemplifies a substantial, detectable change in many palaeoclimate archives with the climate at the geographic poles (representing two possible “end member” teleconnection origins) decoupled, with a Southern Hemisphere lead (Denton *et al.*, 2010; WAIS Divide Project Members, 2013). In the North Atlantic, TI was characterised by colder conditions during Greenland Stade 2.1 (GS-2.1; ~22,900 to 14,700 cal BP) and Greenland Stade 1 (GS-1; ~12,800 to 11,700 cal BP), alternating with warmer conditions during Greenland Interstade 1 (GI-1; ~14,700 to 12,800 cal BP) and the Holocene (~11,700 cal BP onwards) (Rasmussen *et al.*, 2014). GS-2.1, GI-1 and GS-1 were equivalent to the Last Glacial Maximum (LGM), Bølling–Allerød (BA) Interstade and Younger Dryas (YD) Stade of the wider North Atlantic region. In the far Southern Hemisphere, warming was more gradual and interrupted only by the Antarctic Cold Reversal (ACR; 14,500 to 12,900 cal BP), which bestrode GI-1 and GS-1 (EPICA Community Members, 2006; WAIS Divide Project Members, 2013).

Whilst current evidence supports a weakening East Asian Winter Monsoon (EAWM) and strengthening East Asian Summer Monsoon (EASM) during TI on an orbital scale (Wang *et al.*, 1999; Gallagher *et al.*, 2018), centennial- to millennial-scale fluctuations in EAM strength and the relative seasonal contributions to annual precipitation are poorly constrained (particularly in the case of the EAWM; Wen *et al.*, 2016) and appear spatially heterogeneous (Zhang *et al.*, 2019). It is unsurprising, therefore, that there is uncertainty surrounding deglacial EAM evolution on submillennial timescales (Yoshida and Takeuti, 2009; Hayashi *et al.*, 2010; Liu *et al.*, 2022), particularly in terms of conflicting evidence for teleconnections to other regions. A possible source of this uncertainty is the limited number of available high-resolution EAM reconstructions. Consideration of both EAWM and EASM strength in isolation is vital for deconvolving EAM behaviour during TI because they do not always show a perfectly inverse relationship (Wang *et al.*, 2012; Wen *et al.*, 2016; Yan *et al.*, 2020) and hence have the potential to exhibit unique behaviours (and teleconnection signals).

Due to its location, the EAM dominantly controls the climate of Japan; however, the relationship between the EAM and precipitation in Japan is unique. Japan is situated directly beneath the seasonally migrating monsoon front (Figure 3.1B), a critical geoclimatic boundary which moves northwards during summer and southwards during winter and separates the influence of the EAWM and EASM modes (Nakagawa *et al.*, 2006, Yoshida and Takeuti, 2009). The Japanese archipelago lies between two water bodies (the Pacific Ocean and the Sea of Japan), hence both EAM modes bring heavy precipitation to the country; mixed rainfall and snowfall concentrated along the Sea of Japan coast during the EAWM, and rainfall across the entire country during the EASM (Chowdary *et al.*, 2019; Amekawa *et al.*, 2021). This is in contrast to Continental Asia, where the EASM brings heavy rainfall from the Pacific Ocean, Philippine Sea and East China Sea, but the EAWM is predominantly dry because it originates inland (Yancheva *et al.*, 2007; Yan *et al.*, 2020). As such, the annual distribution of rainfall in Japan uniquely reflects a balance between both seasonal modes of the EAM. In light of these distinctive climatic characteristics, EAM records from Japan are well suited to deconvolve the complexities of EAM evolution during TI. In this study we present new stable isotope-based proxy records of both EAWM and EASM evolution in central Japan from the Lake Suigetsu sediment cores and compare these to a series of global benchmark records of EAM variability and temperature changes (Figure 3.1A), to better understand the factors affecting both seasonal modes of the EAM in Japan during this interval.

Lake Suigetsu is a tectonic lake located ~1 km from the Sea of Japan in Fukui Prefecture, Honshu Island (35° 35' N, 135° 53' E; Figure 3.1C; Nakagawa *et al.*, 2012). Suigetsu was a freshwater lake for the last glacial-interglacial cycle, except during global sea level highstands in the Eemian and the mid-Holocene, and post-AD 1664 when the lake was artificially connected to the Sea of Japan (Nakagawa *et al.*, 2021). Four previous deep coring campaigns carried out in 1993 (SG93 core), 2006 (SG06), 2012 (SG12) and 2014 (SG14) recovered a series of overlapping sediment core sections from the present day to >150,000 yr BP (Nakagawa *et al.*, 2012). The preserved sequence, covering >98 m of composite sediment depth, provides a palaeoenvironmental archive that captures two glacial and two full interglacial periods of continuous sedimentation. The Suigetsu cores contain annual laminations (varves) between ~70,000 yr BP and

10,000 cal BP, and between ~50,000 and 10,000 cal BP comprise the longest continuously varve-counted record from the Quaternary (Schlolut *et al.*, 2018). Thin-section microscopic analysis showed that the varves comprise a spring layer of *Aulacoseira* diatoms with some siderite, a detrital layer containing silt-sized quartz and feldspar, a summer layer of light amorphous organic material, an autumn layer of *Encyonema* diatoms within siderite, and a transitional autumn-to-winter clay layer (Schlolut *et al.*, 2012).

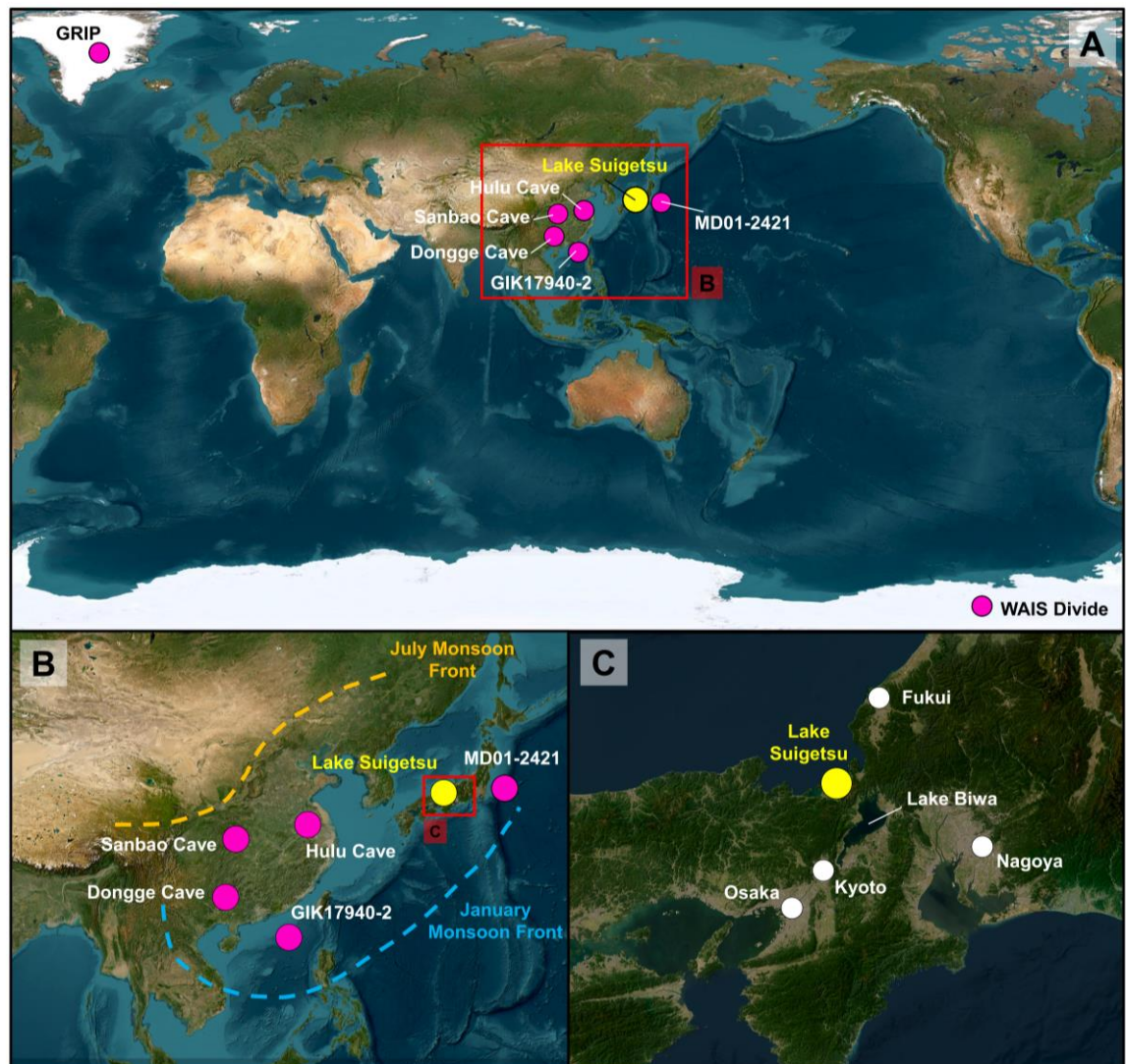


**Figure 3.1 Lake Suigetsu and other key sites.** A) the key global benchmark record sites discussed in the main text. B) the sites within the EAM region, alongside the average positions of the modern monsoon front in January and July (adapted from Nakagawa *et al.*, 2006). C) the location of Lake Suigetsu in Fukui Prefecture, central Honshu, relative to key cities and geographical features in Japan. Red boxes show the extent of subsequent panels in the sequence. Basemap is World Imagery (WGS84) from Esri (2023e) (scale 1:37,314,123 (A), 1:7,851,046 (B), 1:530,430 (C)).

Previous studies of the Suigetsu sediments from TI substantiate that this was a period of significant climatic change at the catchment. Pollen-derived temperature reconstructions of this interval show a structure which resembles that of North Atlantic temperature: abrupt warming at the start of a “Late Glacial Interstade”, a more gradual decrease in temperature into a “Late Glacial Stade”, and an abrupt warming at the start of the Holocene (Nakagawa *et al.*, 2021). However, whilst the onset of the Late Glacial Stade and the Holocene at Lake Suigetsu were synchronous with the Younger Dryas and Holocene periods in the North Atlantic, the Late Glacial Interstade at Lake Suigetsu commenced ~200 years prior to its North Atlantic counterpart (the Bølling–Allerød) (Nakagawa *et al.*, 2021). This behaviour was rationalised by a sudden repositioning of the westerly jet to the north of the Himalayas (a topographical barrier which causes bimodality in the positioning of the jet) during boreal summer, which allowed warm air from the Pacific Ocean to propagate northwards and caused the step-change in summer temperatures in Japan. Conversely, it was an AMOC switch-on ~200 years later (due to a higher threshold response to insolation forcing), which resulted in a shift to interstadial conditions in the North Atlantic. On a subcentennial scale, multiproxy analysis of the Suigetsu cores showed a bipartite structure to the Late Glacial Stade with a transition that was synchronous, albeit slower and more muted, to those observed at Lakes Meerfelder Maar (Germany) and Kråkenes (Norway) (Schlölaut *et al.*, 2017). A shift from *Aulacoseira ambigua* to *Aulacoseira subarctica* dominance during deglaciation was attributed to variations in the EAWM, affecting vegetation coverage and the water nutrient status (Kossler *et al.*, 2011). Carbon and nitrogen isotope ratios from chlorins also suggest an increase in aquatic primary productivity from glacial to interglacial conditions in the lake (Tyler *et al.*, 2010).

Here we present EAM precipitation reconstructions from Lake Suigetsu based on two proxy systems: the oxygen isotope composition of aquatic diatom silica frustules ( $\delta^{18}\text{O}_{\text{diatom}}$ ) and the compound-specific hydrogen isotope composition of n-alkanoic acids ( $\delta^2\text{H}_{\text{acid}}$ ) produced by aquatic algae ( $\text{C}_{16}$  and  $\text{C}_{18}$  homologues) and terrestrial plants ( $\text{C}_{28}$  and  $\text{C}_{30}$  homologues). Analysis was conducted using 100-year contiguous (continuous adjacent) samples. These proxies were selected based on target material abundances in the Lake Suigetsu cores and the ability

to reconstruct both autochthonous (aquatic;  $\delta^{18}\text{O}_{\text{diatom}}$ ,  $\delta^2\text{H}_{\text{C16acid}}$  and  $\delta^2\text{H}_{\text{C18acid}}$ ) and allochthonous (terrestrial;  $\delta^2\text{H}_{\text{C28acid}}$  and  $\delta^2\text{H}_{\text{C30acid}}$ ) changes during TI (Leng and Barker, 2006; Holtvoeth *et al.*, 2019). Both isotope proxy systems are versatile tools in palaeolimnological reconstructions of climate and follow the principle that the isotope composition of palaeo-catchment water was incorporated (via biosynthetic processes) into target materials by diatoms, algae, and plants, and preserved in the lake (Leng and Barker, 2006; Holtvoeth *et al.*, 2019).  $\delta^{18}\text{O}_{\text{diatom}}$  and  $\delta^2\text{H}_{\text{acid}}$  can be affected by fractionation processes during the life cycle of their respective source organisms but are dominantly controlled by the isotope composition of their water source (Leng and Marshall, 2004; Holtvoeth *et al.*, 2019). Hence, broader-scale palaeohydrological inferences can be made, relating to regional-scale shifts in atmospheric circulation and water vapour transport (Leng and Marshall, 2004; García-Alix *et al.*, 2021; Tierney *et al.*, 2022). At Lake Suigetsu, the modern isotope composition of water within the catchment is closely related to that of precipitation (with minimal effects of evaporation in summer), which is dominantly controlled by both the EAWM and EASM (Rex *et al.*, 2024; Chapter 2), supporting the utilisation of  $\delta^{18}\text{O}_{\text{diatom}}$  and  $\delta^2\text{H}_{\text{acid}}$  for reconstructing past EAM behaviour. Other potential influencing factors are water temperature in the aquatic domain, and air temperature and vegetation changes in the terrestrial domain (Leng and Barker, 2006; Castañeda and Schouten, 2011; Sachse *et al.*, 2012).

### 3.3 Materials and Methods

#### 3.3.1 Core Materials

Materials for this study were subsampled from the SG12 core, which was taken from the centre of Lake Suigetsu (35° 35' 08"N, 135° 52' 56"E) and spans a total composite depth of 41.8 m (from the present day to 56,100 cal BP). The core consists of a series of overlapping ~90 cm sections from four boreholes. SG12 is a direct stratigraphic copy of the SG06 core (Nakagawa *et al.*, 2012) due to the proximity of the SG12 and SG06 coring locations (the first borehole of each coring campaign was made within 15 m of each other, and both at a water depth of 34 m). As with the temporally equivalent sediments from the SG06 core, the SG12 sediment is varved throughout and represents continuous sedimentation

(Schlolut *et al.*, 2018). Chronological control for the SG12 cores is given by correlation to the SG06 cores via distinct visible marker layers. The SG06 chronology (Bronk Ramsey *et al.*, 2020; Staff *et al.*, in review) is based on >800 radiocarbon dates for the past ~50 ka BP (Staff *et al.*, 2011; Bronk Ramsey *et al.*, 2020), thin section microscopic varve counts (Schlolut *et al.*, 2018) and tephra tie points (McLean *et al.*, 2018); all ages are presented on the IntCal20 timescale (Reimer *et al.*, 2020).

Subsamples of the SG12 core for this study were taken from 1.2 cm-wide LL-channels (Nakagawa *et al.*, 2012) from the longitudinally cut core across the composite depth (ver. 27 December 2022) range of 1274.8 – 2119.4 cm (9980 ± 30 cal BP to 22,040 ± 38 cal BP). This time period was selected to encompass the maximum range of the existing Lake Suigetsu pollen-derived temperature reconstruction for TI. The LL-channels were cut to produce contiguous subsamples each containing 100 integrated years of sedimentation (based on the SG06 2012 timescale). Sample ages were subsequently converted to the IntCal20 timescale. A contiguous integrated sampling approach was taken to avoid subsampling time periods associated with peaks or troughs of multidecadal cycles, superimposed on the multicentennial and multimillennial scale transitions of interest (Nakagawa *et al.*, 2021). The sampling interval of ~100 years was selected to facilitate the detection of finer resolution variability within the key climatic transitions of the period. The (minimal) core expansion during storage was linearly modelled and accounted for by comparing the difference in event layer depth at the time of subsampling to high resolution photographs taken immediately after core extraction. Event layers (floods, turbidites and tephra) were removed during sampling to prevent skewing of the integrated signal by inclusion of a larger quantity of material from a single event. Particular care was taken to avoid contaminating the  $\delta^2\text{H}_{\text{acid}}$  samples with modern organic compounds. Surfaces and instruments were regularly cleaned with ethanol.

Each subsample was split into two, with each half designated for  $\delta^{18}\text{O}_{\text{diatom}}$  ( $n = 120$ ) and  $\delta^2\text{H}_{\text{acid}}$  ( $n = 120$ ) analysis, respectively. The exposed surfaces of one half (for  $\delta^2\text{H}_{\text{acid}}$  analysis) were scraped with a clean instrument prior to splitting to remove the outer sediments containing potential contamination from past handling. Wet weights ranged from 1.8 – 10.3 g (subsamples for  $\delta^{18}\text{O}_{\text{diatom}}$

analysis) and 1.1 – 7.1 g (subsamples for  $\delta^2\text{H}_{\text{acid}}$  analysis). The largest samples were from the younger end of the section, where the sedimentation rate (and thus depth range equating to ~100 years of integrated time) was high, and the smallest samples were from the older end of the section, where the sedimentation rate was relatively low. All subsamples were frozen and then freeze dried for 24 hours to obtain dry sediment masses before subsequent preparation steps.

### 3.3.2 $\delta^{18}\text{O}_{\text{diatom}}$ Analysis

Subsamples for diatom oxygen isotope analysis were prepared following standard procedures (Swann and Snelling, 2023). Specifically, subsamples were disaggregated overnight in 30 %  $\text{H}_2\text{O}_2$  prior to three successive heavy liquid density separations using sodium polytungstate (SPT) at specific gravities of 2.25  $\text{g cm}^{-3}$ , 2.20  $\text{g cm}^{-3}$  and 2.15  $\text{g cm}^{-3}$ , removing the denser material each time. The subsamples were subsequently treated with 30 %  $\text{H}_2\text{O}_2$  at 70 °C for one week to remove any remaining organic material, followed by 5 % HCl for 12 hours to remove carbonates. Subsamples were then filtered using an 80  $\mu\text{m}$  nylon mesh to remove large sponge spicules and large diatoms and freeze dried ready for analysis. As with other studies, further taxa-specific separation was not performed beyond this sieve stage due to the similar size of many diatom taxa present in the samples, rendering physical separation techniques impossible. Qualitative visual purity checks were made using light microscopy at x800 magnification. The % $\text{Al}_2\text{O}_3$  for each subsample was quantified using a Malvern Panalytical Epsilon 3 X-Ray Fluorescence (XRF) spectrometer. Due to elevated % $\text{Al}_2\text{O}_3$  values in the majority of samples, a Zeiss Sigma 300 VP-FEG Scanning Electron Microscope (SEM) was used to visually identify the source of this aluminium in five samples of varying % $\text{Al}_2\text{O}_3$  (Figure 3.2; image provided by A. Lacinska). Samples with % $\text{Al}_2\text{O}_3$  exceeding 4.2 % ( $\text{Al}/\text{Si} = 0.05$ ) showed particulate Al-bearing contamination (most likely a detrital Al-rich silicate, but undetermined due to grain size) which was external to the diatom frustules. These samples ( $n = 3$ ) were subjected to an additional SPT density separation at 2.15  $\text{g cm}^{-3}$  to remove this contamination. Samples with % $\text{Al}_2\text{O}_3$  below 4.2 % showed only small amounts (on a sub-micron scale) of this Al-bearing contamination adhered to or trapped within the diatom frustules (Figure 3.2). Additional density separations would not remove this contamination due to

electrostatic charges adhering the contamination to the frustule, and air pockets within the cylindrical frustules preventing chemical treatment of internal contamination (Brewer *et al.*, 2008), so a mass balancing approach was taken to correct for the effect of this contamination on the  $\delta^{18}\text{O}_{\text{diatom}}$  values (discussed below).

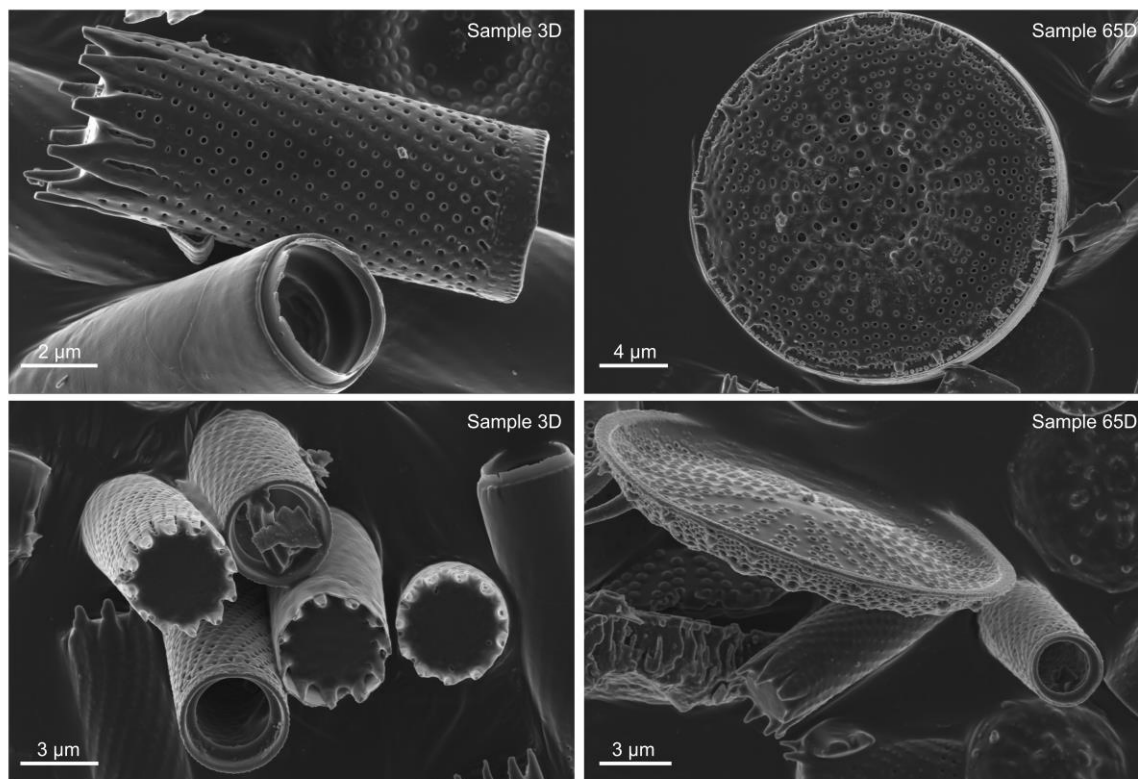


**Figure 3.2 Diatom SEM Imagery.** SEM images for subsample 3D (left) and sample 65D (right) showing Al-bearing contamination adhered to frustules and inside cylindrical *Aulacoseira spp.*, which are representative of the 120 analysed subsamples for  $\delta^{18}\text{O}_{\text{diatom}}$  analysis. Scale bars are indicated on each image. Image provided by A. Lacinska.

The purified diatom material (6 – 7 mg subsamples) was subjected to stepwise fluorination in nickel reaction vessels to liberate structural oxygen following Leng and Sloane (2008) at the British Geological Survey (UK). Briefly, this method involved outgassing samples at 250 °C to remove any water in the sample, “pre-fluorination” at 250 °C using a stoichiometric deficiency of  $\text{BrF}_5$  to remove the exchangeable hydrous silica layer from the diatom frustules and minimise exchange effects, and then fluorination with  $\text{BrF}_5$  overnight at 500 °C. The resulting oxygen gas was cryogenically purified and then converted to  $\text{CO}_2$  by exposure to hot platinized graphite (Clayton and Mayeda, 1963). The average gas yield of this process was between 68 and 75 %. In each batch of diatom samples, an in-house laboratory diatomite standard, BFC, with a known value of

$\delta^{18}\text{O}$  (Chapligin *et al.*, 2011) was also reacted and converted to  $\text{CO}_2$  in the same manner following the principle of identical treatment. The oxygen isotope ratio of the diatom subsamples ( $\delta^{18}\text{O}_{\text{diatom}}$ ) and BFC ( $\delta^{18}\text{O}_{\text{BFC}}$ ) were measured relative to a reference  $\text{CO}_2$  gas on a Thermo Finnigan MAT 253 dual inlet isotope ratio mass spectrometer. Oxygen isotope ratios were calibrated using a single-point anchoring procedure by analysing  $\text{CO}_2$  prepared from an in-house standard (MCS;  $\delta^{13}\text{C}_{\text{VPDB}} = -0.7\text{‰}$  and  $\delta^{18}\text{O}_{\text{VPDB}} = -9.2\text{‰}$ ) via reaction with  $\text{H}_3\text{PO}_4$  (specific gravity = 1.92) at  $25^\circ\text{C}$ . All  $\delta^{18}\text{O}_{\text{VPDB}}$  values were converted to the VSMOW scale using Coplen *et al.* (1983) and normalised such that the  $\delta^{18}\text{O}_{\text{VSMOW}}$  of the within-run BFC =  $+28.9\text{‰}$ . The oxygen isotope composition of BFC has been calibrated via inter-laboratory comparison (Chapligin *et al.*, 2011) using the certified international standard NBS 28 ( $\delta^{18}\text{O}_{\text{VSMOW}} = +9.57\text{‰}$ ; Hut, 1987; Gröning *et al.*, 2007). All oxygen isotope data are expressed in standard delta ( $\delta$ ) notation in per mille (‰) deviations relative to VSMOW. External analytical error ( $1\sigma$ ) was  $\pm 0.13\text{‰}$  for BFC and  $\pm 0.33\text{‰}$  for replicate analysis of the diatom samples.

The  $\delta^{18}\text{O}_{\text{diatom}}$  values were corrected for the aforementioned Al-bearing silicate contamination using a geochemical mass balance approach (Mackay *et al.*, 2011; Swann *et al.*, 2018). End member contamination samples for Lake Suigetsu contained 19.45 %  $\text{Al}_2\text{O}_3$  (from XRF,  $n = 2$ ), a  $\delta^{18}\text{O}$  composition of  $10.36 \pm 0.68\text{‰}$  ( $1\sigma$  range,  $n = 8$ ) and 48.93 wt% oxygen (from XRF,  $n = 2$ ). These were prepared from raw materials ( $n = 2$ ) and the residues of SPT separations from the  $\delta^{18}\text{O}_{\text{diatom}}$  subsamples ( $n = 6$ ), disaggregated overnight in 30 %  $\text{H}_2\text{O}_2$  and treated with 30 %  $\text{H}_2\text{O}_2$  at  $70^\circ\text{C}$  for one week to remove any remaining organic material, followed by 5 %  $\text{HCl}$  for 12 hours to remove carbonates and 8 %  $\text{NaOH}$  at  $70^\circ\text{C}$  for 48 hours to remove biogenic silica. Contamination-corrected  $\delta^{18}\text{O}_{\text{diatom}}$  values were modelled using the % $\text{Al}_2\text{O}_3$  for each sample, the end member quantities above, and assuming a % $\text{Al}_2\text{O}_3$  of pure diatom material of 1.4 % ( $\text{Al}/\text{Si} = 0.016$ ), the minimum value measured across the 120 samples. The uncertainty associated with mass-balancing was calculated assuming a normal distribution for data uncertainty and Monte Carlo simulations (10,000 replicates). Errors presented in Section 3.4 show the  $1\sigma$  range of these simulations (mean =  $\pm 0.36\text{‰}$ ). Of the 120 samples prepared, 113 datapoints are included in the final dataset. Five samples were excluded due to elevated % $\text{Al}_2\text{O}_3$  values ( $>4.2\%$ ;  $\text{Al}/\text{Si} = 0.05$ ); these produced anomalously high values during mass balancing, possibly due to

atypically large quantities of diatom-bound Al which was unaccounted for by our methods. A further two samples were too small in mass for accurate  $\delta^{18}\text{O}_{\text{diatom}}$  determination via the methods presented above.

### 3.3.3 $\delta^2\text{H}_{\text{acid}}$ Analysis

Subsamples for  $\delta^2\text{H}_{\text{acid}}$  analysis were prepared following the Biomarkers for Environmental and Climate Science (BECS) group standard protocol at the University of Glasgow (UK). The total lipid extract (TLE) was extracted by a Dionex ASE 350 Accelerated Solvent Extractor using dichloromethane and methanol (9:1, v:v) and the TLE dried and weighed. The TLE was then separated into neutral and acid fractions using solid phase extraction through a LC-NH<sub>2</sub> silica gel column. The neutral fraction was eluted using dichloromethane:propan-2-ol solution (1:1, v:v) and the acid fraction using 4 % acetic acid in diethyl ether. The acid fraction was derivatised using 100  $\mu\text{L}$  of 12 % boron trifluoride in methanol in sealed glass vials at 70 °C for 60 minutes. This converted n-alkanoic acids into fatty acid methyl esters (FAMES) in preparation for analysis. These FAMES were then cleaned through a silica gel column (35 – 75  $\mu\text{m}$  particle size). Non-FAME material was eluted using hexane and the FAMES eluted using dichloromethane. Subsamples were prepared in batches of 10 or 11, each with a procedural blank to check for contamination introduced by the stages described above.

Identification of the C<sub>16</sub>, C<sub>18</sub>, C<sub>28</sub> and C<sub>30</sub> n-alkanoic acids (as FAMES) was performed on subsample 96B using an Agilent 7890B Gas Chromatograph connected to a 5977A mass spectrometer detector (MSD) with an electron impact (EI) ionisation source (GC-MS). A HP1-MS capillary column was used (60 m length, 0.25 mm internal diameter, 0.25  $\mu\text{m}$  film thickness) with helium carrier gas at a constant flow rate (1.2 mL min<sup>-1</sup>). The FAMES were dissolved in DCM (200  $\mu\text{L}$ ) and a volume of 1  $\mu\text{L}$  used in a splitless injection. The inlet was kept at 315 °C and the following oven programme used: the oven was held for two minutes at 60 °C and raised to 120 °C at 30 °C min<sup>-1</sup>, then increased to 310 °C at 5 °C min<sup>-1</sup> and held for 33 minutes. The auxiliary temperature in the transfer line between the GC and MSD was kept constant at 315 °C. The MS source was set to 230 and the MS quad set to 160. The detector analysed all compounds between 12- and 65-minute retention time, except for the period between 34

and 39 minutes where flow was redirected to avoid a large phthalate compound peak from entering the detector. Data acquisition was performed in full scan mode at 2.4 scans  $s^{-1}$ . Identification of contaminant peaks was also performed using this method. All large contaminant peaks (retention times: ~24.5, ~33 and ~37 minutes) were shown to be phthalate compounds. The largest of these (at ~33 minutes) was present in > 90 % of subsamples, however the others were only present in ~ 10 %. No contaminant peaks obscured the FAME peaks of interest.

The concentration of the  $C_{16}$ ,  $C_{18}$ ,  $C_{28}$  and  $C_{30}$  n-alkanoic acids (as FAMEs) in each subsample were measured using an Agilent 7890B Gas Chromatograph fitted with a flame ionisation detector (GC-FID). A Restek Rtx-1 capillary column was used (60 m length, 0.25 mm internal diameter, 0.25  $\mu m$  film thickness) with helium carrier gas at a constant flow rate (1.2 mL  $min^{-1}$ ). FAMEs were dissolved in DCM (200  $\mu L$  – 1250  $\mu L$ ; depending on FAME yield) and a volume of 1  $\mu L$  used in a splitless injection. The inlet was kept at 320  $^{\circ}C$  and the following oven programme used: the oven was held for two minutes at 60  $^{\circ}C$  and raised to 120  $^{\circ}C$  at 30  $^{\circ}C min^{-1}$ , then increased to 330  $^{\circ}C$  at 5  $^{\circ}C min^{-1}$  and held for 15 minutes. The FID temperature was set to 250  $^{\circ}C$ . A chromatogram showing a representative sample with no phthalate peaks is shown in Figure 3.3. Peak areas were measured, and concentrations calculated from a set of external calibrations using a standard mix of eleven n-alkanes; ten straight-chained ( $C_{16}$ ,  $C_{18}$ ,  $C_{19}$ ,  $C_{23}$ ,  $C_{25}$ ,  $C_{26}$ ,  $C_{28}$ ,  $C_{30}$ ,  $C_{32}$  and  $C_{37}$  n-alkanes) and one branched (squalane). Calibration graphs were made using concentrations of 2.5  $\mu g/mL$ , 5  $\mu g/mL$ , and 10  $\mu g/mL$ . A calibration for the 0 – 25 minute, 25 – 35 minute and 35 – 60 minute retention time intervals were made using the  $C_{16}$ ,  $C_{29}$  and  $C_{39}$  homologues in the standard, respectively. An R-squared value of >0.99 was achieved for each calibration. The n-alkanoic acid (as FAME) concentrations were then normalised to dry sediment weight.

The compound specific hydrogen isotopic composition ( $\delta^2H$ ) of the  $C_{16}$ ,  $C_{18}$ ,  $C_{28}$  and  $C_{30}$  n-alkanoic acids (as FAMEs) were measured using an Agilent 7890B gas chromatography (GC) system connected to an Elementar GC5 furnace and IRMS. The settings of the GC system were identical to those of the GC-FID outlined above with the difference being that the FAMEs were dissolved in between 30 and 120  $\mu L$  of hexane and the injection volume set to either 1 or 2  $\mu L$  depending on FAME yield. This ensured that FAMEs were measured as a similar response to

the reference H<sub>2</sub> gas. Due to the presence of the largest phthalate compound (retention time ~33 mins) in >90 % of the subsamples, flow was redirected between 1700 s and 1975 s to prevent entry into the IRMS. In 13 subsamples, this was extended to the interval 1400 s to 2100 s to remove the second largest phthalate peak (retention time ~37 minutes). The smallest phthalate peak (retention time ~24.5 minutes) was not larger than the FAME peaks and hence did not require redirection of flow. The furnace temperature was set to 1450 °C with an interface temperature of 350 °C. Subsamples were measured in duplicate and  $\delta^2\text{H}$  values of each homologue were calculated relative to a calibrated reference H<sub>2</sub> gas. These values were then converted to the VSMOW scale by linear regression to an in-house standard (containing C<sub>16</sub>, C<sub>19</sub>, C<sub>23</sub>, C<sub>25</sub>, C<sub>28</sub> and C<sub>32</sub> straight chained n-alkanes in addition to squalane) calibrated to the standard Indiana n-alkane mixture B5 containing C<sub>16</sub> to C<sub>30</sub> n-alkanes. The in-house standard was measured four times prior to each batch, after every eight sample measurements, and in duplicate at the end of each batch. All hydrogen isotope data are expressed in standard delta ( $\delta$ ) notation in per mille (‰) deviations relative to VSMOW. Instrument precision was  $\pm 2.53$  ‰ based on the standard deviation of all standard measurements. The H<sub>3</sub><sup>+</sup> correction factor ranged from 4.24 to 4.57.

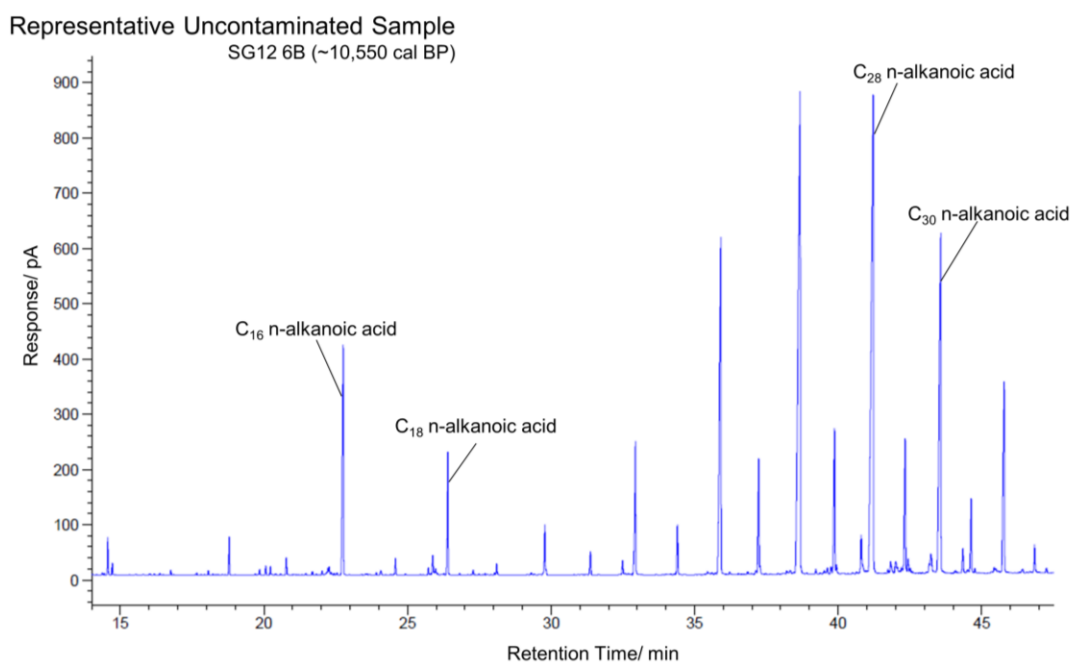


**Figure 3.3 Chromatogram of the n-alkanoic acid fraction of Sample 6B.** GC-FID Chromatogram of a representative uncontaminated sample showing clear, symmetrical peaks of interest with a flat chromatogram baseline, strong even-over-odd preference, and dominant terrestrial chain lengths. All n-alkanoic acids were measured as FAMES.

Reliable  $\delta^2\text{H}$  values for all chain lengths across all subsamples was not achieved due to some subsamples exhibiting raised baselines resulting in poorly defined peak areas and inaccurate determination of  $\delta^2\text{H}$  for at least one homologue (affecting 26 subsamples). Raised baselines in some samples predominantly precluded accurate measurement of the aquatic chain lengths, though it was possible to accurately measure the  $\text{C}_{28}$  and  $\text{C}_{30}$  homologues in many of the impacted subsamples. Low concentrations affected the repeatability of the measurements of  $\delta^2\text{H}_{\text{acid}}$  of at least one homologue in a further 9 subsamples (most commonly  $\text{C}_{16}$  or  $\text{C}_{18}$ ), hence these values were excluded from the final dataset. The mean precision of the  $\delta^2\text{H}_{\text{acid}}$  measurements was  $\pm 2.0 \text{‰}$  ( $1\sigma$  range). The resulting dataset has 95 datapoints for the  $\text{C}_{16}$ , 86 for the  $\text{C}_{18}$ , 112 for the  $\text{C}_{28}$  and 108 for the  $\text{C}_{30}$  n-alkanoic acids. Terrestrial and aquatic composites were not generated due to insufficiently strong statistical relationships between the  $\delta^2\text{H}_{\text{C}_{28}\text{acid}}$  and  $\delta^2\text{H}_{\text{C}_{30}\text{acid}}$  values, and the  $\delta^2\text{H}_{\text{C}_{16}\text{acid}}$  and  $\delta^2\text{H}_{\text{C}_{18}\text{acid}}$  values, although there was some visual correlation between the two pairs. Values were corrected for the methylation process (which removes the exchangeable carboxylic acid hydrogen from each molecule and replaces it with a methyl group with three hydrogens) (Chivall *et al.*, 2012). GC-IRMS measurements of (Z)-hexadec-9-enoic acid ( $\delta^2\text{H} = -154.02 \text{‰}$ ) and methyl (Z)-hexadec-9-enoate ( $\delta^2\text{H} = -143.13 \text{‰}$ ) were made to calculate the  $\delta^2\text{H}$  value of a single methanol-derived methyl hydrogen ( $\delta^2\text{H} = -37.86 \text{‰}$ ), and a mass balance scheme (Chivall *et al.*, 2012) applied to correct the measured FAME  $\delta^2\text{H}$  values to n-alkanoic acid values (excluding the exchangeable hydrogen on the carboxylic acid group).

## 3.4 Results

### 3.4.1 Observations at Lake Suigetsu

The  $\delta^{18}\text{O}_{\text{diatom}}$  values increased smoothly during TI with no abrupt shifts and the Holocene values were  $\sim 2.5 \text{‰}$  higher than in the LGM (Figure 3.4A). Key features of this profile were high frequency centennial-scale fluctuations and higher values between 22,000 and 21,000 cal BP. The  $\delta^2\text{H}_{\text{C}_{16}\text{acid}}$  values followed a smooth trend to lower values through the record, except from 22,000 – 21,000 cal BP (when low values were observed), 19,000 – 17,000 cal BP (when values fluctuated drastically on a centennial scale), and sections of the Late Glacial

Interstade and Late Glacial Stage (when this proxy exhibited periods of lower-than-average values; Figure 3.4B). The difference between the  $\delta^2\text{H}_{\text{C}_{16}\text{acid}}$  values at 21,000 cal BP and 10,000 cal BP was  $\sim 50\%$ . The  $\delta^2\text{H}_{\text{C}_{18}\text{acid}}$  profile resembled that of  $\delta^2\text{H}_{\text{C}_{16}\text{acid}}$ , however long-term trends were harder to identify due to limited data coverage (see Section 3.3.3) and rapid high-amplitude fluctuations (Figure 3.4C). Many of these coincided with equivalent, lower amplitude, variations in the  $\delta^2\text{H}_{\text{C}_{16}\text{acid}}$  values, suggesting that these were closely related. The  $\delta^2\text{H}_{\text{C}_{28}\text{acid}}$  and  $\delta^2\text{H}_{\text{C}_{30}\text{acid}}$  profiles also showed very similar behaviour to one another; decreasing through the LGM and into the Late Glacial Interstade before initially increasing smoothly for  $\sim 2000$  years, and then decreasing from the early Holocene onwards (Figure 3.4D, Figure 3.4E). Like the other  $\delta^2\text{H}_{\text{acid}}$  proxies, the  $\delta^2\text{H}_{\text{C}_{28}\text{acid}}$  and  $\delta^2\text{H}_{\text{C}_{30}\text{acid}}$  records showed a period of lower values between 22,000 and 21,000 cal BP before a marked shift at 21,000 cal BP to higher values. The difference between the  $\delta^2\text{H}_{\text{C}_{30}\text{acid}}$  values at 21,000 cal BP and 10,000 cal BP was  $\sim 35\%$ . The  $\delta^2\text{H}_{\text{C}_{28}\text{acid}}$  and  $\delta^2\text{H}_{\text{C}_{30}\text{acid}}$  profiles were only decoupled between 19,000 and 17,000 cal BP; within this section both proxies showed rapid high amplitude changes which were offset by as little as one sample (100 years).

It appears that the shortest ( $\text{C}_{16}$ ) and longest ( $\text{C}_{30}$ ) chain lengths exhibited  $\delta^2\text{H}_{\text{acid}}$  profiles with the most unique trends and the most complete data coverage, and hence we focus on these in subsequent discussions, whereas the  $\delta^2\text{H}_{\text{C}_{18}\text{acid}}$  values were limited in quantity and the  $\delta^2\text{H}_{\text{C}_{28}\text{acid}}$  values showed some features similar to the  $\delta^2\text{H}_{\text{C}_{18}\text{acid}}$  profile, possibly due to  $\text{C}_{28}$  n-alkanoic acids originating from a combination of aquatic and terrestrial sources. Whilst  $\text{C}_{30}$  n-alkanoic acids originate from strictly terrestrial sources,  $\text{C}_{28}$  n-alkanoic acids have been known to originate from aquatic and terrestrial sources (van Bree *et al.*, 2018; Tierney *et al.*, 2022). None of the trends exhibited by the isotope proxies resembled those of the pollen-derived temperature reconstructions at Lake Suigetsu (mean temperature of the warmest month, MTWA or mean temperature of the coldest month, MTCO; Figure 3.4F, Figure 3.4G; analysed by T. Nakagawa; Nakagawa *et al.*, 2021).

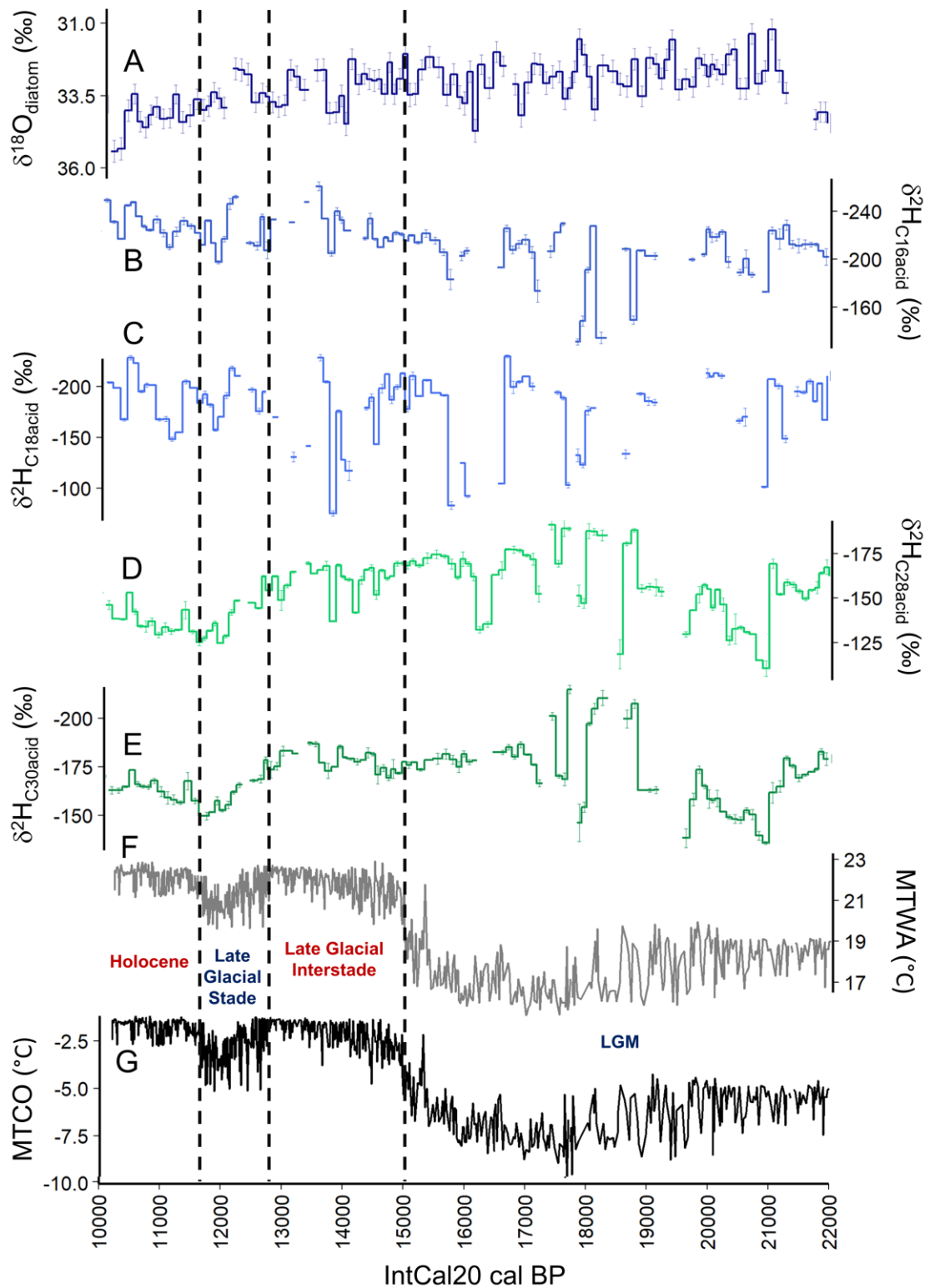


**Figure 3.4 Proxy changes at Lake Suigetsu during Termination I.** A)  $\delta^{18}\text{O}_{\text{diatom}}$  (this study), B)  $\delta^2\text{H}_{\text{acid}}$  of  $\text{C}_{16}$  n-alkanoic acids (this study), C)  $\delta^2\text{H}_{\text{acid}}$  of  $\text{C}_{18}$  n-alkanoic acids (this study), D)  $\delta^2\text{H}_{\text{acid}}$  of  $\text{C}_{28}$  n-alkanoic acids (this study), E)  $\delta^2\text{H}_{\text{acid}}$  of  $\text{C}_{30}$  n-alkanoic acids (this study), F) MTWA; mean temperature of the warmest month (pollen-derived; provided by T. Nakagawa; Nakagawa *et al.*, 2021), G) MTCO; mean temperature of the coldest month (pollen-derived; provided by T. Nakagawa; Nakagawa *et al.*, 2021). Panels A to E are displayed inverted, and show data derived from 100-year integrated contiguous samples. All panels are on the IntCal20 timescale. Vertical dashed lines indicate the phases of temperature change at Suigetsu as designated by the pollen-derived temperature reconstructions (Nakagawa *et al.*, 2021).

The total lipid extract (TLE) exhibited low values in the early part of the section (~2 mg/g) before increasing gradually from ~15,500 cal BP (Figure 3.5). Values were then high (~6 mg/g) and fluctuating. This follows the pattern of sediment total organic carbon (TOC) during this period (analysed by J.J. Tyler; Tyler *et al.*, 2010). Aquatic n-alkanoic acid concentrations did not show this long-term increasing trend, and the concentration profiles for the C<sub>16</sub> and C<sub>18</sub> n-alkanoic acids showed centennial-scale fluctuations throughout (Figure 3.5). Conversely, the terrestrial n-alkanoic acid concentrations were higher in the latter part of the section; the concentration of the C<sub>28</sub> n-alkanoic acid showed a greater increase than the C<sub>30</sub>, but also exhibited larger fluctuations (Figure 3.5). Throughout, the terrestrial n-alkanoic acid concentrations were generally higher than those of the aquatic n-alkanoic acids, aside from in a small number of samples. The close relationship between the terrestrial n-alkanoic acid concentrations and the TLE concentrations suggests that the terrestrial component was driving the observed TLE increase (allowing for the un-resolved non-acid fractions which also contribute but were not measured). The gradual increase in TLE, TOC and terrestrial n-alkanoic acid concentration was similar in character to the changes in EAWM and EASM strength and very different from the temperature reconstruction for the site, suggesting that they were driven by precipitation changes rather than temperature changes. None of these variables show ACR-type inversions, however the seasonality of these variables suggests a relationship to the EASM is more likely than a link to the EAWM, despite the EAWM showing more gradual changes during this interval. Diatom frustule concentration also increased through the section (analysed by M. Saito-Kato; Figure 3.5), but the shift to higher values initiated ~500 cal BP later (~15,000 cal BP) and more abruptly than the TLE concentration. Hence, whilst an overall resemblance between frustule concentration and TOC can be argued, there was some decoupling of these variables between ~16,000 and ~15,000 cal BP. The sudden increase in diatom frustule concentration at ~15,000 cal BP was likely driven by temperature changes, in light of the abruptness of this shift and the coincident timing with the onset of the Late Glacial Interstade. *Aulacoseira* dominated the diatom assemblage counts, most notably at 21,500 cal BP, 20,000 cal BP and between 15,000 and 12,000 cal BP (analysed by M. Saito-Kato; Figure 3.5). Spikes of naviculoid and benthic taxa were observed at 21,000 cal BP. Between 20,000 and 15,000 cal BP there were greater proportions of

*Stephanodiscus*, naviculoid and benthic taxa relative to *Aulacoseira*, and similarly a period of increased *Asterionella* between 12,000 and 10,000 cal BP.

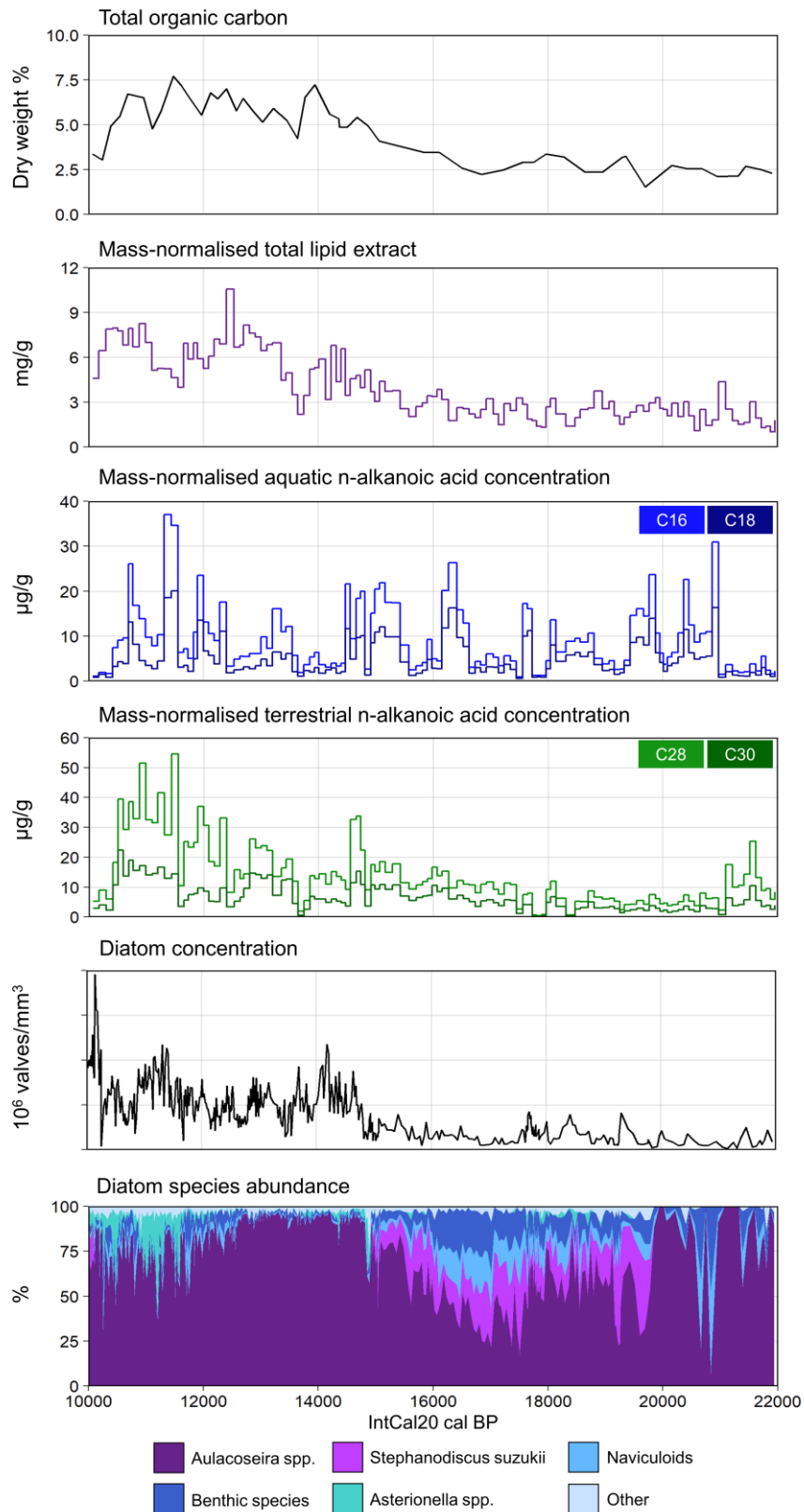


**Figure 3.5 Proxy weights, abundances and concentrations.** Variations in total organic carbon (TOC; provided by J.J. Tyler; Tyler *et al.*, 2010), mass-normalised total lipid extract (TLE), mass normalised n-alkanoic acid concentrations (aquatic (C<sub>16</sub> and C<sub>18</sub>) and terrestrial (C<sub>28</sub> and C<sub>30</sub>)),

diatom frustule concentration (provided by M. Saito-Kato; Saito-Kato *et al.*, in prep) and diatom taxon abundance (provided by M. Saito-Kato; Saito-Kato *et al.*, in prep) during TI in the Lake Suigetsu sediment cores.

### 3.4.2 Proxy Drivers

Determination of the dominant isotope proxy drivers is critical for interpreting the results in the context of EAM behaviour. Whilst multiple factors can affect the proxy values presented here, valuable insights can be made by identifying the dominant driver (which can cause the largest amplitude changes) in each case. There was no identifiable relationship between our isotope proxy values and the pollen-derived temperature or the primary pollen species concentrations, which eliminates air temperature (and thus water temperature) and vegetative change as the main drivers, respectively. There is a temperature dependent fractionation of  $\delta^{18}\text{O}_{\text{diatom}}$  relative to precipitation and a mineral-water fractionation, which have opposing effects, but the impact is likely to be small. Given the amount of variation, we suggest that changes in water source composition were most likely the dominant control on the  $\delta^{18}\text{O}_{\text{diatom}}$  and  $\delta^2\text{H}_{\text{acid}}$  values. The isotope composition of modern catchment waters is principally governed by the composition of EAM-borne precipitation, as shown by extended monitoring (Rex *et al.*, 2024; Chapter 2). EAM precipitation composition is determined by a combination of source composition and transport processes; in general, a “stronger” EAM, associated with strong winds and large quantities of precipitation integrated across the transport pathway, would act to lower  $\delta_{\text{precipitation}}$ , and the reverse qualities (for a “weaker” EAM) would provide higher  $\delta_{\text{precipitation}}$  values (Yuan *et al.*, 2004; Zhang *et al.*, 2018). EAM strength is ultimately driven by an enhanced land-sea pressure gradient, moisture availability and conditions favourable for evaporation at source (Mohtadi *et al.*, 2016). It follows that these were the critical drivers of the isotope proxy systems during TI. On shorter timescales, other influences (e.g., local summer evaporation) could have also affected the isotope proxies, although there is a limited influence of evaporation on catchment isotopes in the modern day (Rex *et al.*, 2024; Chapter 2), so we expect these to have caused small-amplitude effects, if any. The marked seasonality of EAM precipitation at Lake Suigetsu, combined with the short residence time of the lake (on the order of a few months; Rex *et al.*, 2024; Chapter 2) means that isotope proxy seasonality is crucial for attribution to one or both seasonal EAM modes. A key element of this

designation is related to the modern catchment transit lag of approximately three months (Rex *et al.*, 2024; Chapter 2), which signifies that surface lake water isotope composition ( $\delta_{\text{lake}}$ ) reflects that of the precipitation ( $\delta_{\text{precipitation}}$ ) delivered in the preceding season, i.e., spring  $\delta_{\text{lake}}$  is equivalent to that of winter  $\delta_{\text{precipitation}}$  and so on. Consistently, deep water  $\delta_{\text{lake}}$  is homogeneous and reflects annually integrated  $\delta_{\text{precipitation}}$ .

In a palaeo context, different diatom taxa were associated with each of the predominant seasonal blooms in the lake (spring and autumn) and consequently, the  $\delta^{18}\text{O}_{\text{diatom}}$  values reflect a combination of seasonal signals. Of the most abundant diatom taxa, mixed planktonic *Aulacoseira subarctica* and *Aulacoseira ambigua* diatoms bloomed in the spring and captured surficial spring  $\delta^{18}\text{O}_{\text{lake}}$  (winter  $\delta^{18}\text{O}_{\text{precipitation}}$ ), and benthic *Encyonema* diatoms bloomed during the autumn and captured surficial autumn  $\delta^{18}\text{O}_{\text{lake}}$  (summer  $\delta^{18}\text{O}_{\text{precipitation}}$ ) from shallow edges of the lake (bloom season attributions were derived from the varve structure; Schlolaut *et al.*, 2012). The signals captured by other taxa would have been dependent on their habitation depths and bloom seasons, however due to their low abundance relative to *Aulacoseira* and *Encyonema* diatoms, their seasonality was not ascribed as part of the varve structure. “Bulk”  $\delta^{18}\text{O}_{\text{diatom}}$  therefore reflects mixed seasonality, with the relative weighting of each seasonal signal dependent on the mass contribution of each taxon (Leng and Barker, 2006). In the absence of quantified taxon-specific masses within each sample, the abundance (based on frustule counts) of each taxon can be used to provide an indication of the relative seasonal weighting of the  $\delta^{18}\text{O}_{\text{diatom}}$  values; differences in taxon size can introduce uncertainty to this process, but we believe this to be a reasonable assessment because whilst other taxa are larger in size, the smallest genus of diatom, *Aulacoseira*, has thick valves and hence contributes significantly to the total diatom mass. Due to its relationship with winter  $\delta^{18}\text{O}_{\text{precipitation}}$ , *Aulacoseira*  $\delta^{18}\text{O}_{\text{diatom}}$  offers the most robust links to EAWM behaviour. In theory, this connection may have been affected by alterations to the transit lag, however we believe that the relationship was maintained throughout TI, despite climatic variability, because the spring diatom bloom in Lake Suigetsu is closely related to the delivery of the bulk of winter precipitation to the lake (i.e., both are caused by snow and ice melting). Additionally, winter is the wettest season of the year, minimising the

effect of the preceding autumnal precipitation on the composition of surface  $\delta_{\text{lake}}$  (an effect amplified by the short residence time of the lake). In light of this, it is reasonable to utilise the  $\delta^{18}\text{O}_{\text{diatom}}$  values as an indicator of EAWM behaviour (i.e., strongly weighted towards winter  $\delta^{18}\text{O}_{\text{precipitation}}$ ), when *Aulacoseira* was the most abundant genus. This was the case for earlier parts of the interval (22,000 – 19,800 cal BP) and from 15,000 cal BP onwards, when %*Aulacoseira* (*Aulacoseira* frustules as a percentage of total diatom frustules) was consistently greater than 60 % (and often greater than 70 %) on a centennial basis (Figure 3.6). This was likely to have been even greater in our  $\delta^{18}\text{O}_{\text{diatom}}$  samples, which contained only diatoms which were smaller than 80  $\mu\text{m}$ , favouring the (smaller) *Aulacoseira* over other taxa. However, the presence of other taxa may have contributed to the low amplitude centennial-scale variability in the  $\delta^{18}\text{O}_{\text{diatom}}$  record throughout, and had greater influence between 19,800 and 15,000 cal BP. Maturation effects (i.e., post-mortem isotope exchange) remain an unconstrained influence on  $\delta^{18}\text{O}_{\text{diatom}}$  (e.g., van Hardenbroek *et al.*, 2018), however (as with other studies) we do not expect this to be a dominant driver because the hydrous (most readily exchangeable) layer of each diatom was removed prior to measurement (see Section 3.3.2) and only the more resistant structurally bound oxygen fixed during early sedimentation was analysed.

The  $\delta^2\text{H}_{\text{acid}}$  values are associated with less complex seasonality than the  $\delta^{18}\text{O}_{\text{diatom}}$  values, because the growth of terrestrial plants occurs predominantly during spring and summer (Sachse *et al.*, 2012) and lake-based organic matter production in Lake Suigetsu occurs almost exclusively in summer when the lake becomes stratified and aquatic productivity is high (Schlolaut *et al.*, 2012). Indeed, because the terrestrial  $\delta^2\text{H}_{\text{acid}}$  values would have been unaffected by the catchment transit lag (the source water of terrestrial plants being soil pore water not lake water), we expect the  $\delta^2\text{H}_{\text{C30acid}}$  values to have been heavily weighted towards summer (EASM)  $\delta^2\text{H}_{\text{precipitation}}$ . However, not only would the aquatic  $\delta^2\text{H}_{\text{acid}}$  values have been affected by the transit lag (and hence captured the isotope composition of spring  $\delta^2\text{H}_{\text{precipitation}} = \text{summer } \delta^2\text{H}_{\text{lake}}$ ), but during periods of cold winters (which TI typifies), we might expect extension of the transit lag time in the first half of the year due to greater longevity of snow on the surrounding hillsides and hence slower delivery of precipitation to the lake

system (Rex *et al.*, 2024; Chapter 2). As a result, both winter and summer precipitation would enter the lake in quicker succession. Under these circumstances, summer  $\delta^2\text{H}_{\text{lake}}$  would have become a greater seasonal mix of EAWM  $\delta^2\text{H}_{\text{precipitation}}$  (entering the lake in late spring) and EASM  $\delta^2\text{H}_{\text{precipitation}}$  (entering the lake in late summer). Consequently, the  $\delta^2\text{H}_{\text{C}_{16}\text{acid}}$  values reflect the weighted average of annual  $\delta^2\text{H}_{\text{precipitation}}$ .

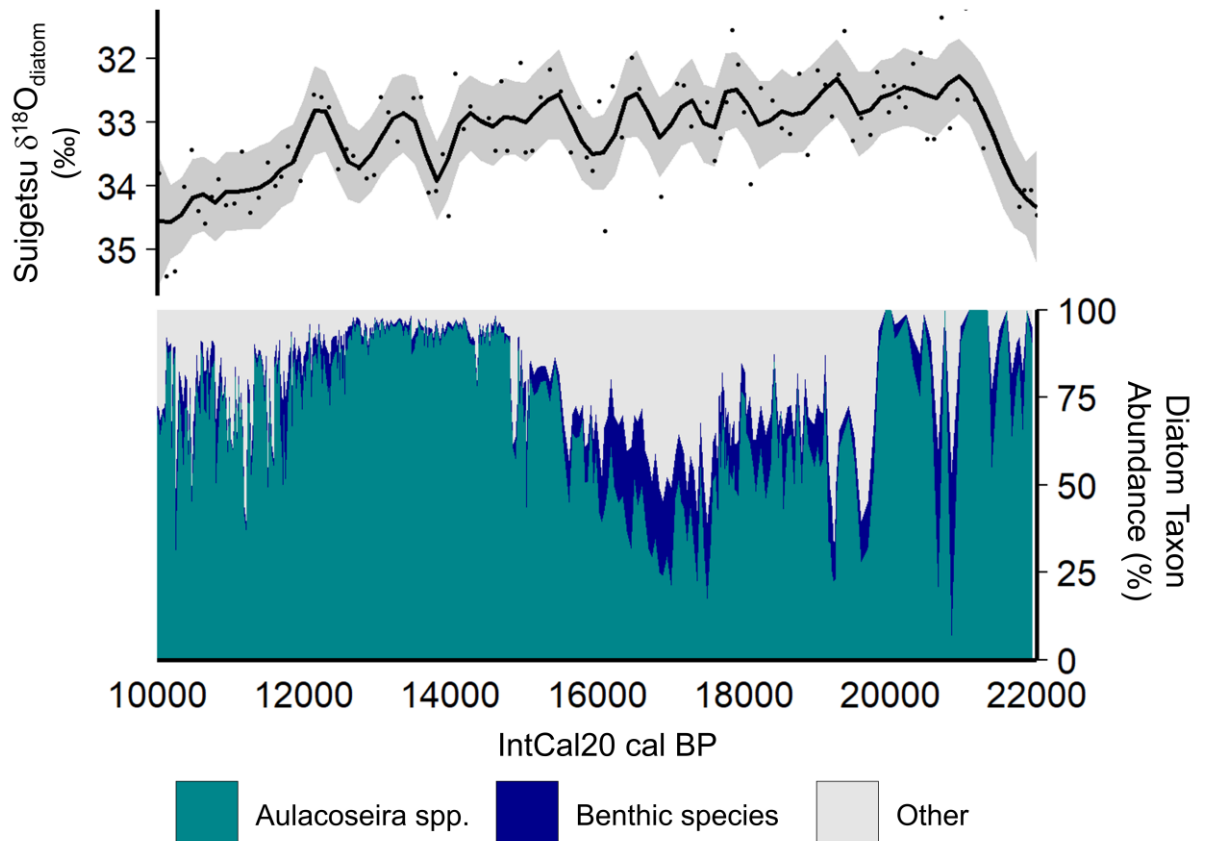


**Figure 3.6 Comparison of Lake Suigetsu bulk  $\delta^{18}\text{O}_{\text{diatom}}$  and Lake Suigetsu diatom taxonomic counts.** Diatom taxonomic counts show varying abundances of seasonally assigned genera (*Aulacoseira* and *Encyonema*, a benthic species) versus other taxa (provided by M. Saito-Kato). Intervals associated with high %*Aulacoseira* are interpreted as a proxy of EAWM strength. The data presented here supports EAWM weakening during Termination I.

By considering the numerical difference between the  $\delta^2\text{H}_{\text{C}_{30}\text{acid}}$  and  $\delta^2\text{H}_{\text{C}_{16}\text{acid}}$  values (Figure 3.7), it is possible to semi-quantify the relative influence of the EAWM and EASM on the  $\delta^2\text{H}_{\text{C}_{16}\text{acid}}$  values. Whilst traditionally used to consider the effect of evaporation on the aquatic  $\delta^2\text{H}$  signal (because the terrestrial  $\delta^2\text{H}$  is not affected by lake evaporation, unlike aquatic  $\delta^2\text{H}$ ), under the circumstances presented here, we interpret this measure to represent the balance between EAWM and EASM influence, based on the inference that the  $\delta^2\text{H}_{\text{C}_{16}\text{acid}}$  values represent a seasonal mix, and the  $\delta^2\text{H}_{\text{C}_{30}\text{acid}}$  values as seasonally constrained to

summer. Following this logic, the numerical difference between these measures indicates increasing EASM influence on aquatic  $\delta^2\text{H}$  during TI (Figure 3.7); larger values indicate greater EASM influence, and smaller values indicate greater EAWM influence (based on the assumption that EAWM  $\delta^2\text{H}_{\text{precipitation}}$  is higher than EASM  $\delta^2\text{H}_{\text{precipitation}}$ ). However, it is inappropriate to apply this interpretation to the ~19,000 – 18,000 cal BP interval, where there was a major amount of scatter in the  $\delta^2\text{H}_{\text{C30acid}}$  values. Additionally, a reduction in lag time with warming temperatures remains a component of this signal, reducing the quantity of EAWM precipitation in the lake during the summer and thus the influence of winter  $\delta^2\text{H}_{\text{precipitation}}$  on the  $\delta^2\text{H}_{\text{C16acid}}$  values.

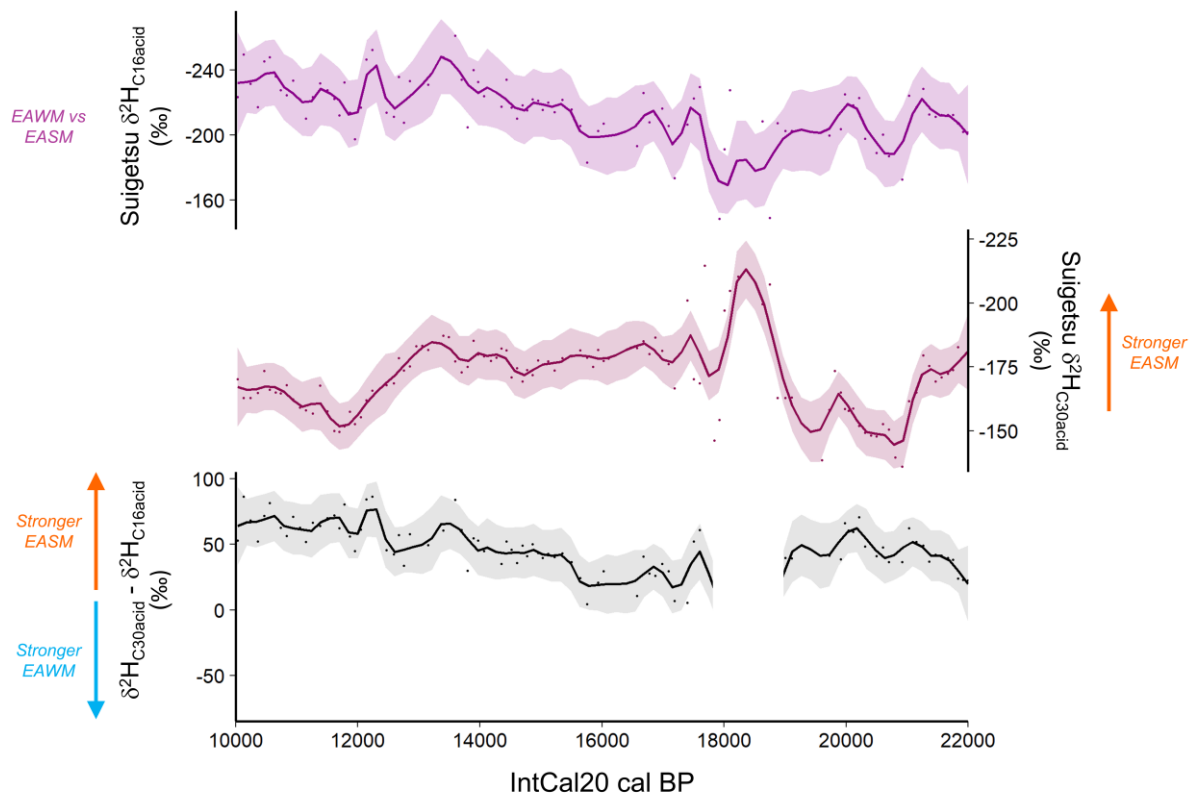


**Figure 3.7 Changing EASM influence on  $\delta^2\text{H}_{\text{acid}}$  at Lake Suigetsu.** Comparison of Lake Suigetsu  $\delta^2\text{H}_{\text{C16acid}}$ ,  $\delta^2\text{H}_{\text{C30acid}}$ , and the numerical difference between these quantities during TI in the Lake Suigetsu sediment cores.  $\delta^2\text{H}_{\text{C30acid}} - \delta^2\text{H}_{\text{C16acid}}$  is interpreted as an indicator of EASM versus EAWM influence, with a component of a reduced lag time with warming temperatures.

### 3.4.3 EAM Evolution in Japan During TI

By considering the high %*Aulacoseira* intervals in isolation (Figure 3.6), variations in the  $\delta^{18}\text{O}_{\text{diatom}}$  values strongly support a reduction in EAWM strength during TI in Japan (Figure 3.8D). This aligns with Japanese stalagmite reconstructions of EAWM behaviour from the LGM and Holocene (Sone *et al.*, 2013; Amekawa *et al.*,

2021). It is possible that EAWM weakening caused higher  $\delta^{18}\text{O}_{\text{diatom}}$  values both directly (as discussed above) and indirectly (by reducing EAWM surface runoff into the Sea of Japan, resulting in a transition from low- to high-salinity conditions in these EAWM source waters (Amekawa *et al.*, 2021)). The  $\delta^{18}\text{O}_{\text{diatom}}$  profile does not exhibit stage-interstage-like fluctuations as seen in the North Atlantic (typified by GRIP  $\delta^{18}\text{O}_{\text{ice}}$ ; Figure 3.8A; Rasmussen *et al.*, 2014) or Antarctica (typified by WAIS Divide  $\delta^{18}\text{O}_{\text{ice}}$ ; Figure 3.8H; WAIS Divide Project Members, 2013), refuting the dominance of any such teleconnection between these regions and the EAWM during TI. Indeed, the  $\delta^{18}\text{O}_{\text{diatom}}$  record does not show long term trends which parallel any of the benchmark records shown in Figure 3.8 suggesting that, instead, EAWM weakening during TI followed a more gradual trend akin to Northern Hemisphere summer insolation (albeit inversely; Figure 3.8J; Laskar *et al.*, 2004). The trend in the  $\delta^{18}\text{O}_{\text{diatom}}$  values between 22,000 and 21,000 cal BP inversely aligns with sea surface temperature (SST) records from the Northwest Pacific (Figure 3.8I; Oba and Murayama, 2004; Oba *et al.*, 2006), suggesting that EAWM strengthening during this 1000-year interval was due to the intensification of glacial conditions in the region.

Variations in the  $\delta^2\text{H}_{\text{C}_{30}\text{acid}}$  values support an overall strengthening of the EASM in Japan during TI (with lower values in the Holocene than the LGM), however this was non-linear and occurred in three phases: EASM strengthening from the LGM into the Late Glacial Interstade, EASM weakening from the Late Glacial Interstade to the early Holocene, and subsequent EASM strengthening (Figure 3.8F). An overall increase of EASM strength in Japan is also sustained by grain size variations within the South China Sea core GIK17940-2 (<63  $\mu\text{m}$  fraction; Figure 3.8G; Wang *et al.*, 1999); although the trend at Lake Suigetsu is not entirely equivalent to this because the South China Sea record shows a gradual, rather than tripartite, increase in EASM strength. Our reconstruction indicates that EASM behaviour in Japan was also characteristically different to EASM behaviour in Continental Asia (Chinese cave composite  $\delta^{18}\text{O}_{\text{speleothem}}$ ; Figure 3.8B; Cheng *et al.*, 2016) and did not show a response to North Atlantic-style stage-interstage fluctuations (Figure 3.8A; Rasmussen *et al.*, 2014). However, a close inverse relationship is observed between EASM strength in Japan and Antarctic temperatures (illustrated by WAIS Divide  $\delta^{18}\text{O}_{\text{ice}}$ , Figure 3.8H; WAIS Divide Project Members, 2013) between 16,000 and 10,000 cal BP, including

coincident timing of inflections at ~14,500 cal BP, ~13,000 cal BP and ~12,000 cal BP (i.e., a response to the ACR). This provides compelling evidence for a teleconnection between the polar southern hemisphere and the EASM during this interval. Prior to this, the  $\delta^2\text{H}_{\text{C}_{30}\text{acid}}$  values were decoupled from WAIS Divide  $\delta^{18}\text{O}_{\text{ice}}$ , suggesting that this teleconnection was only activated at this time. During the LGM, the  $\delta^2\text{H}_{\text{C}_{30}\text{acid}}$  profile was distinctive and showed large amplitude fluctuations which did not occur synchronously with changes in the global benchmark records, but many of these were also observed in the  $\delta^2\text{H}_{\text{C}_{16}\text{acid}}$  values. Interpretation of this time period is complex and is presented in Section 3.5.

The  $\delta^2\text{H}_{\text{C}_{16}\text{acid}}$  values display a composite trend (Figure 3.8E) which encapsulates characteristics of both the  $\delta^{18}\text{O}_{\text{diatom}}$  (Figure 3.8D) and  $\delta^2\text{H}_{\text{C}_{30}\text{acid}}$  (Figure 3.8F) records. The influence of each of these unique behaviours appears to dominate the  $\delta^2\text{H}_{\text{C}_{16}\text{acid}}$  values at different times during the interval: similarities between the  $\delta^2\text{H}_{\text{C}_{16}\text{acid}}$  and  $\delta^2\text{H}_{\text{C}_{30}\text{acid}}$  profiles are observed during the early part of the ACR and the Holocene; in the latter stages of the ACR the  $\delta^2\text{H}_{\text{C}_{16}\text{acid}}$  profile resembles that of  $\delta^{18}\text{O}_{\text{diatom}}$ ; and prior to 17,000 cal BP the  $\delta^2\text{H}_{\text{C}_{16}\text{acid}}$  profile shows mixed behaviour. These observations are consistent with our assertions that the  $\delta^2\text{H}_{\text{C}_{16}\text{acid}}$  values reflect a combined EAWM and EASM signal, weighted to the season with a greater quantity of precipitation, and these results support a changing balance between EAWM and EASM dominance in Japan during TI. The  $\delta^2\text{H}_{\text{C}_{16}\text{acid}}$  values show more EAWM character during the later stages of the ACR, when the EAWM was strong and EASM strength was declining, but shows greater EASM affinity during the early ACR and the Holocene, when there was a strengthened EASM and a weakened EAWM. This is consistent with our observations of the numerical difference between the  $\delta^2\text{H}_{\text{C}_{16}\text{acid}}$  and  $\delta^2\text{H}_{\text{C}_{30}\text{acid}}$  values, which suggests an increasing EASM influence on Lake Suigetsu through time (Figure 3.7), and our independent observations of EAWM and EASM strength from the  $\delta^{18}\text{O}_{\text{diatom}}$  and  $\delta^2\text{H}_{\text{C}_{30}\text{acid}}$  values.

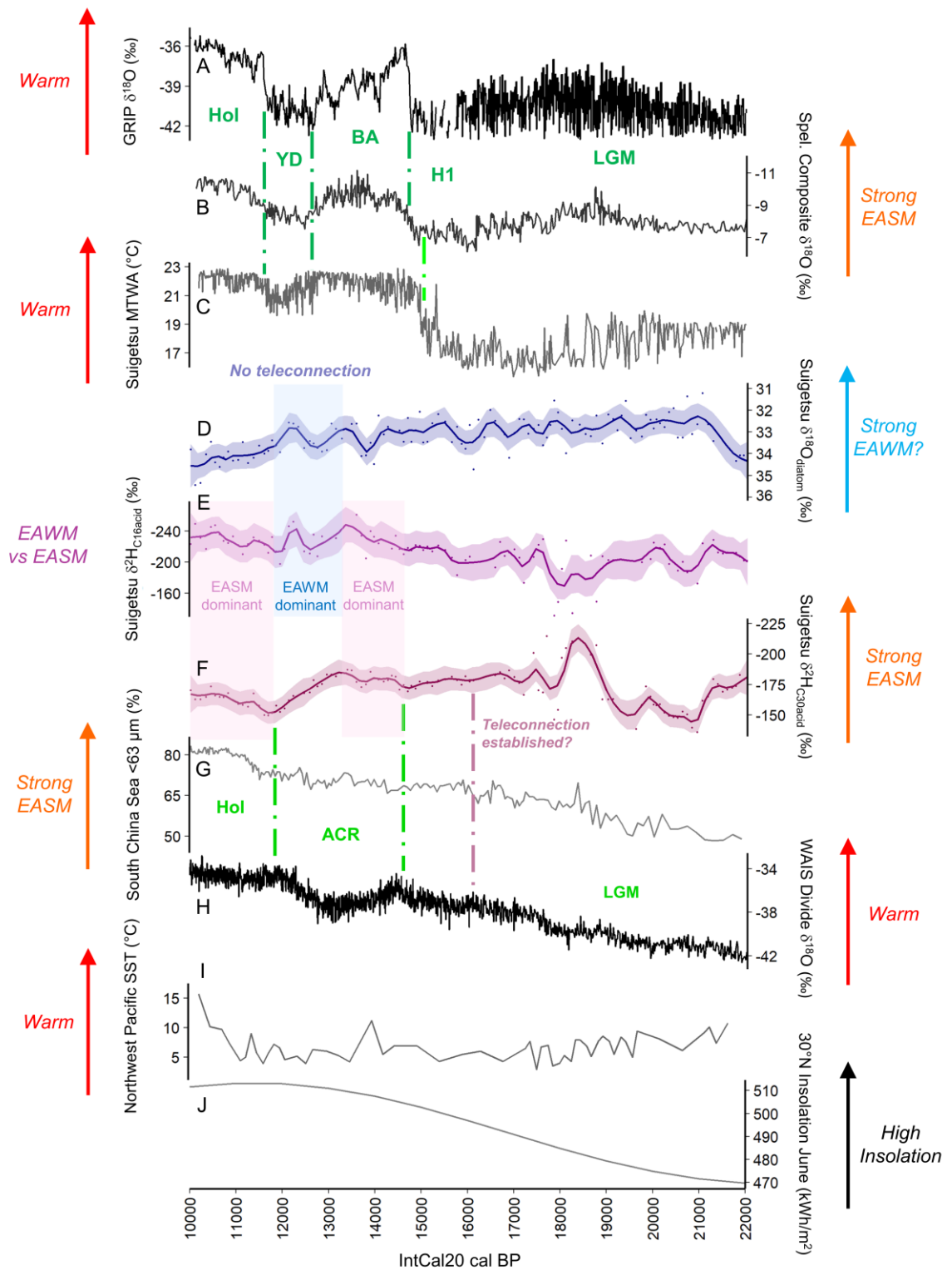


**Figure 3.8 EAM evolution at Lake Suigetsu during Termination I with contextual global benchmark records.** A) GRIP  $\delta^{18}\text{O}_{\text{ice}}$  (Johnsen *et al.*, 1997; Rasmussen *et al.*, 2014; remodelled onto U–Th timescale), B) Chinese Cave Composite (Hulu, Dongge, Sanbao)  $\delta^{18}\text{O}_{\text{speleothem}}$  (Cheng *et al.*, 2016; U–Th timescale), C) Lake Suigetsu MTWA; mean temperature of the warmest month (pollen-derived; provided by T. Nakagawa; Nakagawa *et al.*, 2021; IntCal20 timescale), D) Lake Suigetsu  $\delta^{18}\text{O}_{\text{diatom}}$ , loess smoothed (span = 0.1) with  $1\sigma$  confidence bands (this study; IntCal20 timescale), E)  $\delta^2\text{H}_{\text{acid}}$  for  $\text{C}_{16}$  n-alkanoic acids, loess smoothed (span = 0.1) with  $1\sigma$  confidence bands (this study; IntCal20 timescale), F)  $\delta^2\text{H}_{\text{acid}}$  for  $\text{C}_{30}$  n-alkanoic acids, loess smoothed (span = 0.1) with  $1\sigma$  confidence bands (this study; IntCal20 timescale), G) South China Sea (GIK17940–2) grain size proportion  $<63 \mu\text{m}$  (Wang *et al.*, 1999; remodelled on to IntCal20 timescale), H) WAIS  $\delta^{18}\text{O}_{\text{ice}}$  (WAIS Divide Project Members, 2013; WD2014 timescale), I) Northwest Pacific

(MD01–2421) Sea Surface Temperature reconstruction (Oba *et al.*, 2006; remodelled onto Marine20 timescale), J) 30°N June Insolation (Laskar *et al.*, 2004). Arrows indicate dataset interpretation. Dashed lines approximately align climatic transitions. Abbreviations: Hol = Holocene, YD = Younger Dryas, BA = Bølling–Allerød, H1 = Heinrich Event 1, LGM = Last Glacial Maximum, EAWM = East Asian Winter Monsoon, EASM = East Asian Summer Monsoon, ACR = Antarctic Cold Reversal. Alignment of non–IntCal20/Marine20 timescales was performed as follows: the GRIP  $\delta^{18}\text{O}_{\text{ice}}$  dataset was converted from the GICC05 timescale to the U–Th timescale using the transfer functions of Adolphi and Muscheler (2015) and Adolphi *et al.* (2018). The WD2014 timescale and the U–Th timescale are compatible at the resolution presented here, with a minimal offset at the Holocene onset (Sigl *et al.*, 2016) and an offset of 225 years in the LGM (Sinnl *et al.*, 2023), which has a negligible effect on alignment due to the gradual nature of the changes observed in the WAIS  $\delta^{18}\text{O}$  record. The U–Th and IntCal20 timescales are compatible because IntCal20, beyond the tree ring limit (circa 13,900 cal BP) is dominated by the Hulu Cave U–Th timescale (Reimer *et al.*, 2020).

### 3.5 Discussion

Our results provide novel insights into the evolution of the EAWM and EASM during TI, alongside their driving mechanisms and teleconnections to other regional climate systems. The gradual decrease in EAWM strength and overall increase in EASM strength in Japan strongly support increasing Northern Hemisphere insolation (driven by Milankovitch cycles) as the primary drivers of EAM evolution (Cheng *et al.*, 2016; Mohtadi *et al.*, 2016; Zhang *et al.*, 2019). However, this common orbital driver breaks down as a result of different responses of each seasonal mode to submillennial temperature fluctuations in either hemisphere and it becomes necessary to evoke alternative mechanisms to rationalise these decoupled (rather than inversely related) seasonal behaviours.

EAWM evolution in Japan appears unaffected by stades in either hemisphere, however other records from Continental Asia (e.g., Lake Huguang Maar (Yancheva *et al.*, 2007)) exhibit significant North Atlantic character (i.e., a BA–YD structure). Despite high quality EAWM records being relatively sparse for this interval, we do not dispute the evidence for a North Atlantic–EAWM teleconnection during TI, and suggest that EAWM wind strength increased (decreased) during stades (interstades) in the North Atlantic, driven by Northern Hemisphere cooling (warming) and an intensified (weakened) Siberian High as previously suggested (Nakagawa *et al.*, 2006). Indeed, the pattern of winter temperatures at Lake Suigetsu provides evidence for the impact of North Atlantic temperatures on the Eurasian airmass (Nakagawa *et al.*, 2021). However, as a consequence of the interaction of the EAWM winds with the Sea of Japan, the decrease in EAWM strength here was gradual (Figure 3.8D). Specifically, we suggest that any response to North Atlantic stade–interstade

fluctuations was obscured from our reconstruction by a smoothed, low amplitude response of winter Sea of Japan SSTs to insolation (Wu *et al.*, 2020) and greater inertia in the oceanic domain compared to the terrestrial. Furthermore, we are able to clarify that the previously evidenced bi-partite Late Glacial Stage at Lake Suigetsu (Schlölaut *et al.*, 2017) was not associated with any shifts in EAWM precipitation; whilst there is a 300-year period of lower  $\delta^{18}\text{O}_{\text{diatom}}$  values within this interval (between 12,285 and 12,095 cal BP; Figure 3.8D), this fluctuation is not substantially different from other multi-centennial oscillations seen in the profile. However, it remains possible that there was a bipartite pattern in EAWM wind strength. An Antarctica–EAWM teleconnection was precluded by local EAWM moisture transport, the isolation of the Sea of Japan, and the blocking of Pacific Ocean signals by the monsoon front, all of which limited the influence of interhemispheric teleconnections.

Conversely, evidence from Lake Suigetsu supports a response of the EASM to stadial conditions in the Southern Hemisphere (specifically the ACR) post-16,000 cal BP (Figure 3.8F). Previous studies which have noted a relationship between EASM strength and Antarctic temperatures have evoked the bipolar seesaw and migration of the ITCZ as a mechanism to explain this connection (Han *et al.*, 2016; Zhang *et al.*, 2016). Whilst this would facilitate an inverse correlation between EASM strength in Japan and the ACR, it would also suggest that equivalent shifts in the position of the ITCZ caused by North Atlantic behaviours could affect EASM strength, and we do not see evidence of such a relationship in our records. Instead, we suggest that the Antarctic–EASM teleconnection during TI resulted from Antarctic cooling (warming), which caused coupled atmospheric–ocean circulation changes that resulted in warming (cooling) in the Western Pacific Warm Pool, enhanced (decreased) evaporation and a strengthened (weakened) Western Pacific Subtropical High, which caused a stronger (weaker) EASM (Wang and Fan, 2005; Xu *et al.*, 2020). The coexistence of a North Atlantic teleconnection to summer temperature and an Antarctic teleconnection to summer (EASM) precipitation at Lake Suigetsu is reconcilable by noting that temperature is much more likely to exhibit patterns common to the same hemisphere, whereas the relationship of the EASM to Pacific Ocean behaviours facilitates the influence of the polar Southern Hemisphere on precipitation. Indeed, our observations of EASM strength at Lake Suigetsu,

combined with the pollen-derived summer temperature record, support a “Southern Hemisphere lead” to stade/interstade fluctuations during TI; changes in EASM strength led changes in summer temperature because the former was driven by Antarctic processes and the latter by North Atlantic behaviours.

Our observations of EASM behaviour in Japan directly contradict those of the Chinese cave composite, which supports an EASM response to North Atlantic stade–interstade fluctuations and not Antarctic ones (Figure 3.8B; Cheng *et al.*, 2016). Because all of the caves included in the composite (Hulu, Sanbao and Dongge) and Lake Suigetsu are located south of the monsoon front during the summer (and hence under the influence of the Pacific air mass; Nakagawa *et al.*, 2006), differences cannot be resolved by the blocking of teleconnections by the monsoon front, as previously suggested (Yoshida and Takeuti, 2009), and instead must be determined by a different geoclimatic boundary. One possible mechanism involves the overprinting of Antarctic signals in Continental Asia by the partitioning of precipitation between the EASM and post–EASM stages (jet–transition hypothesis; Zhang *et al.*, 2018). This phenomenon is linked to the prevailing climatic conditions in the North Atlantic by the timing of the pre–summer northwards shift of the westerly jet and would have caused drier (wetter) conditions in central China during stades (interstades) in the North Atlantic. For this to not impact on EASM evolution in Japan, the effect of this partitioning must have been spatially restricted to the continent, or limited to latitudes at, or lower than, the southernmost position of the westerly jet (Lake Suigetsu is located to the north of this position and Hulu, Dongge and Sanbao Cave to the south (Nakagawa *et al.*, 2021)). An alternative explanation is that the speleothem records contain an unresolved temperature–controlled component (demonstrated by their close relationship to the pollen–reconstructed temperature at Lake Suigetsu; both show a remote North Atlantic influence) which obscured the Antarctic signal in favour of a North Atlantic one. Regardless, we posit that the location of Japan at a higher latitude, adjacent to the Pacific Ocean and geographically separated from the rest of East Asia facilitated the preservation of Pacific (and hence Antarctic) signals in our record of EASM behaviour at Lake Suigetsu. Whilst this Antarctica–Japan teleconnection has not been observed in other EASM reconstructions (Wang *et al.*, 1999; Ishiwatari *et al.*, 2009; Hayashi *et al.*, 2010),

this is likely due to differences in proxy system and a direct relationship between the isotope composition of precipitation and EAM evolution.

However, prior to ~16,000 cal BP, EASM strength in Japan and Antarctic temperatures were decoupled. We suggest that the establishment of this teleconnection was as a consequence of the northwards repositioning of the westerly jet (relative to the Himalayas), a phenomenon previously used to explain the onset of the Late Glacial Interstade (BA-equivalent; 15,000 cal BP) at Lake Suigetsu (Nakagawa *et al.*, 2021). Not only did this northwards shift of the westerly jet allow warm Pacific air to reach Japan, but it also moved the EAM front to the north of Lake Suigetsu during boreal summer (because the position of the westerly jet also modulates the seasonal positioning of the EAM front), having been situated permanently (year-round) to the south during the LGM (Chiang *et al.*, 2015; Nakagawa *et al.*, 2021). This would allow the EASM to propagate to Japan and connect summer precipitation to the aforementioned components of the Pacific atmosphere–oceanic circulation (and hence the southern hemisphere). There were no abrupt shifts in the  $\delta^2\text{H}_{\text{C}_{30}\text{acid}}$  values at the onset of the Late Glacial Interstade (15,000 cal BP) to reflect this expansion of EASM operation to include Japan; however, prior to 16,000 cal BP the  $\delta^2\text{H}_{\text{C}_{30}\text{acid}}$  values were highly variable and structurally distinctive from WAIS Divide  $\delta^{18}\text{O}_{\text{ice}}$ . Hence, we suggest that this Antarctic–Japan teleconnection was established at 16,000 cal BP, facilitated in the 16,000–15,000 cal BP period by intermittent northward migrations of the westerly jet and exposure of Japan to the Pacific airmass during summer (captured by our centennial sampling resolution), and then continued post–15,000 cal BP when the EAM front was situated permanently to the north of Lake Suigetsu during summer.

It follows that prior to the establishment of this teleconnection, precipitation falling during summer in Japan would not technically be equivalent to the EASM (because it would originate and transit north of the EASM front), and instead would reflect local transport of precipitation under the influence of the continental airmass (possibly following a similar south–east to north–west trajectory due to pressure gradients, but with a significantly reduced transport distance). The highly variable behaviour of the  $\delta^2\text{H}_{\text{C}_{30}\text{acid}}$  values (and hence the  $\delta^2\text{H}_{\text{C}_{16}\text{acid}}$  values) between 22,000 and 16,000 cal BP may have been caused by the lack of constant, regional driver of summer precipitation (i.e., the EASM) in

contrast to the  $\delta^{18}\text{O}_{\text{diatom}}$  values, which were weighted towards the (enduring) EAWM. These fluctuations in the  $\delta^2\text{H}_{\text{acid}}$  values could be driven by a number of factors, including precipitation amount, changing relative humidity, shifts in precipitation source and variable SSTs (particularly between 22,000 and 21,000 cal BP (Oba *et al.*, 2006)). Another possible component of this signal is summer meltwater (which could have caused large negative excursions in the  $\delta^2\text{H}_{\text{C30acid}}$  values, such as those observed between ~19,000 and 18,000 cal BP). The significant expansion of the EASM system at 16,000 cal BP has critical implications for other records from the region, particularly those derived from more northerly latitudes, where the influence of the westerly jet migration is more pronounced (Nakagawa *et al.*, 2021). Careful consideration of the location of the monsoon front at this time is vital for robust interpretation of proxy changes and whether they indeed represent EASM evolution or, rather, non-monsoonal summer precipitation.

In conclusion, our findings provide centennial-scale reconstructions which highlight the distinctive seasonal behaviours of the EAM during TI, as well as novel insights into the spatially- and temporally- constrained teleconnections acting on the climate of the EAM region during this interval. Our records are unique in their reconstruction of both seasonal EAM modes in Japan from a single archive. These results may begin to explain the observed heterogeneity between site-specific reconstructions of EAM behaviour during deglaciation.

## Chapter 4 Novel Observations of East Asian Summer Monsoon Evolution During Glacial Termination II from Lake Suigetsu, Japan

Rex, Charlie L.<sup>1,2</sup>, Staff, Richard A.<sup>1</sup>, Toney, Jaime L.<sup>2</sup>, Pearson, Emma J.<sup>3</sup>, Francke, Alexander<sup>4,5</sup>, Saito-Kato, Megumi<sup>6</sup>, Nakagawa, Takeshi<sup>7</sup> (unpublished). 'Novel observations of East Asian Summer Monsoon evolution during Glacial Termination II from Lake Suigetsu, Japan'. Submitted to: *Quaternary Science Reviews*. Available on EarthArXiv at: <https://doi.org/10.31223/X5310P>.

<sup>1</sup>*SUERC, University of Glasgow*

<sup>2</sup>*GES, University of Glasgow*

<sup>3</sup>*Newcastle University*

<sup>4</sup>*University of Adelaide*

<sup>5</sup>*Flinders University*

<sup>6</sup>*National Museum of Nature and Science, Japan*

<sup>7</sup>*Ritsumeikan University*

The text presented here is identical to that of the submitted version and preprint, except for the following:

- The numbering of figures,
- The acknowledgement of the contribution(s) of other authors and individuals where appropriate,
- The integration of the supplementary material into the main text for the benefit of the reader of this thesis, and
- Amendments made following the examination of this thesis at the request of the examiners.

Authorship Declaration: C.L.R. performed the core sampling, n-alkane and n-alkanoic acid sample preparation and GC-FID analysis, corrected and analysed the GC-FID and GC-IRMS datasets, and wrote the manuscript (first draft, editing and final draft). R.A.S. and V. Nowinski assisted with the core sampling. R.A.S., J.L.T., E.J.P. and T.N. provided feedback, supervision and guidance. O. Seki performed the GC-IRMS analysis. A.F. provided the pre-50 ka BP extension to

the Suigetsu core age–depth model. J.J. Tyler and A.F. provided the total organic carbon to total nitrogen ratio (TOC/TN) and the carbon isotope ratio of organic matter ( $\delta^{13}\text{C}_{\text{org}}$ ) datasets (Figure 4.5). M.S–K. provided the total diatom frustule abundance and *Cyclotella spp.* frustule count datasets (Figure 4.5). T.N. provided the pollen–derived temperature dataset (Figure 4.7; Figure 4.8; Figure 4.9) and access to core materials.

Funding: This research was financially supported by a Quaternary Research Association New Research Workers Award (QRA NRWA), the Scottish Alliance for Geoscience, Environment and Society (SAGES) Small Grants Scheme and the School of Geographical and Earth Science at the University of Glasgow. The Lake Suigetsu sediment core chronology extension work was supported by an Australian Research Council Discovery Project (DP200101768). C.L.R. was supported by the NERC IAPETUS2 Doctoral Training Partnership.

Accompanying data can be found at

<https://doi.org/10.5525/gla.researchdata.1486>.

## 4.1 Abstract

Glacial terminations offer a unique opportunity to examine how the East Asian Summer Monsoon (EASM) responds to rapid increases in global temperature and accompanying abrupt climatic reorganisation. Reconstructions from contrasting glacial terminations with differently evolving boundary conditions are of particular value to our understanding of deglacial EASM behaviours, e.g., Termination I (from MIS 2 to MIS 1) and Termination II (from MIS 6 to MIS 5e). However, records of EASM evolution across Termination II are substantially fewer in number than Termination I, as well as exhibiting a significant bias towards continental speleothem archives. Japan is a critically understudied, but demonstrably sensitive area of the EASM region and, during other periods, records from Japan often display unique trends not captured by continental records. Here we present a new EASM record derived from the Lake Suigetsu sediment cores, central Japan, based on compound-specific hydrogen isotope analysis of C<sub>30</sub> n-alkanoic acids ( $\delta^2\text{H}_{\text{C}_{30}\text{acid}}$ ), which constitutes the first stable isotope-based EASM record from the Japanese archipelago across Termination II. We also present lipid biomarker (n-alkane and n-alkanoic acid) concentrations and indices, which we use to reconstruct early lake formation. The catchment transitioned from a dynamic fluvial environment to a lacustrine one between 131.0 and 129.8 ka BP. The EASM strengthened from 132.5 to 130.0 ka BP (earlier than in continental China), before weakening toward 125.2 ka BP, with some evidence for submillennial-scale variability during this weakening phase; a pattern common to sites across the EASM region which are closer to the northernmost position of the monsoon front. Whilst our record displays some similar characteristics to EASM reconstructions from mainland China, our observations support the assertion that EASM behaviours during Termination II were spatially heterogeneous. Additionally, comparison of our Termination II  $\delta^2\text{H}_{\text{C}_{30}\text{acid}}$  record to an equivalent record from Lake Suigetsu during Termination I suggests that EASM evolution during the last and penultimate deglaciations were distinct due to differently evolving climatic conditions (including the extreme decoupling of polar temperatures during Termination II). We propose that the spatial heterogeneities in EASM strength during Termination II were a result of competing influences from the Northern and Southern Hemispheres, with Japan

more closely linked to the latter compared to mainland China due to its maritime location.

## 4.2 Highlights

- The first stable isotope-based reconstruction of EASM behaviour from Japan during TII.
- The EASM in Japan strengthened to 130.0 ka BP before weakening to 125.2 ka BP.
- Evidence for submillennial-scale variability in EASM strength.
- EASM strengthening across TII occurred earlier in Japan than mainland China.
- Evidence for competing northern and southern hemisphere influences on the EASM.

## 4.3 Keywords

Quaternary; Palaeoclimatology; Palaeolimnology; Eastern Asia; Continental Biomarkers; Organic Geochemistry; Stable Isotopes; Japan; Glacial Termination; East Asian Summer Monsoon

## 4.4 Introduction

The East Asian Summer Monsoon (EASM) system exerts significant influence on the water resource distribution and climatic hazards of East Asia, making this densely populated region vulnerable to the spatial and temporal redistribution of EASM precipitation due to anthropogenic climate change (Chen *et al.*, 2019; Park *et al.*, 2019). By characterising EASM behaviours across glacial terminations, it is possible to examine how the system operated under, and during the rapid transition between, previous extremes of global temperature (He *et al.*, 2017a; Duan *et al.*, 2019). Critically, glacial terminations exemplify a greater amplitude of climatic change than is currently covered by contemporary observations of the EASM system. Furthermore, whilst there are differences between glacial terminations and present-day anthropogenic warming, the study of the former provides improved knowledge of how EASM evolution coevolves with abrupt global climate system reorganisation (He *et al.*, 2017a). In particular, the

sub-structure of EASM behaviour across deglacial intervals can shed light on the relationship between the EASM and coupled atmosphere–ocean circulations, which can be significant drivers of EASM strength on centennial–to–millennial timescales (Wang *et al.*, 2008; Zhang *et al.*, 2019).

EASM evolution across the last glacial termination (TI; the transition from MIS 2 to MIS 1) is relatively well-studied (albeit less comprehensively than other regional climate systems, such as the North Atlantic) with reasonable coverage provided by a growing network of high-quality palaeoclimate records (e.g., Wang *et al.*, 2001; Wang *et al.*, 2010; Zhang *et al.*, 2018). Contrastingly, records of EASM behaviour across the penultimate glacial termination (TII; the transition from MIS 6 to MIS 5e) are substantially fewer in number (He *et al.*, 2017a; Duan *et al.*, 2019), likely due to a combination of poor archive preservation across this older interval and a preference for studying time periods where high-resolution chronological control is more easily obtained (i.e., within the limit of radiocarbon dating). However, our collective knowledge regarding how the EASM responds to rising temperatures is substantially enriched by reconstructions from across a range of boundary conditions. The sequences of deglacial climate change which occurred during TI and TII were characteristically different (Figure 4.1; Gorbarenko *et al.*, 2019), meaning that there is inherent value in targeting EASM reconstructions from TII to complement the growing compilation of records covering TI (He *et al.*, 2017a). Both TI and TII exhibited asymmetrical hemispheric warming (whereby the southern hemisphere warmed prior to the Northern Hemisphere) (Figure 4.1; Broecker and Henderson, 1998; Masson–Delmotte *et al.*, 2010); however, whilst there is convincing evidence for the submillennial-scale sub-structure of temperature evolution during TI (e.g., the North Atlantic Bølling–Allerød/Younger Dryas, or the Antarctic Cold Reversal (Rasmussen *et al.*, 2014; WAIS Divide Project Members, 2013), the evidence for similar variability during TII is equivocal (Figure 4.1; Cheng *et al.*, 2019; Duan *et al.*, 2019). Furthermore, there is evidence to suggest that TII was associated with more rapid sea surface temperature increases, sea level rise and ice sheet collapse relative to TI (Caley *et al.*, 2013), making it a useful interval to study in order to better understand how the EASM might evolve under future climate scenarios.

Current EASM reconstructions from TII are heavily weighted towards  $\delta^{18}\text{O}_{\text{speleothem}}$  records from China, which provide evidence for a weak EASM in the latter stages of MIS 6 (posited as temporally equivalent to Heinrich Event 11) (Yuan *et al.*, 2004; Cheng *et al.*, 2006; Duan *et al.*, 2019), followed by rapid EASM strengthening across a sub-200-year interval at ~129 ka BP (Kelly *et al.*, 2006; Duan *et al.*, 2019) and a relatively strong EASM during the early stages of MIS 5e (Li *et al.*, 2014), persisting to ~121 ka BP (Kelly *et al.*, 2006). The rate of EASM strengthening at ~129 ka BP has been proposed as evidence for threshold behaviour (Yuan *et al.*, 2004), with this shift coinciding with increasing Northern Hemisphere temperatures and Northern Hemisphere ice sheet collapse (Jiang *et al.*, 2005; Oppo and Sun, 2005; Cheng *et al.*, 2006) but lagging behind Northern Hemisphere summer insolation, Antarctic temperature, atmospheric  $\text{CO}_2$  concentration and sea level rise (Yuan *et al.*, 2004; Wang *et al.*, 2008; Xue *et al.*, 2019).

However, the submillennial-scale structure of EASM strength variations during this period is highly debated (much like the temperature profiles of the same interval). Some records (e.g., Hulu Cave) show smooth EASM strengthening with no evidence for submillennial-scale fluctuations (Cheng *et al.*, 2006), however others show varying degrees of sub-structure within the overall EASM strengthening trend. At Dongge Cave and Sanbao Cave, EASM strength exhibited a post-transition “slowdown” and increased more slowly after a sudden upturn at 129 ka BP (Jiang *et al.*, 2005; Kelly *et al.*, 2006). At Xinglong Cave, there was a notable “pause” in EASM strengthening (Duan *et al.*, 2019), attributed to muted “Younger Dryas”-type stadial conditions in the North Atlantic. It was proposed that this interval was associated with a smaller amplitude of cooling than the TI Younger Dryas due to a severely suppressed Atlantic Meridional Overturning Circulation (AMOC) during TII which was not as significantly perturbed by meltwater pulses. At Shangxiaofeng Cave, a full inversion of EASM strength was detected, likely in response to short lived (~400 year) stadial conditions, again attributed to “Younger Dryas”-type conditions (Xue *et al.*, 2019). These conflicting observations suggest that EASM evolution across TII exhibits greater spatial heterogeneity than across TI (Xue *et al.*, 2019).

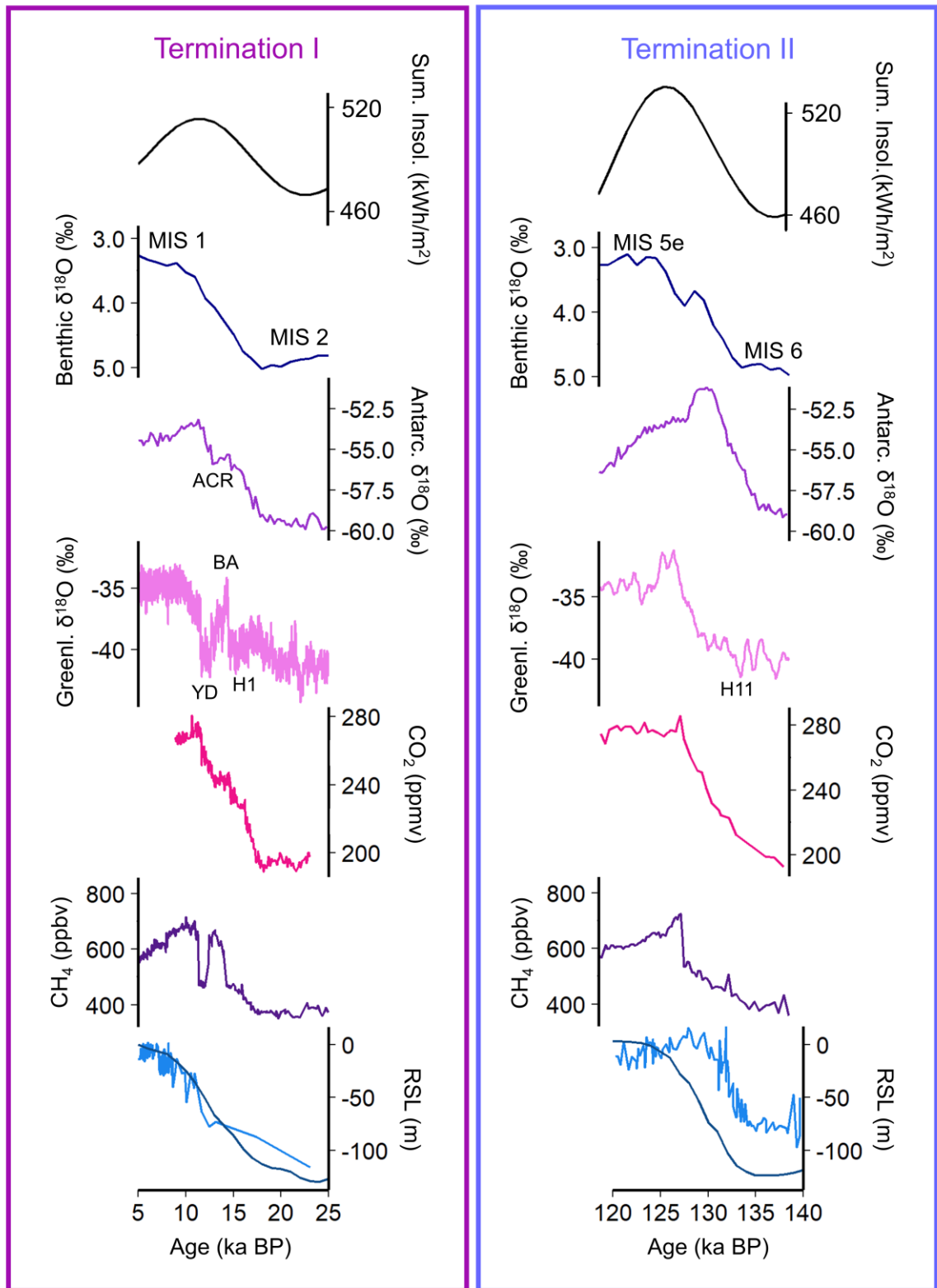


**Figure 4.1** The differences between the climatic sequences of TI and TII. Adapted from Barker and Knorr (2021). The reconstructions shown, from top to bottom, are: June Insolation at 30°N (Laskar *et al.*, 2004); the Global Benthic  $\delta^{18}\text{O}$  stack (Lisiecki and Raymo, 2005); Dome Fuji Antarctic  $\delta^{18}\text{O}_{\text{ice}}$  (Kawamura *et al.*, 2007); GRIP (TI; Johnsen *et al.*, 1997; Rasmussen *et al.*, 2014) and Synthetic (TII; Barker *et al.*, 2011) Greenland  $\delta^{18}\text{O}_{\text{ice}}$ ; WAIS Divide (TI; Marcott *et al.*, 2014) and Dome Fuji (TII; Kawamura *et al.*, 2007) atmospheric  $\text{CO}_2$  concentration; EPICA Dome C Atmospheric  $\text{CH}_4$  concentration (Loulergue *et al.*, 2008); and Relative Sea Level (RSL; Grant *et al.*, 2014 (light blue); Spratt and Lisiecki, 2016 (dark blue)). Abbreviations: MIS = Marine Isotope Stage, ACR = Antarctic Cold Reversal, YD = Younger Dryas, BA = Bølling-Allerød, H1 = Heinrich Event 1, H11 = Heinrich Event 11.

To tackle the uncertainty surrounding EASM evolution across TII and the substantial bias towards continental  $\delta^{18}\text{O}_{\text{speleothem}}$  records, we present a new compound specific stable isotope-based ( $\delta^2\text{H}_{\text{C}_{30}\text{acid}}$ ) EASM record derived from the Lake Suigetsu sediment cores, central Japan. Japan is situated in a critically understudied, yet demonstrably sensitive, area of the East Asian Monsoon region, being situated beneath the seasonally migrating monsoon front (north of it during winter and south of it during summer) and receives a significant proportion of its rainfall annually from the EASM (Nakagawa *et al.*, 2006). Reconstructions of climate (including EASM behaviour) across TI from Japan have shown the potential of this area for deconvolving complexities in the responses of temperature and precipitation to deglaciation (Hayashi *et al.*, 2010; Liepe *et al.*, 2015; Nakagawa *et al.*, 2021). Our new record constitutes the first terrestrial stable isotope-based EASM record from Japan across TII, providing novel insights into EASM evolution across this interval from a region that is sensitive to EASM fluctuations. The results of this study are complemented by equivalent analysis from TI (from Chapter 3), facilitating the direct comparison of EASM evolution at Lake Suigetsu across the penultimate and last glacial terminations.

Our approach constitutes two complementary techniques employing lipid biomarkers preserved within the Lake Suigetsu sediment cores: determination of the compound-specific hydrogen isotope composition of n-alkanoic acids ( $\delta^2\text{H}_{\text{acid}}$ ) from terrestrial leaf waxes to reconstruct regional EASM behaviour; and quantification of terrestrial (leaf wax-derived; long-chained) and aquatic (algae-derived; short-chained) n-alkane and n-alkanoic acid concentrations to account for local (catchment) scale changes. The hydrogen isotope composition of terrestrial leaf waxes preserved within sediments is becoming increasingly utilised for palaeohydrological reconstructions in light of its close relationship to the hydrogen isotope composition of past precipitation ( $\delta^2\text{H}_{\text{precipitation}}$ ) which would have provided the source water for plant growth (Sachse *et al.*, 2012; Holtvoeth *et al.*, 2019). As such,  $\delta^2\text{H}_{\text{acid}}$  can act as a tracer for shifts in atmospheric circulation and vapour transport (Tierney *et al.*, 2008) which is stable on geological timescales (Sachse *et al.*, 2006). Within the context of the Lake Suigetsu catchment,  $\delta^2\text{H}_{\text{precipitation}}$  during the growth season is dominantly controlled by EASM behaviour (Rex *et al.*, 2024; Chapter 2) and hence  $\delta^2\text{H}_{\text{acid}}$  has

demonstrable links to the regional EASM system, facilitating reconstructions of past EASM variability. Owing to the significant catchment evolution which occurred at Lake Suigetsu during TII, we also make use of terrestrial (long-chained) and aquatic (short-chained) homologue concentrations alongside existing diatom taxonomic counts, total organic carbon to total nitrogen ratios (TOC/TN) and the carbon isotope composition of organic matter ( $\delta^{13}\text{C}_{\text{org}}$ ) to examine local environmental change more closely across this hitherto weakly constrained interval.

## 4.5 Study Site

Lake Suigetsu is a ~34 m deep tectonic lake located adjacent to the Sea of Japan in Fukui Prefecture, Honshu Island, central Japan ( $35^{\circ} 35'08''$  N,  $135^{\circ} 52'57''$  E) (Figure 4.2; Nakagawa *et al.*, 2021). The lake is relatively small, with a surface area of approximately 4.2 km<sup>2</sup> (Shigematsu *et al.*, 1961), occupying ~50 % of its total direct catchment area. Suigetsu is one of the “Five Lakes of Mikata”, a lake system which, in the modern day, forms a series of artificially interconnected water bodies linking the Hasu River to the south and Wakasa Bay to the north (Figure 4.2; Shigematsu *et al.*, 1961; Nakagawa *et al.*, 2021). The climate of the catchment is typical of the Sea of Japan coast of Honshu Island; i.e., temperate and monsoonal. Between May and July, the climate of the region is dominated by the moisture-rich south-easterly winds of the EASM (Nakagawa *et al.*, 2006; Chowdary *et al.*, 2019). During these months the area receives large quantities of precipitation during the northward propagation of the EASM front, which usually reaches the catchment in June and delivers water derived from the Pacific Ocean, Philippine Sea and East China Sea (Nakagawa *et al.*, 2006; Scholaut *et al.*, 2014). The region also receives a very large quantity of East Asian Winter Monsoon (EAWM) precipitation (mixed snowfall and rainfall) between December and February each year (Nakagawa *et al.*, 2012). The strong seasonality of precipitation delivered to the catchment means that both East Asian Monsoon modes are detectable in isolation when sampling is undertaken on seasonal timescales (Rex *et al.*, 2024; Chapter 2).

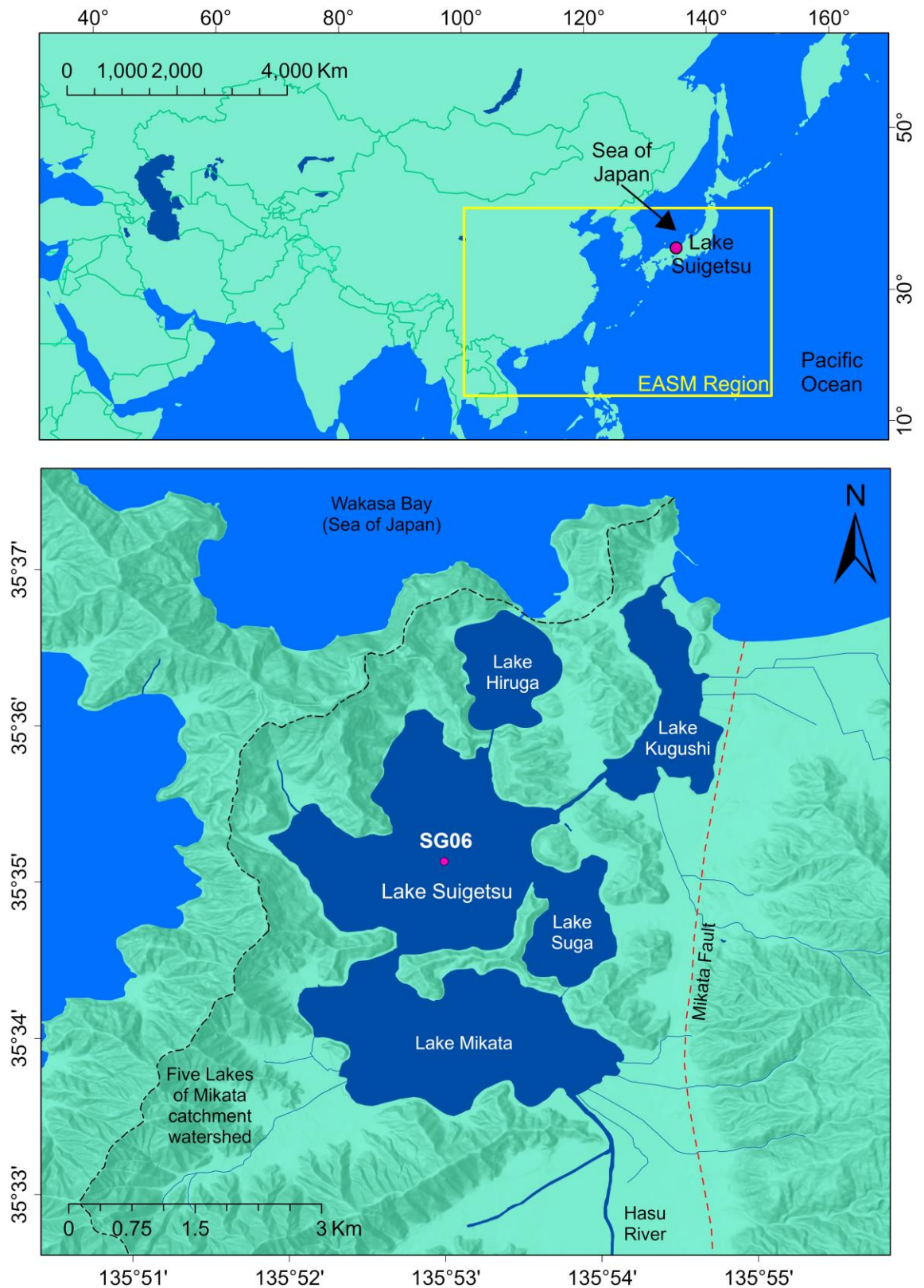


**Figure 4.2** The location of Lake Suigetsu and the Five Lakes of Mikata. The upper panel shows the position of Lake Suigetsu within the EASM region. The lower panel shows the modern-day lake configuration relative to the Mikata Fault, the Hasu River and the Sea of Japan. The catchment watershed is also indicated. Basemap is a custom Light Grey Canvas with World Hillshade from Esri (2023f; 2023g) (scale 1:66,623,747 (upper panel), 1:43,517 (lower panel)).

A series of deep coring campaigns across the past 30 years have excavated materials from below the lake to generate a world-leading palaeoenvironmental archive which spans >98 m of composite depth (from the present day to in excess of 200 ka BP; Nakagawa *et al.*, 2012; McLean *et al.*, 2018). As such, the Lake Suigetsu sediment cores are a rare example of a well preserved, continuous sediment record which extends to the penultimate glacial period (Nakagawa *et al.*, 2012; Rex *et al.*, 2022 (Chapter 5)). Indeed, the upper ~45 m form the longest continuously varved record from the Quaternary (Schlolut *et al.*, 2012; Schlolut *et al.*, 2018). The composition and sedimentology of the cores varies through time, driven by the evolution of the Five Lakes of Mikata system from its origin to the present-day configuration. This process was principally driven by subsidence of the western side of the Mikata Fault (which lies <2 km to the east of the lakes) creating accommodation space for the lakes and causing lake deepening with time (Suzuki *et al.*, 2016). The area was perhaps at its most dynamic during TII; the area shifted between fluvial and shallow water environments during MIS 6 (Nakagawa *et al.*, 2012; Rex *et al.*, 2022 (Chapter 5)), before evolving into a lake system. As such, the oldest sediments from Lake Suigetsu are principally a mixture of peats and clays (the latter sometimes finely laminated; Francke *et al.*, in prep). By MIS 5e, the area was an established lake system, which became saline during the Eemian global sea level highstand due to saltwater incursions from the Sea of Japan, as evidenced by the presence of brackish-tolerant diatom species (Saito-Kato *et al.*, in prep; Nakagawa *et al.*, 2021). Sediments from this interval are finely laminated and it is inferred from this that the water column was sufficiently deep to prevent turbation by surface winds (and possibly had anoxic bottom waters, which hindered bioturbation).

## 4.6 Materials and Methods

### 4.6.1 Core Materials

Materials for this study were obtained from the 73.2 m Lake Suigetsu “SG06” core (Figure 4.2), extracted from the centre of Lake Suigetsu as overlapping core sections from four parallel boreholes (Nakagawa *et al.*, 2012). Alignment of the core sections was conducted using visible marker horizons to create a composite master core. Chronological control for the younger part of the core (upper ~40 m

of composite depth; ~50 ka BP to the present day) is provided by >800 radiocarbon dates, thin section microscopic varve counting and geochemically identified volcanic tephra layers (Bronk Ramsey *et al.*, 2020; Staff *et al.*, in prep). However, the older part of the core (from ~40 – 73 m composite depth) is beyond the limit of the radiocarbon dating technique and contains only discontinuous varved sections (to ~45 m composite depth), and hence alternative chronological techniques must be used to produce an extension of this age depth model. The most recent iteration of this extension (provided by A. Francke; Francke *et al.*, in prep) aligns the relative abundance of *Cryptomeria* pollen in SG06 to the same quantity in MD01–2421, a marine core from offshore Japan in the Pacific Ocean (Oba *et al.*, 2006). This process was supplemented by cross-archive alignment of the Aso–4 tephra ( $86.4 \pm 1.1$  Ar–Ar ka BP) as an absolute chronological tie point (Albert *et al.*, 2019). The oxygen isotope stratigraphy of MD01–2421 was updated as part of this procedure by alignment to the regional benthic isotope stack for the Pacific (Lisiecki and Stern, 2016). The ages presented in this study are given in thousand years before AD 1950 (“ka BP”) because the complete (i.e., combined radiocarbon and non-radiocarbon) Suigetsu core chronology has a datum at AD 1950. This iteration of the chronology indicates that the oldest sediments within the SG06 core were deposited ~146 ka BP (i.e., MIS 6). The age–depth model of MD01–2421 is aligned to other global palaeoclimate archives (e.g., the Greenland ice cores and Chinese speleothems) via the Pacific regional benthic isotope stack (Lisiecki and Stern, 2016).

Sediment was extracted from longitudinally cut core sections as ~58-year ( $n = 56$ ) or ~112-year ( $n = 4$ ) contiguous (continuous adjacent) subsamples spanning  $125.23 \pm 2.26$  to  $132.62 \pm 2.20$  ka BP (6389.5 to 6908.2 cm composite depth (ver. 06 April 2020)). This interval was selected to bracket the period of most rapid EASM change during TII (~128 ka BP) as evidenced by the Chinese speleothems (e.g., Jiang *et al.*, 2005; Cheng *et al.*, 2006), as well as extremes in preliminary, low-resolution pollen-derived temperature from the Suigetsu cores. Core expansion during storage was accounted for by linear interpolation (as in Chapter 3). Care was taken to remove the outer ~3 mm of sediment before subsampling in order to eliminate the possibility of cross-contamination by modern organic compounds from handling during core extraction (Chapter 3). In

the same vein, instruments and surfaces were cleaned with ethanol prior to and during use. Sample wet weights ranged from 5.4 – 13.6 g. To prevent skewing of the results to large instantaneous events, event layers (such as tephra and flood materials) were removed where possible prior to subsampling. It is important to note that because the target sediments were varied in type and colour, some event layers may have been overlooked. However, this cautious approach is preferable to a more stringent one, which could result in accidental omission of non-event material. Plant macrofossils were also removed following the same logic (i.e., that a large amount of material from a single organic fossil could skew the analytical results of that sample). Whilst the sediments extracted as part of this process were well preserved, it is possible that bioturbation and discontinuous deposition was undetected on account of the lack of consistent sedimentary substructure (i.e., varving).

#### **4.6.2 Sample Preparation**

Samples were prepared for analysis (in batches of 10 samples, each with a procedural blank) at the University of Glasgow following an amended version of the preparation methodology presented in Chapter 3. A Total Neutral Fraction (TNF) and a Total Acid Fraction (TAF) were extracted from each freeze-dried sediment sample by an Accelerated Solvent Extractor using dichloromethane and methanol (9:1, v:v) (to yield the Total Lipid Extract), followed by solid phase extraction through a LC-NH<sub>2</sub> silica gel column to separate the TNF and TAF. A dichloromethane:propan-2-ol solution (1:1, v:v) and 4 % acetic acid in diethyl ether were used to elute the TNF and TAF, respectively. The TNF was further separated through a silica gel column; the first neutral fraction (N1, containing aliphatic hydrocarbons), was eluted with hexane, and the other neutral fractions (N2: ketones, esters and aromatics, N3: alcohols, N4: polar compounds) sequentially eluted with dichloromethane, ethyl acetate:hexane (1:3, v:v) and methanol. The TAF fraction was derivatised in sealed vials using 12 % boron trifluoride in methanol at 70 °C for 1 hour to convert any n-alkanoic acids to fatty acid methyl esters (FAMES). A final clean-up was performed using a silica gel column to purify the FAMES; non-FAME compounds (A1 fraction) were eluted with hexane and FAME compounds (A2 fraction) were eluted with dichloromethane. The N1 and A2 fractions were prepared for analysis by dissolving in hexane, and the other fractions archived.

### 4.6.3 GC–MS and GC–FID Analysis

Gas Chromatography – Mass Spectrometry (GC–MS) analysis was performed for compound identification at the University of Glasgow using an Agilent 7890B Gas Chromatogram connected to a 5977A mass spectrometer detector with an electron impact ionisation source. Analysis of 10 representative samples confirmed that the N1 and A2 fractions were dominantly comprised of n–alkanes and n–alkanoic acids (as FAMEs), respectively (Figure 4.3; Figure 4.4). N–alkane and FAME concentrations were then determined using an Agilent 7890B Gas Chromatogram fitted with a flame ionisation detector (GC–FID). For full GC–MS and GC–FID instrument settings, see Chapter 3. The A2 fraction was analysed in 200  $\mu\text{L}$  of hexane, and the N1 fraction in 100  $\mu\text{L}$  to 200  $\mu\text{L}$ , depending on yield. For each sample a volume of 1  $\mu\text{L}$  was injected. Peak areas of the  $\text{C}_{15}$  –  $\text{C}_{33}$  n–alkanes and  $\text{C}_{14}$  –  $\text{C}_{32}$  n–alkanoic acids were converted to concentrations via a set of external calibrations using a standard mix of eleven n–alkanes (following Chapter 3) at three concentrations (2.5  $\mu\text{g}/\text{mL}$ , 5  $\mu\text{g}/\text{mL}$  and 10  $\mu\text{g}/\text{mL}$ ). Concentrations for peaks with a 0 – 25 minute, 25 – 35 minute and 35 – 60 minute retention time were respectively calculated from calibrations based on the  $\text{C}_{16}$ ,  $\text{C}_{29}$  and the  $\text{C}_{39}$  homologues in the standard ( $R^2 > 0.99$ ). Finally, homologue concentrations were normalised to dry sediment mass. The concentration of the  $\text{C}_{22}$  n–alkanoic acid was not measured for all samples due to the presence of phthalate compound peaks at a similar retention time (~34.5 minutes) to this homologue in 38 % of samples (Figure 4.3).

The n–alkane concentrations were then used to quantify a range of indices of environmental change. These were the short–chained Carbon Preference Index ( $\text{CPI}_{15-20}$ ; Equation 4.1), long–chained Carbon Preference Index ( $\text{CPI}_{27-32}$ ; Equation 4.2), Terrestrial to Aquatic Ratio (TAR; Equation 4.3) and the Average Chain Length ( $\text{ACL}_{15-33}$ ; Equation 4.4).  $\text{CPI}_{15-20}$  and  $\text{CPI}_{27-32}$  are indicators of both source and preservation, whereas TAR and  $\text{ACL}_{15-33}$  can be used to distinguish between terrestrial and aquatic sources (Zhang *et al.*, 2020), and hence these indices can be used to reconstruct lacustrine development. The n–alkane concentrations were used instead of the n–alkanoic acid concentrations, despite the latter being higher, because n–alkanoic acids more easily degrade (Meyers and Ishiwatari, 1993) and hence these indices (particularly the CPI values) could be affected by preservation as well as environmental changes.

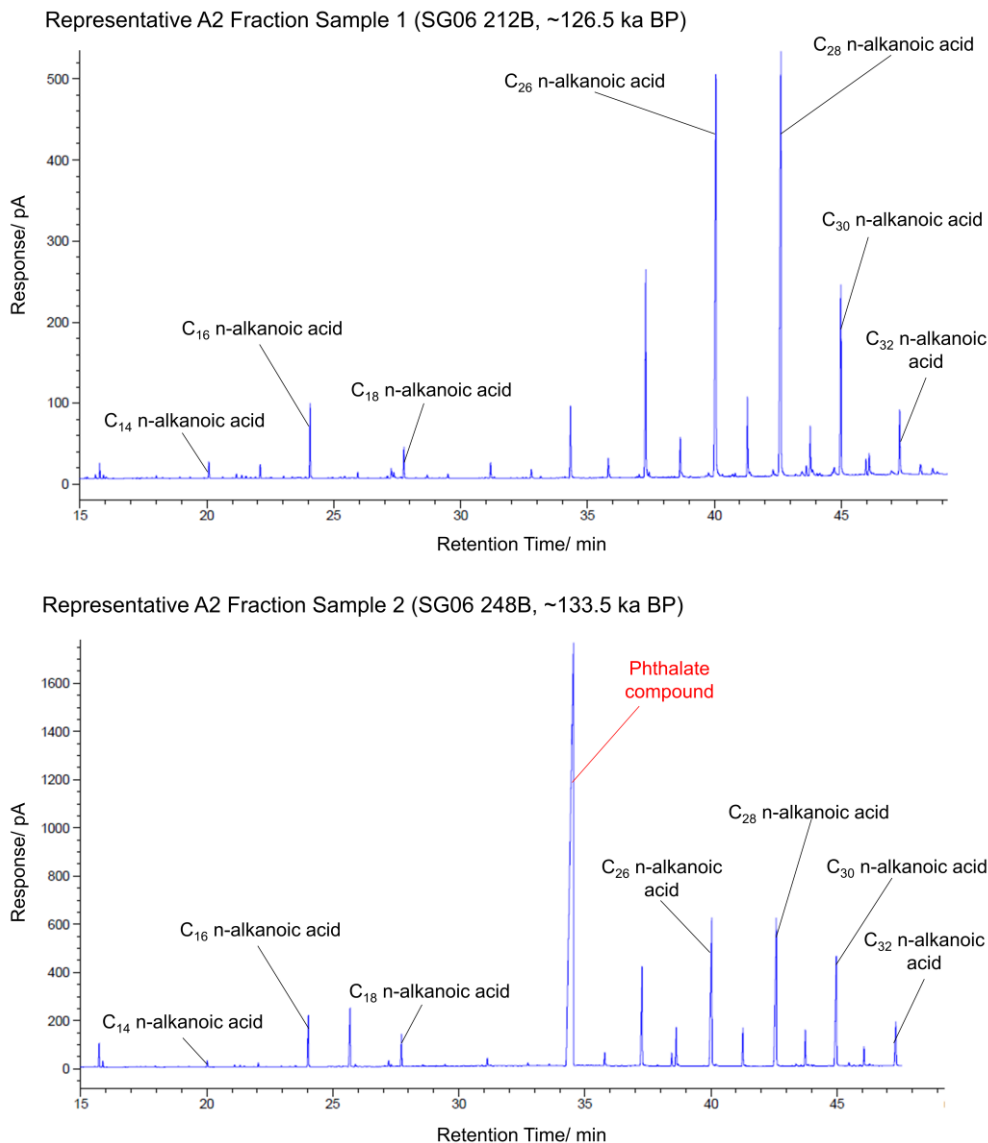


**Figure 4.3 Example GC-FID A2 fraction chromatograms.** Key homologue peaks are indicated. Phthalate compound peaks (lower panel) were detected in some samples but did not interfere with peaks of interest.

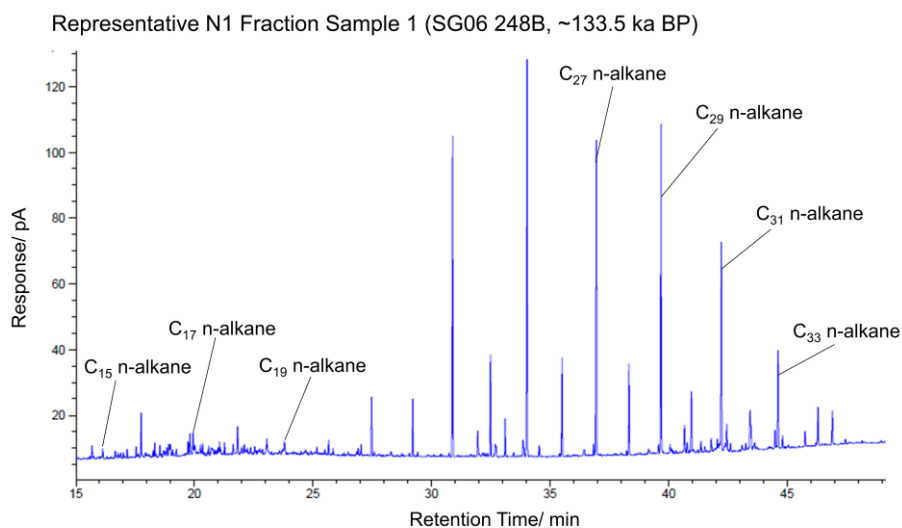


**Figure 4.4 Example GC-FID N1 fraction chromatogram.** Key homologue peaks are indicated.

$$\text{CPI}_{15-20} = \frac{([\text{C}_{15}] + [\text{C}_{17}] + [\text{C}_{19}])}{([\text{C}_{16}] + [\text{C}_{18}] + [\text{C}_{20}])}$$

**Equation 4.1** (Zhang *et al.*, 2020)

$$\text{CPI}_{27-32} = \frac{([\text{C}_{27}] + [\text{C}_{29}] + [\text{C}_{31}])}{([\text{C}_{28}] + [\text{C}_{30}] + [\text{C}_{32}])}$$

**Equation 4.2**

$$\text{TAR} = \frac{([\text{C}_{29}] + [\text{C}_{31}] + [\text{C}_{33}])}{([\text{C}_{15}] + [\text{C}_{17}] + [\text{C}_{19}])}$$

**Equation 4.3** (Zhang *et al.*, 2020)

$$\text{ACL}_{15-33} = \frac{(15[\text{C}_{15}] + 17[\text{C}_{17}] + 19[\text{C}_{19}] + 21[\text{C}_{21}] + 23[\text{C}_{23}] + 25[\text{C}_{25}] + 27[\text{C}_{27}] + 29[\text{C}_{29}] + 31[\text{C}_{31}] + 33[\text{C}_{33}])}{([\text{C}_{15}] + [\text{C}_{17}] + [\text{C}_{19}] + [\text{C}_{21}] + [\text{C}_{23}] + [\text{C}_{25}] + [\text{C}_{27}] + [\text{C}_{29}] + [\text{C}_{31}] + [\text{C}_{33}])}$$

**Equation 4.4** (Zhang *et al.*, 2020)

#### 4.6.4 GC-IRMS Analysis

The compound-specific hydrogen isotope ( $\delta^2\text{H}$ ) composition of the  $\text{C}_{26}$ ,  $\text{C}_{28}$  and  $\text{C}_{30}$  n-alkanoic acids as FAMEs ( $\delta^2\text{H}_{\text{C}_{26}\text{acid}}$ ,  $\delta^2\text{H}_{\text{C}_{28}\text{acid}}$  and  $\delta^2\text{H}_{\text{C}_{30}\text{acid}}$ ) were measured at Hokkaido University (by O. Seki). The n-alkanoic acids were selected for this purpose to be consistent with previous analysis on the Suigetsu cores (Chapter 3) and because  $\delta^2\text{H}$  analysis of the n-alkanes was prohibited by low homologue concentrations. Similarly, the aquatic n-alkanoic acid homologues were also too low in concentration to analyse. Section 4.7.4 considers the effect of n-alkanoic acid degradation on the  $\delta^2\text{H}_{\text{acid}}$  values. Analysis was performed using an Agilent GC7890 gas chromatography (GC) system connected to an Elementar Isoprime vision isotope ratio mass spectrometer (IRMS) via a ceramic tube thermal conversion furnace. The GC employed a DB5 capillary column (60 m length, 0.25 mm internal diameter, 0.25  $\mu\text{m}$  film thickness). The helium carrier gas flow rate was 1.1 mL min<sup>-1</sup>. Each A2 fraction was dissolved in 25 – 330  $\mu\text{L}$  of hexane and 0.50 – 3.90  $\mu\text{L}$  injected (depending on FAME yield). The inlet was kept at 350 °C and the following oven programme used: the oven was held for 4 minutes at 50 °C and raised to 120 °C at 20 °C min<sup>-1</sup>, then increased to 310 °C at 5 °C min<sup>-1</sup> and held for 30 minutes. The furnace temperature was set to 1450 °C with an interface temperature of 350 °C. In samples containing a contaminant phthalate peak, flow was redirected to prevent entry of this contaminant into the IRMS. Subsamples were measured in duplicate and the  $\delta^2\text{H}$  values of each homologue

were calculated relative to a calibrated reference H<sub>2</sub> gas. These values were then converted to the VSMOW scale via a calibration to measurements of the standard n-alkane mixture A6 from Indiana University (containing C<sub>16</sub> to C<sub>30</sub> n-alkanes). All hydrogen isotope data are expressed in standard delta (δ) notation in per mille (‰) deviations relative to VSMOW. Analytical accuracy of the standard measurements was within 5 ‰. The H<sub>3</sub><sup>+</sup> correction factor ranged from 4 to 5. Values were corrected for the methylation process using a mass balance scheme (Chivall *et al.*, 2012) to convert the measured FAME δ<sup>2</sup>H values to n-alkanoic acid values (excluding the exchangeable hydrogen on the carboxylic acid group). GC-IRMS measurements of (Z)-hexadec-9-enoic acid (δ<sup>2</sup>H = -154.02 ‰) and methyl (Z)-hexadec-9-enoate (δ<sup>2</sup>H = -143.13 ‰) were made at the University of Glasgow to calculate the δ<sup>2</sup>H value of a single methanol-derived methyl hydrogen (δ<sup>2</sup>H = -37.86 ‰), which was used in the mass balance calculations. Low concentrations affected the repeatability of the measurements of δ<sup>2</sup>H<sub>C26acid</sub>, δ<sup>2</sup>H<sub>C28acid</sub> or δ<sup>2</sup>H<sub>C30acid</sub> in 11 samples; these were therefore excluded from the final dataset. In 5 samples it was not possible to accurately measure δ<sup>2</sup>H<sub>acid</sub> for any of the three homologues. The mean precision of the δ<sup>2</sup>H<sub>acid</sub> measurements was ± 2.5 ‰ (1σ range). The final dataset comprises 44 datapoints for the δ<sup>2</sup>H<sub>C26acid</sub>, 49 for δ<sup>2</sup>H<sub>C28acid</sub> and 33 for δ<sup>2</sup>H<sub>C30acid</sub>.

## 4.7 Results

### 4.7.1 Lipid Concentration and Index Variations

Down-core fluctuations of measured n-alkane and n-alkanoic acid concentrations and n-alkane indices provide information on the evolution of the Lake Suigetsu catchment across TII and constrain the most major shifts in catchment development to between -131.0 ka BP and -129.8 ka BP (Figure 4.5). These observations support existing TOC/TN and δ<sup>13</sup>C<sub>org</sub> (analysed by A. Francke and J.J. Tyler; Francke *et al.*, in prep) and diatom taxon variations (analysed by M. Saito-Kato; Saito-Kato *et al.*, in prep) across the interval. Terrestrial (long-chained, ≥C<sub>26</sub>) n-alkane and n-alkanoic acid homologue concentrations were generally greater and more variable prior to 129.7 ka BP (<22.0 μg g<sup>-1</sup> for the n-alkanes, <58.0 μg g<sup>-1</sup> for the n-alkanoic acids); after this, the concentrations of both were low and stable (<1.1 μg g<sup>-1</sup> for the n-alkanes, <20.4 μg g<sup>-1</sup> for the n-alkanoic acids). N-alkanoic acid concentrations were generally

greater than the concentration of the n-alkanes for similar chain lengths (e.g., a mean concentration of  $6.7 \mu\text{g g}^{-1}$  for the  $\text{C}_{30}$  n-alkanoic acids, and  $2.6 \mu\text{g g}^{-1}$  for the  $\text{C}_{29}$  n-alkanes), and the concentrations of the  $\text{C}_{26}$  and  $\text{C}_{28}$  n-alkanoic acid homologues were consistently the largest. The concentration of the terrestrial n-alkane homologues decreased abruptly at 130.9 ka BP, whereas the concentration of the terrestrial n-alkanoic acid homologues decreased later at 129.7 ka BP. Only very small fluctuations (on the order of  $\sim 10 \mu\text{g g}^{-1}$ ), limited to the terrestrial n-alkanoic acid concentrations, were observed later in the profile (127.2 ka BP onwards). Aquatic (short-chained,  $\leq \text{C}_{19}$ ) n-alkane concentrations were generally very low; values were slightly elevated prior to 131.0 ka BP, particularly the  $\text{C}_{19}$  homologue, however the difference between these earlier values and the remainder of the profile was  $< 1.8 \mu\text{g g}^{-1}$  (i.e., negligible). The aquatic n-alkanoic acid concentrations were more distinct by comparison; whilst the concentration of the  $\text{C}_{14}$  n-alkanoic acid changed minimally across the study interval, there were peaks with values up to  $\sim 8 \mu\text{g g}^{-1}$  larger than the interval mean  $\text{C}_{16}$  and  $\text{C}_{18}$  n-alkanoic acid concentration between  $\sim 130$  and 128 ka BP.

The  $\text{CPI}_{15-20}$  values ranged from 0.39 to 2.18 with a mean of 0.88, representing very minimal fluctuations with time. Contrastingly, the  $\text{CPI}_{27-32}$  values were more variable, but exhibited consistently higher values (3.14 to 9.39, mean 5.19). The greatest  $\text{CPI}_{27-32}$  values were observed prior to 131.5 ka BP and post-127.0 ka BP. The TAR increased from the start of the study interval to 130.0 ka BP (reaching a maximum of 28.0), before rapidly decreasing over a 300-year interval and subsequently fluctuating about a mean of 8.2 between 129.7 and 125.2 ka BP. Across the entire interval, the mean  $\text{ACL}_{15-33}$  was 27.0, oscillating minimally from 132.7 to 127.2 ka BP before decreasing slightly and exhibiting greater variability to 125.2 ka BP. The bulk TOC/TN ratio and  $\delta^{13}\text{C}_{\text{org}}$  displayed inverse behaviour, with the former exhibiting higher values ( $> 20$ ) prior to 131.0 ka BP and decreasing across a 1.2 ka interval to lower values ( $\sim 10$ ), and the latter exhibiting lower values ( $-30$  to  $-34 \text{‰}$ ) before increasing to a mean of 27 ‰ (Francke *et al.*, in prep). Incursions of (brackish-tolerant) *Cyclotella spp.* occurred at 129.7, 127.5, 126.1 and 125.6 ka BP, coinciding with increases in diatom frustule concentration (Saito-Kato *et al.*, in prep).

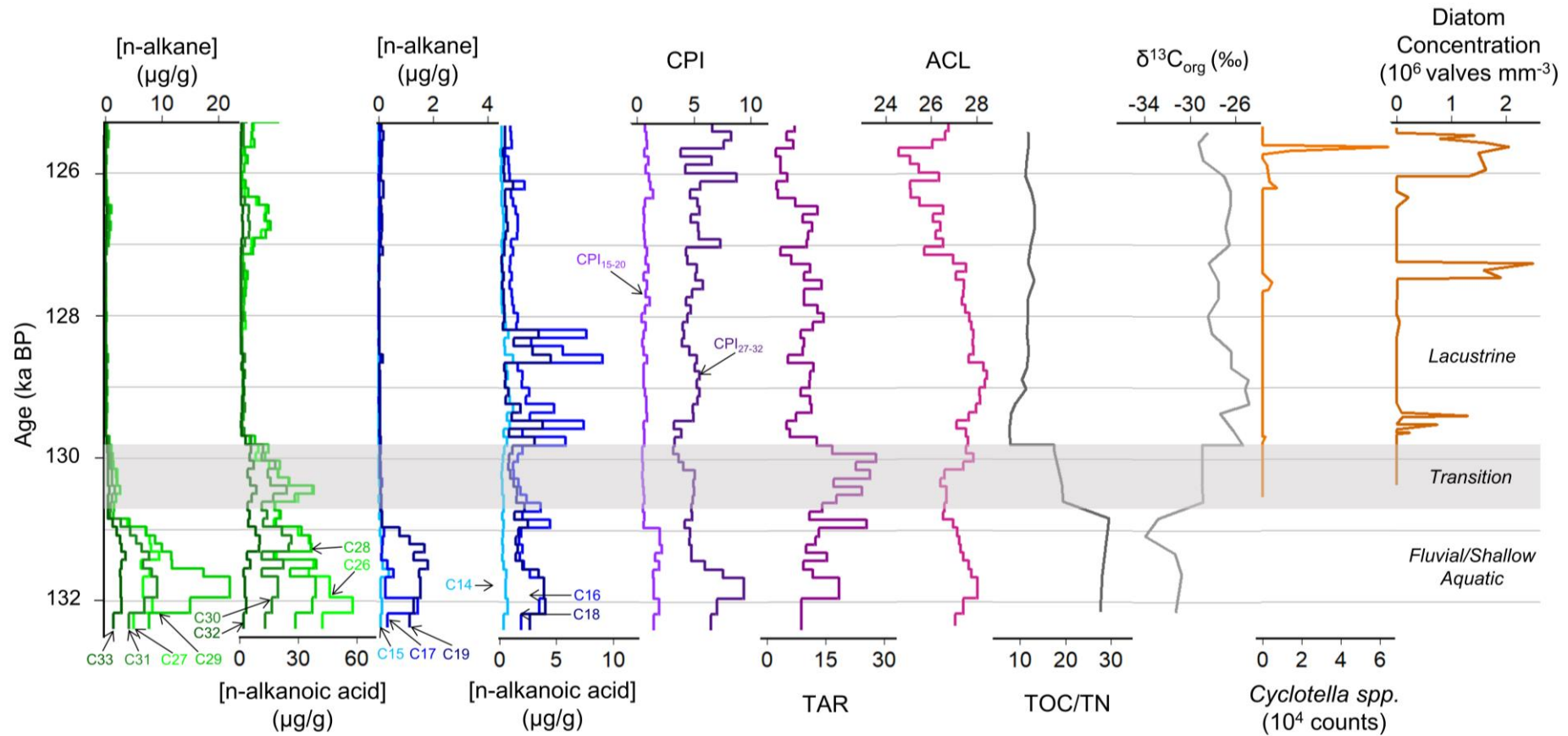


**Figure 4.5 Evidence for catchment evolution at Lake Suigetsu during Glacial Termination II.** Panels show mass-normalised n-alkane and n-alkanoic acid concentrations of key terrestrial (green) and aquatic (blue) chain lengths, short- and long-chained n-alkane Carbon Preference Indices (CPI), n-alkane Terrestrial to Aquatic Ratio (TAR), n-alkane Average Chain Length (ACL<sub>15-33</sub>), ratio of Total Organic Carbon to Total Nitrogen (TOC/TN; provided by A. Francke and J.J. Tyler; Francke *et al.*, in prep), carbon isotope ratio of organic matter ( $\delta^{13}\text{C}_{\text{org}}$ ; provided by A. Francke and J.J. Tyler; Francke *et al.*, in prep), counts of brackish-tolerant *Cyclotella* spp. diatoms (provided by M. Saito-Kato; Saito-Kato *et al.*, in prep) and diatom frustule concentrations (provided by M. Saito-Kato; Saito-Kato *et al.*, in prep). See Section 1204.6.3 for concentration and index calculations. The grey horizontal bar indicates the key environmental transition based on the data.

## 4.7.2 Catchment Evolution

Our observations align with the interpretation of lake evolution presented by Francke *et al.* (in prep); prior to 131.0 ka BP, the area was dominated by a varying fluvial system interspersed with shallow water and peat bog environments, which gradually evolved into a productive lacustrine system. This process occurred over a ~1.2 ka interval. Observations prior to 131.0 ka BP (higher terrestrial n-alkane and n-alkanoic acid homologue concentrations, TAR values, TOC/TN ratios and  $\delta^{13}\text{C}_{\text{org}}$  values, and lower aquatic n-alkanoic acid homologue concentrations), further reinforced by the presence of frequent, thick peat-rich layers, are consistent with a shallow/semi-aquatic setting, with significant amounts of terrestrially-sourced organic inputs and limited aquatic productivity. Conversely, after 129.8 ka BP, our analyses indicate lower terrestrial n-alkane and n-alkanoic acid homologue concentrations, TAR values, TOC/TN ratios and  $\delta^{13}\text{C}_{\text{org}}$  values, as well as major peaks in aquatic n-alkanoic acid homologue and diatom frustule concentrations. These younger sediments are richer in clays and increasingly laminated, implying that there was an increase in aquatic influence (and greater aquatic productivity), which likely resulted from the establishment of a lacustrine system.

Interestingly, some variables exhibited gradual shifts between 131.0 and 129.8 ka BP (including the terrestrial n-alkane and n-alkanoic acid homologue concentrations), however, the changes in the aquatic n-alkanoic acid concentrations and TAR values occurred abruptly at ~129.8 ka BP, coinciding with a major decrease in the TOC/TN ratio and  $\delta^{13}\text{C}_{\text{org}}$ . This suggests that whilst terrestrial influence decreased slowly across the transition from a shallow/semi-aquatic to a lacustrine environment, aquatic productivity may have exhibited some sort of threshold behaviour because it intensified rapidly (on the order of a hundred years). This abrupt shift in aquatic productivity could be due to a water depth threshold being exceeded, likely assisted by tectonic subsidence (and an increase in precipitation, discussed in Section 4.7.5). Whilst the gradual decrease in terrestrial influence could indicate a reduction in the influence of surrounding vegetation, we instead attribute this to decreasing quantities of peat at the coring site (and hence lower TOC values post-transition). Indeed, the consistently high  $\text{CPI}_{27-32}$  and  $\text{ACL}_{15-33}$  values support the notion that terrestrial influence on the lake system after 129.8 ka BP

was still much greater than the aquatic. The dominance of the terrestrial component appears to be an intrinsic characteristic of biomarkers from the Lake Suigetsu sediment cores, consistent with observations of materials from T1 (Chapter 3). Whilst the  $CPI_{15-25}$  values were consistently low (indicative of degradation), we attribute this to very low short-chained n-alkane homologue concentrations (close to the limit of detection), rather than poor preservation (Lupien *et al.*, 2022), although this value ( $\sim 1$ ) could indicate a microorganism source (Zhang *et al.*, 2020). The  $CPI_{27-32}$  values do not suggest degradation of the long-chained n-alkane homologues because these values were much larger than 1. Instead, these values are consistent with a terrestrial source.

Whilst the initial increase in diatom frustule concentration supports the establishment of a lacustrine environment at Lake Suigetsu, diatoms were not consistently present in the core across TII; unlike T1, where diatoms were found in exceptionally high concentrations. This could indicate that the lake was only transiently suitable for diatom bloom development, or that the lake chemistry was not compatible with good diatom preservation. Slightly lower  $ACL_{15-33}$  values were observed in the latter stages of TII, when the diatom frustule concentration was higher, suggesting that aquatic productivity was greater at this time. The sudden increase in the number of *Cyclotella* spp. diatoms post-126 ka BP suggests some seawater incursion during this interval. It is estimated that Lake Suigetsu was situated a few metres above sea level for the last glacial-interglacial cycle (the lake is currently at an elevation of 0 m.a.s.l. and was  $\sim 3$  m.a.s.l. before the AD 1664 Kanbun Earthquake; Staff, 2011), making seawater incursions during a global highstand possible. Despite large quantities ( $>10,000$  counts) of *Cyclotella* spp. diatoms being observed for only  $\sim 100$  years, this likely represents a quasi-continuous occurrence, disguised by spot sampling and lower levels of diatom preservation (Saito-Kato *et al.*, in prep).

### 4.7.3 $\delta^2H_{acid}$ Variations

Profiles of  $\delta^2H_{acid}$  across TII derived from the three key terrestrial homologues ( $\delta^2H_{C26acid}$ ,  $\delta^2H_{C28acid}$  and  $\delta^2H_{C30acid}$ ) share many key features (Figure 4.6), however some differences between homologue compositions are observed. From 132.7 ka BP to 130.1 ka BP, the  $\delta^2H_{acid}$  values were variable and fluctuated on a centennial scale; during this interval the  $\delta^2H_{C30acid}$  values were often higher than

the other homologues (up to as much as  $-147\text{‰}$ , akin to later in the study period). From 130.1 to 129.2 ka BP, all of the  $\delta^2\text{H}_{\text{acid}}$  values increased (equating to a change of  $+93\text{‰}$  in  $\delta^2\text{H}_{\text{C}_{28}\text{acid}}$ ) and, for the most part, smoothly, aside from a singular, large, sub-100-year positive excursion observed in  $\delta^2\text{H}_{\text{C}_{26}\text{acid}}$  and  $\delta^2\text{H}_{\text{C}_{28}\text{acid}}$ . The  $\delta^2\text{H}_{\text{acid}}$  values then exhibited an interval of stable, intermediate values (between 129.1 and 128.7 ka BP, with a mean composition of  $-172\text{‰}$ ). Between 128.7 and 128.1 ka BP,  $\delta^2\text{H}_{\text{C}_{26}\text{acid}}$  and  $\delta^2\text{H}_{\text{C}_{28}\text{acid}}$  rapidly increased and then slowly decreased. This was an interval not constrained by many reliable measurements of  $\delta^2\text{H}_{\text{acid}}$ , however these observations are based on bracketing measurements and a measurement of  $\delta^2\text{H}_{\text{C}_{28}\text{acid}}$  mid-transition. Post-128.1 ka BP, all of the  $\delta^2\text{H}_{\text{acid}}$  values increased gradually, exhibiting some (multi-)centennial variability. The largest deviations from the overall trend in this interval were exhibited by the  $\delta^2\text{H}_{\text{C}_{26}\text{acid}}$  values, which displayed generally lower values than the  $\text{C}_{28}$  and  $\text{C}_{30}$  homologues.

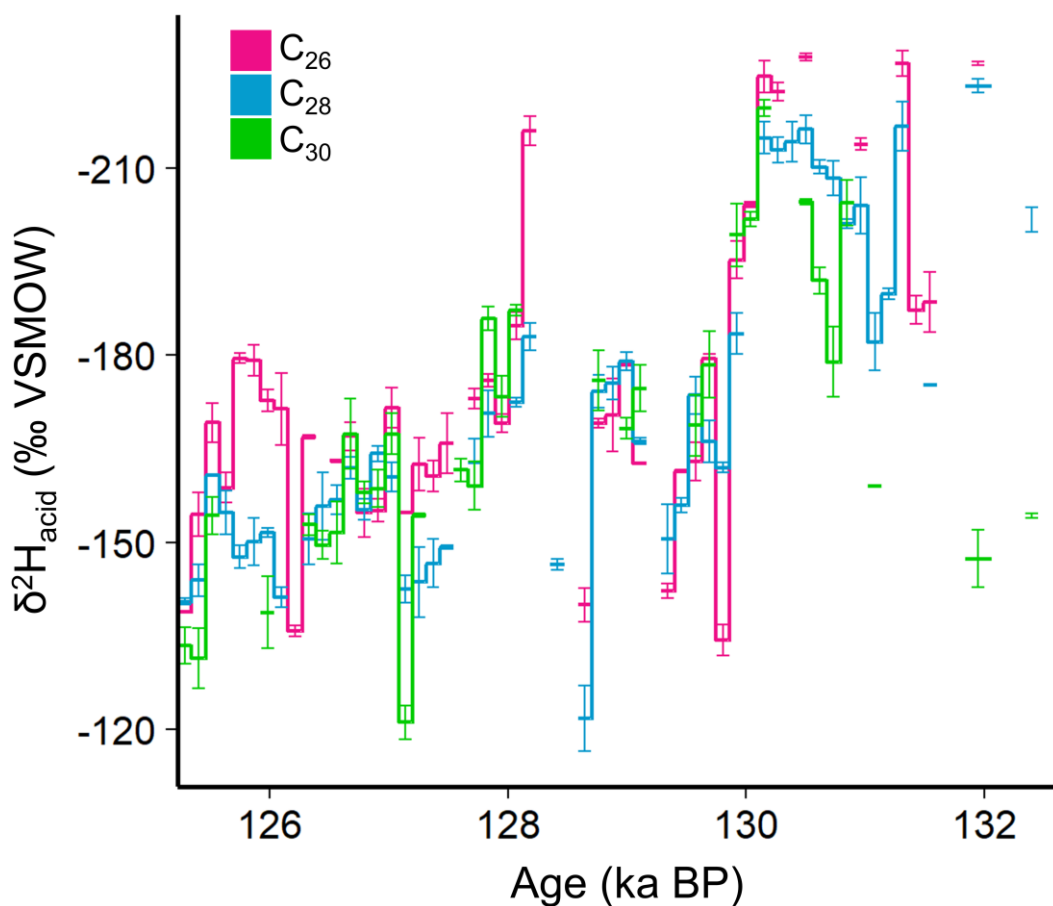


**Figure 4.6**  $\delta^2\text{H}$  derived from the  $\text{C}_{26}$ ,  $\text{C}_{28}$  and  $\text{C}_{30}$  n-alkanoic acid homologues during TII at Lake Suigetsu. Error bars show a  $1\sigma$  range. The vertical axis is shown inverted such that the values reflect increasing depletion of deuterium (i.e., a stronger EASM; see Section 4.7.4 for signal interpretation). Samples were analysed by O. Seki.

#### 4.7.4 Signal Interpretation

It is vital to carefully consider the drivers of  $\delta^2\text{H}_{\text{acid}}$  in order to make robust links between this variable and regional scale hydrological behaviours, particularly within a catchment under the influence of a highly seasonal climate regime.  $\delta^2\text{H}_{\text{acid}}$ , like the hydrogen isotope composition of other lipid biomarkers, is closely related to the  $\delta^2\text{H}$  of soil pore water, which is principally controlled by the  $\delta^2\text{H}$  of precipitation ( $\delta^2\text{H}_{\text{precipitation}}$ ) (Sachse *et al.*, 2012). It is this relationship which facilitates the use of  $\delta^2\text{H}_{\text{acid}}$  as a tracer for shifts in atmospheric circulation and vapour transport (Tierney *et al.*, 2008). Within the context of the Lake Suigetsu catchment, modern monitoring has demonstrated that extended modes of precipitation, including the EASM, dominate the delivery of freshwater (and hence water isotopes) to the area (Rex *et al.*, 2024; Chapter 2). Previous analysis of  $\delta^2\text{H}_{\text{acid}}$  from the Suigetsu cores found the most robust links between this variable and EASM behaviour were established using  $\delta^2\text{H}_{\text{C}_{30}\text{acid}}$  (Chapter 3), due to the strictly terrestrial source of the  $\text{C}_{30}$  n-alkanoic acid homologue (circumventing the influence of the catchment transit lag (Rex *et al.*, 2024; Chapter 2)) and the weighting of  $\delta^2\text{H}_{\text{C}_{30}\text{acid}}$  to summer  $\delta^2\text{H}_{\text{precipitation}}$  (because leaf wax production occurs during the summer growth season). Contrastingly,  $\delta^2\text{H}_{\text{C}_{26}\text{acid}}$  and  $\delta^2\text{H}_{\text{C}_{28}\text{acid}}$  exhibited slightly more aquatic character and hence were influenced by  $\delta^2\text{H}_{\text{precipitation}}$  from other seasons (namely the EAWM) due to the mixed seasonality of lake water during the summer growth period (Chapter 3). This highlights the importance of developing a strong understanding of proxy seasonality to facilitate signal interpretation (Kurita *et al.*, 2015; Rex *et al.*, 2024; Chapter 2). These findings align with other studies, which found that the  $\text{C}_{28}$  n-alkanoic acid homologue can be produced within the water column in some lakes (van Bree *et al.*, 2018) and that  $\delta^2\text{H}_{\text{C}_{30}\text{acid}}$  is derived only from higher plants and hence captures a purely terrestrial signal (Tierney *et al.*, 2022).

We apply the same reasoning to our analysis across TII and posit that the  $\delta^2\text{H}_{\text{C}_{30}\text{acid}}$  values from Lake Suigetsu most faithfully represent a terrestrial signal with the strongest links to EASM  $\delta^2\text{H}_{\text{precipitation}}$ . Furthermore, the solely terrestrial source of  $\delta^2\text{H}_{\text{C}_{30}\text{acid}}$  makes it possible to assume that the aforementioned catchment variability and lake development had a negligible effect on this variable. Hence, we attribute the differences observed between the  $\delta^2\text{H}_{\text{C}_{30}\text{acid}}$  values and those derived from the shorter chained homologues to aquatic

influences on the latter (either lacustrine development or mixed seasonality, or a combination of these effects). Hence, subsequent analysis focusses on the  $\delta^2\text{H}_{\text{C}_{30}\text{acid}}$  values. The  $\text{C}_{30}$  homologue was generally found to be lower in concentration than the  $\text{C}_{26}$  and  $\text{C}_{28}$  homologues, and hence produced fewer data points during  $\delta^2\text{H}_{\text{acid}}$  analysis, however clear patterns could nevertheless be observed in  $\delta^2\text{H}_{\text{C}_{30}\text{acid}}$  (Figure 4.7). Use of the  $\delta^2\text{H}_{\text{C}_{30}\text{acid}}$  values was not prohibited by degradation; we calculated the  $\text{CPI}_{27-32}$  for each sample using the n-alkanoic acid concentrations, rearranging Equation 4.2 for the even-over-odd preference of n-alkanoic acids, and found that the resulting values indicated good preservation of the  $\text{C}_{30}$  n-alkanoic acid (mean 6.9; minimum 2.8). Additionally, least-squares regression analysis of these n-alkanoic acid  $\text{CPI}_{27-32}$  values and  $\delta^2\text{H}_{\text{C}_{30}\text{acid}}$  values displayed a weak correlation ( $R^2 = 0.27$ ), indicating that even the small variations in the degradation of the n-alkanoic acids did not alter the  $\delta^2\text{H}_{\text{C}_{30}\text{acid}}$  values (after Lupien *et al.*, 2022).

Despite the evidence to support a strong link between  $\delta^2\text{H}_{\text{C}_{30}\text{acid}}$  and EASM  $\delta^2\text{H}_{\text{precipitation}}$  at Lake Suigetsu, it is also important to consider the influence of local processes (most crucially temperature and vegetation change) on  $\delta^2\text{H}_{\text{C}_{30}\text{acid}}$  (Holtvoeth *et al.*, 2019). An assessment of the impact of these processes can be made by using preliminary complementary pollen analyses and pollen-derived temperature reconstructions from the cores across TII (albeit at a lower resolution than the  $\delta^2\text{H}_{\text{C}_{30}\text{acid}}$  analyses), which can assist in determining the magnitude of these alternative influences (analysed by T. Nakagawa). These pollen analyses were derived following the methods presented by Nakagawa *et al.* (2021). The impact of vegetative change, particularly the relative amounts of C3 versus C4 plants (Tierney *et al.*, 2010), was negligible, because the dominant species across the TII interval were trees with similar biosynthetic pathways (including *Alnus*, *Carpinus*, *Cryptomeria*, *Fagus*, *Quercus* and *Tsuga*, all of which are classified as C3 vegetation). Conversely, the impact of temperature on  $\delta^2\text{H}_{\text{C}_{30}\text{acid}}$  is more difficult to define. The pollen-reconstructed mean temperature of the warmest month (MTWA) displays some similarities to the  $\delta^2\text{H}_{\text{acid}}$  profiles; it increased from 131.6 ka BP to 129.8 ka BP, decreased to 128.0 ka BP, then increased to a maximum at 126.4 ka BP (Figure 4.7). This trend broadly follows that of  $\delta^2\text{H}_{\text{C}_{30}\text{acid}}$  in the earlier stages of TII (pre-130.0 ka BP), before decoupling. During TI, higher resolution pollen-derived temperature

analyses allowed for a confident assertion that climate (and hence vegetation change) were not major drivers of  $\delta^2\text{H}_{\text{C30acid}}$  (Chapter 3). Whilst ground-truthing these observations in a more intensely studied climatic interval provides strong evidence that the effect of temperature on  $\delta^2\text{H}_{\text{C30acid}}$  was also limited during TII, it is important to note that the magnitude of change observed in  $\delta^2\text{H}_{\text{C30acid}}$  was greater in TII than in TI (particularly in the pre-130.0 ka BP period), and that a qualitative relationship to temperature during this period is apparent (albeit temporally constrained). This suggests that, whilst other drivers are possible, there could be a temperature component to this signal. Whilst some studies have attributed this to the effect of regional temperature on  $\delta^2\text{H}_{\text{precipitation}}$  (e.g., Thomas *et al.*, 2014), this could also be a local effect (via greater soil evaporation and transpiration within the catchment; Sachse *et al.*, 2012). In light of this, it is possible that a combination of decreasing  $\delta^2\text{H}_{\text{precipitation}}$  and rising temperatures contributed to the initial decrease in  $\delta^2\text{H}_{\text{C30acid}}$  prior to 130.0 ka BP. However, a temperature increase alone cannot account for the 72.3 ‰ decrease (maximum to minimum difference) in  $\delta^2\text{H}_{\text{C30acid}}$  between the start of the record and 130.0 ka BP; the 6.7 °C temperature increase ( $\Delta T$ ) indicated by the pollen climate reconstruction would yield only a ~14 ‰ change in  $\delta^2\text{H}_{\text{C30acid}}$ , using the  $\Delta T$ - $\Delta\delta^{18}\text{O}$  relationship presented by Rozanski *et al.* (1993) ( $\Delta\delta^{18}\text{O} = 0.31\Delta T - 0.33$ ) and the global meteoric water line relationship between  $\Delta\delta^{18}\text{O}$  and  $\Delta\delta^2\text{H}$  ( $\Delta\delta^2\text{H}/\Delta\delta^{18}\text{O} = 8$ ). Hence, there must also be a change in  $\delta^2\text{H}_{\text{precipitation}}$  during this interval. Additionally, the relationship between  $\delta^2\text{H}_{\text{C30acid}}$  and temperature breaks down post-130.0 ka BP, suggesting that for the remainder of TII, the  $\delta^2\text{H}_{\text{C30acid}}$  values were dominantly driven by  $\delta^2\text{H}_{\text{precipitation}}$  alone.

#### 4.7.5 EASM Evolution

The EASM system is driven by a series of interconnected climate features, centred around the northwards propagation of the EASM front, which is propagated by the position and intensification of the Western Pacific Subtropical High (Kurita *et al.*, 2015; Xu *et al.*, 2020). It follows that modifications to this scheme which alter EASM strength are the dominant controls on  $\delta^2\text{H}_{\text{C30acid}}$  across much of TII, with an additional temperature component in the pre-130 ka BP interval. We propose that EASM  $\delta^2\text{H}_{\text{precipitation}}$  is controlled by a combination of source composition and transport processes during TII, as during TI, and that a “stronger” EASM would have lower  $\delta^2\text{H}_{\text{precipitation}}$  (and hence  $\delta^2\text{H}_{\text{C30acid}}$ ) values due

to stronger winds and greater quantities of precipitation integrated across the transport pathway (as in Chapter 3). Kurita *et al.* (2015) found a strong inverse relationship between contemporary EASM strength and  $\delta^2\text{H}_{\text{precipitation}}$  in Tokyo, Japan, which supports the notion that  $\delta^2\text{H}_{\text{C}_{30}\text{acid}}$  is related to EASM evolution.

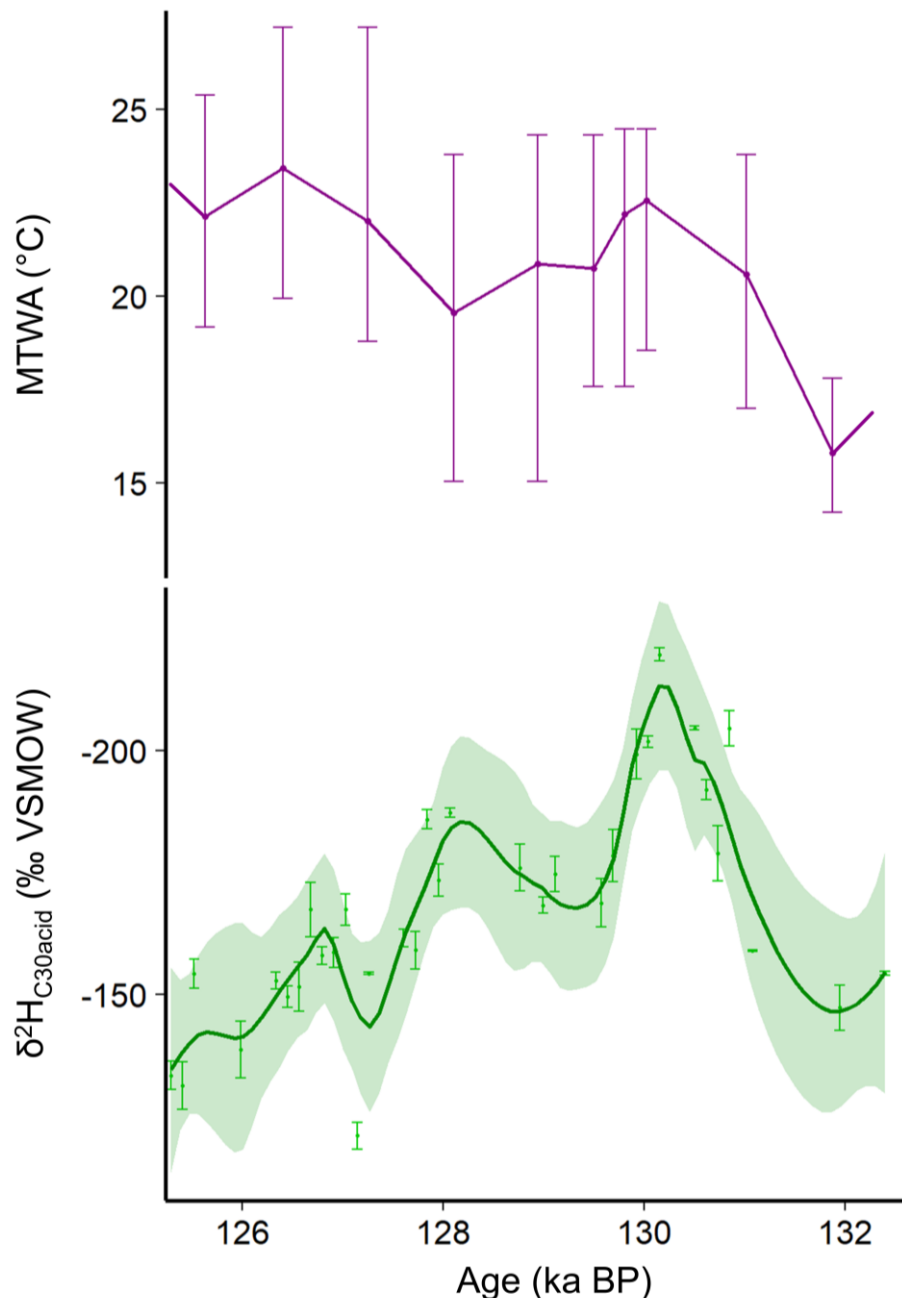


**Figure 4.7  $\delta^2\text{H}_{\text{C}_{30}\text{acid}}$  and pollen-derived temperature evolution during TII at Lake Suigetsu.** The lower panel shows the evolution of  $\delta^2\text{H}_{\text{acid}}$  derived from the  $\text{C}_{30}$  n-alkanoic acid homologue (samples were analysed by O. Seki). Individual data points with  $1\sigma$  error bars are shown, overlying a loess-smoothed trendline (span = 0.25) with  $1\sigma$  confidence bands. The vertical axis is shown inverted such that the values reflect increasing depletion of deuterium (i.e., a stronger EASM; see Section 4.7.4 for signal interpretation). The upper panel shows the pollen-derived mean temperature of the warmest month (MTWA) with error bars showing minimum/maximum values inferred for the same interval (analysed by T. Nakagawa). Timescales are equivalent because both sets of analyses were performed on the SG06 core.

Based on these assertions, our record supports EASM strengthening from the start of TII in the penultimate glacial period to ~130 ka BP (alongside an increase in temperature), before rapid weakening to 129.5 ka BP. There is also some evidence for subsequent strengthening to 129.0 ka BP, albeit more gradual than indicated by  $\delta^2\text{H}_{\text{C}_{26}\text{acid}}$  and  $\delta^2\text{H}_{\text{C}_{28}\text{acid}}$ , followed by continued weakening into the last interglacial period. Interestingly, the most significant period of EASM strengthening during TII occurred immediately prior to, and during, the transition from shallow/semi-aquatic to lacustrine conditions at the catchment between 131.0 and 129.8 ka BP. As mentioned above, it is unlikely that this catchment evolution affected  $\delta^2\text{H}_{\text{C}_{30}\text{acid}}$ , which is derived from terrestrial plants, effectively decoupling this variable from lake behaviours. However, it is possible that this increase in EASM strength also increased freshwater delivery to the area, contributing to lake system formation, alongside tectonic subsidence.

## 4.8 Discussion

### 4.8.1 A Note on Chronological Alignment

Our results support an initial increase in EASM strength in Japan during MIS 6, which reached a maximum at ~130 ka BP, followed by overall weakening with some evidence for submillennial-scale variability (weakening to 129.5 ka BP, strengthening to 129.0 ka BP and then weakening into MIS 5e). Comparing this behaviour to other key regional records of temperature and EASM strength is important for an integrated understanding of EASM evolution across TII. However, chronological alignment across TII is more challenging than for more recent intervals, because many archives (including Lake Suigetsu) lack independent chronologies and hence age control is often obtained by tuning to other sites (sometimes via climate parameters). A conservative approach is therefore required to avoid circular reasoning, and here we present each record on their own chronology solely for orientation. This is also prudent because many archive chronologies are associated with large amounts of error (on the order of a thousand years) and hence distinguishing offsets between shifts in different regions is not practical. However, this does not prevent worthwhile comparisons being made between the structure of records from different archives.

### 4.8.2 Comparison to Continental EASM Records

Comparison of our  $\delta^2\text{H}_{\text{C}_{30\text{acid}}}$  EASM reconstruction to other records from the EASM region supports the notion of a “Weak Monsoon Interval” during MIS 6, and that TII was associated with EASM strengthening, however there are clear differences between records, which adds credence to previous assertions that EASM evolution during TII was extremely spatially heterogenous (Figure 4.8; Xue *et al.*, 2019). Indeed, none of the records presented in Figure 4.8 show the same trends across this interval, aside from perhaps Sanbao Cave and Hulu Cave  $\delta^{18}\text{O}_{\text{speleothem}}$ , although the latter record does not extend past 128 ka BP (U–Th timescale). A common feature of some of the Chinese speleothem records is a rapid increase in EASM strength at ~129 ka BP (U–Th timescale), which was not observed at Lake Suigetsu. Accounting for chronological uncertainty, the largest increase in EASM strength observed at Lake Suigetsu (between ~131 and 130 ka BP, SG timescale) could be equivalent to this rapid shift in  $\delta^{18}\text{O}_{\text{speleothem}}$ ; however, the shift in Suigetsu  $\delta^2\text{H}_{\text{C}_{30\text{acid}}}$  is more similar in duration to the gradual decrease in  $\delta^{18}\text{O}_{\text{speleothem}}$  observed at Hulu Cave and Shangxiaofeng Cave. This observation contradicts previous assertions that the rapidity of the transition in  $\delta^{18}\text{O}_{\text{speleothem}}$  was an indicator of EASM threshold behaviour (Yuan *et al.*, 2004; Kelly *et al.*, 2006), and instead suggests that, in Japan at least, EASM strengthening was a slow response to climate forcing.

Not only is the trend in EASM strength during TII at Lake Suigetsu different from other records from across the region, but so is its apparent relationship with temperature evolution. EASM strength tracks the increase in temperature at Lake Suigetsu prior to 130 ka BP, before fully decoupling from temperature, which continues to rise whilst the EASM exhibits a weakening trend (Figure 4.7, Figure 4.8). Instead of this behaviour, analysis of sediments from the South China Sea found that EASM strengthening lagged behind the temperature increase (He *et al.*, 2017a). Furthermore, EASM strength and temperature were decoupled at Xinglong Cave during the early stages of TII before coupling later on (i.e., the reverse of the trends seen at Lake Suigetsu; Duan *et al.*, 2022). Interestingly, the temperature evolution at Lake Suigetsu and Xinglong Cave exhibit similar structural features (accounting for chronological uncertainty; Figure 4.8). However, whilst our EASM record at Lake Suigetsu indicates

strengthening with the first rise in temperature, the increase in EASM strength at Xinglong Cave does not occur until the second temperature rise, 4 ka later.

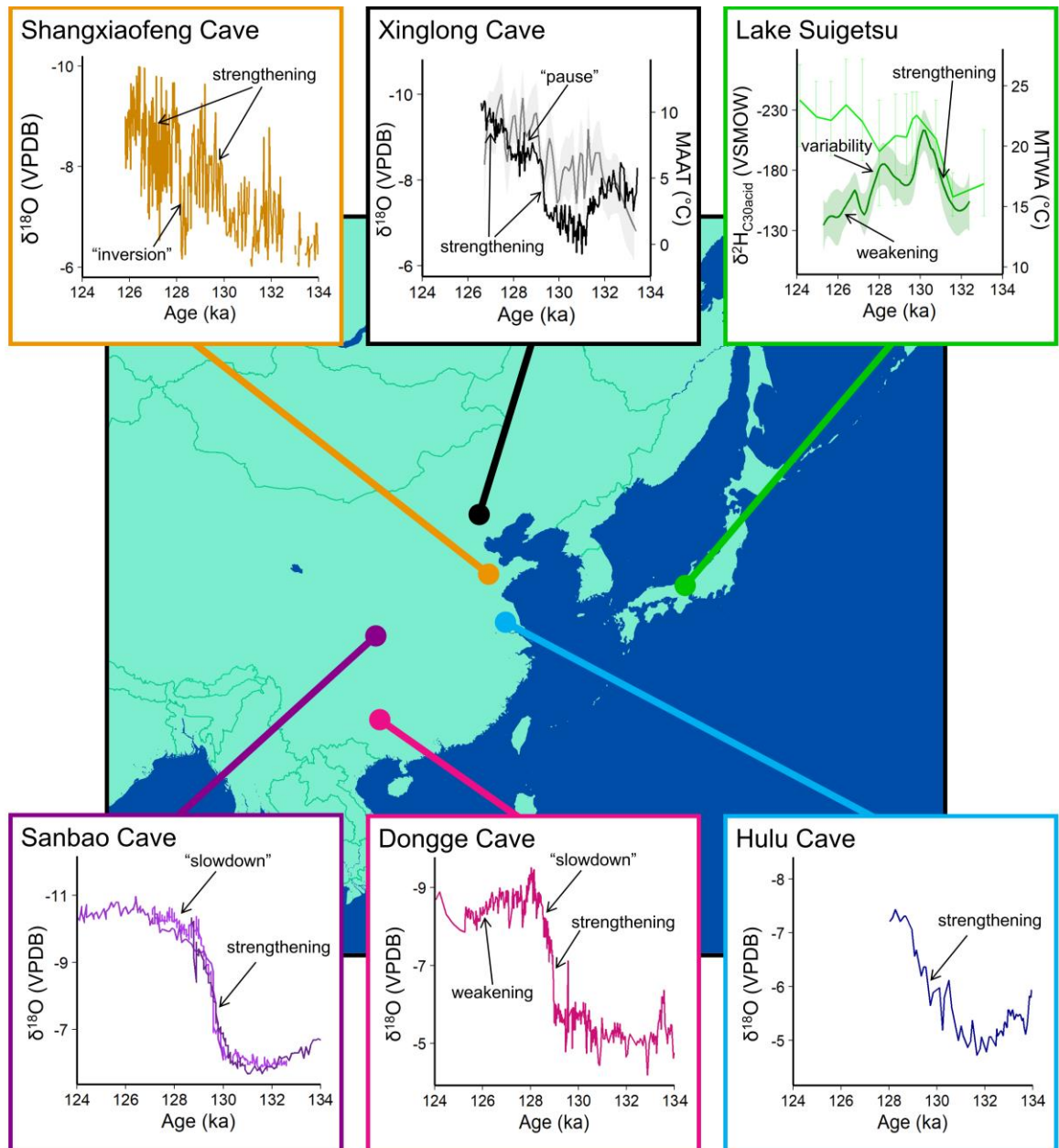


**Figure 4.8 Records of EASM strength between 134 and 124 ka BP and location indicators.**

From top left to bottom right: Shangxiaofeng Cave SD1  $\delta^{18}\text{O}_{\text{speleothem}}$  (U–Th timescale; Xue *et al.*, 2019), Xinglong Cave XL–4  $\delta^{18}\text{O}_{\text{speleothem}}$  in black and loess–smoothed mean annual average temperature (MAAT; span = 0.1) with  $1\sigma$  confidence bands in grey (U–Th timescale; Duan *et al.*, 2019; Duan *et al.*, 2022), loess–smoothed Lake Suigetsu SG06  $\delta^2\text{H}_{\text{C30acid}}$  (span = 0.25) with  $1\sigma$  confidence bands in dark green and MTWA with error bars showing minimum/maximum values in light green (analysed by T. Nakagawa) (SG timescale; this study); Sanbao Cave SB25–2, SB23 and SB11  $\delta^{18}\text{O}_{\text{speleothem}}$  (U–Th timescale; Wang *et al.*, 2008), Dongge Cave D4  $\delta^{18}\text{O}_{\text{speleothem}}$  (U–Th timescale; Kelly *et al.*, 2006), Hulu Cave MSX  $\delta^{18}\text{O}_{\text{speleothem}}$  (U–Th timescale; Cheng *et al.*, 2006).

This suggests that even though quantitative comparison of these records is prohibited by circular reasoning, by assuming that the temperature variations occurred synchronously between these two sites (which is not only reasonable

based on similarities in structure, but also based on observations across TI which found that temperature is likely to conform to regional/hemispheric trends), we can propose that the most major shift in EASM strength at Lake Suigetsu occurred prior to the largest shift at Xinglong Cave (at ~129 ka BP; a sudden change common to all of the Chinese speleothem records). However, the smaller, earlier shift in Xinglong Cave (termed the “Weak Monsoon Interval Interstadial” by Duan *et al.* (2019)) could be equivalent to the largest shift at Lake Suigetsu, because this occurs during the first period of rising temperatures. This suggests that not only did the EASM strengthen more slowly in Japan than many parts of continental China (where records exhibit a step-change in EASM strength), but also that this strengthening occurred earlier; although without robust independent chronologies this remains tentative. It follows that EASM strengthening in Japan does not lag regional temperature increases.

Another key aspect of EASM evolution which differs among sites is the presence (or absence) of submillennial-scale variability during TII. Comparison of the Lake Suigetsu record to these other (speleothem) records is difficult due to critical structural differences (i.e., a lack of rapid strengthening at 128 ka BP (U–Th timescale). However, much like the Shangxiaofeng Cave  $\delta^{18}\text{O}_{\text{speleothem}}$  record, the Suigetsu  $\delta^2\text{H}_{\text{C}_{30}\text{acid}}$  record provides evidence for inversions in EASM strength after an initial increase. Such features are not universally observed; there are contrasting observations from across the monsoon region as to their nature (a true “inversion”, a “pause”, or a “slowdown”; Figure 4.8). Regardless, the evidence from Suigetsu is that there was indeed some submillennial-scale variability in EASM strength during TII, in contrast to observations at Hulu and Sanbao caves (Cheng *et al.*, 2006; Wang *et al.*, 2008). It is interesting to note that the amplitude of millennial-scale variability observed is greater in the reconstructions derived from the most northerly archives (Shangxiaofeng Cave, Xinglong Cave and Lake Suigetsu; discussed further in Section 4.8.5).

### 4.8.3 Contrasting EASM Evolution in Japan During TI and TII

The interpretation of these patterns can be assisted by comparing the findings presented here to EASM and temperature variations across TI. This exercise highlights significant differences between deglacial monsoon behaviours during these intervals (Figure 4.9); whilst Suigetsu pollen-derived temperature during

TI and TII shows some similar character, observations of  $\delta^2\text{H}_{\text{C30acid}}$  suggests unique trends in EASM strength. This is not surprising, given how other records from across the EASM region exhibit different EASM behaviours during TI and TII (e.g., Cheng *et al.*, 2006; Duan *et al.*, 2019). Not only is the range of Suigetsu  $\delta^2\text{H}_{\text{C30acid}}$  values greater across TII than TI, suggesting higher amplitude changes in EASM strength (accounting for a contribution to  $\delta^2\text{H}_{\text{C30acid}}$  from rising temperatures, as mentioned previously), but there are limited similarities in structure.

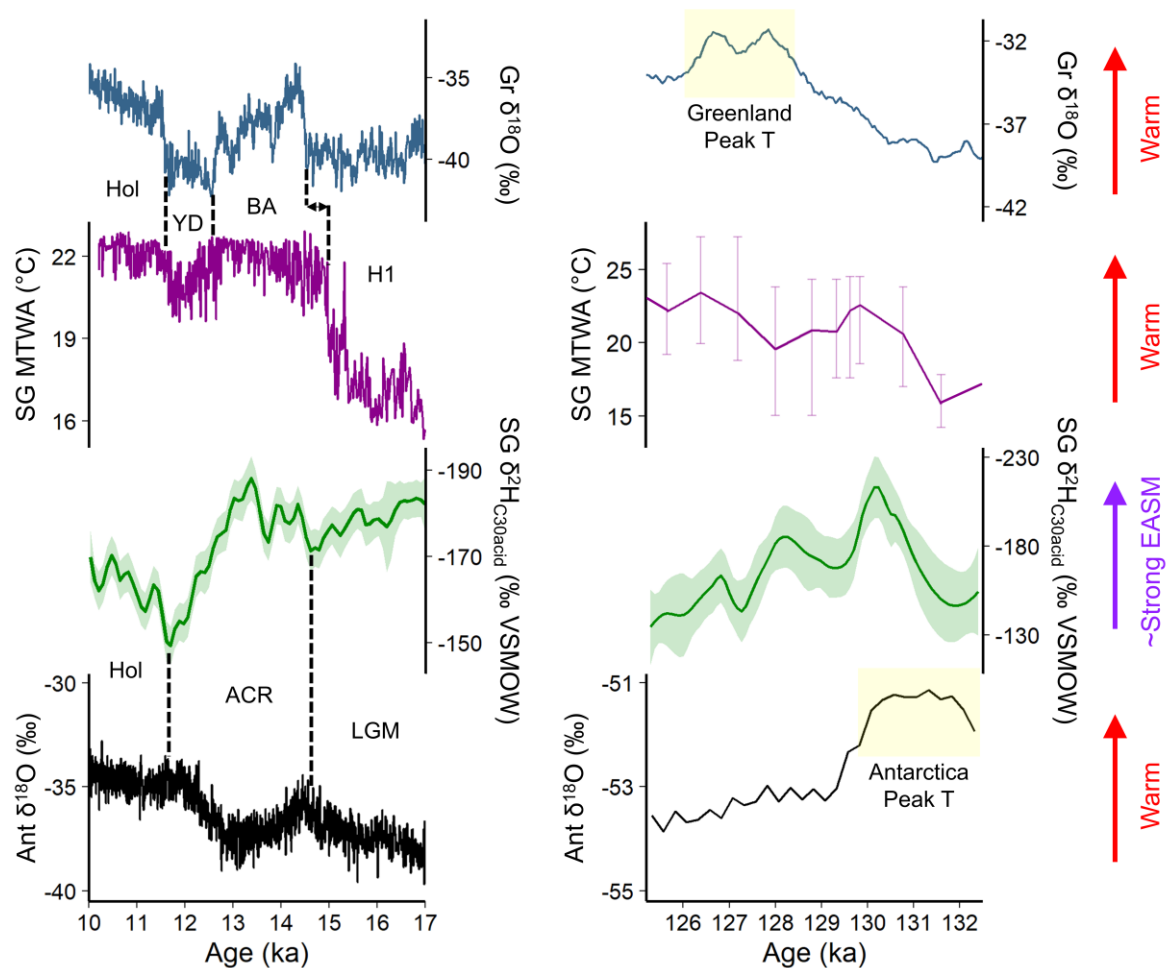


**Figure 4.9 Comparison of records from Greenland (Gr), Lake Suigetsu (SG) and Antarctica (Ant) during TI and TII.** TI records: GRIP  $\delta^{18}\text{O}_{\text{ice}}$  (Johnsen *et al.*, 1997; Rasmussen *et al.*, 2014; remodelled onto the U–Th timescale as per Chapter 3), Suigetsu mean temperature of the warmest month (MTWA; Nakagawa *et al.*, 2021; IntCal20 timescale), loess–smoothed Suigetsu  $\delta^2\text{H}_{\text{C30acid}}$  (span = 0.1) with  $1\sigma$  confidence bands (EASM proxy; Chapter 3; IntCal20 timescale), Antarctica WAIS Divide  $\delta^{18}\text{O}_{\text{ice}}$  (WAIS Divide Project Members, 2013; WD2014 timescale). TII records: Synthetic Greenland  $\delta^{18}\text{O}_{\text{ice}}$  (Barker *et al.*, 2011; EDC3 timescale), Suigetsu MTWA with error bars showing minimum/maximum values (this study; SG timescale; analysed by T. Nakagawa), loess–smoothed Suigetsu  $\delta^2\text{H}_{\text{C30acid}}$  (span = 0.25) with  $1\sigma$  confidence bands (this study; SG timescale), Antarctica Dome Fuji  $\delta^{18}\text{O}_{\text{ice}}$  (DFO–2006 age) (Kawamura *et al.*, 2007).

Other reconstructions have suggested that EASM change appears to lag behind many other significant climatic shifts during TII (including increasing southern hemisphere temperature, global carbon dioxide concentration and initial increases in methane concentration; Yuan *et al.*, 2004). These studies instead aligned the increase in EASM strength to Northern Hemisphere temperatures (Masson–Delmotte *et al.*, 2010; Li *et al.*, 2014). Under these circumstances, EASM strengthening would denote the full inception of global interglacial conditions (Yuan *et al.*, 2004; Kelly *et al.*, 2006). Wang *et al.* (2008) suggested that this delay to EASM strengthening was due to the persistence of cold conditions during Heinrich Event 11 in the North Atlantic, which suppressed AMOC and forced the Intertropical Convergence Zone (ITCZ) to the south, a key component of the argument for an EASM–North Atlantic teleconnection during TII (Xue *et al.*, 2019). However, our record from Lake Suigetsu suggests that EASM strengthening in Japan occurred prior to this, challenging this North Atlantic–centric viewpoint and allowing for alternative teleconnections and forcing mechanisms to be explored.

EASM strength in Japan across TI displayed an inverse response to the ACR (Chapter 3), whereas pollen–derived temperature was closely related to Greenland (i.e., North Atlantic) temperature (albeit with an earlier late glacial interstade onset (Nakagawa *et al.*, 2021)). Chapter 3 proposed that insolation was the key driver of EASM strengthening across TI on multi–millennial timescales but attributed the propagation of an inverse response to the ACR to Pacific climate variability. It was suggested that the preservation of these Antarctic signals was enhanced by Japan’s location at a higher latitude, adjacent to the Pacific regime and isolated from mainland China. Applying these principles to our interpretation of EASM variability during TII can help to rationalise our observations from Lake Suigetsu.

#### **4.8.4 Climate Forcing**

The most likely driver of EASM variability during TII is Northern Hemisphere summer insolation. The relationship between the EASM and insolation is well–established on orbital timescales (Kelly *et al.*, 2006; Cheng *et al.* 2019) and was considered a major driver of EASM variability during TI, and we propose that this was also the case during TII. However, insolation is only one component of

the global deglacial climate sequence, and other elements of the climate system (in particular, polar temperatures) can help to rationalise our observations. Across TI, aside from Southern Hemisphere stage–interstage fluctuations leading those in the Northern Hemisphere, Antarctic and Greenlandic temperatures followed similar trends, reaching a peak in the early Holocene. However, during TII, the interhemispheric temperature gradient was significantly greater due to a large (up to 2 ka) temporal offset between peak temperatures in Greenland and Antarctica (Nilsson–Kerr *et al.*, 2019). During TI, we observed discrepancies between records from Japan and continental China when polar temperatures were decoupled during low amplitude stage–interstage fluctuations (Chapter 3); aside from these intervals, the EASM system exhibited coherent strengthening patterns. During TII, this decoupling is even more significant; stage–interstage fluctuations were extremely muted (and highly debated), and instead we observe extremely different hemispheric glacial–interglacial fluctuations. This is critical for EASM operation because perturbations in the interhemispheric temperature gradient are intrinsically linked to atmospheric circulation and ITCZ positioning, and hence have the potential to significantly alter EASM behaviour.

We propose that these different climate behaviours during TII relative to TI, combined with greater ice volumes pre–transition (during MIS 6) and more rapid deglaciation associated with a larger solar insolation change during TII (Caley *et al.*, 2013), were the cause of the differences in the pattern and magnitude of EASM change during TI and TII at Lake Suigetsu. Furthermore, because tangible inter–regional links have been made from both Antarctic and North Atlantic temperatures to EASM behaviour during other intervals, it follows that the observed spatial heterogeneities in EASM behaviour during TII could be due to competing influences from each pole. The Suigetsu pollen–derived temperature profile shows submillennial–scale variability during TII which cannot be explained solely by a Northern Hemisphere influence (because Greenland temperature lacks substructure), but could be due to a combination of the temperature profiles of both poles; an earlier peak due to the insolation increase and Antarctic warming, and a later peak due to Greenlandic warming (which is also observed in South China Sea temperatures (Clemens *et al.*, 2018)). This implies that when decoupled, polar temperatures can both have a tangible effect on the mid–latitudes.

Given the evidence for an Antarctica–Japan EASM teleconnection during TI, it is not surprising that we observe the most major shift in EASM strength in Japan during the earlier stages of TII (when the largest changes in insolation and Antarctic temperature occurs) relative to mainland China, which displayed a strong North Atlantic teleconnection during TI. Indeed, EASM evolution in Japan appears to maintain a closer relationship to Antarctic temperatures during TII. However, it is also arguable that all sites display some degree of mixed character; for example, the Weak Monsoon Interval Interstadial at Xinglong Cave, albeit more muted than the main shift, could be representative of a Pacific influence on EASM strength at this site. Site location may be a key component of the relative influence of each teleconnection; much like TI, we propose that the location of Japan makes precipitation here especially sensitive to Pacific (and ultimately, Antarctic) changes. Hulu Cave, Shangxiaofeng Cave and Lake Suigetsu are at similar latitudes and lower elevations than the other sites, as well as being located closer to the coast, and all exhibit slower increases in EASM strength. The other sites, situated further inland, display more rapid increases in EASM strength akin to threshold behaviour, possibly due to greater influences of Heinrich Event 11 (and a stronger North Atlantic teleconnection, via the westerly jet) in these areas. The relationship between the EASM in Japan and Antarctic temperature during TII was not inverse, like during the ACR, but instead likely positively related, as with the remainder of TI, suggesting that this inverse relationship was a feature of Southern Hemisphere stadial, rather than glacial, conditions. The decrease in Antarctic temperatures during the latter stages of TII might also explain EASM weakening in Japan as indicated by our  $\delta^2\text{H}_{\text{C30acid}}$  record.

#### 4.8.5 Submillennial Variability

Our comparison of EASM evolution during TI and TII also highlights that the observed submillennial–scale variability during TII was non–analogous to TI, and hence it is important to be tentative when suggesting that such fluctuations are akin to “Younger Dryas”–type cold inversion responses. It is not possible to say whether such cold inversion responses should be anticipated pre– or post– the major transition (i.e., whether such transitions share greater character with EASM strengthening at the onset of a late–glacial interstade (“Bølling–Allerød”–type warm period) or interglacial period (Holocene)).

Instead, it is more prudent to assess whether there is any substructure to these transitions, for which the Lake Suigetsu record provides supporting evidence. However, it is likely that there is still spatial heterogeneity in such variability, as well as the potential for differences between archive type. One possible mechanism to explain these fluctuations is perturbations of AMOC, however Duan *et al.* (2019) suggested that meltwater pulses would have a reduced effect on AMOC, which was more strongly suppressed during TII due to the greater rapidity of ice sheet collapse (Landais *et al.*, 2013). If these climatic conditions resulted in more muted hydrological responses to small scale temperature fluctuations (which are more difficult to preserve and detect), this could explain the ambiguous evidence for such EASM variability. An alternative explanation is that more northerly sites, situated towards the edge of the EASM domain (including Shangxiaofeng Cave, Lake Suigetsu and Xinglong Cave), were more sensitive to westerly jet repositioning as a result of subtle changes to AMOC than the more southerly cave sites.

#### **4.8.6 Future Work**

Future work should focus on growing the network of EASM records from across the region, allowing for better clarification of signal heterogeneities during TII. Of particular value to this is the inclusion of records from alternative (non-speleothem) archives to generate a more well-rounded analysis of EASM behaviours by overcoming archive-specific limitations, although the development of independent age models is challenging in these contexts. The application of other chronological techniques to non-speleothem archives should also be a focus for future development. This is especially pertinent for those archives with the potential to discern submillennial-scale fluctuations and provide robust evidence to support or refute teleconnections. A greater number of temperature reconstructions from the region would also be beneficial in order to better understand the alignment of EASM evolution with temperature and the potential for temporally-constrained teleconnections to both poles.

#### **4.9 Conclusions**

Expanding current observations of deglacial EASM variability to include extremes of temperature and a variety of boundary conditions is crucial for a more

comprehensive understanding of this influential climate system. Using lipid biomarkers and hydrogen isotopes from the Lake Suigetsu sediment cores, we examined local catchment evolution and EASM behaviour during the penultimate glacial termination (Termination II). Prior to 131.0 ka BP, the Lake Suigetsu catchment consisted of a dynamic fluvial system dominated by shallow water and peat bog environments. A deep-water lacustrine system then developed in the area, becoming fully established after ~1.2 ka, possibly driven by a combination of increased freshwater input and tectonic subsidence. There is some evidence for threshold behaviour in aquatic productivity, which initiated at 129.8 ka BP. Due to its strictly terrestrial origin, our EASM reconstructions are based on the compound-specific hydrogen isotope analysis of the C<sub>30</sub> n-alkanoic acid ( $\delta^2\text{H}_{\text{C30acid}}$ ), which provided the strongest connection to the hydrogen isotope composition of summer (EASM) precipitation and would have been negligibly affected by lake development. EASM  $\delta^2\text{H}_{\text{precipitation}}$  (and ultimately EASM strength) was the predominant driver of  $\delta^2\text{H}_{\text{C30acid}}$  during TII, although there was some evidence to support a temperature contribution before 130.0 ka BP. Our analysis found that the EASM strengthened from 132.5 to 130.0 ka BP before weakening to 125.2 ka BP. There is evidence to support submillennial-scale variability during this weakening phase, with weakening to 129.5 ka BP, strengthening to 129.0 ka BP and then weakening to 125.2 ka BP, in contrast to some Chinese speleothem reconstructions which exhibit smooth transitions with no/limited internal structure. Our record shares some common features with other EASM reconstructions (a “Weak Monsoon Interval” during MIS 6, and strengthening across the transition), however the distinctive character in our record (and that of other records) supports extreme spatial heterogeneity in EASM strength during TII. Alignment of temperature reconstructions at Lake Suigetsu and Xinglong Cave, China, facilitate the assertion that the increase in EASM strength in Japan was earlier and slower than the largest shift in EASM strength in continental China, partially overcoming circularity in chronological alignment.

Comparison of  $\delta^2\text{H}_{\text{C30acid}}$  EASM reconstructions from Lake Suigetsu during TI and TII suggest characteristically different behaviours during these intervals, attributed to different climatic sequences, greater ice volumes and more rapid deglaciation during TII. A key component of this was the decoupling of peak

temperatures at the north and south poles during TII. We propose that insolation was a major driver of EASM variability during both TI and TII, but that offset glacial–interglacial fluctuations at the poles caused the much greater spatial heterogeneity in EASM evolution during TII relative to TI. Much like during TI, Japan showed greater Antarctic (Pacific) character relative to mainland China, which displayed more coeval trends with the North Atlantic. Site location appears to be a key control of whether local EASM strength more closely tracked insolation and Antarctic temperatures or North Atlantic behaviours. Similarly, greater submillennial–scale variability was observed for the most northerly sites. Ambiguity in such trends could be attributed to difficulties in detecting low amplitude fluctuations (muted as a result of extreme AMOC suppression), or because sites towards the edge of the EASM domain were more sensitive to westerly jet repositioning. Our observations of the EASM using  $\delta^2\text{H}_{\text{C}_{30}\text{acid}}$  are the first derived using stable isotope–based climate proxies from the Japanese archipelago, and future work should continue to contribute records of EASM strength and temperature from a range of locations and archive types to assist in unravelling the complexities in deglacial EASM evolution during TII.

## Chapter 5 Controls on Luminescence Signals in Lake Sediment Cores: a Study from Lake Suigetsu, Japan

Rex, Charlie L.<sup>1</sup>, Staff, Richard A.<sup>1</sup>, Sanderson, David C.W.<sup>1</sup>, Cresswell, Alan J.<sup>1</sup>, Marshall, Michael H.<sup>2</sup>, Hyodo, Masayuki<sup>3</sup>, Horiuchi, Daishi<sup>4</sup>, Tada, Ryuji<sup>4</sup> and Nakagawa, Takeshi<sup>5</sup> (2022) 'Controls on luminescence signals in lake sediment cores: A study from Lake Suigetsu, Japan', *Quaternary Geochronology*, 71, article 101319. Available at: <https://doi.org/10.1016/j.quageo.2022.101319>.

<sup>1</sup>*SUERC, University of Glasgow*

<sup>2</sup>*Aberystwyth University*

<sup>3</sup>*Kobe University*

<sup>4</sup>*University of Tokyo*

<sup>5</sup>*Ritsumeikan University*

The text presented here is identical to that of the original publication, except for the following:

- The numbering of figures and tables,
- The enlargement of figures for readability,
- The acknowledgement of the contribution(s) of other authors and individuals where appropriate,
- The integration of the supplementary material into the main text for the benefit of the reader of this thesis, and
- Amendments made following the examination of this thesis at the request of the examiners.

The original formatted publication can be viewed in Appendix 1 – Publications. The publisher (Elsevier) permits inclusion of published articles in full or in part in a thesis for non-commercial purposes.

Authorship Declaration: C.L.R. performed the core sampling, prepared and analysed the portable optically stimulated luminescence and laboratory profiling samples, interpreted the data, and wrote the manuscript (first draft, editing and final draft). R.A.S., D.C.W.S., A.J.C. and T.N. provided feedback, supervision

and guidance. D.C.W.S. assisted with the dose rate determinations. A.J.C. assisted with the laboratory profiling analysis. M.H.M. provided the ITRAX dataset (Figure 5.3). M.H. provided the relative palaeointensity (normalised depositional remanent magnetism) dataset (Figure 5.4). D.H. and R.T. provided the XGT MnO and Fe<sub>2</sub>O<sub>3</sub> datasets (Figure 5.5). T.N. provided the pollen-derived climate datasets, core photographs, and access to core materials. V. Olive performed the ICP-MS and ICP-OES analysis.

Funding: This research did not receive any specific grant from funding agencies in the public, commercial, or not-for-profit sectors. C.L.R. was supported by the NERC IAPETUS2 Doctoral Training Partnership. The SG06 core was recovered under a Natural Environment Research Council (NERC) grant (NE/D000289/1) awarded to T.N..

Accompanying data can be found at

<http://doi.org/10.5525/gla.researchdata.1263>.

## 5.1 Abstract

The luminescence characteristics of sediments are driven by a range of environmental factors and can be used as indicators of both local and regional environmental shifts. Hence, rapid luminescence profiling techniques are increasingly employed during multiproxy analysis of sediment cores, overcoming the practical limitations of traditional (dating) methods. One emerging application of luminescence profiling is in the palaeoenvironmental investigation of lake cores. This study demonstrates the versatility of rapid core profiling using portable optically stimulated luminescence and laboratory profiling techniques for appraising the luminescence characteristics of the Lake Suigetsu (Japan) sediment cores. These techniques were employed across four key time periods, each selected for their unique environmental context and significance on either a local or global scale, in order to identify relationships between down-core luminescence and environmental change. We demonstrate that the luminescence characteristics of the cores are susceptible to a range of environmental perturbations and can therefore act as proxies of past change. Additionally, the quantification of these luminescence signals, alongside an assessment of dose rate variations down-core, supports the notion that future luminescence dating is feasible. The results of this analysis contribute to the wider understanding of the application of luminescence techniques – both profiling and dating – to lake sediment cores.

## 5.2 Highlights

- Rapid down-core profiling techniques are applied to sediment cores from Lake Suigetsu, Japan.
- Down-core luminescence signals are sensitive to a range of catchment-scale environmental changes.
- Estimates of dose rate are made from elemental concentrations and provide an assessment of chronometric accuracy.

## 5.3 Keywords

Portable OSL; Laboratory profiling; Luminescence dating; Lake sediment; Palaeoenvironment

## 5.4 Introduction

Optically Stimulated Luminescence (OSL) dating is a versatile chronological tool which can be applied to both marine and terrestrial sediment cores (e.g., Kadereit *et al.*, 2012; Gao *et al.*, 2017). The use of this technique has been aided by well-defined methodologies for extracting OSL-appropriate (light-tight) samples from core material (Armitage and Pinder, 2017; Nelson *et al.*, 2019). OSL dating is often applied to complement other chronological tools, such as radiocarbon dating, during age-depth model construction (Zhao *et al.*, 2019; Li *et al.*, 2020). However, where other chronometers cannot be applied (e.g., if the material is older than the limit of radiocarbon dating), OSL dating can form a major component of the core chronology (e.g., Long, 2012; Hu *et al.*, 2018).

However, the value of luminescence techniques to core analysis is not limited to dating alone (Munyikwa *et al.*, 2021). It has been widely observed that the luminescence characteristics of sediments are driven by a range of environmental factors. Hence, down-core luminescence characterisation has the potential to contribute to our understanding of environmental change through time. However, most traditional luminescence techniques are both time- and core material-intensive (Bateman and Catt, 1996; Stone *et al.*, 2015), which limits the number of samples that it is feasible to analyse and delays the final output of results until some months after sampling (Porat *et al.*, 2019). As a result, rapid luminescence profiling techniques are increasingly employed to characterise the luminescence behaviour of core sediments and elucidate environmental changes, typically as part of multiproxy analysis (e.g., Ghilardi *et al.*, 2015; Sanderson and Kinnaird, 2019; Pears *et al.*, 2020).

In this study, we examine the versatility of rapid down-core profiling techniques (portable OSL (POSL) analysis and laboratory (lab) profiling) for the detection of luminescence proxies of environmental change in lake sediment cores (from Lake Suigetsu, Japan). Such luminescence proxies have only recently been investigated in a lacustrine setting for this purpose (Pířková *et al.*, 2019). Variations in luminescence characteristics (both natural signals and sensitivities) are examined and compared to known environmental shifts, supported by existing proxy data. The Suigetsu cores offer a unique opportunity to probe this

relationship across a ~140,000-year age range in a lacustrine setting. A secondary aim of our study was to provide an assessment of the dating potential of the Suigetsu core material across a range of ages by comparing the quartz and polymineral fractions as potential chronometers, and to identify complexities which could hinder future age calculations. The motivation for this aspect of the work was the extension of the absolute Suigetsu chronology beyond the limit of radiocarbon dating.

The luminescence characteristics of the Suigetsu cores were appraised during four key time periods, each selected for their distinctive environmental context and significance on either a local or global scale. This facilitates the examination of a range of prominent environmental shifts on the luminescence characteristics of the cores, following the logic that the most pronounced shifts would cause changes that are most easily detectable by the chosen methods. The time periods span almost the full temporal range of the Suigetsu cores, including sections both covered by the existing radiocarbon chronology (in order to tether our findings in a chronologically well-constrained period) and older than the radiocarbon limit (to consider the potential of materials from Lake Suigetsu for future dating). The youngest of these (Time Period 1, “the Last 500 Years”) spans from ~550 cal BP to the present day; a period comprising a series of local environmental perturbations, including the artificial connection of the lake to the Sea of Japan and a number of local flood events. The next (Time Period 2, “the Laschamp Excursion”) extends from ~45,000 to 35,000 cal BP; a period of global change containing the Laschamp geomagnetic excursion and variable average annual temperatures (concomitant with Greenland Interstades 12 to 7; Rasmussen *et al.*, 2014). The third time period (Time Period 3, “the Varve Limit”) spans from ~73,000 to 69,000 yr BP and is centred on the initiation of varving, which represents a significant alteration in lake biogeochemistry. The final time period (Time Period 4, “Termination II”) extends from ~140,000 to 118,000 yr BP, encapsulating the global transition from MIS 6 to MIS 5e, which is associated with broadly increasing temperatures and a strengthening Summer Monsoon in East Asia (Duan *et al.*, 2019).

## 5.5 Regional Setting

Lake Suigetsu is a tectonic lake located on the western side of the active Mikata fault in Fukui Prefecture, Honshu Island, central Japan ( $35^{\circ} 35' N$ ,  $135^{\circ} 53' E$ ; Figure 5.1). The western side of the fault is subsiding and hence the lake has deepened through time. During late-MIS 7/early-MIS 6, Lake Suigetsu was a transient shallow fluvial-lacustrine environment (Nakagawa *et al.*, 2012), which became a brackish lake during the MIS 5e global sea level highstand. Diatom assemblage analysis indicates that the lake experienced freshwater conditions from MIS 5d to the Holocene. In the present day, the lake is ~34 m deep and brackish, having been artificially connected to the Sea of Japan via the Urami Canal (Figure 5.1) in 286 cal BP (AD 1664; Saito-Kato *et al.*, 2013).

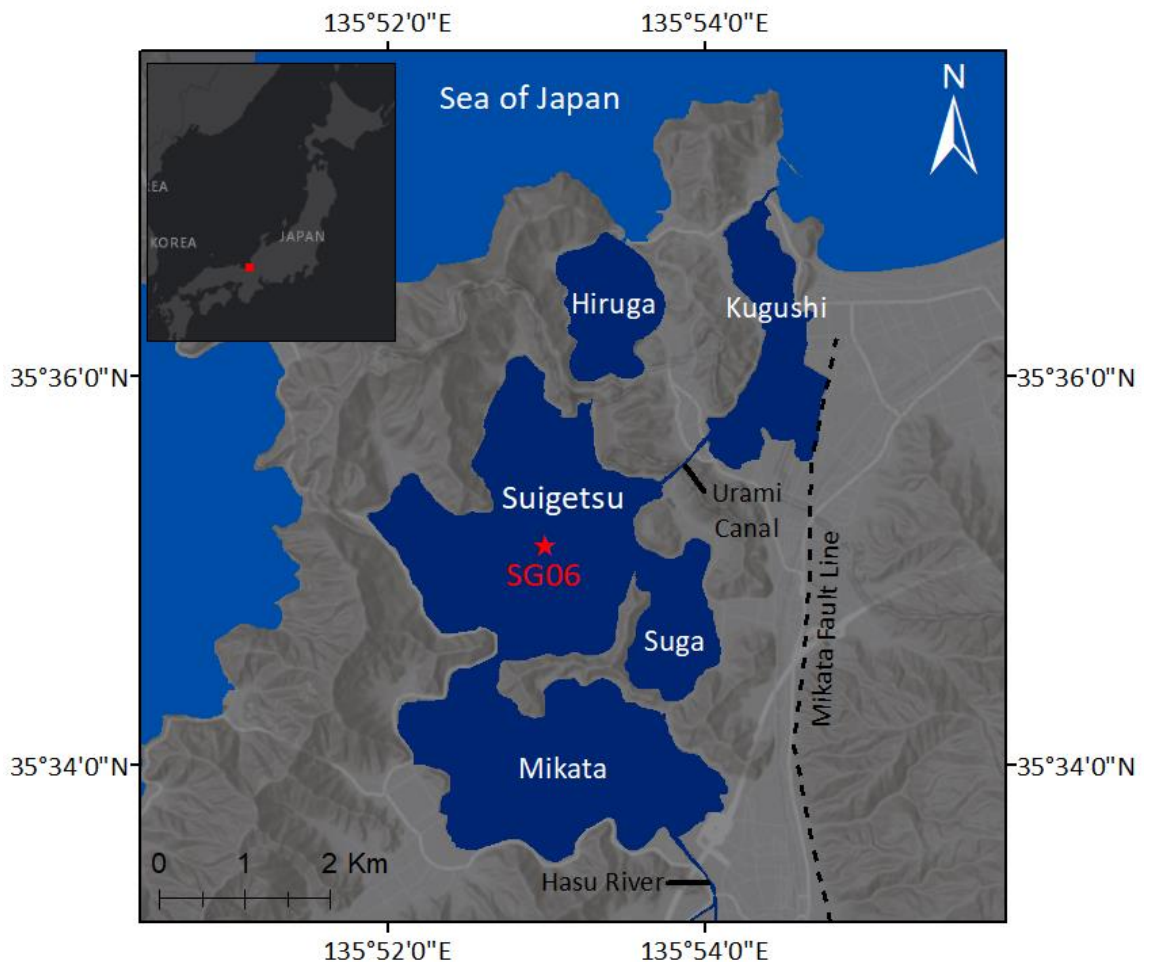


**Figure 5.1 Location of Lake Suigetsu.** Location of Lake Suigetsu and neighbouring lakes Mikata, Suga, Hiruga and Kugushi. The location of the Urami Canal, Hasu River and Mikata Fault Line are also indicated. The location of the SG06 cores are shown with a red star. Adapted from Scholaut *et al.* (2018). Basemaps: World Dark Gray Base, World Hillshade from Esri (2022c; 2022d) (insert scale 1:40,000,000, main map scale 1:60,000).

The Suigetsu sediments are continuously, countably varved between ~50,000 and ~10,000 cal BP, providing the longest such record from the Quaternary (Schlölaut *et al.*, 2018). Varve counting, coupled with a radiocarbon dataset consisting of over 800 measurements (Staff *et al.*, 2011; Bronk Ramsey *et al.*, 2012) and tephra tie points (e.g., McLean *et al.*, 2018; Albert *et al.*, 2019) constitute the robust core chronology to 50,000 cal BP, which is aligned to the IntCal20 timescale (Bronk Ramsey *et al.*, 2020). Beyond 50,000 cal BP, a provisional chronology is loosely constrained by wiggle matching of *Cryptomeria* pollen from Suigetsu to the LR04 benthic stack.

Four previous coring campaigns (SG93, SG06, SG12 and SG14) recovered a series of overlapping sediment core sections from the present day to >200,000 yr BP (98 m of composite depth; Nakagawa *et al.*, 2012; McLean *et al.*, 2018). The preserved sequence encapsulates two glacial and two full interglacial periods of continuous sedimentation. Any effects of disturbance are minimal; the presence of laminations during MIS 5e and varves between ~70,000 yr BP and the present day (indicating bottom water anoxia and good conditions for preservation) and further sedimentological inspection suggests that the core material does not contain hiatuses or disturbed sections (Nakagawa *et al.*, 2012). This provides a palaeoenvironmental archive that comprises well-preserved millennial, centennial, decadal, annual, and even subannual-scale environmental oscillations which are the subject of ongoing multiproxy analysis. The Suigetsu cores are suitable for luminescence analysis because they contain detrital particles which have remained in-situ within the sequence post-deposition.

## 5.6 Materials and Methods

### 5.6.1 Core Materials

Sixty samples were obtained from the SG06 cores for luminescence characterisation. To mitigate against exposure of samples to light prior to measurement, the top 1 mm of sediment was removed from longitudinally split cores under dim red-light conditions to access unexposed material. Beyond this depth the influence of natural light has been shown to be smaller than the analytical error, so this material was deemed suitable for analysis (Armitage and Pinder, 2017). Sampling strategies varied based on availability of material,

duration of time period, and structure of the event(s) to be studied. Contiguous (continuous adjacent) sampling was employed for Time Periods 1 and 3, because these spanned shorter intervals. Spot sampling was employed for Time Periods 2 and 4.

For Time Period 1, 4 cm integrated samples were taken along the length of core section A(N)01–upper, starting at 5 cm depth (avoiding the uppermost sediments, which were disturbed during coring) ( $n = 24$ ). The 100–year integrated samples for Time Period 2 were taken every 1,000 years between 45,000 and 35,000 cal BP inclusive ( $n = 11$ ). For Time Period 3, the sampling resolution was determined by half the depth of the clay layer separating the varved and non–varved sections ( $6.85 \text{ cm} \approx 230\text{--}330$  years). Contiguous samples were taken at this depth resolution along the length of core section A(S)24 ( $n = 12$ ). The samples for Time Period 4 were required to span a much longer time interval, so were taken approximately 2,000 years apart between 139,400 to 118,000 yr BP. Samples constituted 100–year integrated intervals, which were chosen semi–randomly to give round numbers (to the nearest 100 years) ( $n = 13$ ).

In addition, six samples were subsequently taken from across the four time periods for estimated dose rate ( $ED_R$ ) determination. These samples were analysed to compare the selected mineral fractions as potential chronometers and identify  $ED_R$  variations down–core which could affect the POSL and lab profiling results. These were taken post–luminescence analysis; one sample from each time period at a depth associated with representative natural luminescence values, and two additional samples at positions in the stratigraphy associated with relatively elevated natural luminescence values (within Time Periods 2 and 3).

### **5.6.2 Sample Analysis**

Each sample was subjected to two sets of analysis. First, measurements of IR– and blue light– stimulated luminescence were conducted using a Scottish Universities Environmental Research Centre (SUERC) POSL reader (Sanderson and Murphy, 2010) in Wakasa, Japan, where the Lake Suigetsu cores are in storage at the Fukui Prefectural Varve Museum. After the samples were removed from the relevant core sections, they were spread to cover a clear 5 cm diameter Petri

dish (ensuring a consistent exposed surface area for all samples) and then subjected to a Continuous Wave Proxy (“CWproxy”) measurement scheme to yield a suite of analytical values (Sanderson and Murphy, 2010; Kinnaird *et al.*, 2015). The applied CWproxy scheme consists of seven periods of photon counting: a 15 s dark count, two 30 s IR (880 nm) stimulations, another 15 s dark count, two 30 s blue light (470 nm) stimulations and a final 15 s dark count (Sanderson and Murphy, 2010). From these seven photon counts, the following variables were calculated. Two net values (POSLnet and PIRSLnet) were calculated by summing the photon counts from the relevant pair of stimulations (blue and IR) and subtracting the bracketing dark counts; these values are a proxy for age, sensitivity and dose rate. Two depletion indices (Depletion Index (Blue) and Depletion Index (IR)) were calculated by subtracting the photon count of the second stimulation from the first (and then subtracting the bracketing dark counts); these values are a proxy for mineralogical change, bulk properties and previous bleaching extent. And finally, the PIRSL/POSL ratio was calculated by taking a ratio of the PIRSLnet and POSLnet values; this value is a proxy for mineralogical change. Empty chamber measurements were taken every two samples to check for instrument contamination. A measurement of the POSL standards (Morar Sand and Granulite) was taken at the start and end of each ~12-sample batch to verify instrument performance.

Second, samples underwent lab profiling at SUERC, UK, which consisted of a short chemical preparation before measurement in a Risø TL/OSL system (TL-DA-15; Burbidge *et al.*, 2007; Sanderson and Murphy, 2010). Chemical pretreatment isolated two fractions: a Polymineral Fine (PMF) fraction, comprising mixed mineralogy grains ~5 – 50 µm in size; and a Quartz Fine (QF) fraction, comprising HF etched material (predominantly quartz; although some samples contained some larger feldspar grains), again 5 – 50 µm in size (as determined by a scanning electron microscope). The lab profiling methodology used to isolate these fractions was adapted from Burbidge *et al.* (2007) to account for the grain size distribution of the Suigetsu cores. Each sample was first wet sieved to retain the <90 µm fraction, and then left to settle for ~45 minutes before the finest grains in suspension were poured off. Samples were covered in 1 mol dm<sup>-3</sup> HCl for 10 minutes and then rinsed three times with deionised water, leaving the grains to settle out of suspension for ~2 minutes

between rinses. This step was then repeated using 10 % HF and then 1 mol dm<sup>-3</sup> HCl. Next, the samples were split into two containers: one for each mineralogy (QF and PMF). The PMF fraction was saturated in acetone and then loaded onto two 11 mm discs via settling tubes. The QF fraction underwent additional chemical preparation via a 40 % HF etch and a final 10-minute HCl wash (each followed by 3 rinses in deionised water), before being dried and loaded onto discs in the same manner as the PMF. Each set of discs (two PMF and two QF for each sample) were then measured in a Risø TL/OSL system (TL-DA-15) with a <sup>90</sup>Sr source. Both fractions underwent shortened Single Aliquot Regenerative Dose protocols (Figure 5.2). The Risø outputs were used to determine an estimated equivalent dose (ED<sub>e</sub>) in Gy by using the natural signal and the response of each aliquot to a 50 Gy dose (5 Gy doses were also included in the measurement scheme, but the relatively low sensitivity of the material precluded use of the response to such doses during sensitivity assessment). Each PMF aliquot was measured under both IR and blue light (yielding PMF-IR and PMF-blue signals, respectively), and the QF aliquots were measured under blue light only (to give a QF-blue signal).

| <u>PMF Measurement Scheme</u>                               |                               | <u>QF Measurement Scheme</u>                                 |                      |
|---|-------------------------------|--|----------------------|
| Preheat   | 200 °C / 10 s                 | Preheat  | 200 °C / 10 s        |
| IRSL  | 830 nm/30 s @ 50 °C           | OSL  | 470 nm/30 s @ 125 °C |
| OSL   | 470 nm/30 s @ 125 °C          | 1 Gy Test Dose   |                      |
| TL  | 500 °C @ 5 °C s <sup>-1</sup> | Preheat  | 200 °C / 10 s        |
|   |                               | OSL  | 470 nm/30 s @ 125 °C |
| Dose*   |                               | Dose*  |                      |
| Preheat   | 200 °C / 10 s                 | Preheat  | 200 °C / 10 s        |
| IRSL  | 830 nm/30 s @ 50 °C           | OSL  | 470 nm/30 s @ 125 °C |
| OSL   | 470 nm/30 s @ 125 °C          | 1 Gy Test Dose   |                      |
| TL  | 500 °C @ 5 °C s <sup>-1</sup> | Preheat  | 200 °C / 10 s        |
|   |                               | OSL  | 470 nm/30 s @ 125 °C |
| *3 doses were applied sequentially:<br>5 Gy, 50 Gy and 5 Gy |                               | * 3 doses were applied sequentially: 5<br>Gy, 50 Gy and 5 Gy |                      |

**Figure 5.2 Lab profiling measurement schemes.** Lab profiling measurement schemes for the Polymineral Fine (PMF) and Quartz Fine (QF) aliquots (adapted from Burbidge *et al.*, 2007).

The six samples for ED<sub>R</sub> determination were dried and homogenised by grinding prior to measurement of key elemental concentrations following the multi-acid digestion procedure in Olive *et al.* (2001). A set of five standards were run alongside the samples (consisting of incremental ratios of Basalt:Granulite (1:0, 3:1, 1:1, 1:3, 0:1)). Elemental concentrations of uranium (U) and thorium (Th)

were determined by Inductively Coupled Plasma Mass Spectrometry (ICP–MS) and potassium (K), iron (Fe) and manganese (Mn) by Inductively Coupled Plasma Optical Emission Spectrometry (ICP–OES). This analysis was performed by V. Olive. To determine  $ED_R$  values, ICP–MS and ICP–OES elemental concentrations of uranium, thorium and potassium were first converted to infinite matrix alpha, beta and gamma dose rates assuming decay series equilibrium. Effective alpha, beta and gamma dose rates were then calculated for two scenarios: 1) assuming a 30  $\mu\text{m}$  mean grain size and activity–free grains; and 2) assuming a 30  $\mu\text{m}$  mean grain size and that the internal contents of the grains were equal to that of the matrix. For Scenario 1, effective dose rates were calculated using the relevant alpha or beta relative attenuation fractions ( $1-\phi$ ) and assuming an alpha efficiency of 0.07 (Mejdahl, 1979; Bell, 1980). Water content corrections were applied to all terms. For Scenario 2, internal dose rates were scaled by absorbed dose fractions ( $\phi$ ) and external by relative attenuation fractions ( $1-\phi$ ), and water content corrections applied to the external dose component. Water content was calculated by using direct measurements of % wet weight during drying and then estimating a time integral average water content post–deposition based on sedimentological understanding of the cores (including amount of compression and clay content). Corrections were made for alpha, beta, and gamma dose rates using these values and a factor to reflect absorption by water ( $F_w$ ). A small ( $0.05 \text{ mGy yr}^{-1}$ ) cosmic dose rate component was included for the two oldest samples, which were deposited when the lake was shallow, but omitted for the four youngest samples which were deposited when the lake was deep (quantified by the presence of varves). The alpha, beta, gamma and cosmic effective dose rates were then combined to give an  $ED_R$  for each sample in each scenario. The QF–blue, PMF–IR and PMF–blue  $ED_e$  values were considered alongside the  $ED_R$  values in order to resolve first–order age approximations that can be compared to the existing Suigetsu chronology.

## 5.7 Results and Interpretation

### 5.7.1 Time Period 1, the Last 500 Years

Signals from both the POSL and lab profiling were small in magnitude for the last 500 years, reflecting the young age of the sediments (Figure 5.3). Most samples contained only small quantities of quartz; hence data collection from the QF

fraction was limited to a minority of discs and no clear trends were observed. The transition from fresh to brackish water in Lake Suigetsu had no detectable influence on the luminescence properties of the sediment, and all variables remained constant across this boundary. Flood layers (visible as pale layers in the core photograph and highlighted in orange in Figure 5.3) had the greatest impact on the luminescence profiles, producing high amplitude peaks at approximately -30 cal BP (AD 1980) and 120 cal BP (AD 1830) in the POSLnet and PIRSLnet profiles (Figure 5.3A), which correspond with elevated  $ED_e$  values from lab profiling (Figure 5.3C). This suggests that across this section, POSLnet, PIRSLnet and PMF  $ED_e$  can be used as an indicator of the presence of flood-related material. These peaks were not observed in either of the depletion indices, nor in the PIRSL/POSL ratio (Figure 5.3B), suggesting that they cannot be attributed to mineralogical variations and are unlikely to have resulted from different bleaching histories, and instead that these samples contained residual elevated dose values. The preservation of these elevated signals could be a result of delivery of this material in a manner that did not expose it to light, such as slumping of water-saturated hillsides, or large volumes of suspended sediments in river flow.

One sample (highlighted in yellow in Figure 5.3) that did not visually correlate with flood layers or produce large POSLnet or PIRSLnet values did nevertheless exhibit large  $ED_e$  values (predominately as a result of high natural signals), however the aliquots were inconsistent. This sample corresponded to a peak in titanium (Ti) content, as measured by ITRAX X-ray fluorescence (XRF) analysis (analysed by M.H. Marshall; Marshall *et al.*, 2012; Figure 5.3A). In Suigetsu, Ti can be interpreted as a proxy for detrital inwash, which suggests that this sample also contained flood material (despite there being no large visible flood layer) that resulted in elevated  $ED_e$  values. The disparity between aliquots may be attributable to a relatively small volume of flood material within the sample, which was not exposed during measurement in the POSL reader, and then unevenly partitioned between aliquots as grains were randomly loaded onto the discs for measurement, yielding different signal magnitudes during lab profiling.

A relatively high Ti content was also observed at the base of the profile, and whilst this did not correlate with elevated  $ED_e$  values, the samples taken from this period were associated with higher PMF sensitivities under both IR and blue

light (Figure 5.3D). This suggests that this older material had a distinct source—possibly the hillsides surrounding the lake as opposed to delivery via Lake Mikata (which acts to filter large detrital grains)—but that the delivery mechanism into the lake was more gradual than that of the flood material described above (encouraging bleaching prior to burial, and thus smaller  $ED_e$  values).

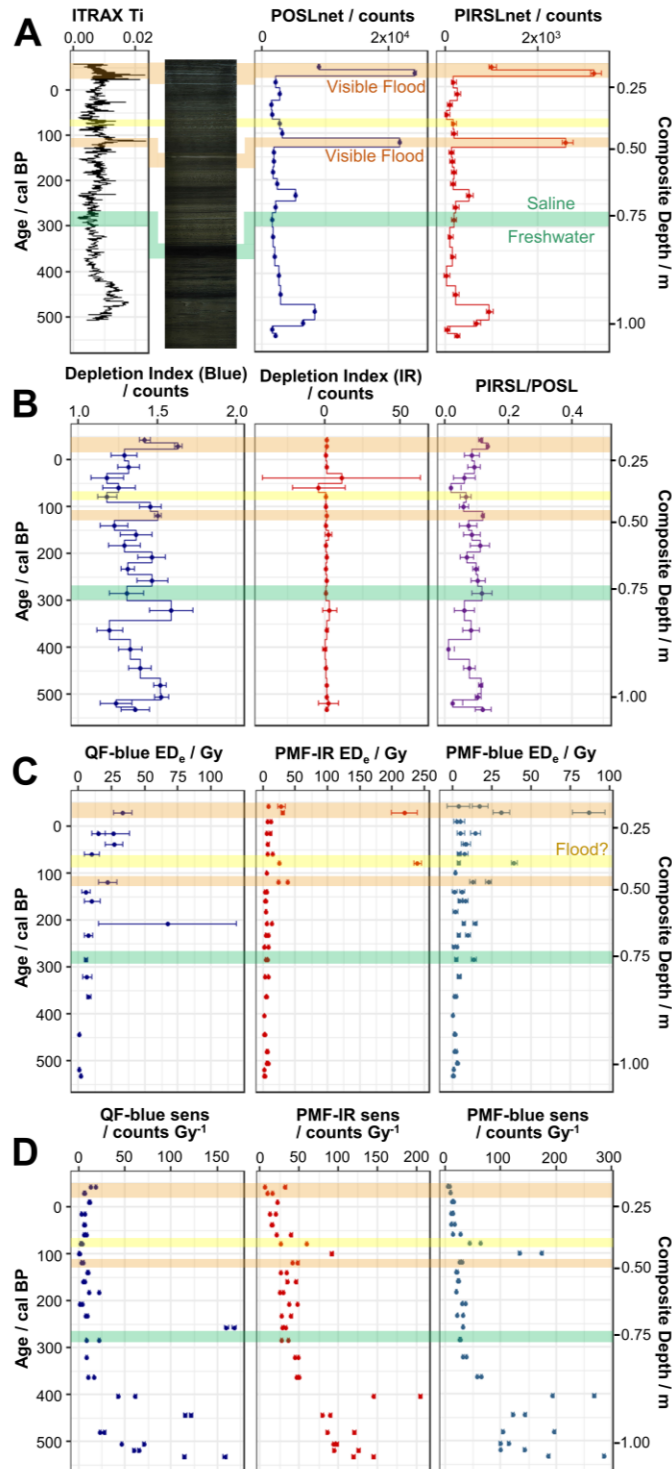


**Figure 5.3 Results of the POSL and lab profiling analysis of Time Period 1.** Results of the POSL (panels A and B) and lab profiling (panels C and D) analysis for the 24 samples in Time Period 1. Panel A also shows contextual data (core photograph taken by T. Nakagawa and ITRAX XRF Ti analysed by M.H. Marshall (Marshall *et al.*, 2012)). Visible flood layers are highlighted in

orange. An additional posited flood layer is highlighted in yellow. The transition from fresh to brackish lake water during 286 cal BP (AD 1664) is highlighted in green.

### 5.7.2 Time Period 2, the Laschamp Excursion

The POSLnet and PIRSLnet profiles across Time Period 2 showed two key transitions– one to a larger net signal at the Laschamp geomagnetic excursion itself (~42,000 cal BP) and a second to a smaller net signal at ~39,000 cal BP (Figure 5.4A). Much like Time Period 1, there were no fluctuations in the depletion indices or the PIRSL/POSL ratio that corresponded to these transitions (Figure 5.4B), suggesting that this trend was not driven by mineralogical variations or bleaching histories. Additionally, there was no clear relationship between these variables and the pollen–derived temperature reconstruction (Figure 5.4A). This suggests that there was no obvious connection between temperature and core luminescence characteristics, despite the variability of the climate during this period.

The lab profiling–derived  $ED_e$  profiles (Figure 5.4C) presented similar trends to the POSLnet and PIRSLnet with some subtle variations in the shape of the profile. In the  $ED_e$  profiles, the younger (~39,000 cal BP) shift was greater in magnitude than the older (~42,000 cal BP) shift, and in the QF–blue profile, only the younger shift was beyond the margin of error. Unlike the POSLnet and PIRSLnet, the PMF  $ED_e$  profiles were not smooth, with the excursion only consisting of two samples (at 39,500 cal BP and 40,500 cal BP).  $ED_R$  values calculated for this material suggest that it was associated with an elevated dose rate (~0.3 – 0.5 mGy yr<sup>-1</sup> greater than the underlying material), but not sufficiently elevated to account for the ~100 – 200 Gy difference in the PMF  $ED_e$  values. Despite the sensitivities varying significantly between aliquots, the  $ED_e$  values were consistent within each aliquot pair. This suggests that these trends were not reflecting a signal from a very short event within each sample window, and instead a signal that is common to the bulk of each sample (as statistically, the likelihood of even loading of aliquots is lower for events which form a smaller proportion of the sample volume).

Whilst this positive excursion in  $ED_e$  values does not coincide directly with the magnetic field reversal during the Laschamp geomagnetic excursion, it aligns with a ~3,000–year period of higher relative palaeointensity (normalised

depositional remanent magnetism) (analysed by M. Hyodo; Hyodo *et al.*, 2022; Figure 5.4A). This apparent correlation is of note at the sampling resolution used in this study. Confirming this observation with higher resolution luminescence characterisation and supporting evidence for a mechanism linking these variables will be the focus of future work.

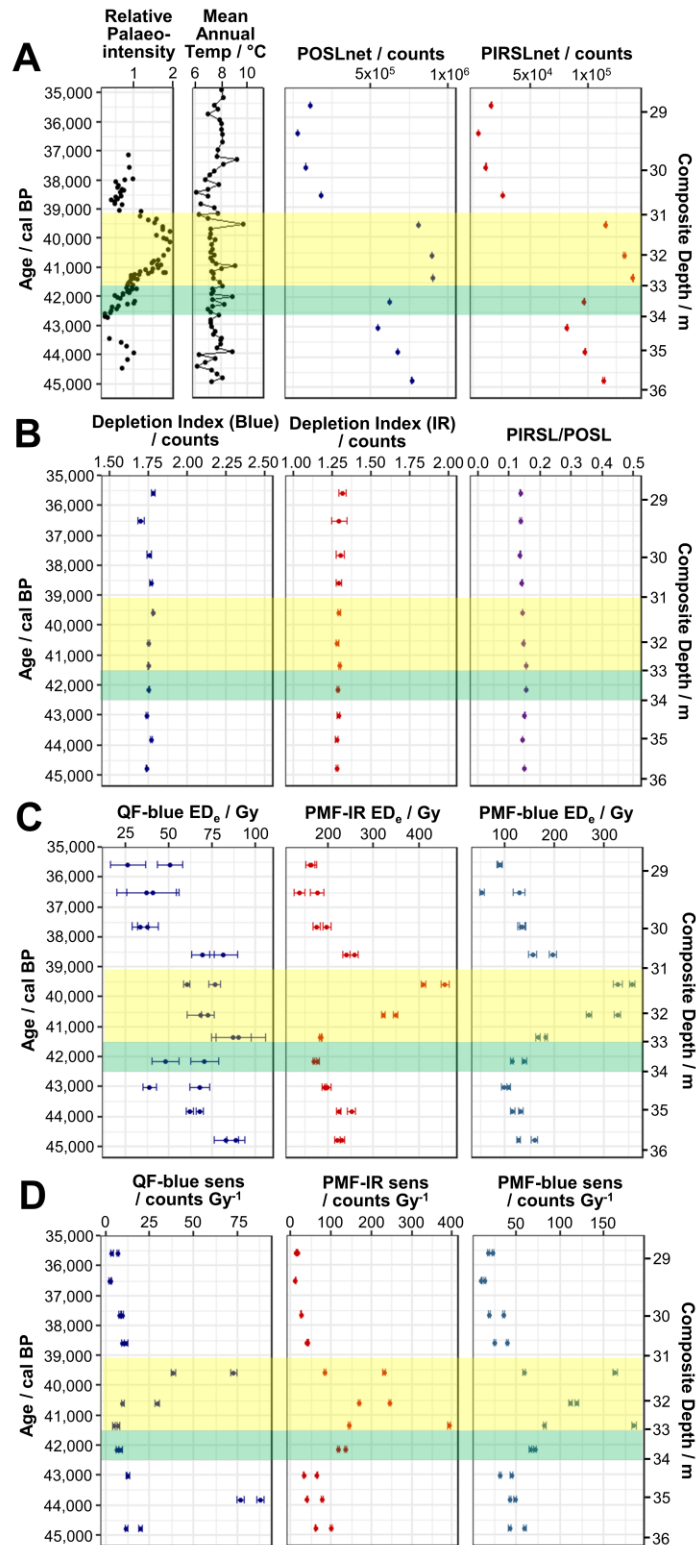


**Figure 5.4 Results of the POSL and lab profiling analysis of Time Period 2.** Results of the POSL (panels A and B) and lab profiling (panels C and D) analysis for the 11 samples in Time

Period 2. Panel A also shows contextual data (relative palaeointensity ( $J_{200^\circ\text{C}}/X_{200^\circ\text{C}}$ ; analysed by M. Hyodo; Hyodo *et al.*, 2022) and pollen-reconstructed mean annual temperature from Suigetsu). Green horizontal bars highlight the Laschamp geomagnetic excursion. Yellow horizontal bars highlight the period of higher relative palaeointensity following the Laschamp.

### 5.7.3 Time Period 3, the Varve Limit

A marked shift in a number of variables was observed across the varve limit (between 71,500 yr BP and 71,000 yr BP; Figure 5.5), with samples taken from the varved sediment exhibiting larger POSLnet and PIRSLnet values (Figure 5.5A),  $ED_e$  values (Figure 5.5C) and sensitivities (Figure 5.5D) than the underlying non-varved sediment. The two samples taken from within the transitional clay produced intermediate signals between these end members. The transition from low to high  $ED_e$  was most dramatic in the PMF-IR and PMF-blue profiles despite the younger samples also showing higher sensitivities, however the QF-blue  $ED_e$  profile also showed elevated values post-transition. The different luminescence characteristics observed in each sedimentological regime suggest a major shift in catchment conditions during this period, however there were no distinct changes in the depletion indices or PIRSL/POSL ratio, suggesting that changes in mineralogy and dose history did not contribute to the variations in POSLnet, PIRSLnet and  $ED_e$  (Figure 5.5B).

The conflicting presence of higher  $ED_e$  values in the younger sediment may be associated with a change in dose rate resulting from abrupt changes to lake chemistry. It is thought that varve formation was initiated in Lake Suigetsu due to an abrupt deepening of the lake (possibly due to movement of the adjacent Mikata fault) which induced bottom water anoxia (Nakagawa *et al.*, 2012), a process which is associated with incomplete mixing during lake overturning. This change in oxygenation (and therefore redox conditions) is corroborated by large differences in Fe and Mn concentrations above and below the onset of varving, as detected in the ICP-OES measurements (analysed by V. Olive), and an increase in the MnO/Fe<sub>2</sub>O<sub>3</sub> ratio analysed using a Horiba XGT-2700 (by D. Horiuchi and R. Tada; Figure 5.5A). The varved sediments also contain elevated U, Th and K concentrations in relation to the underlying non-varved sediment (analysed by V. Olive; Table 5.1), resulting in a factor of ~2 increase in the  $ED_R$  which, when applied to the  $ED_e$  values in Figure 5.5, aligns the first-order age approximations of the varved and non-varved sediment, supporting the thesis that the observed variation in  $ED_e$  is one driven by dose rate. It is possible that

the change in redox conditions at this transition resulted in this enrichment of radiogenic elements, however, further assessment of decay series disequilibria and the time-dependency of chemical alterations (including U-enrichment) is required to better characterise this transition.

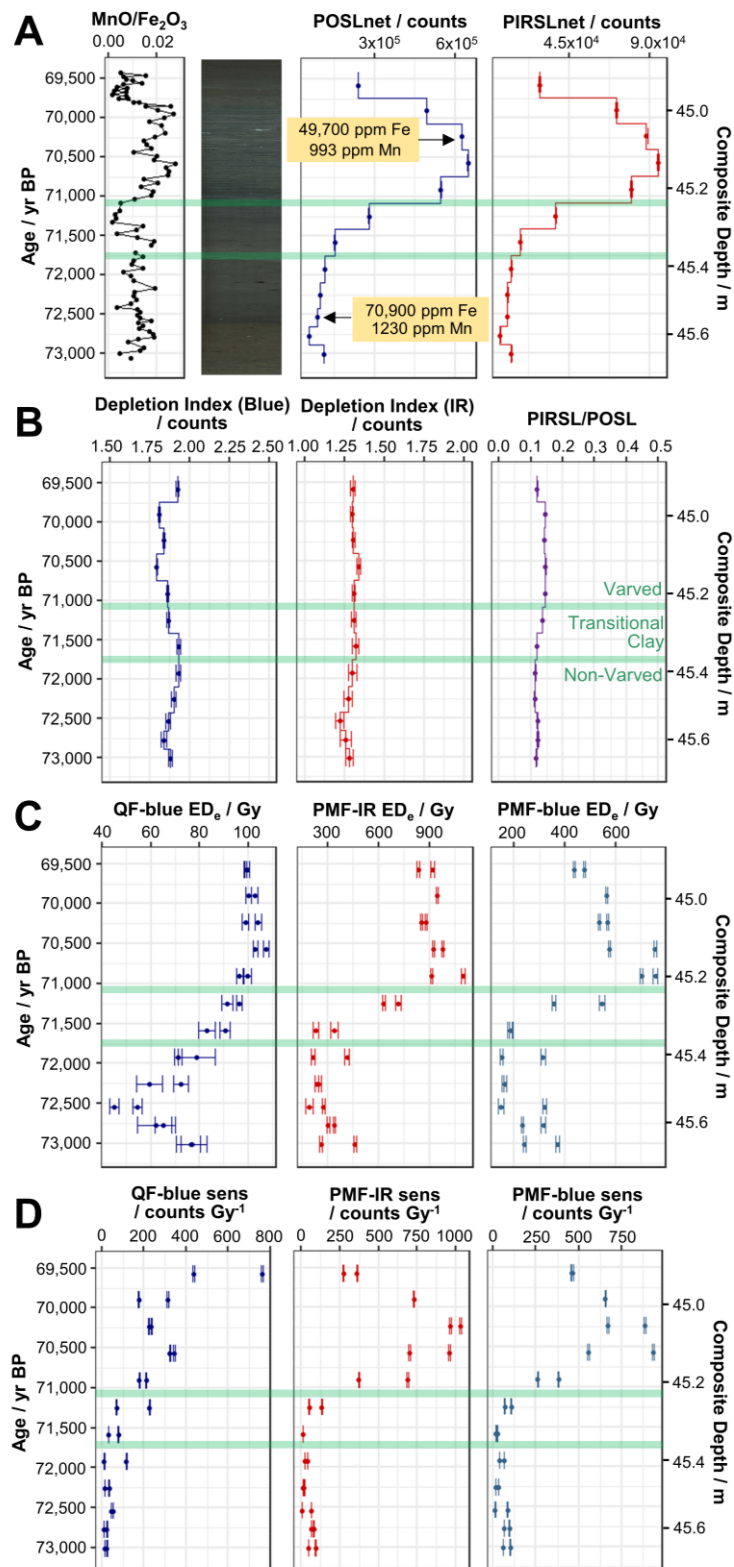


**Figure 5.5 Results of the POSL and lab profiling analysis of Time Period 3.** Results of the POSL (panels A and B) and lab profiling (panels C and D) analysis for the 12 samples in Time

Period 3. Panel A also shows contextual data (core photograph taken by T. Nakagawa, MnO/Fe<sub>2</sub>O<sub>3</sub> analysed by D. Horiuchi and R. Tada on a Horiba XGT-2700 and Fe and Mn contents from ICP-OES analysed by V. Olive (yellow boxes)). Green horizontal bars bracket the transitional clay layer, which separates varved from non-varved sediment.

**Table 5.1 Results of the ICP-MS and ICP-OES analysis and water content calculations.**

Uranium (U), thorium (Th) and potassium (K) concentrations from ICP-MS/ICP-OES (analysed by V. Olive) and estimated water content as used in the microdosimetry calculations.

| Sample Code<br><i>Mean Age</i>      | U<br>concentration<br>/ ppm | Th<br>concentration<br>/ ppm | K<br>concentration<br>/ ppm | Est. water<br>content/<br>%dry weight |
|-------------------------------------|-----------------------------|------------------------------|-----------------------------|---------------------------------------|
| HOL-12<br><i>184 cal BP</i>         | 4.74 ± 0.03                 | 8.51 ± 0.03                  | 12400 ± 63.9                | 350 ± 50                              |
| LAS-05<br><i>39,583 cal BP</i>      | 4.59 ± 0.02                 | 14.1 ± 0.18                  | 18800 ± 271                 | 80 ± 15                               |
| LAS-05 (R)<br><i>39,583 cal BP</i>  | 4.67 ± 0.05                 | 14.3 ± 0.05                  | 18800 ± 269                 | 80 ± 15                               |
| LAS-09<br><i>43,010 cal BP</i>      | 4.03 ± 0.05                 | 11.2 ± 0.10                  | 15900 ± 260                 | 80 ± 15                               |
| VAR-03<br><i>70,234 yr BP</i>       | 3.75 ± 0.02                 | 16.3 ± 0.06                  | 21500 ± 250                 | 80 ± 15                               |
| VAR-10<br><i>72, 541 yr BP</i>      | 2.29 ± 0.02                 | 9.34 ± 0.11                  | 13300 ± 156                 | 150 ± 30                              |
| TERM-04<br><i>123,450 yr BP</i>     | 7.76 ± 0.06                 | 8.54 ± 0.06                  | 13000 ± 107                 | 150 ± 30                              |
| TERM-04 (R)<br><i>123,450 yr BP</i> | 7.86 ± 0.04                 | 8.68 ± 0.09                  | 12700 ± 260                 | 150 ± 30                              |

#### 5.7.4 Time Period 4, Termination II

The POSLnet and PIRSLnet profiles for Termination II were broadly similar in shape, and both measures showed an overall increase with depth (Figure 5.6A). There were some small anomalies in the blue depletion index and the PIRSL/POSL ratio (Figure 5.6B) corresponding to some of the more extreme net values, which suggests that such values could be driven by different bleaching histories or mineralogical variations (changing quartz contents). It was not possible to determine sensitivity and ED<sub>e</sub> values for all samples due to low mineral abundances and sensitivities. Where it was achievable, the values were shown to be highly variable between aliquots, between measurement techniques, and through time (Figure 5.6C and Figure 5.6D).

Termination II covers the broadest time range in this study and thus variability was anticipated, given the multiple high-amplitude environmental and sedimentological variations occurring during this transition from cold to warm temperatures. Lake Suigetsu itself was non-static during this period, and sedimentological evidence suggests that it transitioned from fluvio-lacustrine in

MIS 6 to lacustrine (and brackish) during MIS 5e, representing a dynamic environment both physically and geochemically. Another possible contributor to the lack of distinct trends is the implementation of spot sampling at low resolution over a large age range, which can result in additional noise (as samples capture extremes of environmental conditions without context from adjacent material). Despite it being difficult to isolate individual influences without relevant complementary data from sedimentological analysis, these observations suggest that the luminescence characteristics of this sediment are sensitive to a variety of competing environmental factors which could include lake depth, catchment drainage patterns, lake geochemistry, sediment source, flood events and climatic factors.

### 5.7.5 Estimated Dose Rates

The  $ED_R$  values showed down-core variations as a result of changing elemental concentrations, estimated water content and cosmic dose rate (Table 5.1). The values were on the order of  $\sim 1$  to  $3 \text{ mGy yr}^{-1}$  (Table 5.2). When the  $ED_R$  values are considered alongside the  $ED_e$  values from the lab profiling, differences between chronometers are apparent; both the QF-blue and the PMF-blue  $ED_e$  values yield first order approximate ages which are broadly consistent (within an order of magnitude) with the existing Suigetsu timescale ages across Time Periods 2, 3 and 4, with the former underestimating age for  $ED_R$  values approaching the upper bound ( $\sim 3 \text{ mGy yr}^{-1}$ ) and the latter typically overestimating age for the  $ED_R$  values approaching the lower bound ( $\sim 1 \text{ mGy yr}^{-1}$ ). The  $ED_e$  values derived from the PMF-IR measurements consistently overestimate the existing Suigetsu ages, and the signals from all three fractions overestimate the true age of the sediment from Time Period 1. Constraining ages beyond these tentative observations would be erroneous, given the uncertainties in  $ED_R$  calculation (namely assumptions relating to the estimation of alpha efficiency, grain size and internal grain activity) and  $ED_e$  calculation (given that the samples are not mineralogically pure and only two aliquots were measured per fraction). However, these estimations do suggest that the PMF-IR signal is better suited as an environmental tracer, and that the QF-blue and PMF-blue signals show greater chronometric accuracy.

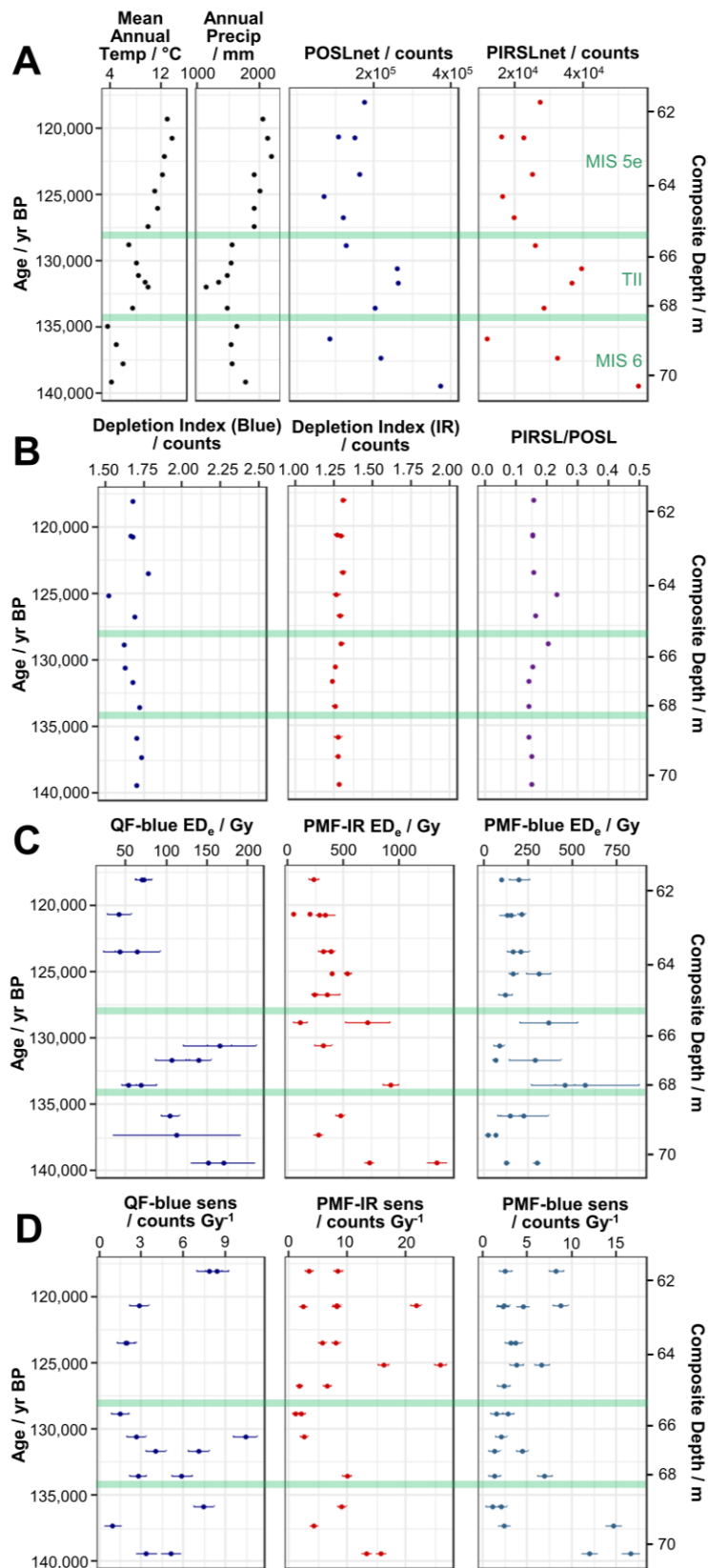


**Figure 5.6 Results of the POSL and lab profiling analysis of Time Period 4.** Results of the POSL (panels A and B) and lab profiling (panels C and D) analysis for the 13 samples in Time Period 4. Panel A also shows contextual data (pollen-reconstructed mean annual temperature and pollen-reconstructed total annual precipitation from Suigetsu, provided by T. Nakagawa). Green horizontal bars indicate approximate boundaries between MIS 6, TII and MIS 5e, based on the pollen-reconstructed average annual temperature.

**Table 5.2 Results of the microdosimetry calculations.** Results of the microdosimetry calculations for scenarios 1 and 2, assuming activity-free grains in the former and that the internal contents are equal to the matrix in the latter. The cosmic dose rate is inferred from sedimentological information, the remainder are calculated from the ICP-MS/ICP-OES results in Table 5.1.

| Sample Code<br><i>Mean Age</i>      | Scenario 1 (Activity-Free Grains)        |   |  |                                 |   | Scenario 2 (Internal Contents Equal to Matrix) |   |  |                                 |   |
|-------------------------------------|--|---|--|---------------------------------|---|--|---|--|---------------------------------|---|
|                                     | Effective Alpha/<br>mGy yr <sup>-1</sup> | Effective Beta/<br>mGy yr <sup>-1</sup> | Effective Gamma/<br>mGy yr <sup>-1</sup> | Cosmic/<br>mGy yr <sup>-1</sup> | Total ED <sub>R</sub> /<br>mGy yr <sup>-1</sup> | Effective Alpha/<br>mGy yr <sup>-1</sup>       | Effective Beta/<br>mGy yr <sup>-1</sup> | Effective Gamma/<br>mGy yr <sup>-1</sup> | Cosmic/<br>mGy yr <sup>-1</sup> | Total ED <sub>R</sub> /<br>mGy yr <sup>-1</sup> |
| HOL-12<br><i>184 cal BP</i>         | 0.141 ± 0.023                            | 0.354 ± 0.001                           | 0.262 ± 0.000                            | 0.000                           | 0.757 ± 0.023                                   | 0.621 ± 0.001                                  | 0.415 ± 0.001                           | 0.262 ± 0.000                            | 0.000                           | 1.299 ± 0.792                                   |
| LAS-05<br><i>39,583 cal BP</i>      | 0.483 ± 0.068                            | 1.228 ± 0.004                           | 0.902 ± 0.001                            | 0.000                           | 2.612 ± 0.068                                   | 1.040 ± 0.002                                  | 1.355 ± 0.004                           | 0.902 ± 0.001                            | 0.000                           | 3.297 ± 1.932                                   |
| LAS-05 (R)<br><i>39,583 cal BP</i>  | 0.492 ± 0.044                            | 1.079 ± 0.004                           | 0.914 ± 0.001                            | 0.000                           | 2.485 ± 0.044                                   | 1.060 ± 0.002                                  | 1.365 ± 0.003                           | 0.914 ± 0.001                            | 0.000                           | 3.339 ± 1.955                                   |
| LAS-09<br><i>43,010 cal BP</i>      | 0.406 ± 0.056                            | 0.993 ± 0.004                           | 0.754 ± 0.001                            | 0.000                           | 2.153 ± 0.056                                   | 0.878 ± 0.003                                  | 1.149 ± 0.004                           | 0.754 ± 0.001                            | 0.000                           | 2.780 ± 1.630                                   |
| VAR-03<br><i>70,234 yr BP</i>       | 0.472 ± 0.041                            | 1.399 ± 0.004                           | 0.945 ± 0.001                            | 0.000                           | 2.816 ± 0.041                                   | 1.003 ± 0.001                                  | 1.439 ± 0.002                           | 0.945 ± 0.001                            | 0.000                           | 3.388 ± 1.993                                   |
| VAR-10<br><i>72, 541 yr BP</i>      | 0.189 ± 0.058                            | 0.594 ± 0.003                           | 0.399 ± 0.001                            | 0.050                           | 1.233 ± 0.058                                   | 0.504 ± 0.003                                  | 0.625 ± 0.004                           | 0.399 ± 0.001                            | 0.050                           | 1.579 ± 0.897                                   |
| TERM-04<br><i>123,450 yr BP</i>     | 0.386 ± 0.055                            | 0.856 ± 0.003                           | 0.617 ± 0.001                            | 0.050                           | 1.909 ± 0.055                                   | 1.084 ± 0.002                                  | 0.910 ± 0.003                           | 0.617 ± 0.001                            | 0.050                           | 2.662 ± 1.544                                   |
| TERM-04 (R)<br><i>123,450 yr BP</i> | 0.391 ± 0.055                            | 0.852 ± 0.005                           | 0.621 ± 0.001                            | 0.050                           | 1.914 ± 0.056                                   | 1.099 ± 0.002                                  | 0.907 ± 0.005                           | 0.621 ± 0.001                            | 0.050                           | 2.677 ± 1.554                                   |

## 5.8 Discussion

### 5.8.1 Luminescence Characteristics and Environmental Change

Throughout all four time periods it was possible to quantify a range of luminescence characteristics from the Suigetsu sediments. In most cases, the trends detected by the POSL and lab profiling approaches were very similar, and both techniques identified the same key environmental shifts in each of the four periods. The differences between the POSLnet and PIRSLnet profiles and the  $ED_e$  profiles can be attributed to variations in sensitivity, and as such, it could be argued that by removing the sensitivity component, the lab profiling approach provided a more accurate representation of down-core luminescence characteristics and should be the principal methodology for future studies. Moreover, the lab profiling analysis was conducted on chemically treated fractions with better (albeit not perfect) mineralogical constraint, which, by virtue, provides more accurate  $ED_e$  values. However, the POSL approach provided a more comprehensive suite of measurements (including depletion indices and PIRSL/POSL) which have the potential to capture a broader range of environmental shifts (albeit that they did not serve this function within the context of the present study). Additionally, the trends were clearer when a more intense, contiguous sampling approach (such as that used for Time Periods 1 and 3) was used, as this provided key contextual information and continuous data across transitions. The POSL approach is more suited to this type of sampling because it allows for rapid, non-destructive measurement of samples without a requirement for chemical preparation. Furthermore, the POSL analysis was conducted on larger samples (reducing geostatistical scatter). As a result, using both methods in a paired approach has advantages, as this offers both a more accurate determination of luminescence characteristics and a breadth of proxies for consideration. However, if large quantities of samples are necessary to clearly isolate trends, then the POSL approach is demonstrably sufficient for this purpose, especially in conjunction with complementary data. Calibrating the sensitivity of the POSL using an external radiation source could offer a means to ascertain sensitivity-corrected approximations of  $ED_e$  whilst minimising processing time for large sample quantities (Munyikwa and Brown, 2014; Stone *et al.*, 2015).

The principal signals seen in the key variables: POSLnet; PIRSLnet and  $ED_e$  were interpreted as relating to the different predominant environmental factors in each of the four time periods, allowing us to well-characterise the effects (and non-effects) of a range of distinctive perturbations. Hence, any common drivers between the time periods were masked by high amplitude variations of a single driver in each case. Differences in sampling approaches also preclude common interpretation of the variables as a result of different intervals between samples (and hence probing the variables on different timescales), amounts of integrated time within each sample (providing different weightings to single event layers) and the proficiency of contiguous versus spot-sampling approaches to identify trends on different scales, as discussed above. Not all of the luminescence variables could be attributed to a specific environmental change, however this could be due to our incomplete understanding of past catchment changes. Further “ground-truthing” of these proxies is required in other lacustrine settings (building on the work of Pířková *et al.* (2019)) to extend the applicability of this technique elsewhere. Nonetheless, it is highly promising that some of the selected variables were sensitive to known catchment changes, and that drivers could be hypothesised for other variables. This shows that by using POSL and lab profiling analysis, it was possible to gain further insight into environmental change at Lake Suigetsu.

### 5.8.2 Assessment of Dating Potential

Future luminescence dating of the Suigetsu cores is feasible based on the approximations of  $ED_e$  and  $ED_R$  shown above in Section 5.7. All the samples from Time Periods 3 and 4 (which are older than the limit of radiocarbon dating, and hence targets for future dating) produced quantifiable natural signals. Responses were consistently measurable for large doses (50 Gy) but not small (5 Gy), suggesting that the grains are low in sensitivity, but not insufficiently sensitive so as to preclude future construction of dose response curves. A comparison of quartz and polymineral chronometric accuracy tentatively suggested that the QF-blue and PMF-blue signals were consistent with the existing Suigetsu chronology. Hence, blue light OSL dating of quartz is one possible future dating method (because the QF-blue fraction was highly dominated by quartz), however, the QF-blue fraction showed lower sensitivities and the quantity of quartz within the sediment was lower than other mineralogies. A key

consideration for sampling will be how this (alongside the availability of core material) will direct sampling. Another possible method is blue light OSL dating of feldspar. The luminescence signal of feldspars dominates the PMF–blue signals (which showed good chronometric accuracy) from the Suigetsu cores because of the low abundance and sensitivity of quartz within the PMF–blue fraction (which therefore contributes very small amounts of signal). The PMF–IR signals consistently overestimated the age of the material and hence will not be suitable for dating (however, these signals are valuable contributors of information regarding catchment environmental change).

Additional considerations for dating are a better appraisal of quartz saturation via the construction of dose response curves, and an assessment of the feldspar fraction for evidence of incomplete bleaching to avoid an over–estimate of age. Further to this, it will be important to refine any calculations of dose rate; particularly by quantifying decay series disequilibrium (through alpha spectrometry) and developing a model of water content variability in order to reduce age uncertainty. Additionally, in light of the other key finding of this study (that luminescence signals from this material are influenced by environmental change), it would be incorrect to interpret any calculations of age as if this were not the case. Careful sampling (e.g., by avoiding the sampling of flood layers) will be vital when looking to determine full OSL ages for the Suigetsu cores, as will making use of further luminescence profiling to characterise these effects around target horizons for dating. Despite these complexities, the evidence suggests that luminescence dating can contribute accurate, meaningful age information to the current Suigetsu age–depth model.

## 5.9 Conclusions

A combined approach of POSL analysis and lab profiling provided a complementary suite of variables which detected a range of environmental changes at Lake Suigetsu, Japan. Across the four time periods, the luminescence characteristics of the sediment showed a clear response to flood events (Time Period 1) and the initiation of varving (Time Period 3), and broad fluctuations which coincided with variations in magnetic palaeointensity (Time Period 2) and a complex response to environmental changes during Termination II (Time Period 4). There was no response of the luminescence proxies to the connection of Lake

Suigetsu to the Sea of Japan (Time Period 1). Local environmental perturbations which caused a sedimentological change across decadal to centennial timescales showed the clearest trends in the luminescence profiles when probed with contiguous, high-resolution sampling. The value of these techniques in a lacustrine setting was demonstrated across a ~140,000-year age range. POSL analysis and lab profiling provide a practical solution to the time- and core material-constraints of traditional luminescence analysis, whilst allowing the detection of catchment-sensitive signals. The core material produced quantifiable luminescence signals and hence future luminescence dating is feasible. First order approximate ages from the PMF-IR signals suggest that these produce an overestimation of age, and hence future dating will target the QF-blue signal (which equates to blue light OSL dating of quartz) and PMF-blue signal (which equates to blue light OSL dating of feldspar), alongside a more accurate assessment of dose rate. The contribution of this work to our understanding of past dynamics at Lake Suigetsu demonstrates the applicability of rapid luminescence profiling of lake sediment cores for characterising past environmental change.

## Chapter 6 Summary and Future Work

This thesis was motivated by the uncertainty surrounding EAWM and EASM evolution during periods of global warming. An improved understanding of how the EAM responds to rising temperatures is vital because the spatial and temporal redistribution of precipitation as a result of anthropogenic climate change could increase the vulnerability of this densely populated area in the coming decades. A means to achieving a better understanding of deglacial EAM behaviours is provided by palaeo-EAM reconstructions which have the temporal coverage, resolution, and chronological control to effectually assess EAM evolution during previous periods of warming. Reconstructing EAWM and EASM evolution during TI and TII (which exemplify accessible, contrasting examples of deglaciation) in Japan (using the archipelago's unique hydrological distribution) is of particular interest in pursuit of this goal.

This chapter firstly provides a summary of the research presented in this thesis (Section 6.1). These findings are then considered in the context of the thesis aim and objectives set out in Section 1.3.4 (Section 6.2). This is supplemented by discussions of the broader relevance of the findings (Section 6.3), and suggestions for future work (Section 6.4).

### 6.1 Summary of Findings

#### 6.1.1 The Contemporary Stable Isotope Hydrology of Lake Suigetsu and Surrounding Catchment (Japan) and its Implications for Sediment-Derived Palaeoclimate Records (Chapter 2)

The relationship between contemporary  $\delta_{\text{lake}}$  and  $\delta_{\text{precipitation}}$  at the Five Lakes of Mikata catchment was explored in Chapter 2. The first key finding of this monitoring study was that the behaviour of  $\delta_{\text{precipitation}}$  was closely linked to the duality of the EAM and its operation as two contrasting seasonal modes.

- There were limited seasonal differences in  $\delta^{18}\text{O}$  and  $\delta^2\text{H}$  due to the similar compositions of EAWM and EASM precipitation, aside from subtle minima in winter and summer attributed to greater quantities of precipitation in these seasons.

- Contrastingly,  $d$ -excess showed very strong seasonality due to contrasting evaporation conditions in the source regions of EAWM and EASM precipitation. Relative to Tokyo, this seasonal contrast in  $d$ -excess values was enhanced by the location of the Five Lakes of Mikata adjacent to the Sea of Japan; this area experiences more balanced EAWM and EASM influences than other parts of Japan.
- Temperature effects on  $\delta_{\text{precipitation}}$  were not supported statistically, however there was some qualitative evidence to suggest a local amount effect, albeit dwarfed by the seasonality of precipitation. This was reinforced by qualitative observations of minima during the wettest seasons of the year.
- Short-term high intensity precipitation events, including typhoons, were also detected at the catchment.

The second key finding of Chapter 2 was that the compositional patterns observed in the precipitation delivered to the catchment were detectable in the surface waters of the lake system, strongly supporting isotope signal propagation from precipitation to Lake Suigetsu.

- The seasonal trends observed in  $\delta_{\text{lake}}$  paralleled  $\delta_{\text{precipitation}}$  and were attributed to the same causes. Hence, we concluded that surface  $\delta_{\text{lake}}$  was closely related to fluctuations in the composition of EAWM and EASM precipitation across the ~150 ka covered by the Lake Suigetsu sediment cores.
- The influence of isolated events (including typhoons) was negligible relative to the extended seasons of precipitation associated with both EAM modes.
- The effects of local processes on  $\delta_{\text{lake}}$  varied in magnitude, and included in-catchment homogenisation, a two- to three-month transit lag, summer evaporative enrichment and the influence of saline water from the Sea of Japan.
- We inferred that, of these, only the homogenisation and transit lag effects were influential in a palaeo context, because Lake Suigetsu was isolated from the Sea of Japan until AD 1664 (aside from known intervals assigned by diatom assemblage counts) and evaporation would have been

reduced under the influence of the cooler climate which typified much of the period covered by the cores.

- In contrast to the seasonal fluctuations in surface  $\delta_{\text{lake}}$ , the deep water at Lake Suigetsu was stable and exhibited a homogenous, annually integrated composition.
- These observations (alongside the transit lag) highlighted the importance of understanding proxy seasonality during palaeoclimate reconstructions (especially for generating reconstructions of EAWM and EASM  $\delta_{\text{precipitation}}$  based on  $\delta^{18}\text{O}$  and  $\delta^2\text{H}$ , and not d-excess) and knowing whether a proxy captured surficial  $\delta_{\text{lake}}$ , deepwater  $\delta_{\text{lake}}$ , or  $\delta_{\text{precipitation}}$ .
- The findings presented in this chapter were limited to contemporary observations on an event or weekly basis, and hence it was not possible to make concrete inferences about long-term drivers of EAM  $\delta_{\text{precipitation}}$  at a (sub)centennial resolution, however, possible controls, including monsoon strength (supported by observations at the Suigetsu catchment and across Japan), were explored.
- It was, nonetheless, possible to infer that changes to EAM  $\delta_{\text{precipitation}}$  would have been detectable in  $\delta_{\text{lake}}$  and thus captured by the  $\delta^{18}\text{O}$  and  $\delta^2\text{H}$  proxy systems described in subsequent chapters.

### 6.1.2 Insights into Deglacial East Asian Monsoon Seasonality and Inter-Regional Teleconnections from Lake Suigetsu, Japan (Chapter 3)

Now able to support proxy interpretation with the contemporary dataset presented in Chapter 2, the seasonal behaviours of the EAM during Glacial Termination I were explored in Chapter 3. The first key finding of this study was based on oxygen isotope analysis of aquatic diatom silica during high %*Aulacoseira* intervals, which was used to reconstruct EAWM strength between 22,000 and 10,000 cal BP.

- The EAWM in Japan showed a gradual weakening trend across this period.
- The evolution of the EAWM during this interval exhibited no fluctuations coeval with stade-interstade shifts in either hemisphere, nor any similarities to winter temperatures at Lake Suigetsu (derived from pollen analysis of the cores).

- These observations suggested that EAWM weakening was driven by a gradual increase in northern hemisphere summer insolation across this transition, and that North Atlantic–style variations (typified by BA–YD fluctuations) did not affect the evolution of precipitation at Lake Suigetsu because this was principally driven by a smooth response of winter SSTs in the Sea of Japan to insolation.
- The unique nature of the trend observed at Lake Suigetsu relative to continental EAWM records, which exhibit clearer North Atlantic teleconnection signals during TI, can be explained by the location of Japan as geographically separate from Continental Asia.

The second key finding of Chapter 3 was based on compound–specific hydrogen isotope analysis of C<sub>30</sub> n–alkanoic acids (from terrestrial plants), which was used to reconstruct EASM evolution during TI.

- The EASM in Japan showed overall strengthening from the LGM to Holocene (driven by insolation), superimposed by an inverse relationship with Antarctic temperatures during the ACR (i.e., evidence for a Japan–Antarctica teleconnection post–16,000 cal BP).
- Reconstructions of EAWM versus EASM dominance reinforced this observation by noting a greater influence of the EASM on the Lake Suigetsu catchment during the early stages of the ACR and during the Holocene.
- These observations at Lake Suigetsu were distinctive relative to other EASM records from Continental Asia, which typically provide evidence for a North Atlantic teleconnection during TI, highlighting spatial heterogeneity in the expression of EASM signals during this period.
- The observations of EASM strength in Japan exhibited a different structure to a reconstruction of summer temperature at Lake Suigetsu, which also displayed North Atlantic character.
- It was proposed that an inverse ACR relationship with the EASM in Japan was caused by changes to coupled atmospheric–ocean circulation in the Pacific domain, which directly influenced the EASM in Japan but not temperature.

- The observations also suggested that the preservation of Antarctic-like signals at Lake Suigetsu was enhanced by the high latitude of the site and the location of Japan close to the Pacific Ocean.
- This Japan–Antarctica teleconnection was established between 16,000 and 15,000 cal BP, and it was posited that this was due to a northwards repositioning of the westerly jet (and thus the maximum northerly extent of the EAM front).
- Prior to this, the hydrogen isotope signals derived from C<sub>30</sub> n-alkanoic acids were variable due to a lack of a consistent regional driver of summer precipitation in Japan.

### **6.1.3 Novel Observations of East Asian Summer Monsoon Evolution During Glacial Termination II from Lake Suigetsu, Japan (Chapter 4)**

In order to compare the findings of Chapter 3 to a contrasting deglacial interval, EASM evolution and lake development at Lake Suigetsu during Glacial Termination II was explored in Chapter 4. The first key finding of this study was that the most major shifts in the early development of the Five Lakes of Mikata system occurred between ~131.0 and ~129.8 ka BP.

- Evidence for this was provided by the quantification of n-alkanoic acid and n-alkane concentrations, as well as n-alkane indices.
- Prior to this, the area was a dynamic, semi-aquatic fluvial system with shallow water and peat bogs, and after, a productive lacustrine system.
- The increase in aquatic productivity associated with this shift occurred rapidly (on the order of ~100 years), providing evidence for threshold behaviour.
- It was proposed that lake development was caused by a combination of tectonic subsidence and increased freshwater inputs from precipitation.
- Lake Suigetsu became saline during the Eemian global sea level highstand, which caused seawater to enter the lakes from the nearby Sea of Japan.

The second key finding of Chapter 4 was that the EASM in Japan strengthened between 132.5 and 130.0 ka BP, driven by Northern Hemisphere summer insolation, before weakening to 125.2 ka BP.

- These observations, based on  $\delta^2\text{H}$  analysis of  $\text{C}_{30}$  n-alkanoic acids, also suggested that there was submillennial-scale variability in EASM strength post-130.0 ka BP, which was consistent with some (but not all) existing EASM records from continental China during this interval.
- This ambiguity might have arisen due to the difficulty of detecting subtle fluctuations on this timescale during a period associated with a severely suppressed AMOC, or the influence of site location, with more northerly sites displaying submillennial-scale variability because they were more sensitive to subtle migrations of the westerly jet.
- The early EASM strengthening in Japan detected by this analysis was likely accompanied by an increase in temperature at the site.
- A comparison of EASM evolution at Lake Suigetsu and sites across China indicated that EASM behaviours during TII were extremely spatially heterogeneous, attributed to competing hemispheric influences.
- EASM strengthening occurred earlier and more slowly in Japan than mainland China, leading to the assertion that the EASM in Japan had a closer relationship to Antarctic temperatures due to its maritime location, and the EASM in China had a closer relationship to North Atlantic processes (although all sites have some degree of mixed character).
- Whilst these observations were broadly consistent with those from TI, EASM evolution during these two intervals was very different, with higher amplitude changes in EASM strength during TII and limited structural similarities between records from the Suigetsu cores.
- This was attributed to the different changing boundary conditions during these periods, including greater ice volumes in MIS 6 relative to MIS 2, and more rapid deglaciation with a larger insolation change during TII, but especially decoupled polar temperatures during TII, which would have enhanced the interhemispheric temperature gradient.

#### **6.1.4 Controls on Luminescence Signals in Lake Sediment Cores: a Study from Lake Suigetsu, Japan (Chapter 5)**

The application of luminescence techniques to the Suigetsu cores was explored in Chapter 5, partly with a view to assessing the feasibility of future OSL dating to facilitate a more robust comparison of records during TII (Chapter 4). The first key finding of this analysis was that the selected rapid core profiling

techniques (POSL analysis and lab profiling) were applicable to lake sediment cores, and that it was possible to detect environmental changes with these methods across the ~140 ka target age range.

- These techniques were suitable for detecting flood material (Time Period 1) and the onset of varving (related to changes in lake water chemistry; Time Period 3), as well as showing a possible relationship with normalised depositional remanent magnetism (Time Period 2) and complex environmental trends across TII (Time Period 4).
- However, no relationship to the salinity of the lake was observed (Time Period 1), so it was not possible to detect all types of environmental change using these methods.
- The clarity of the detectable trends was enhanced by focusing on the detection of local (catchment) changes by producing POSLnet and PMF-IR  $ED_e$  profiles using high resolution, contiguous sampling.
- Both the POSL and lab profiling approaches provided valuable contributions to the detection of each environmental change; the POSL offered rapid, non-destructive analysis and provided a broad suite of measurements, whereas the lab profiling provided sensitivity-corrected (and therefore more accurate)  $ED_e$  values.
- A combined methodology approach was recommended for future applications with a similar aim to this study. However, given their similarities, it would be reasonable to use POSL analysis in isolation, or only perform lab profiling on a small subset of samples, if the quantity of samples to analyse were large in number.

The second key finding of Chapter 5 was that the Suigetsu cores contain materials compatible with future OSL dating.

- Signals derived from the Time Period 3 and Time Period 4 samples (which were older than the existing radiocarbon-based chronology) were low in sensitivity, but not so severely as to preclude dose response curve construction.
- Critically, the signals detected from these samples were quantifiable.

- The first order age approximations derived from  $ED_e$  and  $ED_R$  quantities suggested that the QF–blue and PMF–blue signals showed greater chronometric accuracy than the PMF–IR signals. It followed that blue light OSL dating of quartz and feldspar grains should be targets for future dating efforts.
- One limitation of this technique was the low relative abundance of quartz grains within the sediments, and hence it was concluded that blue light OSL dating of feldspar grains was the most practical option.

## 6.2 Response to Thesis Aims and Objectives

The overall aim of this thesis was *to deconvolve East Asian Monsoon evolution in Japan during the last two glacial terminations*. Chapter 3 and Chapter 4 addressed this overarching aim most directly because they involved the construction of isotope–based EAM records from the Lake Suigetsu sediment cores for T1 and TII respectively. The findings of Chapter 3 supported those of Chapter 4 by providing the opportunity for the ground–truthing of proxy interpretation in a period associated with more contextual information about the catchment, as well as allowing for EASM behaviours during T1 and TII to be compared (Figure 1.9). The contemporary isotope monitoring presented in Chapter 2 was vital for the interpretation of the  $\delta^{18}O$  and  $\delta^2H$  records presented in Chapter 3 and Chapter 4, and critically underpinned these studies. Chapter 2 provided analysis which allowed for a more robust connection between  $\delta_{lake}$  and  $\delta_{precipitation}$  to be made and inferences to be drawn in a palaeo–context, including accounting for the seasonality of the isotope–based proxies utilised in subsequent chapters. Chapter 5 built on the findings of Chapter 4 by identifying the continuing need to seek independent age control for the Suigetsu cores in the pre–50 ka BP interval and investigated the luminescence characteristics of the cores (in the context of environmental change) and the potential of core materials for future luminescence dating.

The first objective of this thesis was *to contribute new records of palaeo–EAM behaviour to the growing regional record network*. This was met in Chapter 3 and Chapter 4, in which EAWM strength during T1 was reconstructed using oxygen isotope analysis of diatom silica, and EASM strength during T1 and TII was reconstructed using compound–specific hydrogen isotope analysis of  $C_{30}$

n-alkanoic acids. The balance between EAWM and EASM influence on Lake Suigetsu during TI was also inferred using compound-specific hydrogen isotope analysis of C<sub>16</sub> n-alkanoic acids and calculating the difference between this quantity and the hydrogen isotope analysis of C<sub>30</sub> n-alkanoic acids in each sample. Not only do all of these records offer high-resolution insights into the behaviours of each seasonal EAM mode, but they were also all lake core-derived, and hence begin to counteract the poor archive diversity currently exhibited by the existing regional record network. The TI records from the Suigetsu cores are associated with an excellent chronology, which is a rare quality, but exceptionally valuable for a better understanding of signal leads and lags when compared to records with similarly good age control.

The second objective of this thesis was *to consider the response of the EAM to warming temperatures*. This was met in Chapter 3 and Chapter 4, the former with respect to both EAM modes and the latter with respect to the EASM. The findings of these chapters support EAWM weakening and EASM strengthening with increasing Northern Hemisphere summer insolation, suggesting that these behavioural features occurred in response to rising global temperatures. However, the relationship of the EAM to temperature fluctuations on a submillennial scale (both locally and in remote regions) was more complex. None of the records generated as part of this thesis supported an association between the EAM and pollen-derived local temperature at Lake Suigetsu during either termination. This suggests that the EAM did not directly respond to rising temperatures in East Asia. However, the findings suggested that EASM strength varied synchronously with temperature changes in Antarctica (discussed further below in response to objective four). These observations highlight that on orbital timescales, when it is possible to consider global temperature increases as synchronous, a relationship between the EAM and temperature is clear. However, on centennial to millennial timescales, when regional temperature patterns diverge, this relationship becomes more ambiguous, and the EAM responded to temperature fluctuations in some regions and not others. Under these circumstances, rising temperatures and deglacial EAM evolution are better described as features of the sequence of changes which occurred during glacial terminations, rather than a simple isolated relationship.

The third objective of this thesis was *to deconvolve the different behaviours of the two seasonal modes of the EAM*. This was met in Chapter 3, which showed that EAWM and EASM evolution were fully decoupled during TI. The EAWM gradually weakened during this transition, whereas the EASM exhibited three-phase strengthening in line with Antarctic temperature changes. This showed that EAWM and EASM strength had opposite responses to orbital-scale changes, but that the coherency of their responses was lost when each seasonal mode was, or was not, affected by different teleconnection signals. This highlights the importance of reconstructing both seasonal modes in isolation for a more comprehensive view of EAM behaviours; currently, EASM records are significantly more common, leaving EAWM evolution overlooked and poorly constrained. Additionally, this emphasises the importance of understanding proxy seasonality thoroughly prior to making assertions about the behaviour of either mode; an incorrect seasonal assignment could provide a false description of EAM behaviours. The use of “annually integrated” proxies can provide information on the relative influence of each seasonal mode, but can also be affected by seasonally-specific teleconnection signals. In these cases, where the observed patterns can become complicated by multiple effects, it is necessary to exercise caution during interpretation.

The fourth objective of this thesis was *to determine the persistence of teleconnections and signal transfer into the EAM region*. This was principally met in Chapter 3, with some subsidiary observations in Chapter 4. Despite existing records strongly supporting a North Atlantic teleconnection to the EAM region, manifesting as variations in EAWM and EASM strength which aligned with stade-interstade fluctuations as detailed by the Greenland ice cores, the findings presented here suggested that these features are absent in EAM records from Japan. In terms of EAWM evolution, this may have been due to these signals being obscured by the interaction of EAWM winds with the Sea of Japan. For the EASM, an alternative teleconnection was detected; that connecting Japan and Antarctica. During TI and TII, EASM strength showed behaviour inverse to temperature progressions during the Antarctic cold reversal, and had a positive relationship with Antarctic warming, respectively. This suggests that this teleconnection expressed itself in different ways (inversely on suborbital timescales and positively on orbital timescales) but nonetheless provides strong

evidence that Antarctic temperature evolution had a relationship with the EASM in Japan during glacial terminations, likely propagated via the Pacific Ocean. During TI, it was also discussed that this teleconnection was temporally restricted to post-16,000 cal BP, and activated by a northwards shift of the westerly jet around this time. Similar discussions relating to behaviours during TII were prohibited by limitations to chronological control, but this concept remains an important consideration for future research.

The fifth and final objective of this thesis was *to rationalise spatial heterogeneities in these behaviours across the region*. This was met in Chapter 3 and Chapter 4, with particular emphasis on understanding the difference in EASM evolution between Continental Asia and Japan. Throughout, it was proposed that the unique signals detected in the records from Lake Suigetsu were as a result of a southern hemisphere (Antarctic) teleconnection as opposed to the “typical” North Atlantic teleconnection detected by continental archives. Furthermore, it was suggested that these different teleconnections were spatially restricted, and that Japan displayed greater Antarctic character as a result of its location directly adjacent to the Pacific Ocean, allowing for southern hemisphere signals to be propagated to the site. Conversely, North Atlantic behaviours were detected further inland, where down-stream influences via the westerlies and the westerly jet were greater. Greater spatial heterogeneity in EASM evolution was observed during TII relative to TI (even solely considering sites across mainland China), and it was posited that this was due to decoupled polar temperatures during this period, possibly combined with a latitudinal effect, which caused greater submillennial-scale variability at more northerly sites which are more sensitive to westerly jet migration. However, this ambiguity could be due to difficulties in detecting small amplitude signals during a period of severely suppressed AMOC.

### **6.3 Relevance of Findings**

Continuing to expand our collective knowledge of EAM behaviour is critical, and the greatest contribution of this thesis is to this cause. The EAM system operates across some of Earth’s most densely populated regions, for which research of deglacial behaviours is critical in the context of anthropogenic warming. The high-quality, high-resolution records presented as part of this thesis (alongside

the contemporary monitoring underpinning their interpretation and consideration of the pre-50 ka chronology extension) contribute directly to the expanding network of records which help to comprehend the complex behaviours of the EAM in the past, underpinning efforts for future predictions.

The contemporary monitoring of catchment water isotopes in Chapter 2 demonstrates the importance of this approach for understanding processes affecting catchment isotopes on palaeo-timescales in the absence of historical datasets. This is especially vital in the context of a highly seasonal climate system. This work also assists in reducing the uncertainty associated with the interpretation of other proxies from the Lake Suigetsu sediment cores which are the subject of ongoing investigations. Of particular interest is oxygen isotope analysis of siderite (which forms in the anoxic waters at the bottom of the lake), and our results suggest that this proxy will capture an integrated isotope signal over multiple seasons, possibly even years. As highlighted by the findings of Chapter 2, the development of paired  $\delta^{18}\text{O}$  and  $\delta^2\text{H}$  proxy measurements with the potential to produce reconstructions of palaeo d-excess is an exciting prospect because this variable is highly seasonal (allowing for distinction between EAM modes) and a potentially powerful proxy of past monsoon dynamics. If a proxy of deep water  $\delta^2\text{H}$  could also be identified and developed, then combination with siderite  $\delta^{18}\text{O}$  could facilitate palaeo d-excess calculation which would overcome the need for seasonally equivalent measures of  $\delta^{18}\text{O}$  and  $\delta^2\text{H}$  (which is necessary for d-excess calculations from surficial proxies).

The reconstructions of EAWM and EASM behaviour during TI presented in Chapter 3 not only highlight the value of season-specific analysis of the EAM (evidenced by the decoupled, rather than inversely related, evolution of each seasonal mode), but also demonstrate that multiple teleconnection signals can be preserved in records of EAM strength derived from different areas. Evidence shown in this chapter supports the notion that teleconnections between the EAM and other climate systems globally can be seasonally, spatially and temporally restricted. This suggests that EAM evolution has the potential to exhibit significant levels of complexity. This challenges previous perspectives that simplified EAM behaviours on suborbital timescales as responses to upstream (North Atlantic) processes, and provides additional evidence for cross-hemispheric signal transfer into the region. This work also adds to the

regional collection of records whilst highlighting the propensity of records from Japan to show unique trends due to its location on the Pacific margin, which should encourage more attention to this sector of the EAM domain.

The reconstruction of EASM behaviour during TII presented in Chapter 4 highlights the importance of studying EASM evolution across contrasting deglaciations in order to understand the evolution of this system more comprehensively. Whilst both T1 and TII have similarly evolving boundary conditions on an orbital scale, the differences on suborbital scales can result in very different patterns in EASM strength, which allows for drivers to be examined more closely. Additionally, the development of this new EASM reconstruction for TII from the Suigetsu cores demonstrates the value of expanding the geographic range of existing reconstructions and providing records from non-speleothem archives. The findings of Chapter 4, in addition to those of Chapter 3, also challenge the hitherto North Atlantic-centric interpretation of EASM drivers and allow for a broader consideration of global climate system processes during the penultimate deglaciation. On a more local scale, the greater understanding of catchment evolution at Lake Suigetsu during TII will assist in the interpretation of other proxy-based reconstructions from the Suigetsu cores during this interval. In particular, it will be vital to consider how the transition from a semi-aquatic to lacustrine environment could affect aquatic proxies, if these are to be utilised for reconstructing regional-scale climate behaviours.

Finally, the relevance of the investigation into sediment core luminescence characteristics (Chapter 5) is twofold. Firstly, the study demonstrates the application of luminescence techniques (both profiling and dating) to lake sediment cores. This was a relatively understudied intersection of Quaternary disciplines, but this work shows that luminescence techniques can be a valuable contribution to lake core analysis. Hence, they should be a consideration for future coring campaigns globally. Secondly, this study will underpin future efforts to refine the >50 ka BP Suigetsu core chronology. Realistically, the uncertainties of OSL dating will preclude the incorporation of this technique into the younger (<50 ka BP) chronology because it would not reduce the uncertainty in the radiocarbon dataset (nevertheless, there is utility in performing some dating measurements from the intervals where good chronological control exists,

by way of independently assessing the reliability of the technique). However, the older part of the chronology currently only contains one absolute age (that of the Ar–Ar dated Aso–4 volcanic eruption at ~86.4 ka BP), and hence there is significant potential for the inclusion of absolute OSL dates to supplement the existing wiggle–matching process. Chapter 5 demonstrates the potential for luminescence dating of the Suigetsu cores and shows that blue light–stimulated signals provided the highest chronometric accuracy, with blue light OSL of feldspars the most practical option based on mineral abundance.

## 6.4 Directions for Future Research

### 6.4.1 Contemporary Stable Isotope Monitoring

Future research relating to the contemporary catchment monitoring presented in Chapter 2 should consider how to enhance our understanding of the long–term drivers of  $\delta_{\text{precipitation}}$  at the Lake Suigetsu catchment and strengthen the quantitative relationship between  $\delta_{\text{precipitation}}$  and  $\delta_{\text{lake}}$ . This could be achieved via an extension of current monitoring, lake mass balance modelling (which has the additional benefit of constraining groundwater contributions), or the development of complementary historical palaeo–isotope and climate records. Integration of these findings with climate models would also enhance our knowledge of how variations in EAM strength affect  $\delta_{\text{lake}}$  (and hence the Suigetsu core proxies). Another avenue involves the examination of how different climate regimes would impact on the local processes affecting  $\delta_{\text{lake}}$ , including how glaciation affects the transit lag and how variations in summer temperature and precipitation quantity affect the influence of evaporative enrichment. This could be achieved with catchment modelling. Additionally, a more comprehensive view of freshwater propagation through the catchment could be accomplished with a higher temporal resolution study of the Hasu River to assess how rapidly (and to what extent) the river responds to precipitation events and changes in  $\delta_{\text{precipitation}}$ .

### 6.4.2 Applications of Luminescence Techniques to Lake Sediment Cores

Subsequent applications of POSL and lab profiling analysis to lake sediment cores in light of Chapter 5 should focus on expanding knowledge of what signals these

techniques are able to detect in terms of the amplitude and type of environmental change. Refining this technique in other lacustrine settings would be immensely valuable for understanding its general applicability. For example, within the context of Chapter 5 there was some evidence provided to support a relationship between POSLnet/ $ED_e$  and normalised depositional remanent magnetism, which should be further investigated using higher resolution sampling in order to robustly investigate this linkage and determine an underlying mechanism. Additionally, further multiproxy analysis across Time Period 4 would assist in deconvolving POSL signal evolution across this interval. In order to achieve independent OSL ages from the older part of the Suigetsu cores, more accurate  $D_R$  determinations are of critical importance, potentially via gamma spectrometry, or the quantification of decay series equilibrium via alpha spectrometry. The production of a model to reconstruct time-dependent water content at each target horizon is also vital to account for dose attenuation. Furthermore, mineralogically pure subsamples will be required for accurate determination of  $D_e$  values. It is likely that additional profiling to bracket any target horizons for dating will also be required to account for environmental effects (because the materials are also sensitive to these).

### 6.4.3 East Asian Monsoon Behaviours

Potential avenues for future work to build on the findings of Chapter 3 regarding EAM behaviours during TI include the addition of these records to regional scale syntheses of deglacial monsoon behaviours. Japan is often omitted from spatial analysis, due to its peripheral position in the EAM region, northerly latitude, and lack of high-resolution, well-dated records. However, as demonstrated, EAM reconstructions from Japan have a great deal to offer synthesis studies, as they exhibit alternative trends and different teleconnection signals, which provide vital information regarding the operation of the EAM system. In light of this, generating other records from Japan (and the Sea of Japan coast of Continental Asia) which span TI from across a diverse range of archives can provide a deeper perspective on the spatial limit of Antarctic versus North Atlantic teleconnections. Additionally, more records from a range of northerly latitudes could help to better understand the relationship between the Japan–Antarctica teleconnection and the migration of the westerly jet and EAM front. This work would have direct relevance for studies looking to reconstruct EASM behaviours

at northerly latitudes during glacial periods, when the EAM front was situated further to the south and summer precipitation may not have been monsoonal in nature.

Future work in the wake of the reconstruction of EASM behaviours during TII presented in Chapter 4 should continue to develop more records of EASM evolution during TII to help understand the behaviour of this system and rationalise system heterogeneities. Records from the northernmost extent of the EASM system are of particular interest, because these appear to display higher amplitude submillennial-scale fluctuations and hence could be more sensitive to remote climatic processes. Japan remains an important part of the EAM region and the potential of this area for the production of high quality EASM records should not be overlooked in the future. The dominance of speleothem-derived records continues to be a challenge for interpreting EASM strength during TII, and future work should aim to develop records from a greater variety of archive types. In line with this, it is vital that independent chronologies are developed for as many archives as possible, in order to facilitate the investigation of system leads and lags. In particular, decoupling the Greenland ice core chronology from the Hulu Cave speleothem record across this interval is vital in order for EASM behaviours to be compared to North Atlantic temperatures without introducing circularity. A further extension of this work would be the reconstruction of EAWM behaviours at Lake Suigetsu across this interval using oxygen isotope analysis of diatom silica, in order to compare these to the equivalent analyses from TI presented in Chapter 3. Contrasting EAWM evolution across TI and TII from a range of sites remains an important unresolved aspect of deglacial EAM behaviours not covered by this thesis.

Additionally, a natural extension of the work presented in Chapter 3 and Chapter 4 is the development of high-resolution records of EAWM and EASM evolution across earlier glacial terminations (including Terminations V – III) from across the region. Whilst archive preservation and chronological control become increasingly challenging in these earlier intervals, each of these periods have subtly different boundary conditions which would allow for further hypothesis testing of the ideas presented in this thesis. The Suigetsu cores do not extend to these terminations, but other archives from Japan (for example, Lake Biwa; Yasakawa *et al.*, 1973) should be a consideration for this work, especially in light

of the findings shown in Chapter 3 and Chapter 4, which highlight the value of reconstructions from this archipelago as part of comprehensive understanding of system behaviours. An important consideration of such research would be the impact of lower sedimentation rates on the records produced and whether these would limit the resolution of submillennial fluctuations. A possible extension to this work could involve circum-Pacific analysis, which could be used to deconvolve spatial trends and teleconnection methods during all Quaternary glacial terminations. Ultimately, it is hoped that by fully rationalising the behaviours of the EAM during a wide range of glacial terminations with different boundary conditions and deglacial sequences, it will be possible to compare these findings to the evolution of other monsoon systems, allowing for a holistic interpretation of how the “global monsoon” responds to deglaciation.

## Chapter 7 Conclusions

The East Asian Monsoon is a highly dynamic element of the global climate system operating across a ~10 million km<sup>2</sup> area spanning China, Korea and Japan. The central characteristic of the East Asian Monsoon system is semi-annually (twice a year) reversing surface level winds which propagate from the southeast during boreal summer and the northwest during boreal winter. These contrasting trajectories give rise to two dominant modes, known as the East Asian Summer Monsoon and East Asian Winter Monsoon, respectively. Whilst the East Asian Winter Monsoon is generally not associated with large quantities of precipitation due to its continental origins, the intense oceanic-derived rainfall brought to the area by the East Asian Summer Monsoon is a defining climatic characteristic of the region. Indeed, East Asian Summer Monsoon precipitation forms a key component of freshwater delivery for over 1.6 billion people. The drivers of the East Asian Monsoon are intricate because the system operates within both tropical and subtropical realms, and hence are affected by climate system perturbations in both.

In light of the dynamic, complex nature of the East Asian Monsoon, understanding how this system operates under contrasting climatic regimes and across key transitions is of particular interest, not least in light of recent anthropogenically-driven climate change. Glacial terminations (i.e., the rapid global transitions from glacial to interglacial conditions) are key features of late Pleistocene climate evolution, however knowledge of East Asian Monsoon behaviours across such intervals is limited, particularly on decadal to millennial timescales. Reconstructions of palaeo-East Asian Monsoon evolution from Japan offer an exciting opportunity to meet the need for records from across the East Asian Monsoon region, whilst providing insights into the behaviour of each seasonal mode in isolation. The latter is made possible as a consequence of the Japanese archipelago being situated between two water bodies; hence, both the East Asian Summer Monsoon and the East Asian Winter Monsoon deliver precipitation to Japan, resulting in a semi-annual precipitation pattern which is unique within the broader East Asian Monsoon region.

This thesis aimed to deconvolve East Asian Monsoon evolution in Japan during the two most recent glacial terminations using materials from the Lake Suigetsu

sediment cores. The Suigetsu cores comprise a high-quality archive from central Japan spanning >150,000 years across >98 m of composite depth and are associated with excellent chronological control for the most recent ~50,000 years. The location of Suigetsu on the Sea of Japan coast of Honshu Island optimises the lake for receiving large amounts of precipitation from both seasonal modes of the East Asian Monsoon annually. The composition of the Suigetsu cores makes it an ideal target for multiproxy analysis of materials with specific formation seasons, allowing for reconstruction of the East Asian Summer Monsoon and East Asian Winter Monsoon separately.

First, analysis of the stable isotope composition of contemporary catchment waters was used to facilitate the interpretation of isotope-based proxy reconstructions of past climate from the Lake Suigetsu sediment cores. Extended (multi-year) monitoring of precipitation, river water and lake water was used to establish the factors affecting the isotope composition across the catchment. Particular focus was placed on evaluating linkages between the composition of precipitation (which provides a link to regional scale hydrological change) and lake water (which is captured by sedimentary organic compounds, minerals, and fossils). This monitoring showed that the isotopes in precipitation were influenced by the East Asian Monsoon, although clear differences between EAWM and EASM precipitation reflecting the seasonality of this climate system was not observed in all isotope variables due to equifinality effects. The signals detected in the composition of precipitation were then transferred to the lake system and combined with secondary local influences, including catchment homogenisation, a transit lag, seasonal saline water incursions from the nearby Sea of Japan, and evaporative enrichment during summer. These observations suggested that reconstructions of past East Asian Monsoon behaviour can be derived from isotope-based proxies within the Lake Suigetsu sediment cores. This work also highlighted the importance of understanding lake stratification and proxy seasonality for robust interpretation of palaeo-isotope variability.

Second, these observations from contemporary monitoring were applied to isotope-based proxy analysis of the Lake Suigetsu sediment cores in order to separately reconstruct East Asian Winter Monsoon and East Asian Summer Monsoon behaviours during Glacial Termination I (from MIS 2 to MIS 1). East Asian Winter Monsoon evolution was analysed using oxygen isotope analysis of diatom

silica during periods where the abundance of spring-blooming *Aulacoseira* spp. diatoms was high. This demonstrated that the East Asian Winter Monsoon gradually weakened from 21.0 to 10.0 thousand years ago, exhibiting no correlation with stade-interstade fluctuations in either hemisphere. This was likely because East Asian Winter Monsoon precipitation in Japan is uniquely derived from the Sea of Japan, and gradual changes in this domain overprinted any influence of North Atlantic climate on winter wind strength. Contrastingly, East Asian Summer Monsoon behaviours (reconstructed using compound-specific hydrogen isotope analysis of C<sub>30</sub> n-alkanoic acids) showed an overall strengthening trend, with an inverse relationship to Antarctic temperatures during the Antarctic Cold Reversal (14.5 to 12.9 thousand years ago), likely propagated via the Pacific Ocean. This observation (when contrasted to other, continental, records) highlighted the potential for the East Asian Summer Monsoon to exhibit seasonally, spatially and temporally restricted remote links to different climate systems, including those in the opposite hemisphere. The distinctive trends exhibited by these reconstructions demonstrated the value of East Asian Monsoon records from the Japanese archipelago and their potential to contribute to a better, more comprehensive understanding of this climate system whilst challenging existing North Atlantic-centric drivers of East Asian Monsoon strength.

East Asian Summer Monsoon behaviours during Glacial Termination II (from MIS 6 to MIS 5e) were then reconstructed in order to examine how the system evolved during a contrasting example of rapidly rising global temperatures. Observations of East Asian Summer Monsoon strength were made using compound-specific hydrogen isotope analysis of C<sub>30</sub> n-alkanoic acids, which demonstrated that the East Asian Summer Monsoon strengthened to 130.0 thousand years ago before weakening into the Eemian. The concentrations of aquatic and terrestrial alkyl lipids were also used to reconstruct early lake development, and showed that Lake Suigetsu evolved from a shallow aquatic environment to a lacustrine one between 131.0 and 129.8 thousand years ago. This analysis showed that the East Asian Summer Monsoon strengthened earlier and more slowly in Japan than Continental China and highlights the extreme spatial heterogeneity across the East Asian Summer Monsoon regime during this interval, particularly in terms of submillennial-scale variability. Critically, these observations indicated that the

behaviour of the East Asian Summer Monsoon during Glacial Terminations I and II were distinctive due to the contrasting boundary conditions associated with each deglacial period. The different behaviours of polar temperatures during each termination appeared to be a key driver of these differences, and it was posited that this also caused the dissonance between records during Glacial Termination II. However, Japan consistently displayed closer links to Antarctic temperatures than North Atlantic processes across both terminations. This was in contrast to the well-established relationship between speleothem records from China and the climate of the North Atlantic.

The study of materials from Glacial Termination II in the Suigetsu cores (which are older than the limit of radiocarbon dating) provoked consideration of chronological control for intervals older than ~50 thousand years ago. Subsequently, the application of luminescence techniques to Suigetsu core materials for the detection of environmental change was investigated, and an assessment of the potential for optically stimulated luminescence dating was made. Rapid core profiling techniques (portable optically stimulated luminescence and laboratory profiling) were applied to four distinctive time periods, each selected for their unique environmental context and either local or global relevance, to ascertain if these methods were able to detect environmental shifts. This analysis showed that the luminescence characteristics of the Suigetsu sediments exhibited clear responses to flood events and the initiation of varving, as well as broad fluctuations during periods of variable magnetic palaeointensity and complex, compound responses to periods of environmental variability. No relationship to lake salinity was observed. The techniques were best applied to detect decadal to centennial local environmental changes via contiguous, high-resolution sampling. Secondly, the laboratory profiling results were combined with estimates of down-core dose rate variations to evaluate the feasibility of future luminescence dating. The presence of quantifiable luminescence signals indicated that the material is suitable for luminescence dating. Furthermore, the ages derived from blue light stimulations of quartz- and polymineral-dominated fractions were more accurate than those derived from infrared stimulations and should be the target of future dating efforts.

The results of this thesis emphasise the importance of contemporary stable isotope monitoring for the robust interpretation of palaeoclimate proxies derived from lake cores, expand current knowledge regarding the potential of the Lake Suigetsu sediment cores for luminescence dating, and contribute to the ongoing development of our collective knowledge of deglacial East Asian Monsoon behaviours. By generating new records of each seasonal mode, it was shown that major changes in East Asian Monsoon strength occurred alongside rising global temperatures during Glacial Terminations I and II. The different behaviours of each seasonal mode and their teleconnection signals were evaluated, and the most significant findings were that each seasonal mode evolved differently during Glacial Termination I, and that East Asian Summer Monsoon evolution in Japan was more closely aligned with Southern Hemisphere temperature patterns than in Continental Asia (which instead exhibited North Atlantic-like character) during Glacial Terminations I and II.

This highlights the value of reconstructions from Japan for demonstrating alternative East Asian Monsoon behaviours and remote links to Antarctica, the implication of which is a better understanding of how the East Asian Monsoon responded to submillennial temperature fluctuations in both hemispheres, and how such effects might have been spatially and temporally restricted. Additionally, this emphasises the importance of examining the East Asian Monsoon and its remote links to other areas in order to achieve a holistic understanding of how the global climate system operated during glacial terminations. It is hoped that a continuation of this work and creation of a high-density regional network of East Asian Monsoon records will develop knowledge to a level where discussions can be expanded to include other systems constituting the “global monsoon”. The findings of this thesis reduce uncertainty surrounding East Asian Monsoon evolution during periods of rapid global warming, which is vital for a better comprehension of this system in the context of anthropogenic warming and for the future vulnerability of the region.

# Appendices

## Appendix 1 – Publications

### Chapter 5 (Published Version)

Quaternary Science Advances 13 (2024) 100145



Contents lists available at ScienceDirect

Quaternary Science Advances

journal homepage: [www.sciencedirect.com/journal/quaternary-science-advances](http://www.sciencedirect.com/journal/quaternary-science-advances)



### The contemporary stable isotope hydrology of Lake Suigetsu and surrounding catchment (Japan) and its implications for sediment-derived palaeoclimate records

Charlie L. Rex<sup>a,\*</sup>, Jonathan J. Tyler<sup>b</sup>, Kazuyoshi Nagaya<sup>c</sup>, Richard A. Staff<sup>a</sup>, Melanie J. Leng<sup>d</sup>, Keitaro Yamada<sup>e</sup>, Ikuko Kitaba<sup>e</sup>, Junko Kitagawa<sup>c</sup>, Hideaki Kojima<sup>f</sup>, Takeshi Nakagawa<sup>e</sup>

<sup>a</sup> Scottish Universities Environmental Research Centre (SUERC), University of Glasgow, Scottish Enterprise Technology Park, Rankine Avenue, East Kilbride, G75 0QF, UK

<sup>b</sup> Department of Earth Sciences, University of Adelaide, Adelaide, South Australia, 5000, Australia

<sup>c</sup> Varve Museum, 122-12-1 Torihama, Wakasa-cho, Mikatakaminaka-gun, Fukui Prefecture, 919-1331, Japan

<sup>d</sup> National Environmental Isotope Facility, British Geological Survey, Keyworth, NG12 5GG, UK

<sup>e</sup> Research Centre for Palaeoclimatology, Ritsumeikan University, 1-1-1 Noji-higashi, Kusatsu, Shiga Prefecture, 525-8577, Japan

<sup>f</sup> Wakasa Mikata Jomon Museum, 122-12-1 Torihama, Wakasa-cho, Mikatakaminaka-gun, Fukui Prefecture, 919-1331, Japan

#### ARTICLE INFO

##### Keywords:

Stable isotopes  
Precipitation isotopes  
Lake water isotopes  
East Asian monsoon  
Sediment cores

#### ABSTRACT

The Lake Suigetsu sediment cores exemplify a high-quality archive of palaeoclimatic change in East Asia during the past 150 ka. Robust interpretation of stable isotope-based proxy reconstructions from the Suigetsu cores can be aided by a greater understanding of the factors affecting the isotope composition of the lake and how it relates to that of precipitation. Here we use extended contemporary monitoring to establish the factors affecting the stable isotope composition ( $\delta^{18}\text{O}$ ,  $\delta^2\text{H}$  and d-excess) of precipitation, river water and lake water in the catchment surrounding Lake Suigetsu, central Japan. We show that the composition of precipitation is influenced by the dual East Asian Monsoon system, producing minima in  $\delta^{18}\text{O}$  and  $\delta^2\text{H}$  and semi-annually varying d-excess values across the year. These signals are then transferred to the lake system, where they are combined with secondary local influences on lake water composition: homogenisation with existing catchment waters, a catchment transit lag, the interaction with saline water from the nearby Sea of Japan, and evaporative enrichment during summer. Our observations suggest that the palaeo-isotope composition of Lake Suigetsu was closely related to the behaviour of the East Asian Monsoon. We highlight lake stratification and proxy seasonality as critical components of signal interpretation.

#### 1. Introduction

The Five Lakes of Mikata are a collection of tectonic lakes located in Fukui Prefecture, central Japan, and comprise Lake Mikata, Lake Suigetsu, Lake Suga, Lake Kugushi and Lake Hiruga (Fig. 1). To-date, much of the Quaternary research undertaken on the lakes has focussed on Lake Suigetsu, the central lake of the system, by virtue of its unique underlying sedimentary sequence. This sequence is exceptionally well-preserved by a deep water column (34 m) and surrounding hills, which hinder wind turbation; bottom water anoxia, which prevents bioturbation; and a shallow connection (the Seto Channel) between Lake Suigetsu and Lake Mikata (upstream of Lake Suigetsu, Fig. 1C), which prevents disturbances by high energy events (Nakagawa et al., 2021). A

series of previous deep coring campaigns have extracted sediment from Lake Suigetsu to generate a high-quality archive of environmental change ("the Lake Suigetsu sediment cores") spanning >98 m from the present day to in excess of 150 ka BP (Nakagawa et al., 2012). A distinctive characteristic of the Suigetsu cores is that they contain annual laminations (varves) between ~50 and 10 ka BP, comprising the longest continuously varved record from the Quaternary (Schlollaut et al., 2012). The youngest sediments (up to 50.3 ka BP) have been dated to high precision using radiocarbon dating of >800 macrofossils (Staff et al., 2011; Bronk Ramsey et al., 2012, 2020), varve counting using optical microscopy (Schlollaut et al., 2012, 2018), and analysis of volcanic tephra deposits with independent ages (e.g., Smith et al., 2011; McLean et al., 2016). Between 50.3 ka BP and 13.9 ka BP, Lake Suigetsu

\* Corresponding author.

E-mail address: [c.rex.1@research.gla.ac.uk](mailto:c.rex.1@research.gla.ac.uk) (C.L. Rex).

<https://doi.org/10.1016/j.qsa.2023.100145>

Received 5 October 2023; Received in revised form 3 November 2023; Accepted 6 November 2023

Available online 19 November 2023

2666-0334/© 2023 The Author(s). Published by Elsevier Ltd. This is an open access article under the CC BY license (<http://creativecommons.org/licenses/by/4.0/>).

contributes the only non-reservoir corrected dataset within the international consensus radiocarbon calibration curve, "IntCal".

It is this excellent archive preservation and world-leading chronological control which makes multiproxy palaeoenvironmental analyses of the Suigetsu cores an exciting prospect. Indeed, the location of Lake Suigetsu at a lower latitude than other global benchmark records (e.g., the Greenland and Antarctic Ice Cores) makes this archive an avenue for establishing a more holistic global perspective on past climatic change. Additionally, the Japanese archipelago is situated within the East Asian Monsoon (EAM) regime, a critical, yet complex, component of the global

climate system for which palaeoclimate reconstructions offer a means to greater understanding. Not only is Japan situated directly beneath the seasonally migrating EAM front, making it sensitive to changes in the EAM system (Jun-Mei et al., 2013; Nakagawa et al., 2012; Gallagher et al., 2018), but unlike continental areas, Japan experiences EAM precipitation semi-annually (twice a year), because both the winter (EAWM) and summer (EASM) prevailing monsoon winds pass over large bodies of water before reaching the Japanese Islands. Therefore, both seasonal modes have tangible hydrological influence over precipitation in Japan, and reconstructions from here have the unique potential to

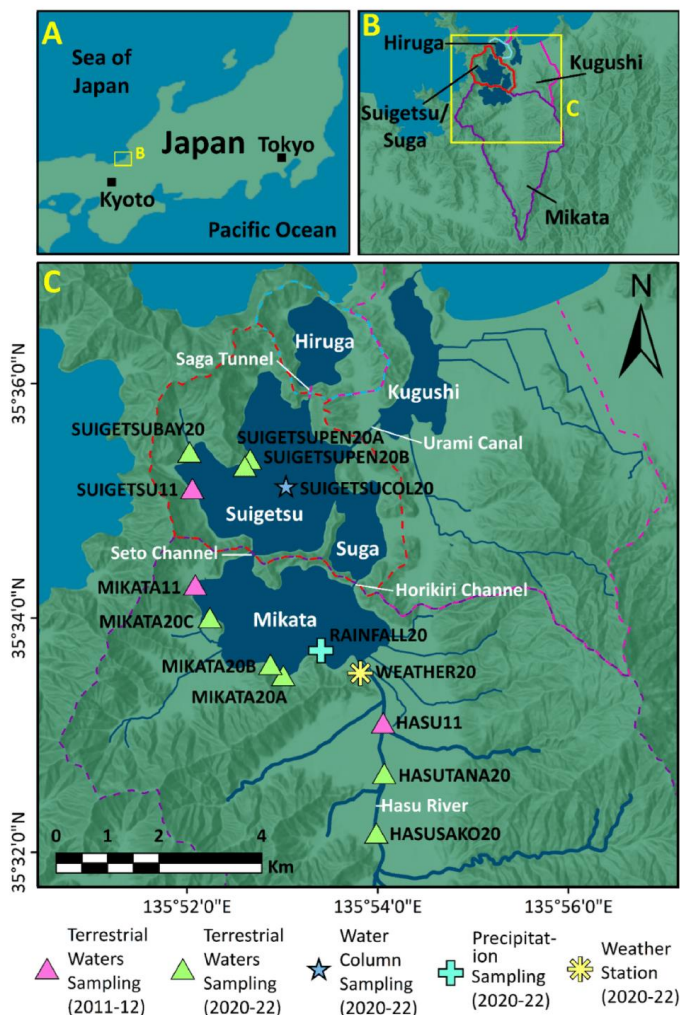


**Fig. 1.** Map of the Five Lakes of Mikata catchment. Yellow outlines show the extent of subsequent panels in the sequence. Panel A shows the location of the region in relation to major Japanese cities. Panel B shows the catchment area of each lake. Panel C shows the sampling locations for this study, including precipitation sampling, river and lake sampling, and sampling of the Lake Suigetsu water column, as well as the location of the weather station. Full details of locations shown here are available in Appendix A. Basemaps: custom World Dark Grey Base and World Hillshade from Esri (2022a, 2022b) (scale 1:10,000,000 (Panel A), 1:400,000 (Panel B), 1:67,946 (Panel C)). (For interpretation of the references to colour in this figure legend, the reader is referred to the Web version of this article.)

determine the behaviours of both the EAWM and the EASM. In light of this, the Suigetsu cores continue to be the subject of an ever-growing collection of investigations into climatic change over the last glacial-interglacial cycle (e.g., Scholaut et al., 2017; Nakagawa et al., 2021), including contributing to the definition of the Holocene onset as an auxiliary stratotype (Walker et al., 2009). An ongoing avenue of research is the development of palaeoclimate reconstructions derived from oxygen and hydrogen isotope compositions of pollen grains, biogenic silica and siderite (all of which are abundant components of the cores), because these offer a means to infer past hydrological change (including links to EAM behaviour).

Robust interpretation of such sedimentary proxies is predicated on a strong understanding of the controls acting on lake isotope composition ( $\delta_{\text{lake}}$ ), which, in the absence of historical datasets, can be achieved by extended contemporary monitoring. Of particular interest is the extent to which variability in the isotope composition of precipitation ( $\delta_{\text{precipitation}}$ ), which provides a link to regional-scale hydrological change) is reflected in the isotope composition of river water ( $\delta_{\text{river}}$ ) and  $\delta_{\text{lake}}$  and, in turn, lake sedimentary components; however, this depends strongly on catchment and lake hydrology. Variability in groundwater, river, and in rare cases, marine contributions to the lake water balance can act to dampen and sometimes conceal the isotope composition of recent precipitation (e.g., Seal and Shanks, 1998; Lacey and Jones, 2018). In addition, evaporation of lake waters can strongly modify  $\delta_{\text{lake}}$  compared to inflowing water (Gonfiantini, 1986; Russell and Johnson, 2006; Wassenaar et al., 2011). These concepts are commonly used in modern hydrology (Gibson et al., 2016); for example, during mass balance modelling to determine the surface versus groundwater contribution to Lake Ohrid, south-eastern Europe (Lacey and Jones, 2018) or to consider mass losses due to evaporation, such as for Lake Edward, East Africa (Russell and Johnson, 2006). Monitoring for an extended period (on the order of years) is required in order to fully understand the evolution of  $\delta_{\text{lake}}$ , particularly in regions where the climate is so seasonal. This approach allows for both local influences (such as changing inputs and evaporation) to be identified alongside regional scale climatic shifts.

In this study we aimed to better understand the controls acting on the isotope composition of water within Lake Suigetsu and its surrounding catchment, in order to facilitate interpretation of isotope-based proxy reconstructions of past climate from the Lake Suigetsu sediment cores. By monitoring  $\delta_{\text{precipitation}}$ ,  $\delta_{\text{river}}$  and  $\delta_{\text{lake}}$  over a total observation period of two years and ten months across 2011–2012 and 2020–2022, we assessed the factors affecting the relationships between these variables. Conceptualising  $\delta_{\text{lake}}$  of Lake Suigetsu is particularly important because whilst the lake and catchment receive high volumes of precipitation annually, there are other controls which could act to alter or obscure this precipitation signal; namely, that expected evaporation rates are high due to a warm summer climate, and in the present day there is some interaction between the lake and the Sea of Japan. Consequently, resolving the relative influence of  $\delta_{\text{precipitation}}$  (and the propagation of  $\delta_{\text{precipitation}}$  signals to  $\delta_{\text{lake}}$ ) is crucial to understanding the major controls over long term  $\delta_{\text{lake}}$  within the context of regional scale hydrological (and thus climatic) change.

## 2. Study site

### 2.1. Hydrology

The Five Lakes of Mikata are located adjacent to the towns of Wakasa and Mihama in Fukui Prefecture, Honshu Island, central Japan. The lakes lie to the west of the active Mikata fault line and were formed as the western side of the fault subsided over time (Fig. 1C; Nakagawa et al., 2012). Over the last ~400 years, the Five Lakes of Mikata catchment has been anthropogenically influenced by the construction of channels and tunnels to connect the lakes. In the present day, the lakes form a route between the freshwater Hasu River and the saline Sea of

Japan (Fig. 1C). Lake Mikata, the southernmost lake, is fed by the Hasu River to the south, has an area of ~3.61 km<sup>2</sup> and a maximum depth of 5.8 m and has the largest discrete catchment area (~50 km<sup>2</sup>; Fig. 1B). Lake Mikata is connected to Lake Suigetsu via the shallow (~2 m deep) Seto Channel, and to the adjacent Lake Suga via the artificial (<0.5 m deep) Horikiri Channel. Lake Suigetsu, which has an area of ~4.2 km<sup>2</sup> and a maximum depth of 34.0 m, then feeds Lake Hiruga (via the subterranean Saga Tunnel, which was sealed during the observation period) and Lake Kugushi (via the surficial Urami Canal), which both flow directly into the Sea of Japan (Shigematsu et al., 1961, Fig. 1C). In the past, prior to the construction of the Horikiri Channel, Saga Tunnel and Urami Canal, Lake Kugushi was a coastal lagoon (part of Wakasa Bay), and Lake Hiruga was not connected to the sea (except during flooding), so four of the five lakes were freshwater (Shigematsu et al., 1961; Masuzawa and Kitano, 1982). At this time, the outflow from Lake Suigetsu was via Lake Suga (effectively a side basin of Lake Suigetsu), which was connected to Lake Kugushi via a channel (the Kiyama River) through low ground to the east of the lakes.

Principally, water flows in a south-to-north direction through the catchment, driven by the large quantities of precipitation in the region. However, in the present-day, seawater washes back into Lake Suga, Lake Suigetsu and Lake Mikata during high tide in autumn (Kondo and Butani, 2007). As a result, all five lakes now have some degree of marine-derived salinity and observations show that salinity in the lakes increases during the autumnal high tide and then decreases due to continued freshwater input via precipitation and surface runoff during winter. Lake Hiruga and Lake Kugushi are saline, and Lake Mikata is fresh to brackish (0–3 g kg<sup>-1</sup>). Lake Suigetsu and Lake Suga are both meromictic (permanently stratified), with an upper mixolimnion (aerobic, brackish to saline water; 2–8 g kg<sup>-1</sup>) separated from a lower monimolimnion (anaerobic, saline water; ~13 g kg<sup>-1</sup>) by a chemocline at ~8 m depth (Matsuyama, 1974; Kondo et al., 2000; Kondo and Butani, 2007). The mixolimnion exhibits a salinity gradient between the surface (fresh) and the chemocline (saline) (Matsuyama, 1974; Kondo et al., 2000). Mixing in the mixolimnion occurs once each year, during the autumn, resulting in an increase in surface water salinity, a raised chemocline and a steepening of the salinity gradient (Kondo et al., 2000). The chemocline then lowers and a shallower salinity gradient is re-established during winter. The monimolimnion is a persistent seawater-derived saline layer, confirmed by geochemical analysis (Shigematsu et al., 1961), and has a limited freshwater influence (Matsuyama, 1973). This layer is replenished annually at the autumnal high tide (Kondo and Butani, 2007). It is not known whether this autumn seawater incursion drives mixing in the upper ~8 m of the water column, or if these two processes are merely coincident, although the latter is suspected. No significant long-term increases in salinity have been observed in the monimolimnion in the past 70 years; salinity remained approximately 12–16 g kg<sup>-1</sup> in the intervals 1951–1966 and 2008–10 (Matsuyama, 1973; Kondo et al., 2014). Complete lake water vertical mixing events are unusual but have been detected (in 1997; Kondo et al., 2000).

The residence time of Lake Suigetsu was calculated to be on the order of ~1 year, assuming a total annual precipitation of ~2.3 m (Japan Meteorological Agency, 2022) across a ~60 km<sup>2</sup> catchment (~0.14 km<sup>3</sup> precipitation annually) and then applying this to a simple single box model (surface area of ~4.3 km<sup>2</sup> and ~34 m depth equating to a ~0.15 km<sup>3</sup> volume). However, when considering the evidence for a stable monimolimnion in Lake Suigetsu with a very long residence time (Shigematsu et al., 1961), a two-box model is more appropriate, with water effectively flushing solely through the top ~8 m of the lake (Matsuyama, 1973). In this case, the residence time of the mixolimnion is on the order of ~3 months.

### 2.2. Climate

The climate of the Five Lakes of Mikata catchment is temperate with

high levels of precipitation. The temperature profile is typical of Japan, with low temperatures in winter (reaching a minimum in January with a mean temperature of 4.3 °C) and high in summer (reaching a maximum in August with a mean temperature of 27.0 °C). The annual distribution of precipitation is more unusual, because a large proportion of the total annual precipitation falls during winter (Fig. 2). This is unlike much of Japan, where summer is the wettest season. The large quantities of precipitation received in winter are a result of the catchment being located on the Sea of Japan coast, where it receives a significant input of EAWM precipitation annually. This EAWM precipitation falls as both rain and snow and is concentrated in December and January. Spring (March to May) is the driest season of the year, which precedes a second rainy period in early summer which accompanies the EASM. The EASM rainy season is known as the *Tsuyu* or *Baiu*, which occurs at Lake Suigetsu around late June into July, immediately prior to the period of maximum temperature. This is followed by typhoon season from August to September, during which a series of low-pressure systems pass over Japan from the Pacific Ocean to the south, resulting in a third annual period of rain. Winter (EAWM) and summer (EASM) precipitation are the most significant extended (persistent) freshwater inputs to the catchment; typhoon season precipitation comprises a series of intense isolated precipitation events.

### 3. Materials and methods

#### 3.1. Sampling methods

Samples of lake and river waters ( $n = 463$ ) were taken from the Hasu River, Lake Mikata and Lake Suigetsu (Fig. 1C) on a weekly basis between 1<sup>st</sup> March 2011 and 3<sup>rd</sup> January 2012, and again between 15<sup>th</sup> July 2020 and 29<sup>th</sup> July 2022. Water was collected by submerging a collection vessel in the top ~50 cm of water before subsampling using a vial leaving no or minimal head space. Precise sampling locations were altered between the 2011/12 and 2020/22 sampling intervals, and during periods of inaccessibility (e.g., due to bridge repairs, snowfall, lake freezing and flooding; Appendix A). The slight changes in sampling location are unlikely to affect the isotope composition recorded, being within the same water depth range and situated away from lake inputs. If visible algae were present in the water, the samples were filtered using a 50 µm polyethylene terephthalate (PET) mesh filter. Surface water data from the 2011–2012 observation period do not have the accompanying (precipitation and water column) data described below in

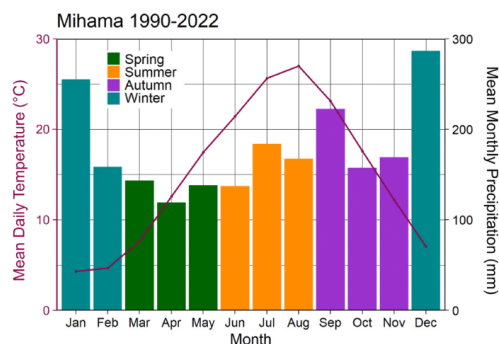


Fig. 2. Climate at the Five Lakes of Mikata. Monthly variations in mean daily temperature (pink curve) and mean total monthly precipitation (bars) at Mihama, adjacent to Lake Kugushi (35°36'00"N 135°55'00"E). Data from the Japan Meteorological Agency, 1<sup>st</sup> January 1990 to 28<sup>th</sup> February 2022. (For interpretation of the references to colour in this figure legend, the reader is referred to the Web version of this article.)

Section 4 because this was an extended pilot study focussed on the river and lake waters; however, we have nevertheless included these 2011–2012 data in our analysis because there are subtle differences in these data that contribute to a more comprehensive view of isotope variations in the catchment.

Precipitation samples ( $n = 120$ ) were captured between 13<sup>th</sup> July 2020 and 29<sup>th</sup> July 2022 using a purpose built (3D printed) funnel and glass bottle holder in Wakasa (at the location indicated in Fig. 1C). Silicone oil was added to the collection bottle to prevent evaporation. Water subsamples were taken from the bottle using a Teflon pipette. Subsamples were taken on an event basis; every day during periods of frequent precipitation, but less often during periods of reduced precipitation. The water was allowed to overflow the sample vial in order to remove the floating silicone oil. Fresh snowfall samples were collected from pristine areas of snow after deposition and melted with silicone oil in a lidded container before being transferred to the collection vial. An automated Netatmo weather station (location also shown in Fig. 1C) was deployed to provide temperature, humidity, precipitation amount and wind data to accompany the isotope data. Backwards air parcel trajectory analysis was performed for four precipitation events (representative of each season) using the NOAA Air Resources Laboratory HYSPLIT model (Stein et al., 2015; Rolph et al., 2017). The selected events ended on 27<sup>th</sup> December 2020, 16<sup>th</sup> September 2021, 2<sup>nd</sup> May 2022 and 7<sup>th</sup> July 2022, respectively. Back trajectories were generated for air parcels arriving at the catchment every 12 h at 1500 m.a.s.l. across a 72-h window prior to the end of each event.

Water column profiling was conducted ~quarterly on 22<sup>nd</sup> December 2020, 8<sup>th</sup> April 2021, 5<sup>th</sup> August 2021, 17<sup>th</sup> November 2021, 23<sup>rd</sup> April 2022 and 21<sup>st</sup> July 2022 at the approximate centre of Lake Suigetsu (Fig. 1C). Samples were taken every 2 m between the surface and 10 m depth, every 5 m between 10 m and 30 m depth, and then every 2 m between 30 m and 34 m ( $n = 70$ ). A sealable van Dorn water sampler was used to prevent mixing of the sample with water at different depths during transit to the surface. A Hydrolab DS5 water quality meter was also used to measure temperature and salinity profiles on each sampling date; higher resolution geochemical data were collected for the December 2020, April 2021, November 2021, April 2022 and July 2022 dates. The low-resolution data collected for the August 2021 date (using a TOA-DKK WQC-24 m) are also shown in Section 4 below.

#### 3.2. Analytical methods

Oxygen isotope ( $\delta^{18}\text{O}$ ) measurements were made using an Isoprime 100 mass spectrometer with an Aquaprep dual-inlet system using the  $\text{CO}_2$  equilibration method. Subsamples (totalling 200 µl) were placed in a heated sample tray at 40 °C before the air was evacuated and each exetainer was flushed with  $\text{CO}_2$ . The samples were then left to equilibrate for between 12 (first sample) and 37 (last sample) hours. Any remaining water vapour was then removed on a sample-by-sample basis using a cryogenic water trap, before each sample was expanded into the dual inlet isotope ratio mass spectrometer (IRMS) for analysis. The samples were measured in alternate pulses alongside a reference  $\text{CO}_2$  gas, and the integrated values of the sample were compared to the reference gas values to determine  $^{18}\text{O}/^{16}\text{O}$ . Two internal laboratory standards (CA-HI and CA-LO) were analysed in each run. The value of these standards has been determined accurately by comparison with international calibration and reference materials (VSMOW2, SLAP2 and GISP). This facilitated the calculation of the  $^{18}\text{O}/^{16}\text{O}$  ratio of each sample versus VSMOW2, and subsequent expression of the oxygen isotope ratio in delta ( $\delta$ ) units ( $\delta^{18}\text{O}$ ) in parts per mille (‰). The typical standard deviation is < 0.05 ‰.

Hydrogen isotope ( $\delta^2\text{H}$ ) measurements were made in duplicate using a continuous flow, high temperature conversion elemental analyser - IRMS (TC-EA-IRMS) (EuroprOH-Isoprime) with liquid autosampler. Subsamples (0.5 µl) were injected into a heated septa-sealed port at 160 °C and converted to water vapour. The vapourised sample was then

C.L. Rex et al.

Quaternary Science Advances 13 (2024) 100145

flushed through a chromium-packed reactor at 980 °C by the helium carrier gas, which reduced the water to hydrogen gas. A reference hydrogen gas pulse was introduced to the IRMS prior to the gas pulse from each sample. The sample peaks were then integrated and corrected for the H<sub>3</sub> contribution before comparison to the reference gas to yield <sup>2</sup>H/<sup>1</sup>H. Each sample was measured five times. As with the oxygen isotope measurements, the samples were then compared to measurements of CA-HI and CA-LO to calculate the <sup>2</sup>H/<sup>1</sup>H ratio of each sample versus VSMOW2, and expression of the hydrogen isotope ratio in delta units as for the oxygen isotopes. The typical standard deviation is < 0.5 ‰.

The aforementioned <sup>18</sup>O and <sup>2</sup>H measurements were then used to calculate d-excess (Equation (1)), a second-order parameter which can be considered as a measure of deviation from the Global Meteoric Water Line (GMWL, which has a gradient of 8). This occurs when there is a greater amount of <sup>2</sup>H relative to <sup>18</sup>O, caused by diffusive fractionation during evaporation of water molecules (Bershaw, 2018).

$$d - excess = \delta^2H - (8 * \delta^{18}O) \tag{Equation 1}$$

4. Results and interpretation

4.1. Precipitation <sup>18</sup>O and <sup>2</sup>H

Values of <sup>18</sup>O for the precipitation at Wakasa (July 2020 to July 2022) ranged from -13.2 ‰ to -2.4 ‰, with a mean value of -7.0 ‰ and standard deviation of 1.6 ‰ (Fig. 3A). <sup>2</sup>H values ranged from -96.4 ‰ to 2.3 ‰, with a mean of -39.1 ‰ and standard deviation of 11.9 ‰. Fig. 3A shows only small seasonal differences in <sup>18</sup>O and <sup>2</sup>H because there was considerable intra-seasonal variability and overlap. Throughout the study period, <sup>18</sup>O and <sup>2</sup>H were associated with rapid high amplitude fluctuations with time (Fig. 4); however, winter and summer minima were observed when the data were considered on a monthly basis; likely due to greater quantities of precipitation (Fig. 2) during these seasons (discussed in Section 4.4). This trend was clearest in the <sup>18</sup>O values, but a summer minimum was also observed in the <sup>2</sup>H

values (Fig. 4); the winter minimum likely obscured by high d-excess values (described in Section 4.2). Back trajectory analysis of four precipitation events from across our sampling period indicates that air parcels arriving at the catchment predominately originated over Continental Asia during the winter, in the oceanic domain (Pacific Ocean, Philippine Sea and East China Sea) during summer, and a mixture of the two during the spring and autumn (Fig. 5).

These trajectories, which ultimately reflect the operation of the EAM as dual EAWM and EASM modes, highlight the influence of the EAM on the climate of Japan, and can explain the lack of distinctive seasonal precipitation <sup>18</sup>O and <sup>2</sup>H trends at Wakasa. EAWM and EASM precipitation over Japan generally have very similar compositions (Taniguchi et al., 2000; Uemura et al., 2012) in direct contrast to Continental Asia, where EAWM and EASM precipitation exhibit distinct compositions due to continental (<sup>18</sup>O<sub>precipitation</sub> ~ -4 ‰) versus oceanic sources (<sup>18</sup>O<sub>precipitation</sub> ~ -10 ‰), and hence vary seasonally (Araguás-Araguás et al., 1998). EAWM air masses originate in central Asia and Siberia and are predominately cold and dry, and hence whilst distillation and moisture recycling earlier in the trajectory is possible, the isotope signal of EAWM precipitation over Japan is dominated by the interaction of this air mass with the Sea of Japan. The evaporation from the Sea of Japan in winter has a light isotope signal (<sup>18</sup>O ~ -8 ‰; Uemura et al., 2012) and the transport distance is short (on the order of <1000 km), so this signal is retained in winter precipitation <sup>18</sup>O and <sup>2</sup>H (i.e., little further depletion of the heavier isotopes occurs during transport). Conversely, EASM air masses originate over the Pacific Ocean and track towards the Japanese archipelago via the Philippine Sea and East China Sea (the trajectory ultimately determined by the positioning of the Western Pacific Subtropical High (Xu et al., 2020, Fig. 5). Evaporation from this oceanic domain has a range of isotope compositions (from <sup>18</sup>O ~ -4 ‰ in the Western Pacific Warm Pool to <sup>18</sup>O ~ -8 ‰ in the East China Sea; Uemura et al., 2012); however, the distance from the sources with a heavier isotope signal to Japan is greater, such that overall depletion of the heavier isotopes during transport acts to minimise differences between proximal and distal sources. As such, EASM <sup>18</sup>O and <sup>2</sup>H is low, as with the EAWM.

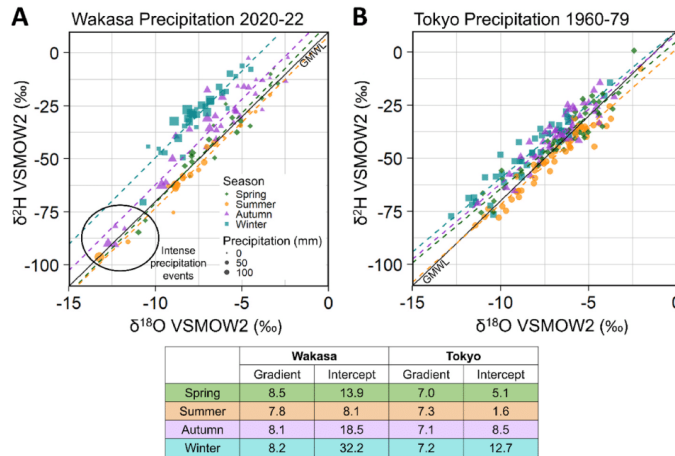


Fig. 3. Precipitation <sup>18</sup>O and <sup>2</sup>H at Wakasa and Tokyo. A comparison of isotopes in precipitation at (A) Wakasa 2020–22 (event basis, Sea of Japan Coast) and (B) Tokyo 1960–79 (monthly averages, Pacific Ocean Coast). Linear regression local meteoric water lines for each season are shown and numerically described in the table. Black diagonal lines represent the Global Meteoric Water Line (GMWL). The points plotted for the composition of Wakasa are scaled by quantity of precipitation (as calculated from the Wakasa weather station; WEATHER20 in Fig. 1). Seasons are defined as: Spring (Mar–May), Summer (Jun–Aug), Autumn (Sep–Nov), Winter (Dec–Feb). d-excess is higher for points above the GMWL. (For interpretation of the references to colour in this figure legend, the reader is referred to the Web version of this article.)

C.L. Rex et al.

Quaternary Science Advances 13 (2024) 100145

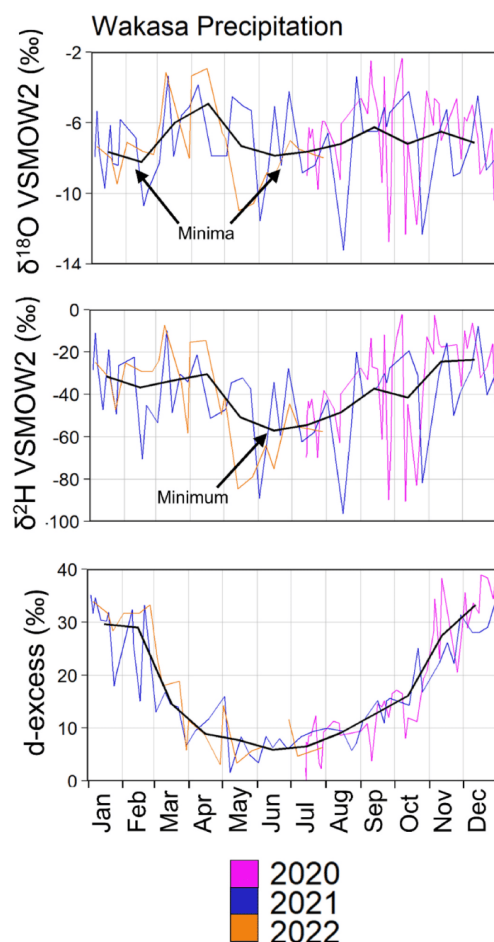


Fig. 4. Variations in  $\delta_{\text{precipitation}}$  with time.  $\delta^{18}\text{O}$ ,  $\delta^2\text{H}$  and d-excess values from precipitation at Wakasa from across the study period (colour lines). Black lines represent monthly averages of each dataset. (For interpretation of the references to colour in this figure legend, the reader is referred to the Web version of this article.)

This similarity in the composition of precipitation from each end member trajectory likely results in the limited seasonality that we observed at Wakasa. The air parcel trajectories during spring and autumn exhibited mixed behaviour, and we suggest that this lack of strong prevailing wind direction and a mixture of vapour sources during these intermediate seasons produced precipitation with a similar composition to the EAM months, although we suspect that the spring and autumn values were slightly higher due to relatively reduced quantities of precipitation during these seasons (discussed in Section 4.4). Intra-seasonal variability was likely due to subtle differences in the airmass trajectories associated with each precipitation event.

Very low  $\delta^{18}\text{O}$  and  $\delta^2\text{H}$  values (in the  $\delta^{18}\text{O}$  range of  $-13.2\text{‰}$  to  $-11.0\text{‰}$ ) were uncommon at Wakasa; however, a minor cluster of precipitation events was nevertheless associated with such values

(Fig. 3A). The majority of these datapoints represent precipitation from August to October (Fig. 4) and include rains from Tropical Storm Dolphin (2020). Given the seasonality of such events, a simple explanation could be that this precipitation was derived from tropical storms (typhoons), which are associated with  $\delta^{18}\text{O}$  values up to  $6\text{‰}$  lower than other summer precipitation events, driven by strong fractionation processes in heavy cyclonic precipitation (Lawrence and Gedzelman, 1996; Fudeyasu et al., 2008; Li et al., 2010; Jackisch et al., 2022). However, it is worth noting that precipitation from earlier months of the year also occasionally exhibited these values, and other typhoon events did not. Instead, we posit that these compositions were associated more generally with intense precipitation events. Whilst they do not universally correspond to periods with large quantities of precipitation, this does not preclude a relationship with intense precipitation events because our analysis considered only the total amount of precipitation which fell in the collection period, not the intensity. Not all typhoon events result in intense precipitation at Wakasa due to its location, and many typhoons are associated with high wind speeds alone; hence, some were not associated with very low isotope values during the study period.

#### 4.2. Precipitation d-excess

In contrast to the  $\delta^{18}\text{O}$  and  $\delta^2\text{H}$  datasets, we observed very clear high-amplitude seasonal patterns in precipitation d-excess, which exhibited an average value of  $17.1\text{‰}$  and range of  $35.6\text{‰}$  across the entire dataset (Fig. 3A). The values for summer precipitation fell broadly along the GMWL, whereas winter precipitation consistently expressed higher d-excess values, offset yet parallel to the GMWL (Fig. 3A). The autumn and spring d-excess values exhibited intermediate values with some overlap with summer and winter, particularly so for the autumn. Regression lines between  $\delta^{18}\text{O}$  and  $\delta^2\text{H}$  applied to each season had similar gradients ( $\sim 8$ ), with minor differences due to the relatively limited amount of data across a narrow range. The difference in intercept between the summer and winter regression lines was  $24.1\text{‰}$  (equating to a difference in seasonally averaged d-excess of  $23.5\text{‰}$ ).

Collective observations of d-excess at sites across Japan suggest that this variable shows this distinct pattern regardless of location (Uemura et al., 2012; Hasegawa et al., 2014; Ichinagi and Tanoue, 2016). High values of d-excess in winter precipitation and low values in summer precipitation can be attributed to contrasting relative humidity values in the precipitation source regions, which overprints the d-excess of the source water itself (Xia et al., 2018; Uemura et al., 2012). Due to cooler sea surface temperatures (and thus low relative humidity) over the Sea of Japan during the winter, we suggest that winter (EAWM) precipitation exhibits higher d-excess values relative to summer (EASM) precipitation, which originates from the oceanic domain during the summer where relative humidity is high (Araguás-Araguás et al., 1998; Kurita et al., 2015). Relative humidity can affect d-excess via multiple mechanisms, but in the low latitudes the dominant control is the amount of raindrop re-evaporation, and in the mid latitudes oceanic evaporation conditions show greater significance (Xia et al., 2022). The gradual transition of influence between these contrasting extremes suggests that there were no abrupt shifts or interfaces between systems at play in this region during spring or autumn and instead, hydrologically, Japan transitioned gradually between the influence of the EAWM and EASM operational modes; supported by the back trajectory analysis (Fig. 5).

#### 4.3. Quantity-weighted composition

The largest precipitation events during our study interval occurred during winter and, to a lesser extent, during the late summer and early autumn (Fig. 3A), which is in line with the long-term climate data from nearby Mihama (Fig. 2). The largest winter events exhibited higher d-excess values, whilst the largest late summer/early autumn events showed low  $\delta^{18}\text{O}$  and  $\delta^2\text{H}$  values (as discussed above). This has important implications for the introduction of precipitation to the catchment;

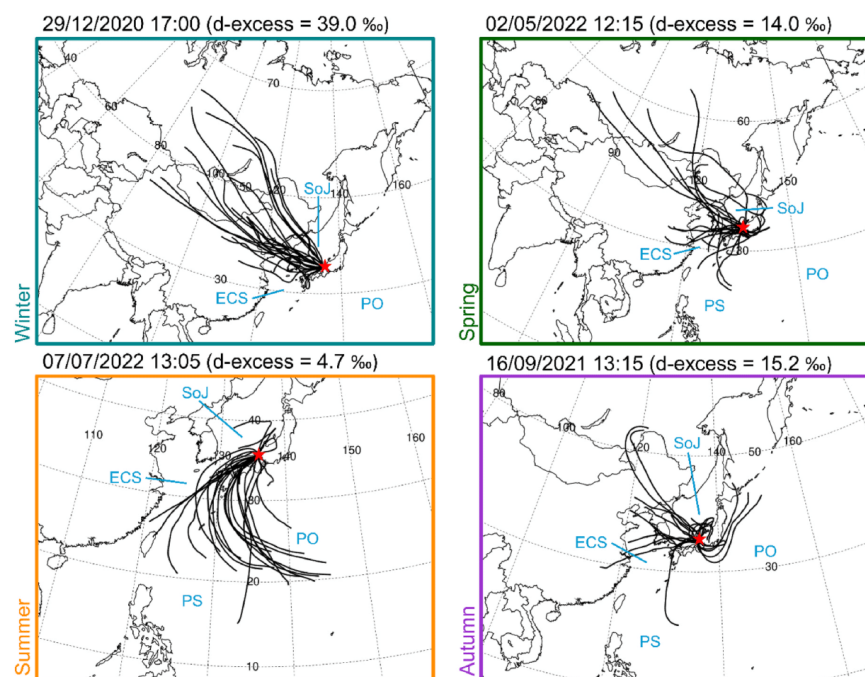


**Fig. 5.** HYSPLIT back trajectory model results. HYSPLIT back trajectory model results for four rainfall events across the 2020-22 rainfall study period. Events were selected to cover a range of d-excess values which are typical of each of the four seasons. Dates and times indicate the end of each sampling interval. Red stars indicate the position of the catchment; backtrace analysis was performed to the exact position of the precipitation sampler (RAINFALL20 in Figure 1.1). Surrounding seas and oceans are labelled as follows: SoJ = Sea of Japan, ECS = East China Sea, PS = Philippine Sea, PO = Pacific Ocean. (For interpretation of the references to colour in this figure legend, the reader is referred to the Web version of this article.)

most notably, this indicates that the largest contribution to the catchment on an annual basis is that of a mid-range isotope composition (with high d-excess), with a secondary component having low  $\delta^{18}\text{O}$  and  $\delta^2\text{H}$  values (with low d-excess). When weighted by precipitation amount, the annual mean  $\delta^{18}\text{O}$  was  $-7.4\text{‰}$ , the annual mean  $\delta^2\text{H}$  was  $-39.7\text{‰}$  and the annual mean d-excess was  $19.8\text{‰}$ , which lies between the winter and autumn regression lines. A caveat to this is that the values used to calculate precipitation amount for this analysis were measured by the Netatmo weather station, which did not contain a heating element, so the quantity of precipitation may be underestimated for snowfall events and hence the precipitation-weighted annual mean  $\delta^{18}\text{O}$  and  $\delta^2\text{H}$  values may lie closer to the winter average. Snowfall events are likely to be amongst the smallest winter precipitation events in Fig. 3A, however, the relatively tight grouping of winter values suggests that the difference between snowfall and rainfall isotope values was not particularly marked across the observation period.

#### 4.4. Temperature and amount effects

Additional analysis (least-squares linear regression) was performed using the precipitation  $\delta^{18}\text{O}$  and  $\delta^2\text{H}$  values to provide an indication of the influence of a “temperature effect” or precipitation “amount effect”. The isotope data were compared to the average temperature and the total precipitation amount (square root transformed) during each collection period, as measured by the Netatmo weather station (position indicated in Fig. 1C). These analyses were conducted using monthly

average  $\delta^{18}\text{O}$  and  $\delta^2\text{H}$  values (to reduce the influence of noise) and then repeated using datapoints from each season in isolation, and the full results are presented in Appendix B. All of the calculated  $R^2$  values were low (0.00–0.34), suggesting that neither temperature nor precipitation amount explained a large proportion of variability in precipitation  $\delta^{18}\text{O}$  or  $\delta^2\text{H}$ . Our findings are in line with other studies, which have suggested that local meteorological parameters are not as prominent as source region and transport effects on precipitation isotopes in Japan (e.g., Hasegawa et al., 2014; Ichianagi and Tanoue, 2016); however, others have found that they can retain moderate influence on a local scale (Ichianagi and Tanoue, 2016). Our  $R^2$  values are similar to those presented by Ichianagi and Tanoue (2016), who found that the  $\delta^{18}\text{O}$  of precipitation in Fukui City,  $\sim 60$  km from Lake Suigetsu, showed weak to no correlation with either temperature ( $R^2 = 0.02$ ) or precipitation amount ( $R^2 = 0.14$ ).

Analysing the data by season allows for changes in more dominant influences (e.g., opposing precipitation sources) to be minimised, and thus any obscured temperature and amount effects to be more easily identified. Indeed, this method reveals a stronger relationship between precipitation amount and isotope composition in spring, summer and autumn (but no relationship to temperature during those seasons). This suggests that there was a small amount effect acting on isotopes in precipitation at Wakasa, but no observable temperature effect on event-based timescales. Conversely, winter precipitation isotopes were very weakly correlated with temperature ( $R^2(\delta^{18}\text{O}) = 0.18$ ) and not correlated with precipitation amount ( $R^2(\delta^{18}\text{O}) = 0.00$ ). However, as

previously mentioned, the Netatmo weather station did not contain a heating element and hence snowfall amount was underestimated. Hence, we posit that there may have been a small amount effect influencing precipitation isotopes during winter, in line with other seasons, but this was not accounted for by our methods. This analysis suggests that the amount effect was a second-order control on isotopes in precipitation at Wakasa but was obscured by seasonality. Indeed, our dataset provides further qualitative evidence for such an amount effect because we observed minima in precipitation  $\delta^{18}\text{O}$  and  $\delta^2\text{H}$  coinciding with the periods of greatest precipitation amount (excluding the winter  $\delta^2\text{H}$  minimum, observed by high d-excess values) and attributed very low  $\delta^{18}\text{O}$  and  $\delta^2\text{H}$  values to intense precipitation events. It might be expected that a clearer relationship would be observed between precipitation  $\delta^{18}\text{O}$  and  $\delta^2\text{H}$  and the integrated amount of precipitation from across the entire transport pathway (as proposed by Uemura et al. (2012)). A lack of any temperature effect was not unexpected, because it has been posited that temperature effects merely explain spatial, not temporal, differences in precipitation isotope composition (Ichiyangui and Tanoue, 2016).

4.5. Comparison to Tokyo

The isotope composition of precipitation at Wakasa and the nearest GNIP station at Tokyo (350 km to the east) was very similar, albeit with some key disparities (Fig. 3B). The same seasonal patterns in d-excess were observed at both locations, with the summer and winter values

acting as end members, and intermediate spring and autumn values. However, compared to Wakasa, the seasonal difference at Tokyo was much less distinct, and the difference between the summer and winter regression line intercept was only 11.1 ‰ (reflecting a difference in seasonally averaged d-excess of 13.0 ‰). This is most likely due to a smaller relative influence of EAWM precipitation (which is associated with the highest d-excess values); Wakasa is located on the Sea of Japan coast, where there is a strong EAWM (and thus Sea of Japan) influence, and Tokyo is located on the Pacific coast, where these influences are significantly weaker. Instead, winter precipitation at Tokyo generally falls in short duration events that result from recycled local water. The local meteoric water line gradients were also shallower and more consistent at Tokyo across the seasons; however, this is likely to be the result of a larger dataset from Tokyo which captured values over a longer timescale. It is important to note that these datasets do not have the same resolution or cover the same period (the Wakasa precipitation dataset is on an event-basis over 2020–22, and the Tokyo precipitation dataset is monthly from 1961–79); however, the same trends are observed when the Wakasa precipitation data is considered at a monthly resolution, and also in comparison to event-based data from Tokyo in 2013 (Appendix C; Ichiyangui and Tanoue, 2016). Hence, the comparisons made here are reasonable.

4.6. Catchment effects

The seasonal patterns in Hasu River  $\delta_{\text{river}}$  and Lake Mikata and Lake

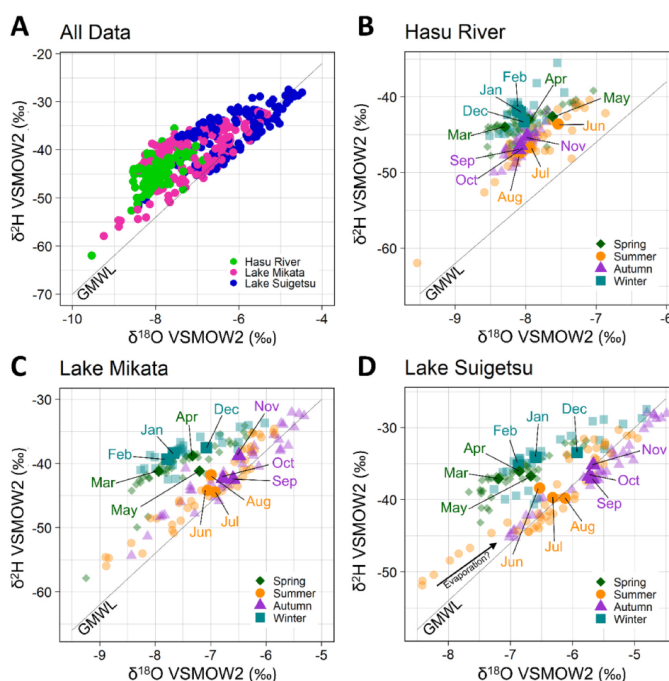


Fig. 6. Surface water  $\delta^{18}\text{O}$  and  $\delta^2\text{H}$ . The isotope composition of surface waters from the Hasu River, Lake Mikata and Lake Suigetsu. Panel A shows differences in composition between parts of the catchment, with colour corresponding to location. Subsequent panels show seasonal variations in composition at (B) the Hasu River, (C) Lake Mikata and (D) Lake Suigetsu. In Panels B–D, monthly averages are shown as opaque symbols and labelled, whilst underlying data points are shown as transparent symbols. Points in Panels B–D are colour-coded by season as in Fig. 3. (For interpretation of the references to colour in this figure legend, the reader is referred to the Web version of this article.)

Suigetsu surface  $\delta_{lake}$  paralleled those of  $\delta_{precipitation}$  showing that the precipitation signals were transferred to the catchment, although there is evidence for some internal modification (Fig. 6). All three locations (the Hasu River, Lake Mikata and Lake Suigetsu) exhibit a smaller range of  $\delta^{18}O$  and  $\delta^2H$  values than precipitation, and hence plot as a tighter grouping of points (range( $\delta^{18}O$ ) =  $-9.5$  to  $-4.5$  ‰,  $\sigma(\delta^{18}O)$  =  $1.0$  ‰ for river and lake water (Fig. 6A) versus  $-13.0$  to  $-2.5$  ‰ and  $2.3$  ‰ respectively for precipitation (Fig. 3A)), which indicates homogenisation of precipitation inputs with existing catchment waters (likely both surficial water and groundwater). Whilst the isotope composition of groundwater was not quantified as part of this study, and hence remains an unknown input to the lake system, we posit that groundwater composition was merely a slower average of precipitation composition; otherwise, lake water  $\delta^{18}O$  and  $\delta^2H$  would be offset to that of precipitation. We also observed that in-catchment homogenisation attenuated the effect of peripheral values and thus there was a limited influence of isolated events (including the aforementioned intense precipitation events with very low  $\delta^{18}O$  and  $\delta^2H$  values) on the lake system. Instead, prolonged precipitation modes were the more dominant control. Despite annually averaged precipitation being strongly weighted to winter, signals from all four seasons were detectable in the river and lakes (discussed in Section 4.8).

The evolution of  $\delta^{18}O$  and  $\delta^2H$  as water moves through the catchment from the Hasu River to Lake Mikata and then to Lake Suigetsu, also reveals some interesting patterns (Fig. 6A). The Hasu River exhibit a

very tight grouping ( $\sigma(\delta^{18}O)$  =  $0.36$  ‰) of low isotope ratios (mean ( $\delta^{18}O$ ) =  $-7.98$  ‰). Isotope values then increased, parallel to the GMWL, as the water moved through to Lake Mikata (mean( $\delta^{18}O$ ) =  $-7.13$  ‰,  $\sigma(\delta^{18}O)$  =  $0.83$  ‰) and then to Lake Suigetsu (mean( $\delta^{18}O$ ) =  $-6.32$  ‰,  $\sigma(\delta^{18}O)$  =  $0.85$  ‰). This suggests some mixing with seawater (which has higher  $\delta^{18}O$  and  $\delta^2H$ ) in the lakes, with a greater departure in values for Lake Suigetsu, which is the most saline of the three locations (discussed in Section 4.8). Comparatively, the compositions of Lake Mikata and Lake Suigetsu also covered a greater range than the Hasu River. Prior to this study, it was assumed that the Hasu River was the primary input to the lakes, however the differences in the range of their isotope compositions suggests that there was an additional overland (responsive) flow component feeding the lake system and that the river received a substantial groundwater input, producing a more homogenised isotope signal (Fig. 6B). Despite this, the river still reflected the seasonality of precipitation composition, and whilst monthly average composition values for the Hasu River exhibited smaller variations than Lake Mikata and Lake Suigetsu, the signals from the river maintained coincident timing with these parts of the catchment (Fig. 7). These observations suggest that the Hasu River had both direct and groundwater influences on its isotope composition, but we cannot rule out the possibility that weekly sampling of the river did not fully capture the most extreme isotope values here, due to the rate of river flow relative to the sampling resolution and the large catchment area.

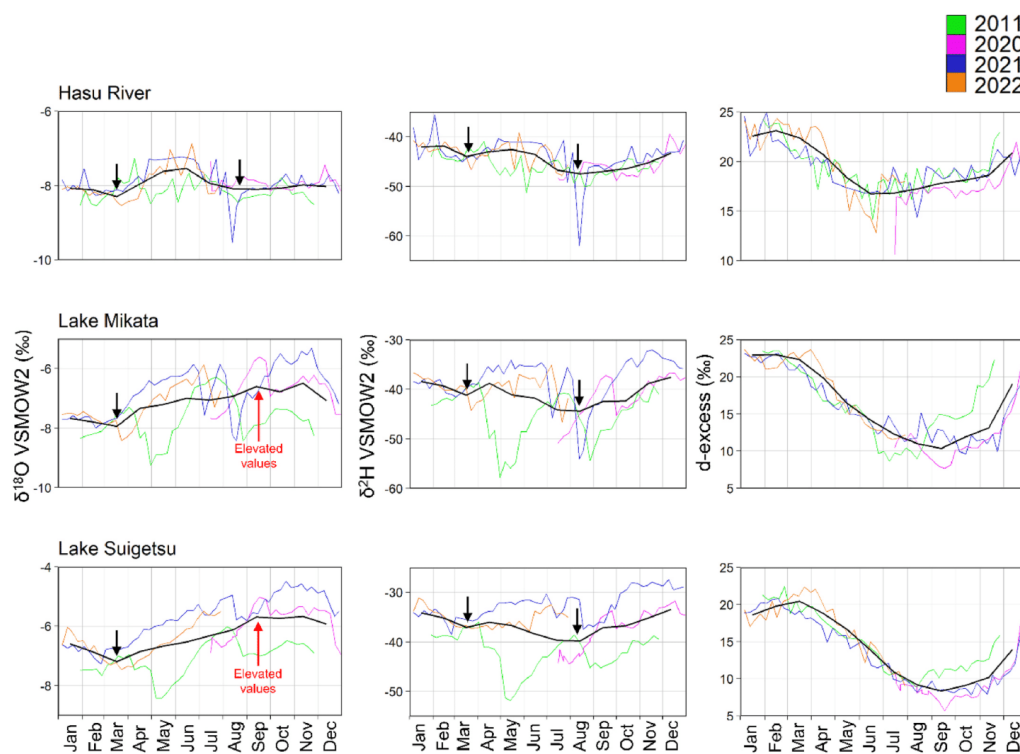


Fig. 7. Variations in  $\delta_{river}$  and  $\delta_{lake}$  with time.  $\delta^{18}O$ ,  $\delta^2H$  and d-excess values from the Hasu River, Lake Mikata and Lake Suigetsu from across the study period (colour lines). Black lines represent monthly averages of each dataset. Vertical scales are non-equivalent to best represent the shape of the data for each location. (For interpretation of the references to colour in this figure legend, the reader is referred to the Web version of this article.)

#### 4.7. River and lake water d-excess

Despite the signal homogenisation, seasonal variations in river and lake water d-excess were very similar to precipitation d-excess, with clear differences observed across the year (Fig. 6B–D) which can be interpreted in line with the precipitation signals. This offers the most convincing evidence that  $\delta_{\text{precipitation}}$  signals are detectable in  $\delta_{\text{lake}}$ . However, the difference between lake water (Fig. 7) and precipitation d-excess seasonality (Fig. 4) highlights a significant modification of the precipitation signals delivered to the catchment. The seasonal extremes observed in the lakes fell during spring (high d-excess) and autumn (low d-excess; Fig. 7), in contrast to the winter and summer extremes observed in precipitation d-excess (Fig. 4). This indicates a lag of  $\sim 1$ – $3$  months between an input of precipitation and detection of this signal in lake water composition, which we attribute to the average time taken for the water to transit through the catchment. Incidentally, this interval is equivalent to the residence time of the mixolimnion, providing support for our estimation that every three months the upper  $\sim 8$ m of the water column is replaced with precipitation from three months previously. A comparison of Lake Suigetsu d-excess to Wakasa precipitation d-excess suggests that the transit lag was proportional to the amount of precipitation and was longer (two to three months) for the drier summer months and shorter (one to two months) during the wetter winter months. A shorter winter lag compared to summer contrasts with what might be expected for a season associated with the accumulation of snow in the catchment (which can persist on high ground for weeks at a time) and the delayed release of snowmelt to the lakes. This appears to suggest that either the snowmelt lag was negligible compared to catchment transit time, possibly because only precipitation falling on the highest ground in the catchment was delayed, or that there was still sufficient winter rainfall or rapidly melting snow to cause a response in the lake and river water within one to two months.

#### 4.8. River and lake water $\delta^{18}\text{O}$ and $\delta^2\text{H}$

The river and lake water  $\delta^{18}\text{O}$  and  $\delta^2\text{H}$  values were also very similar to precipitation, exhibiting intra-seasonal variability with significant overlap (Fig. 6B–D). The Hasu River showed  $\delta^{18}\text{O}$  minima in spring and late summer, a  $\delta^2\text{H}$  minimum in late summer and slight downward inflection in  $\delta^2\text{H}$  during spring, which were reflected in both the raw datasets and in the monthly averages (Fig. 7). Lake Mikata and Lake Suigetsu showed greater inter- and intra-annual differences than the Hasu River, but monthly averaged data from these parts of the catchment also exhibited minima in  $\delta^{18}\text{O}$  in the spring and  $\delta^2\text{H}$  in the late summer, as well as a downward inflection in  $\delta^2\text{H}$  during the spring (Fig. 7). We relate these minima to winter (EAWM) precipitation and summer (EASM) precipitation, as detailed above in relation to precipitation  $\delta^{18}\text{O}$  and  $\delta^2\text{H}$ ; importantly, accounting for the aforementioned transit lag. However, unlike precipitation  $\delta^{18}\text{O}$ , lake  $\delta^{18}\text{O}$  lacked a minimum coinciding with summer (EASM) water entering the lake; instead, there were elevated  $\delta^{18}\text{O}$  values in the autumn in Lake Suigetsu (and to a lesser extent, Lake Mikata). The autumnal  $\delta^{18}\text{O}$  peak (based on monthly averages) in Lake Suigetsu was approximately 3 ‰ greater than the  $\delta^{18}\text{O}$  of summer precipitation. We attribute this trend to a combination of lake water mixing and saline water incursion, which brings saline water with high  $\delta^{18}\text{O}$  and  $\delta^2\text{H}$  values to the surface, causing elevated lake isotope values in autumn (discussed in Section 4.9) and a small amount of summer evaporative enrichment. We might also expect to see this trend in  $\delta^2\text{H}$ , given our proposed mechanisms, however this was not observed, likely as an artefact of a relatively small spring  $\delta^2\text{H}$  inflection (due to high d-excess values).

Besides these elevated values of lake water  $\delta^{18}\text{O}$  in summer and autumn, there is very limited evidence for an evaporation effect on the composition of lake water; a subset of summer values in each lake expressed a  $\delta^{18}\text{O}$  versus  $\delta^2\text{H}$  relationship with a reduced slope (similar to a local evaporation line), however this was restricted to the data

collected in 2011 and was not present in the 2020–2022 data (Fig. 6C and D). Additionally, the  $\delta^{18}\text{O}$  versus  $\delta^2\text{H}$  slope for other seasons did not suggest evaporation effects. This highlights the potential for inter-annual variability in the influence of evaporation on lake water isotopes, but demonstrates that this effect was a secondary one and affected summer  $\delta^{18}\text{O}$  and  $\delta^2\text{H}$  alone. We posit that the enhanced evaporation in summer 2011 was due to lower relative humidity. Relative humidity data was not available from the local Mihama weather station, but the nearest data from Tsuruga, 14 km to the northeast shows that relative humidity in 2011 was on average 5 % lower than summer 2021 (Japanese Meteorological Agency, 2023). Whilst Tsuruga experiences subtly different weather conditions, it is reasonable to compare these locations on seasonal timescales.

As well as this evaporation trend,  $\delta_{\text{lake}}$  in 2011 showed some discrepancies relative to the 2020–2022 interval (the data from which were broadly consistent). The data from 2011 showed a distinctive trend (a minimum in  $\delta^{18}\text{O}$  and  $\delta^2\text{H}$  in May, and an earlier increase in d-excess in the autumn). Because these trends were not observed for the Hasu River, they can be attributed to within-lake processes; however, there is no comparable precipitation isotope data available for this period in order to further interrogate this interpretation. Data from the local Mihama weather station shows intense precipitation during May 2011 (448 mm), which could have resulted in a significant direct input of low  $\delta^{18}\text{O}$  and  $\delta^2\text{H}$  water into Lake Mikata and Lake Suigetsu during this month; however, with available data this remains speculative. Overall high precipitation amounts in 2011, and hence a shorter residence time, might also explain the earlier increase in lake d-excess in autumn 2011 compared to the 2020–2022 observation period.

#### 4.9. Vertical profiles of lake water isotopes in Lake Suigetsu

The  $\sim$ quarterly depth profiling of Lake Suigetsu shows seasonal variations in the mixolimnion (above the chemocline) but compositions were consistent and homogenous in the monimolimnion year-round (Fig. 8). In the monimolimnion, temperature and salinity were consistently at  $\sim 16$  °C and  $\sim 14$  g kg<sup>-1</sup>, respectively. Above the chemocline, the water temperature was highest in the summer and lowest in the winter. A salinity minimum was observed during the spring and maximum during the autumn, with summer and winter exhibiting intermediate values. These observations are in agreement with the findings of Kondo et al. (2000), which presented long term monitoring of changes in temperature and salinity with depth at Lake Suigetsu. Throughout the sampling period the monimolimnion waters had higher  $\delta^{18}\text{O}$  and  $\delta^2\text{H}$  values relative to the mixolimnion and showed no variation with depth between  $\sim 8$  m and the lake bottom at 34 m. The d-excess values in the monimolimnion were also invariant and generally lower than the mixolimnion. In the mixolimnion, the  $\delta^{18}\text{O}$ ,  $\delta^2\text{H}$  and d-excess values showed smooth gradients between the chemocline and the surface, which suggests that the shape of each depth profile was driven by the difference between deepwater and surficial  $\delta_{\text{lake}}$ . The d-excess depth profiles in Fig. 8 matched the seasonal fluctuations discussed above, with the highest values in spring and lowest values in autumn.

The  $\delta^{18}\text{O}$ ,  $\delta^2\text{H}$  and d-excess profiles did not show any correlation with temperature and hence lake water temperature is unlikely to have been a controlling factor. However, there was an increase in salinity,  $\delta^{18}\text{O}$  and  $\delta^2\text{H}$  through summer and autumn which suggests common drivers. We theorise that this trend was a result of saline water incursion and mixolimnion mixing during autumn (evidenced by Kondo et al., 2000). Summer evaporation could have enhanced this effect via the enrichment of heavier isotopes at the surface and by increasing the relative concentration of dissolved ions. There is evidence for a combination of these effects at play, because both the summer (August) and winter (November) profiles exhibited raised surface  $\delta^{18}\text{O}$  and  $\delta^2\text{H}$  values (Fig. 8); however, the evidence for evaporation trends in the surface water samples (discussed above) was limited to 2011, so we suggest that in most years evaporation was less influential than mixing. These effects

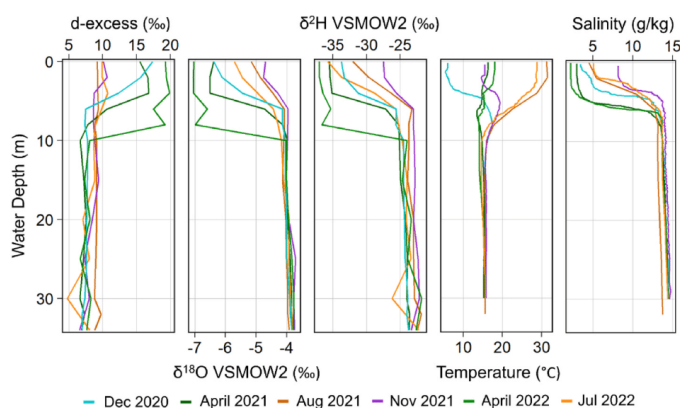


**Fig. 8.** Variations in Suigetsu  $\delta_{lake}$  with depth. d-excess,  $\delta^{18}O$ ,  $\delta^2H$ , temperature and salinity profiles across the study interval. Data were collected (approximately quarterly) on 22<sup>nd</sup> December 2020, 8<sup>th</sup> April 2021, 5<sup>th</sup> August 2021, 17<sup>th</sup> November 2021, 23<sup>rd</sup> April 2022 and 21<sup>st</sup> July 2022. (For interpretation of the references to colour in this figure legend, the reader is referred to the Web version of this article.)

explain the absence of a late summer  $\delta^{18}O$  minimum in Lake Mikata and Lake Suigetsu (in contrast to precipitation  $\delta^{18}O$ ) and elevated autumn values (discussed above; Fig. 7). D-excess did not appear to change significantly in autumn; possibly due to the overwhelming influence of seasonality, but most likely because the d-excess values at the surface and in the saline deep water were similar during the autumn. Hence, any amount of incursion or mixing would not result in a change in d-excess at the surface.

The combined influence of saline water incursion, mixing and evaporation did not persist through the entirety of the year; evidence from the surface water isotopes indicates that evaporation was limited to the summer, and extended monitoring by Kondo et al. (2000) suggested that mixolimnion mixing was temporally constrained to autumn. Our observations suggest that heavy winter precipitation delivered to the catchment regenerated the freshwater mixolimnion in Lake Suigetsu and effectively “reset” the effects described above, producing the minima in  $\delta^{18}O$  and  $\delta^2H$  in the surface waters (Fig. 7) and reinstating the relationship between precipitation and lake  $\delta^{18}O$  and  $\delta^2H$ . However, since the surface waters of Lake Suigetsu retain some salinity year-round, the influence of saline water is never zero, merely diminished in relation to the effect of precipitation inputs. We observed an increase in  $\delta^{18}O$  and  $\delta^2H$  of the surface waters from the freshwater Hasu River to the fresh-brackish Lake Mikata and then to the brackish-saline Lake Suigetsu (Fig. 6), which was likely due to increasing quantities of Sea of Japan-derived waters (with higher isotope compositions). The composition of Lake Suigetsu showed the greatest departure from the Hasu River composition during autumn, but there was still  $\sim 1$  ‰ difference in  $\delta^{18}O$  during spring between the locations which can be attributed to this non-zero salinity. Lake Mikata existed between the compositions of Lake Suigetsu and the Hasu River because it is a shallower water body with no persistent saline deepwater but does experience a small degree of saline water incursion during autumn (Kondo et al., unpublished data) and possibly some evaporation.

## 5. Discussion

The key motivation of this study was to understand the major controls of  $\delta_{river}$  and  $\delta_{lake}$  within the Five Lakes of Mikata catchment and hence direct future interpretation of isotope-based palaeoclimate proxies from the Lake Suigetsu sediment cores. Our results show that a dominant control of Lake Suigetsu  $\delta_{lake}$  (as well as Lake Mikata  $\delta_{lake}$ ) was

the isotope composition of precipitation, and whilst there were internal catchment processes (homogenisation, a transit lag, seawater influences and evaporation) that affected the composition of river and lakes, for the most part (excluding autumn) these did not obscure the  $\delta_{precipitation}$  signals, or prevent their detection in  $\delta_{lake}$ . Indeed, the predominant effect of the signal homogenisation was to limit the effect of  $\delta_{precipitation}$  dataset noise on  $\delta_{lake}$ . In order to better understand the propagation of  $\delta_{precipitation}$  signals to  $\delta_{lake}$  across the span of the Suigetsu cores, it is important to consider the ways in which the current lake configuration is non-analogous to the past.

Our observations also indicate that evaporation effects were not particularly influential during the study period (with the strongest evidence limited to a single year) and were limited to the summer months. This would be expected to be the case for much of the interval covered by the Suigetsu cores, given that, aside from the Eemian, our monitoring period existed at the upper limit of temperatures experienced at the Five Lakes of Mikata for the last 150 ka. Whilst it is important to consider that evaporation is not singularly related to air temperature, but rather a range of interconnected physical processes, Lake Suigetsu receives large quantities of precipitation annually which limits the impact of evaporation on  $\delta_{lake}$  (Vystavna et al., 2021). It follows that evaporation is not likely to have been a major driver of  $\delta_{lake}$  across the history of Lake Suigetsu sedimentation, as long as the region was not significantly more arid in the past, but should still be considered when interpreting proxies of summer  $\delta_{lake}$ .

Marine influences are also negligible from a palaeo-isotope perspective. In the modern day, saline water incursions and mixing of surface lake water with low  $\delta^{18}O$  and  $\delta^2H$  deepwater originating from the Sea of Japan had a demonstrable effect on lake  $\delta^{18}O$  and  $\delta^2H$  in the autumn months. However, the connection between Lake Suigetsu and the Sea of Japan is anthropogenic and there were no marine influences on the lakes for most of the late Pleistocene (exceptions being at  $\sim 7$  ka during a highstand in the Sea of Japan, and during the Eemian global highstand) as corroborated by diatom assemblage counts of freshwater versus brackish-tolerant species (Saito-Kato et al., unpublished data). Aside from these intervals, we predict that  $\delta_{lake}$  was not affected by seawater, either via saline water incursions or mixing. There is evidence for stratification in the past (deepwater anoxia is supported by varve preservation, and surface water oxygenation is supported by aquatic productivity); however, we would not expect to see the same stark difference in isotope compositions above and below the palaeo-chemocline

as the present-day chemocline because the deepwater and surficial waters would have had the same meteoric source. As a result, there would be no influence of the Sea of Japan to Lake Suigetsu outside of these periods and the elevated autumn  $\delta^{18}\text{O}$  and  $\delta^2\text{H}$  values that partially obscure the summer precipitation  $\delta^{18}\text{O}$  minima would not be observed. Hence, in the intervals where Lake Suigetsu was a freshwater lake, we would expect  $\delta_{\text{precipitation}}$  and  $\delta_{\text{lake}}$  to be more closely aligned, and no offset between the Hasu River, Lake Mikata and Lake Suigetsu.

However, persistence of this stratification regime, evidenced by the preservation of varves that required basal water anoxia, suggests that the mechanistic elements of signal homogenisation (muting the seasonal precipitation signal in the surface water and homogenising the deep-water) and seasonal lags in the surface water were still active during this time, although subject to some variability. As a result, on longer timescales, palaeoclimate proxies that record deepwater conditions (e.g., isotopes of siderite ( $\text{FeCO}_3$ ), abundant in Lake Suigetsu) would record an averaged  $\delta_{\text{precipitation}}$  signal, possibly over a number of years (accounting for other fractionation processes involved in signal capture by the proxy system). Conversely, palaeoclimate proxies that record surface water conditions (e.g., diatoms and other algae) will record seasonally lagged  $\delta_{\text{precipitation}}$ , i.e., spring-weighted proxies will capture winter  $\delta_{\text{precipitation}}$ , and so forth. This relationship is of course subject to variations in the lag time (which, if lengthened, could cause greater overlap of seasonal signals) and differences in climate, which could alter the timing of delivery to the lakes. During glacial intervals, pollen reconstructed temperature for the coldest month is consistently below  $0^\circ\text{C}$ , suggesting that the limited snowmelt lag in the present day would be more prominent. Additionally, the lakes were likely frozen on the surface for much of the winter. Overall, this would be expected to have stalled the movement of water through the catchment and extend the transit lag between delivery of winter (EAWM) precipitation and detection in the lake into the spring season. Under these circumstances, palaeoclimate proxies that capture the spring  $\delta_{\text{lake}}$ , such as spring blooming diatoms, would capture winter (EAWM)  $\delta_{\text{precipitation}}$  (arguably with even greater certainty than the present day). Proxies that capture summer  $\delta_{\text{lake}}$ , such as algal biomarkers would, by contrast, capture a mix between winter, spring and summer  $\delta_{\text{precipitation}}$  because these would enter the lake in quicker succession (although spring precipitation quantities are very small in comparison to winter and summer, and hence are unlikely to have a significant effect). Autumn  $\delta_{\text{lake}}$ -capturing proxies, such as autumn blooming diatoms, would still predominately capture summer (EASM)  $\delta_{\text{precipitation}}$  composition. Terrestrial proxies (e.g.,  $\delta^{18}\text{O}$  of pollen grains and  $\delta^2\text{H}$  of long-chained n-alkanes and n-alkanoic acids) would be unaffected by changes to the transit lag as they capture soil pore water rather than lake water and would be expected to more closely reflect changing  $\delta_{\text{precipitation}}$ .

Having established that the dominant driver of  $\delta_{\text{lake}}$  is  $\delta_{\text{precipitation}}$ , it is prudent to consider what could affect this quantity in the past. We anticipate that palaeo-EAM precipitation from both seasonal modes was a dominant influence on  $\delta_{\text{precipitation}}$  delivered to the catchment because winter and summer are associated with large quantities of precipitation (and hence  $\delta_{\text{precipitation}}$  will be weighted towards the composition of the EAWM and EASM). Additionally, whilst autumn (predominately typhoon) precipitation provides a third period of rain annually, and we observe the influence of intense precipitation events on  $\delta^{18}\text{O}$  and  $\delta^2\text{H}$  of precipitation, these signals were not detected in the lakes. For this reason, we anticipate that unless typhoon frequency was significantly greater in the past, the tendency of  $\delta_{\text{lake}}$  to reflect only extended seasonal precipitation events (i.e., the EAM) will limit the influence of typhoon precipitation, even if it is recorded in  $\delta_{\text{precipitation}}$ . It is not unreasonable, therefore, to exclude the typhoon season influence on  $\delta_{\text{precipitation}}$  and consider  $\delta_{\text{precipitation}}$  at Wakasa to be most closely linked with EAM behaviour. Importantly, the influence of both EAWM and EASM components were observed at the catchment, establishing that the area is a sensitive location – even optimised, especially relative to Tokyo – for studying both components of the EAM. This is particularly useful given

the skew in existing palaeoclimate reconstructions towards the summer months.

However, our findings were consistent with others from central Japan (e.g., Taniguchi et al., 2000), which note that for contemporary isotopes there is no significant difference in  $\delta^{18}\text{O}$  and  $\delta^2\text{H}$  between EAWM and EASM precipitation. As such, it is important to note that unlike Continental Asia, annually integrated  $\delta^{18}\text{O}$  and  $\delta^2\text{H}$  do not reflect the changing relative input of EAWM and EASM precipitation, because their compositions are so alike. Isotope composition averaged on multi-annual timescales will not reflect the balance between these systems unless either one of EAWM or EASM changes in strength and the other remains stable, or one increases in strength and the other decreases concurrently. These changes in behaviour can be caused by different climatic regimes (such as glacial periods) or across climatic transitions. Under such conditions, the changing strength of the EAWM and EASM would be expected to impact on both the annually averaged deep  $\delta_{\text{lake}}$  and the seasonally-lagged surface water  $\delta_{\text{lake}}$ ; the former by affecting the balance between the two seasonal modes, and the latter by affecting either EAWM or EASM  $\delta_{\text{precipitation}}$ . Under these circumstances, EAWM and EASM  $\delta_{\text{precipitation}}$  would diverge, and hence terrestrial and surface water palaeoclimate proxy seasonality becomes extremely important for interpretation. It is therefore vital to know which composition (winter-weighted, summer-weighted or mixed) is captured by each palaeoclimate proxy before interpreting the signal, accounting also for changes to the lag time.

Our observations are restricted to the study interval, and hence provide limited contributions to the interpretation of long-term drivers of  $\delta^{18}\text{O}$  and  $\delta^2\text{H}$  associated with EAM behaviour, however this remains an important component of palaeoclimate proxy interpretation. EAM rainfall  $\delta_{\text{precipitation}}$  tends to respond inversely to monsoon strength, due to a combination of preferential rainout of the heavier isotopes, enhanced by increased quantities of precipitation and increased cloud top height with a stronger monsoonal convection, which is associated with low condensation temperatures (Cai and Tian, 2016). Our results show that the amount effect does not have a strong relationship within the catchment in the modern day; however, that does not preclude a relationship to monsoon intensity; Uemura et al. (2012) noted a limited influence of local precipitation amount on  $\delta^{18}\text{O}$  in Okinawa (Southern Japan), but that the precipitation amount integrated over the full transport pathway was significant. Furthermore, the Fukugaguchi stalagmite record (Itoigawa, central Japan) shows a strong relationship of  $\delta^{18}\text{O}$  to EAWM precipitation amount despite modern  $\delta_{\text{precipitation}}$  showing a statistically weak relationship to precipitation amount (Sone et al., 2013). Other factors which could contribute to the overall signal are changes at source: composition, temperature and relative humidity (e.g., Amekawa et al., 2021), and, in the EASM mode, the positioning of the EAM front (Kurita et al., 2015). Furthermore, the prevalence of sea ice during glacial periods, particularly in the relatively isolated Sea of Japan, might be expected to limit evaporation despite changes to EAWM strength. Hence, it is vital to consider how EAM  $\delta_{\text{precipitation}}$  was controlled by the evolution of the climate of the region as a whole and how this affected  $\delta_{\text{precipitation}}$  at Wakasa.

Finally, the clearest seasonal signal derived from the catchment was undoubtedly that of d-excess, and this was the only isotope parameter which demonstrated the ability to distinguish precipitation from different seasons. Not only this, but the transfer of the d-excess signal from precipitation to lake was clearer than for  $\delta^{18}\text{O}$  and  $\delta^2\text{H}$ , possibly due to the amplitude of seasonal changes and the limited influence of other competing controls. However, it is much more difficult to calculate d-excess using palaeo-isotope reconstructions, because it requires the combination of temporally and spatially equivalent  $\delta^{18}\text{O}$  and  $\delta^2\text{H}$  values. If compatible palaeoclimate proxy records are produced and d-excess calculation becomes possible, this should be a consideration for future research based on the excellent seasonal distinctions observed in this variable and its potential as a powerful proxy of past monsoon dynamics.

## 6. Conclusions

Understanding the relationship between climate variability, the isotope composition of precipitation and the transfer of precipitation isotope signals into lake waters is essential to support the interpretation of past climates using isotope-based proxies derived from lake sediments. Using contemporary monitoring of the isotope composition of precipitation ( $\delta_{\text{precipitation}}$ ), river water ( $\delta_{\text{river}}$ ) and lake water ( $\delta_{\text{lake}}$ ) across the Five Lakes of Mikata catchment, Japan, we assessed the factors affecting  $\delta_{\text{lake}}$ , with a particular focus on Lake Suigetsu. Precipitation  $\delta^{18}\text{O}$  and  $\delta^2\text{H}$  exhibited only small seasonal differences across the year due to the similar compositions of winter (EAWM) and summer (EASM) precipitation, which act as end members with opposing trajectories. Precipitation d-excess, by contrast, clearly demarcated the different seasonal influences due to different evaporation conditions at the moisture sources of the EAWM (Sea of Japan) and EASM (Pacific Ocean domain), with a gradual shift between the two during the spring and autumn. The difference between winter and summer d-excess was enhanced by the location of the catchment. There was limited statistical evidence to support a temperature effect over precipitation  $\delta^{18}\text{O}$  or  $\delta^2\text{H}$ ; however, when considering the data on a seasonal basis, there was some evidence to support a local amount effect, with minima in monthly averaged  $\delta^{18}\text{O}$  and  $\delta^2\text{H}$  during the wettest (EAM) seasons of the year.

We found that  $\delta_{\text{lake}}$  and  $\delta_{\text{precipitation}}$  were directly related, although the spread of values of  $\delta_{\text{lake}}$  was more limited due to in-catchment homogenisation. Despite this, compositional patterns were preserved, and it was still possible to detect seasonal trends in  $\delta_{\text{lake}}$ , which paralleled those of  $\delta_{\text{precipitation}}$  and were attributed to the same causes. A two to three-month transit lag between  $\delta_{\text{precipitation}}$  and  $\delta_{\text{lake}}$  was observed and the length of this lag related to the quantity of precipitation. The influence of isolated precipitation events on  $\delta_{\text{lake}}$  (including typhoons) was negligible in comparison to significant extended freshwater inputs to the catchment from the East Asian Monsoon. The incursion of saline water from the Sea of Japan and autumnal mixing resulted in elevated  $\delta^{18}\text{O}$  and  $\delta^2\text{H}$  values in the lakes during late summer and autumn (obscuring the  $\delta^{18}\text{O}$  minimum equated to the EASM) and caused a greater effect for Lake Suigetsu than Lake Mikata. This was possibly combined with summer evaporation effects, although evidence for the influence of evaporation varied between years. The large influx of winter precipitation to the catchment re-established the relationship between  $\delta_{\text{lake}}$  and  $\delta_{\text{precipitation}}$  which extended from winter to early summer. Deep water composition in Lake Suigetsu was stable and homogenous across the study period.

These results will facilitate interpretation of palaeoclimate reconstructions derived from oxygen and hydrogen isotope analysis of the Lake Suigetsu sediment cores. It is expected that  $\delta_{\text{precipitation}}$  (and thus  $\delta_{\text{lake}}$ ) will be closely related to East Asian Summer Monsoon and East Asian Winter Monsoon  $\delta_{\text{precipitation}}$  fluctuations across the ~150 ka of the late Quaternary covered by the Suigetsu cores. The seasonal patterns in  $\delta_{\text{lake}}$  could be altered under different climatic regimes by large scale drivers (such as monsoon strength and balance of seasonal precipitation), along with the influence of local factors, including the transit lag. However, not all of the factors affecting  $\delta_{\text{lake}}$  observed during this contemporary monitoring will be significant on longer timescales. The incursion of sea water is a consequence of anthropogenic catchment alteration and, as such, is not expected to have affected the lake water isotope hydrology prior to the last ~400 years. Evaporation is also expected to have minimal effects on down-core  $\delta_{\text{lake}}$  reconstructions which are limited to the summer months. Robust interpretation is predicated on sound understanding of proxy seasonality and whether the proxy captures surficial or deepwater  $\delta_{\text{lake}}$ .

### Declaration of competing interest

The authors declare that they have no known competing financial interests or personal relationships that could have appeared to influence

the work reported in this paper.

### Data availability

Data is available at <https://doi.org/10.5525/gla.researchdata.1429>

### Acknowledgements

The authors would like to thank T. Tanabe for their contribution to collecting the water samples in 2011–2012, K. Ichinaga and M. Tanoue for permission to use their precipitation isotope data from Tokyo and R. Kondo for access to contemporary salinity data for the Five Lakes of Mikata. All other isotope analysis was conducted by C. Arrowsmith; J. Lacey contributed to the writing of the methodology section; and M. Ankor designed and built the rainwater sampler. Water quality data for the water column of Suigetsu Lake were provided by Dr Yasushi Miyamoto. This research was financially supported by an Australian Research Council Discovery Project [grant number DP200101768], a JSPS KAKENHI Grant [grant number 19K20442] and C.L.Rex was supported by the NERC IAPETUS2 Doctoral Training Partnership. The authors declare no conflicts of interest.

### Appendix A. Supplementary data

Supplementary data to this article can be found online at <https://doi.org/10.1016/j.qsa.2023.100145>.

### References

- Amekawa, S., Kashiwagi, K., Hori, M., Sone, T., Kato, H., Okumura, T., Yu, T.L., Shen, C., Kano, A., 2021. Stalagmite evidence for East Asian winter monsoon variability and 18O-depleted surface water in the Japan Sea during the last glacial period. *Prog. Earth Planet. Sci.* 8 (1) <https://doi.org/10.1186/s40645-021-00409-8>.
- Araguás-Araguás, L., Froehlich, K., Rozanski, K., 1998. Stable isotope composition of precipitation over southeast Asia. *J. Geophys. Res. Atmos.* 103 (D22), 28721–28742. <https://doi.org/10.1029/98JD02582>.
- Bershaw, J., 2018. Controls on deuterium excess across Asia. *Geosciences* 8 (7), 257. <https://doi.org/10.3390/geosciences8070257>.
- Bronk Ramsey, C., Staff, R.A., Bryant, C.L., Brock, F., Kitagawa, H., Van Der Plicht, J., Scholaut, G., Marshall, M.H., Brauer, A., Lamb, H.F., Payne, R.L., Tarasov, P.E., Haraguchi, T., Gotanda, K., Yonenobu, H., Yokoyama, Y., Tada, R., Nakagawa, T., 2012. A complete terrestrial radiocarbon record for 11.2 to 52.8 kyr B.P. *Science* 338 (6105), 370–374. <https://doi.org/10.1126/science.1226660>.
- Bronk Ramsey, C., Heaton, T.J., Scholaut, G., Staff, R.A., Bryant, C.L., Brauer, A., Lamb, H.F., Marshall, M.H., Nakagawa, T., 2020. Reanalysis of the atmospheric radiocarbon calibration record from Lake Suigetsu, Japan. *Radiocarbon* 62 (4), 989–999. <https://doi.org/10.1017/RDC.2020.18>.
- Esri, 2022a. "World Dark Grey base" [basemap] 1:10,000,000 (panel A), 1:400,000 (panel B), 1:67,946 (panel C). <https://www.arcgis.com/home/item.html?id=a284a9b99b3446a3910d4144a50990f6>. (Accessed 12 September 2022).
- Esri, 2022b. "World Hillshade" [basemap] 1:10,000,000 (panel A), 1:400,000 (panel B), 1:67,946 (panel C). <https://www.arcgis.com/home/item.html?id=1b243539f4514b6ba35e7d995890db1d>. (Accessed 12 September 2022).
- Fudeyasu, H., Ichinaga, K., Sugimoto, A., Yoshimura, K., Ueta, A., Yamanaka, M.D., Ozawa, K., 2008. Isotope ratios of precipitation and water vapor observed in Typhoon Shanshan. *J. Geophys. Res. Atmos.* 113 <https://doi.org/10.1029/2007JD009313> article D12113.
- Gallagher, S.J., Sagawa, T., Henderson, A.C.G., Saavedra-Pellitero, M., De Vleeschouwer, D., Black, H., Itaki, T., Toucanne, S., Bassetti, M.A., Clemens, S., Anderson, W., Alvarez-Zarikian, C., Tada, R., 2018. East Asian monsoon history and paleoceanography of the Japan sea over the last 460,000 years. *Paleoceanogr. Paleoclimatol.* 33 (7), 683–702. <https://doi.org/10.1029/2018PA003331>.
- Gibson, J.J., Birks, S.J., Yi, Y., 2016. Stable isotope mass balance of lakes: a contemporary perspective. *Quat. Sci. Rev.* 131, 316–328. <https://doi.org/10.1016/j.quascirev.2015.04.013>.
- Gonfiantini, R., 1986. Environmental isotopes in lake studies. In: Fritz, P., Fontes, J.C. (Eds.), *Handbook of Environmental Isotope Geochemistry Volume Two, the Terrestrial Environment*. Elsevier, B. Netherlands, pp. 113–168. <https://doi.org/10.1016/B978-0-444-42225-5.50008-5>.
- Hasegawa, H., Akata, N., Kawabata, H., Sato, T., Chikuchi, Y., Hisamatsu, S., 2014. Characteristics of hydrogen and oxygen stable isotope ratios in precipitation collected in a snowfall region, Aomori Prefecture, Japan. *Geochem. J.* 48 (1), 9–18. <https://doi.org/10.2343/geochemj.2.0279>.
- Ichinaga, K., Tanoue, M., and on behalf of the Isotope Mapping Working Group of the Japanese Society of Hydrological Science (IMWG/JAHS), 2016. Spatial analysis of annual mean stable isotopes in precipitation across Japan based on an intensive

- observation period throughout 2013. *Isotopes Environ. Health Stud.* 52 (4–5), 353–362. <https://doi.org/10.1080/10256016.2015.1132215>.
- Ichiyangi, K., Tanoue, M., 2016. Stable isotopes in precipitation across Japan during an intensive observation period throughout 2013. *J. Jpn. Assoc. Hydrol. Sci.* 46 (2), 123–138. <https://doi.org/10.4145/jahs.46.123>.
- Jackisch, D., Yeo, B.X., Switzer, A.D., He, S., Cantarero, D.L.M., Siringan, F.P., Goodkin, N.F., 2022. Precipitation stable isotopic signatures of tropical cyclones in Metropolitan Manila, Philippines, show significant negative isotopic excursions. *Nat. Hazards Earth Syst. Sci.* 22 (1), 213–226. <https://doi.org/10.5194/nhess-22-213-2022>.
- Japanese Meteorological Agency, 2022. Mihama (Fukui Prefecture) JMA Weather Station Data, Electronic Dataset, Japanese Meteorological Agency viewed 10/02/2022. <https://www.data.jma.go.jp/risk/obsdl/index.php>.
- Japanese Meteorological Agency, 2023. Tsuruga (Fukui Prefecture) JMA Weather Station Data, Electronic Dataset, Japanese Meteorological Agency viewed 23/06/2023. <https://www.data.jma.go.jp/risk/obsdl/index.php>.
- Jun-Mei, L., Jian-Hua, J., Shi-Yan, T., 2013. Re-discussion on East Asian Meiyu rainy season. *Atmos. Oceanic Sci. Lett.* 6, 279–283. <https://doi.org/10.3878/j.issn.1674-2834.13.0024>.
- Kondo, R., Butani, J., 2007. Comparison of the diversity of sulfate-reducing bacterial communities in the water column and the surface sediments of a Japanese meromictic lake. *Limnology* 8, 131–141. <https://doi.org/10.1007/s10201-007-0201-9>.
- Kondo, R., Kasashima, N., Matsuda, H., Hata, Y., 2000. Determination of thiosulfate in a meromictic lake. *Fish. Sci.* 66 (6), 1076–1081. <https://doi.org/10.1046/j.1444-2906.2000.00171.x>.
- Kondo, R., Kodera, M., Mori, Y., Okamura, T., Yoshikawa, S., Ohki, K., 2014. Spatiotemporal distribution of bacteriochlorophylls in the meromictic Lake Suigetsu, Japan. *Limnology* 15, 77–83. <https://doi.org/10.1007/s10201-013-0415-y>.
- Kurita, N., Fujiyoshi, Y., Nakayama, T., Matsumi, Y., Kitagawa, H., 2015. East Asian Monsoon controls on the inter-annual variability in precipitation isotope ratio in Japan. *Clim. Past* 11, 339–353. <https://doi.org/10.5194/cp-11-339-2015>.
- Lawrence, R.J., Gedzelman, D.S., 1996. Low stable isotope ratios of tropical cyclone rains. *Geophys. Res. Lett.* 23 (5), 527–530. <https://doi.org/10.1029/96GL00425>.
- Li, C., Kano, N., Ueno, Y., Hanabusa, M., Jiao, Y., Imaizumi, H., Watanabe, N., 2010. Characteristics of oxygen stable isotopic ratio in precipitations in Niigata Prefecture, Japan. *Radioisotopes* 59 (2), 93–102. <https://doi.org/10.3769/radioisotopes.59.93>.
- Masuzawa, T., Kitano, Y., 1982. Diagenetic deposition of manganese in sediment of a historically meromictic lake, Lake Suigetsu, Japan. *J. Oceanogr. Soc. Jpn.* 38, 73–80. <https://doi.org/10.1007/BF02110293>.
- Matsuyama, M., 1973. Changes in the Limnological features of a meromictic Lake Suigetsu during the years, 1926–1967. *J. Oceanogr. Soc. Jpn.* 39, 131–139. <https://doi.org/10.1007/BF02109088>.
- Matsuyama, M., 1974. Vertical distributions of some chemical substances in surface sediments of a meromictic Lake Suigetsu. *J. Oceanogr. Soc. Jpn.* 30, 209–215. <https://doi.org/10.1007/BF02111046>.
- McLean, D., Albert, P.G., Nakagawa, T., Staff, R.A., Suzuki, T., Smith, V.C., 2016. Identification of the Changbaishan 'Millennium' (B-Tm) eruption deposit in the Lake Suigetsu (SG06) sedimentary archive, Japan: synchronisation of hemispheric-wide palaeoclimate archives. *Quat. Sci. Rev.* 150, 301–307. <https://doi.org/10.1016/j.quascirev.2016.08.022>.
- Nakagawa, T., Gotanda, K., Haraguchi, T., Danhara, T., Yonenobu, H., Brauer, A., Yokoyama, Y., Tada, R., Takemura, K., Staff, R.A., Payne, R.L., Bronk Ramsey, C., Bryant, C.L., Brock, F., Scholaut, G., Marshall, M.H., Tarasov, P.E., Lamb, H.F., 2012. SG06, a fully continuous and varved sediment core from Lake Suigetsu, Japan: stratigraphy and potential for improving the radiocarbon calibration model and understanding of late Quaternary climate changes. *Quat. Sci. Rev.* 36, 164–176. <https://doi.org/10.1016/j.quascirev.2010.12.013>.
- Nakagawa, T., Tarasov, P., Staff, R., Bronk Ramsey, C., Marshall, M., Scholaut, G., Bryant, C., Brauer, A., Lamb, H., Haraguchi, T., Gotanda, K., Kitaba, I., Kitagawa, H., van der Plicht, J., Yonenobu, H., Omori, T., Yokoyama, Y., Tada, R., Yasuda, Y., 2021. The spatio-temporal structure of the Lateglacial to early Holocene transition reconstructed from the pollen record of Lake Suigetsu and its precise correlation with other key global archives: Implications for palaeoclimatology and archaeology. *Global Planet. Change* 202, 103493. <https://doi.org/10.1016/j.gloplacha.2021.103493>.
- Rolph, G., Stein, A., Stunder, B., 2017. Real-time environmental applications and display system: READY. *Environ. Model. Software* 95, 210–228. <https://doi.org/10.1016/j.envsoft.2017.06.025>.
- Russell, J.M., Johnson, T.C., 2006. The water balance and stable isotope hydrology of Lake Edward, Uganda-Congo. *J. Great Lake. Res.* 32 (1), 77–90. [https://doi.org/10.3394/0380-1330\(2006\)32\[77:TWBAS\]2.0.CO;2](https://doi.org/10.3394/0380-1330(2006)32[77:TWBAS]2.0.CO;2).
- Scholaut, G., Marshall, M.H., Brauer, A., Nakagawa, T., Lamb, H.F., Staff, R.A., Bronk Ramsey, C., Bryant, C.L., Brock, F., Kossler, A., Tarasov, P.E., Yokoyama, Y., Tada, R., Haraguchi, T., 2012. An automated method for varve interpolation and its application to the Late Glacial chronology from Lake Suigetsu, Japan. *Quat. Geochronol.* 13, 52–69. <https://doi.org/10.1016/j.quageo.2012.07.005>.
- Scholaut, G., Brauer, A., Nakagawa, T., Lamb, H.F., Tyler, J.J., Staff, R.A., Marshall, M.H., Bronk Ramsey, C., Bryant, C.L., Tarasov, P.E., 2017. Evidence for a bi-partition of the younger dryas Stadial in East Asia associated with inverted climate characteristics compared to Europe. *Sci. Rep.* 7, 44983. <https://doi.org/10.1038/srep44983>.
- Scholaut, G., Staff, R.A., Brauer, A., Lamb, H.F., Marshall, M.H., Bronk Ramsey, C., Nakagawa, T., 2018. An extended and revised Lake Suigetsu varve chronology from ~50 to ~10 ka BP based on detailed sediment micro-facies analyses. *Quat. Sci. Rev.* 200, 351–366. <https://doi.org/10.1016/j.quascirev.2018.09.021>.
- Seal, R.R., Shanks, W.C., 1998. Oxygen and hydrogen isotope systematics of Lake Baikal, Siberia: implications for paleoclimate studies. *Limnol. Oceanogr.* 43 (6), 1251–1261. <https://doi.org/10.4319/lo.1998.43.6.1251>.
- Shigematsu, T., Tabushi, M., Nishikawa, Y., Muroga, T., Matsunaga, Y., 1961. Geochemical study on lakes Mikata. *Bull. Inst. Chem. Res. Kyoto Univ.* 39 (1), 43–56.
- Smith, V.C., Mark, D.F., Staff, R.A., Blockley, S.P., Bronk Ramsey, C., Bryant, C.L., Nakagawa, T., Han, K.K., Wei, A., Takemura, K., Danhara, T., 2011. Toward establishing precise <sup>40</sup>Ar/<sup>39</sup>Ar chronologies for Late Pleistocene palaeoclimate archives: an example from the Lake Suigetsu (Japan) sedimentary record. *Quat. Sci. Rev.* 30 (21–22), 2845–2850. <https://doi.org/10.1016/j.quascirev.2011.06.020>.
- Sone, T., Kano, A., Okumura, T., Kashiwagi, K., Hori, M., Jiang, X., Shen, C.C., 2013. Holocene stalagmite oxygen isotopic record from the Japan Sea side of the Japanese Islands, as a new proxy of the East Asian winter monsoon. *Quat. Sci. Rev.* 75, 150–160. <https://doi.org/10.1016/j.quascirev.2013.06.019>.
- Staff, R.A., Ramsey, C.B., Bryant, C.L., Brock, F., Payne, R.L., Scholaut, G., Marshall, M.H., Brauer, A., Lamb, H.F., Tarasov, P.E., Yokoyama, Y., Haraguchi, T., Gotanda, K., Yonenobu, H., Nakagawa, T., 2011. New <sup>14</sup>C determinations from Lake Suigetsu, Japan: 12,000 to 0 cal BP. *Radiocarbon* 53 (3), 511–528. <https://doi.org/10.1017/S003822200034627>.
- Stein, A.F., Draxler, R.R., Rolph, G.D., Stunder, B.J.B., Cohen, M.D., Ngan, F., 2015. NOAA's HYSPLIT atmospheric transport and dispersion modeling system. *Bull. Am. Meteorol. Soc.* 96 (12), 2059–2077. <https://doi.org/10.1175/BAMS-D-14-00110.1>.
- Taniguchi, M., Nakayama, T., Tase, N., Shimada, J., 2000. Stable isotope studies of precipitation and river water in the Lake Biwa basin, Japan. *Hydro. Process.* 14 (3), 539–556. [https://doi.org/10.1002/\(SICI\)1099-1085\(20000228\)14:3<539::AID-HYP953>3.0.CO;2-L](https://doi.org/10.1002/(SICI)1099-1085(20000228)14:3<539::AID-HYP953>3.0.CO;2-L).
- Uemura, R., Yonezawa, N., Yoshimura, K., Asami, R., Kadana, H., Yamada, K., Yoshida, N., 2012. Factors controlling isotopic composition of precipitation on Okinawa Island, Japan: implications for paleoclimate reconstruction in the East Asian Monsoon region. *J. Hydrol.* 475, 314–322. <https://doi.org/10.1016/j.jhydrol.2012.10.014>.
- Vystavna, Y., Harjung, A., Monteiro, L.R., Matiatos, I., Wassenaar, L.L., 2021. Stable isotopes in global lakes integrate catchment and climatic controls on evaporation. *Nat. Commun.* 12, 1–7. <https://doi.org/10.1038/s41467-021-27569-x>.
- Walker, M.J., Johnsen, S.J., Rasmussen, S.O., Popp, T., Steffensen, J.-P., Gibbard, P., Hoek, W.Z., Lowe, J., Andrews, J., Bjo, S., Cwynar, L.C., Hughen, K.A., Kershaw, P., Kromer, B., Litt, T., Lowe, D.J., Nakagawa, T., Newnham, R., Schwander, J., Rck, B., 2009. Formal definition and dating of the GSSP (Global Stratotype Section and Point) for the base of the Holocene using the Greenland NGRIP ice core, and selected auxiliary records. *J. Quat. Sci.* 24 (1), 3–17. <https://doi.org/10.1002/jqs.1227>.
- Wassenaar, L.L., Athanopoulos, P., Hendry, M.J., 2011. Isotope hydrology of precipitation, surface and ground waters in the Okanagan Valley, British Columbia, Canada. *J. Hydrol.* 411 (1–2), 37–48. <https://doi.org/10.1016/j.jhydrol.2011.09.032>.
- Xia, C., Liu, G., Hu, Y., Meng, Y., 2018. Precipitation stable isotope variability in tropical monsoon climatic zone of Asia. *Int. J. Geophys. Geophys.* 392 (4) <https://doi.org/10.1088/1757-899X/392/4/042028>.
- Xia, Z., Welker, J.M., Winnick, M.J., 2022. The seasonality of deuterium excess in non-polar precipitation. *Global Biogeochem. Cycles* 36 (10), e2021GB007245. <https://doi.org/10.1029/2021GB007245>.
- Xu, H., Goldsmith, Y., Lam, J., Tan, L., Wang, X., Zhou, X., Cheng, J., Lang, Y., Liu, C., 2020. juxtaposition of western Pacific subtropical high on Asian summer monsoon shapes subtropical East Asian precipitation. *Geophys. Res. Lett.* 47 (3), e2019GL084705 <https://doi.org/10.1029/2019GL084705>.

## Chapter 5 (Published Version)

Quaternary Geochronology 71 (2022) 101319



Contents lists available at ScienceDirect

## Quaternary Geochronology

journal homepage: [www.elsevier.com/locate/quageo](http://www.elsevier.com/locate/quageo)

## Controls on luminescence signals in lake sediment cores: A study from Lake Suigetsu, Japan

Charlie L. Rex<sup>a,\*</sup>, Richard A. Staff<sup>a</sup>, David C.W. Sanderson<sup>a</sup>, Alan J. Cresswell<sup>a</sup>,  
Michael H. Marshall<sup>b</sup>, Masayuki Hyodo<sup>c</sup>, Daishi Horiuchi<sup>d</sup>, Ryuji Tada<sup>d</sup>, Takeshi Nakagawa<sup>e</sup>

<sup>a</sup> Scottish Universities Environmental Research Centre (SUERC), University of Glasgow, Scottish Enterprise Technology Park, Rankine Avenue, East Kilbride, G75 0QF, UK

<sup>b</sup> Institute of Geography and Earth Sciences, Aberystwyth University, Aberystwyth, SY23 3DB, UK

<sup>c</sup> Research Center for Inland Seas, Kobe University, Kobe, 657-8501, Japan

<sup>d</sup> Department of Earth and Planetary Sciences, University of Tokyo, Hongo, Bunkyo-ku, Tokyo, 113-0033, Japan

<sup>e</sup> Ritsumeikan University, 1-chōme-1 Nojihigashi, Kusatsu, Shiga, 525-0058, Japan

## ARTICLE INFO

## Keywords:

Portable OSL  
Laboratory profiling  
Luminescence dating  
Lake sediment  
Palaeoenvironment

## ABSTRACT

The luminescence characteristics of sediments are driven by a range of environmental factors and can be used as indicators of both local and regional environmental shifts. Hence, rapid luminescence profiling techniques are increasingly employed during multiproxy analysis of sediment cores, overcoming the practical limitations of traditional (dating) methods. One emerging application of luminescence profiling is in the palaeoenvironmental investigation of lake cores. This study demonstrates the versatility of rapid core profiling using portable optically stimulated luminescence and laboratory profiling techniques for appraising the luminescence characteristics of the Lake Suigetsu (Japan) sediment cores. These techniques were employed across four key time periods, each selected for their unique environmental context and significance on either a local or global scale, in order to identify relationships between down-core luminescence and environmental change. We demonstrate that the luminescence characteristics of the cores are susceptible to a range of environmental perturbations and can therefore act as proxies of past change. Additionally, the quantification of these luminescence signals, alongside an assessment of dose rate variations down-core, supports the notion that future luminescence dating is feasible. The results of this analysis contribute to the wider understanding of the application of luminescence techniques – both profiling and dating – to lake sediment cores.

## 1. Introduction

Optically Stimulated Luminescence (OSL) dating is a versatile chronological tool which can be applied to both marine and terrestrial sediment cores (e.g., Kadereit et al., 2012; Gao et al., 2017). The use of this technique has been aided by well-defined methodologies for extracting OSL-appropriate (light-tight) samples from core material (Armitage and Pinder, 2017; Nelson et al., 2019). OSL dating is often applied to complement other chronological tools, such as radiocarbon dating, during age-depth model construction (Zhao et al., 2019; Li et al., 2020). However, where other chronometers cannot be applied (e.g., if the material is older than the limit of radiocarbon dating), OSL dating can form a major component of the core chronology (e.g., Long, 2012; Hu et al., 2018).

However, the value of luminescence techniques to core analysis is not limited to dating alone (Munyikwa et al., 2021). It has been widely observed that the luminescence characteristics of sediments are driven by a range of environmental factors. Hence, down-core luminescence characterisation has the potential to contribute to our understanding of environmental change through time. However, most traditional luminescence techniques are both time- and core material-intensive (Batteman and Catt, 1996; Stone et al., 2015), which limits the number of samples that it is feasible to analyse and delays the final output of results until some months after sampling (Porat et al., 2019). As a result, rapid luminescence profiling techniques are increasingly employed to characterise the luminescence behaviour of core sediments and elucidate environmental changes, typically as part of multiproxy analysis (e.g., Ghilardi et al., 2015; Sanderson and Kinnaird, 2019; Pears et al., 2020).

\* Corresponding author.

E-mail address: [c.rex.1@research.gla.ac.uk](mailto:c.rex.1@research.gla.ac.uk) (C.L. Rex).

<https://doi.org/10.1016/j.quageo.2022.101319>

Received 1 December 2021; Received in revised form 1 April 2022; Accepted 19 April 2022

Available online 29 April 2022

1871-1014/© 2022 Elsevier B.V. All rights reserved.

In this study, we examine the versatility of rapid down-core profiling techniques (portable OSL (POSL) analysis and laboratory (lab) profiling) for the detection of luminescence proxies of environmental change in lake sediment cores (from Lake Suigetsu, Japan). Such luminescence proxies have only recently been investigated in a lacustrine setting for this purpose (Příšková et al., 2019). Variations in luminescence characteristics (both natural signals and sensitivities) are examined and compared to known environmental shifts, supported by existing proxy data. The Suigetsu cores offer a unique opportunity to probe this relationship across a ~140,000-year age range in a lacustrine setting. A secondary aim of our study was to provide an assessment of the dating potential of the Suigetsu core material across a range of ages by comparing the quartz and polymineral fractions as potential chronometers, and to identify complexities which could hinder future age calculations. The motivation for this aspect of the work was the extension of the absolute Suigetsu chronology beyond the limit of radiocarbon dating.

The luminescence characteristics of the Suigetsu cores were appraised during four key time periods, each selected for their distinctive environmental context and significance on either a local or global scale. This facilitates the examination of a range of prominent environmental shifts on the luminescence characteristics of the cores, following the logic that the most pronounced shifts would cause changes that are most easily detectable by the chosen methods. The time periods span almost the full temporal range of the Suigetsu cores, including sections both covered by the existing radiocarbon chronology (in order to tether our findings in a chronologically well-constrained period) and older than the radiocarbon limit (to consider the potential of Suigetsu for future dating). The youngest of these (Time Period 1, “the Last 500 Years”) spans from ~550 cal BP to the present day; a period comprising a series of local environmental perturbations, including the artificial connection of the lake to the Sea of Japan and a number of local flood events. The next (Time Period 2, “the Laschamp Excursion”) extends from ~45,000 to 35,000 cal BP; a period of global change containing the Laschamp geomagnetic excursion and variable average annual temperatures (concomitant with Greenland Interstadials 12 to 7; Rasmussen et al., 2014). The third time period (Time Period 3, “the Varve Limit”) spans from ~73,000 to 69,000 yr BP and is centred on the initiation of varving, which represents a significant alteration in lake biogeochemistry. The final time period (Time Period 4, “Termination II”) extends from ~140,000 to 118,000 yr BP, encapsulating the global transition from MIS 6 to MIS 5e, which is associated with broadly increasing temperatures and a strengthening Summer Monsoon in East Asia (Duan et al., 2019).

## 2. Regional setting

Suigetsu is a tectonic lake located on the western side of the active Mikata fault in Fukui Prefecture, Honshu Island, central Japan (35° 35' N, 135° 53' E; Supplementary Fig. 1). The western side of the fault is subsiding and hence the lake has deepened through time. During late-MIS 7/early-MIS 6, Suigetsu was a transient shallow fluvial-lacustrine environment (Nakagawa et al., 2012), which became a brackish lake during the MIS 5e global sea level highstand. Diatom assemblage analysis indicates that the lake experienced freshwater conditions from MIS 5d to the Holocene. In the present day, the lake is ~34 m deep and brackish, having been artificially connected to the Sea of Japan via the Urami Canal (Supplementary Fig. 1) in 286 cal BP (AD 1664; Saito-Kato et al., 2013).

The Suigetsu sediments are continuously, countably varved between ~10,000 and ~50,000 cal BP, providing the longest such record from the Quaternary (Schlölaut et al., 2018). Varve counting, coupled with a radiocarbon dataset consisting of over 800 measurements (Staff et al., 2011; Bronk Ramsey et al., 2012) and tephra tie points (e.g., McLean et al., 2018; Albert et al., 2019) constitute the robust core chronology to 50,000 cal BP, which is aligned to the IntCal20 timescale (Bronk Ramsey

et al., 2020). Beyond 50,000 cal BP, a provisional chronology is loosely constrained by wiggle matching of *Cryptomeria* pollen from Suigetsu to the LR04 benthic stack.

Four previous coring campaigns (SG93, SG06, SG12 and SG14) recovered a series of overlapping sediment core sections from the present day to >200,000 yr BP (98 m of composite depth; Nakagawa et al., 2012; McLean et al., 2018). The preserved sequence encapsulates two glacial and two full interglacial periods of continuous sedimentation. Any effects of disturbance are minimal; the presence of laminations during MIS 5e and varves between ~70,000 yr BP and the present day (indicating bottom water anoxia and good conditions for preservation) and further sedimentological inspection suggests that the core material does not contain hiatuses or disturbed sections (Nakagawa et al., 2012). This provides a palaeoenvironmental archive that comprises well-preserved millennial, centennial, decadal, annual, and even sub-annual-scale environmental oscillations which are the subject of ongoing multiproxy analysis. The Suigetsu cores are suitable for luminescence analysis because they contain detrital particles which have remained in-situ within the sequence post-deposition.

## 3. Materials and methods

### 3.1. Core materials

Materials were obtained from the SG06 cores for luminescence characterisation, totalling 60 samples. To mitigate against exposure of samples to light prior to measurement, the top 1 mm of sediment was removed from longitudinally split cores under dim red-light conditions to access unexposed material. Beyond this depth the influence of natural light has been shown to be smaller than the analytical error, so this material was deemed suitable for analysis (Armitage and Pinder, 2017). Sampling strategies varied based on availability of material, duration of time period, and structure of the event(s) to be studied (Supplementary Information 1). Contiguous (continuous adjacent) sampling was employed for Time Periods 1 and 3, because these spanned shorter intervals. Spot sampling was employed for Time Periods 2 and 4.

In addition, six samples were subsequently taken from across the four time periods for estimated dose rate ( $ED_R$ ) determination. These samples were analysed to compare the selected mineral fractions as potential chronometers and identify  $ED_R$  variations down-core which could affect the POSL and lab profiling results. These were taken post-luminescence analysis; one sample from each time period at a depth associated with representative natural luminescence values, and two additional samples at positions in the stratigraphy associated with relatively elevated natural luminescence values (within Time Periods 2 and 3).

### 3.2. Sample analysis

Each sample was subjected to two sets of analysis. First, measurements of IR- and blue light-stimulated luminescence were conducted using a POSL system (Supplementary Information 2). Each sample was spread to cover a 5 cm diameter Petri dish (ensuring a consistent exposed surface area for all samples) and then subjected to a Continuous Wave Proxy (CWproxy) measurement scheme to yield a suite of analytical values (Sanderson and Murphy, 2010; Kinnaird et al., 2015). These values comprised: two net quantities (POSLnet and PIRSLnet; calculated from total photon counts under blue-light and IR stimulations respectively, a proxy for age, sensitivity and dose rate); two depletion indices (Depletion Index (Blue) and Depletion Index (IR); calculated from the difference between the total photon count during the first and second 30 s of blue/IR stimulation, a proxy for mineralogical change, bulk properties and previous bleaching extent); and a PIRSL/POSL ratio (calculated by taking a ratio of the POSLnet and PIRSLnet values, a proxy for mineralogical change; Supplementary Information 2). Empty chamber measurements were taken every two samples to check for contamination in the instrument. A measurement of the POSL standards

(Morar Sand and Granulite) was taken at the start and end of each ~12-sample batch to verify instrument performance.

Second, samples underwent lab profiling, which consisted of a short chemical preparation before measurement in a Risø TL/OSL system (TL-DA-15; Supplementary Information 3 and Supplementary Fig. 2; Burbidge et al., 2007; Sanderson and Murphy, 2010). Chemical pretreatment isolated two fractions: a Polymineral Fine (PMF) fraction, comprising mixed mineralogy grains ~5–50 µm in size; and a Quartz Fine (QF) fraction, comprising HF etched material (predominantly quartz; although some samples contained some larger feldspar grains), again 5–50 µm in size. Two aliquots were measured per fraction as a monolayer on an 11 mm diameter disc. The Risø outputs were used to determine an estimated equivalent dose ( $ED_e$ ) in Gy by using the natural signal and the response of each aliquot to a 50 Gy dose (5 Gy doses were also included in the measurement scheme, but the relatively low sensitivity of the material precluded use of the response to such doses during sensitivity assessment). Each PMF aliquot was measured under both IR and blue light (yielding PMF-IR and PMF-blue signals, respectively), and the QF aliquots were measured under blue light only (to give a QF-blue signal).

The six samples for  $ED_R$  determination were dried and homogenised by grinding prior to measurement of key elemental concentrations following the procedure in Olive et al. (2001). A set of five standards were run alongside the samples (consisting of incremental ratios of Basalt:Granulite (1:0, 3:1, 1:1, 1:3, 0:1)). Elemental concentrations of uranium (U) and thorium (Th) were determined by Inductively Coupled Plasma Mass Spectrometry (ICP-MS) and potassium (K), iron (Fe) and manganese (Mn) by Inductively Coupled Plasma Optical Emission Spectrometry (ICP-OES).  $ED_R$  values were calculated using microdosimetry (Supplementary Information 4; Supplementary Table 2). The QF-blue, PMF-IR and PMF-blue  $ED_e$  values were considered alongside the  $ED_R$  values in order to resolve first-order age approximations that can be compared to the existing Suigetsu chronology.

#### 4. Results and interpretation

##### 4.1. Time Period 1, the last 500 years

Signals from both the POSL and lab profiling were small in magnitude for the last 500 years, reflecting the young age of the sediments (Fig. 1). Most samples contained only small quantities of quartz; hence data collection from the QF fraction was limited to a minority of discs and no clear trends were observed. The transition from fresh to brackish water in Suigetsu had no detectable influence on the luminescence properties of the sediment, and all variables remained constant across this boundary. Flood layers (visible as pale layers in the core photograph and highlighted in orange in Fig. 1) had the greatest impact on the luminescence profiles, producing high amplitude peaks at approximately ~30 cal BP (AD 1980) and 120 cal BP (AD 1830) in the POSLnet and PIRSLnet profiles (Fig. 1A), which correspond with elevated  $ED_e$  values from lab profiling (Fig. 1C). This suggests that across this section, POSLnet, PIRSLnet and PMF  $ED_e$  can be used as an indicator of the presence of flood-related material. These peaks were not observed in either of the depletion indices, nor in the PIRSL/POSL ratio (Fig. 1B), suggesting that they cannot be attributed to mineralogical variations and are unlikely to have resulted from different bleaching histories, and instead that these samples contained residual elevated dose values. The preservation of these elevated signals could be a result of delivery of this material in a manner that did not expose it to light, such as slumping of water-saturated hillsides, or large volumes of suspended sediments in river flow.

One sample (highlighted in yellow in Fig. 1) that did not visually correlate with flood layers or produce large POSLnet or PIRSLnet values did nevertheless exhibit large  $ED_e$  values (predominately as a result of high natural signals), however the aliquots were inconsistent. This sample corresponded to a peak in titanium (Ti) content, as measured by

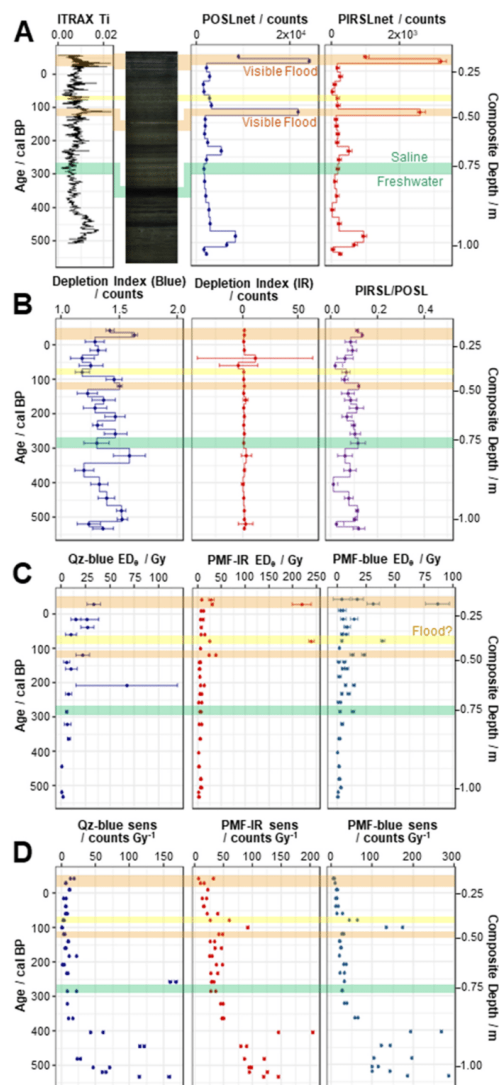


Fig. 1. Results of the POSL (Panels A and B) and lab profiling (Panels C and D) analysis for the 24 samples in Time Period 1. Panel A also shows contextual data (core photograph and ITRAX XRF Ti (Marshall et al., 2012)). Visible flood layers are highlighted in orange. An additional posited flood layer is highlighted in yellow. The transition from fresh to brackish lake water during 286 cal BP (AD 1664) is highlighted in green.

ITRAX X-ray fluorescence (XRF) analysis (Marshall et al., 2012; Fig. 1A). In Suigetsu, Ti can be interpreted as a proxy for detrital in wash, which suggests that this sample also contained flood material (despite there being no large visible flood layer) that resulted in elevated  $ED_e$  values. This disparity between lab profiling aliquots may be attributable to a relatively small volume of flood material within the sample, which was

not exposed during measurement in the POSL reader, and then unevenly partitioned between aliquots as grains were randomly loaded onto the discs for measurement, yielding different signal magnitudes during lab profiling.

A relatively high Ti content was also observed at the base of the profile, and whilst this did not correlate with elevated  $ED_e$  values, the samples taken from this period were associated with higher PMF sensitivities under both IR and blue light (Fig. 1D). This suggests that this older material had a distinct source-possibly the hillsides surrounding the lake as opposed to delivery via Lake Mikata (which acts to filter large detrital grains)- but that the delivery mechanism into the lake was more gradual than that of the flood material described above (encouraging bleaching prior to burial, and thus smaller  $ED_e$  values).

4.2. Time Period 2, the Laschamp Excursion

The POSLnet and PIRSLnet profiles across Time Period 2 showed two key transitions-one to a larger net signal at the Laschamp geomagnetic excursion itself (~42,000 cal BP) and a second to a smaller net signal at ~39,000 cal BP (Fig. 2A). Much like Time Period 1, there were no fluctuations in the depletion indices or the PIRSL/POSL ratio that corresponded to these transitions (Fig. 2B), suggesting that this trend was not driven by mineralogical variations or bleaching histories. Additionally, there was no clear relationship between these variables and the pollen-derived temperature reconstruction (Fig. 2A). This suggests that there was no obvious connection between temperature and core luminescence characteristics, despite the variability of the climate during this period.

The lab profiling-derived  $ED_e$  profiles (Fig. 2C) presented similar trends to the POSLnet and PIRSLnet with some subtle variations in the shape of the profile. In the  $ED_e$  profiles, the younger (~39,000 cal BP) shift was greater in magnitude than the older (~42,000 cal BP) shift, and in the QF-blue profile, only the younger shift was beyond the margin of error. Unlike the POSLnet and PIRSLnet, the PMF  $ED_e$  profiles were not smooth, with the excursion only consisting of two samples (at 39,500 cal BP and 40,500 cal BP).  $ED_R$  values calculated for this material suggest that it was associated with an elevated dose rate (~0.3–0.5 mGy/yr greater than the underlying material), but not sufficiently elevated to account for the ~100–200 Gy difference in the PMF  $ED_e$  values. Despite the sensitivities varying significantly between aliquots, the  $ED_e$  values were consistent within each aliquot pair. This suggests that these trends were not reflecting a signal from a very short event within each sample window, and instead a signal that is common to the bulk of each sample (as statistically, the likelihood of even loading of aliquots is lower for events which form a smaller proportion of the sample volume).

Whilst this positive excursion in  $ED_e$  values does not coincide directly with the magnetic field reversal during the Laschamp geomagnetic excursion, it aligns with a ~3000-year period of higher relative palaeointensity (normalised depositional remanent magnetism) (Fig. 2A, Hyodo et al., 2022). This apparent correlation is of note at the sampling resolution used in this study. Confirming this observation with higher resolution luminescence characterisation and supporting evidence for a mechanism linking these variables will be the focus of future work.

4.3. Time Period 3, the varve limit

A marked shift in a number of variables was observed across the varve limit (between 71,500 yr BP and 71,000 yr BP; Fig. 3), with samples taken from the varved sediment exhibiting larger POSLnet and PIRSLnet (Fig. 3A),  $ED_e$  values (Fig. 3C) and sensitivities (Fig. 3D) than the underlying non-varved sediment. The two samples taken from within the transitional clay produced intermediate signals between these end members. The transition from low to high  $ED_e$  was most dramatic in the PMF-IR and PMF-blue profiles despite the younger samples also showing higher sensitivities, however the QF-blue  $ED_e$

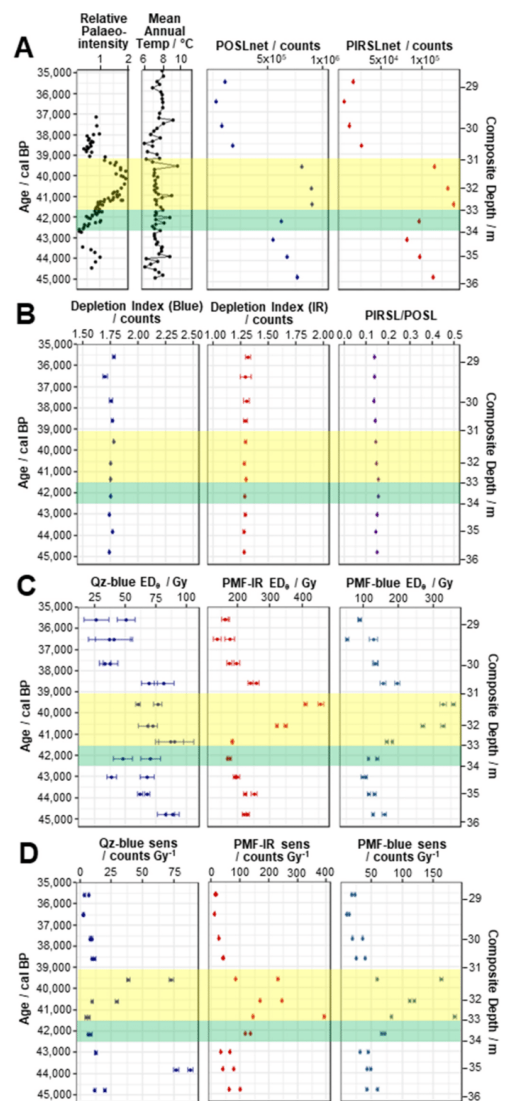
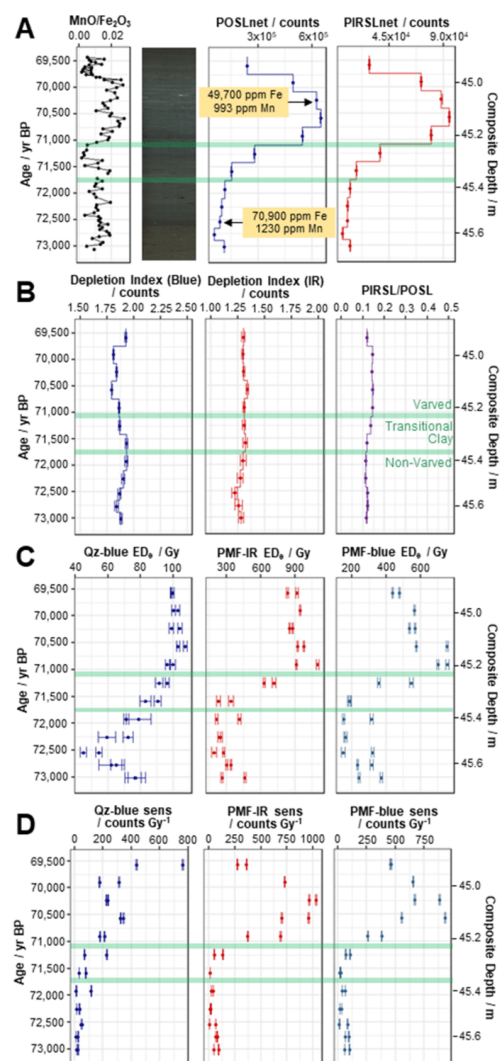


Fig. 2. Results of the POSL (Panels A and B) and lab profiling (Panels C and D) analysis for the 11 samples in Time Period 2. Panel A also shows contextual data (relative palaeointensity ( $J_{200C}/J_{200G}$ ; Hyodo et al., 2022) and pollen-reconstructed mean annual temperature from Suigetsu). Green horizontal bars highlight the Laschamp geomagnetic excursion. Yellow horizontal bars highlight the period of higher relative palaeointensity following the Laschamp.

profile also showed elevated values post-transition. The different luminescence characteristics observed in each sedimentological regime suggest a significant shift in catchment conditions during this period, however there were no distinct changes in the depletion indices or



**Fig. 3.** Results of the POSL (Panels A and B) and lab profiling (Panels C and D) analysis for the 12 samples in Time Period 3. Panel A also shows contextual data (core photograph, MnO/Fe<sub>2</sub>O<sub>3</sub>, measured on a Horiba XGT-2700 and Fe and Mn contents from ICP-OES measurements). Yellow boxes highlight the Mn and Fe contents from ICP-OES measurements. Green horizontal bars bracket the transitional clay layer, which separates varved from non-varved sediment.

PIRSL/POSL ratio, suggesting that changes in mineralogy and dose history did not contribute to the variations in POSLnet, PIRSLnet and ED<sub>e</sub> (Fig. 3B).

The conflicting presence of higher ED<sub>e</sub> values in the younger sediment may be associated with a change in dose rate resulting from abrupt changes to lake chemistry. It is thought that varve formation was initiated in Suigetsu due to an abrupt deepening of the lake (possibly due to movement of the adjacent Mikata fault) which induced bottom water

anoxia (Nakagawa et al., 2012), a process which is associated with incomplete mixing during lake overturning. This change in oxygenation (and therefore redox conditions) is corroborated by large differences in Fe and Mn concentrations above and below the onset of varving, as detected in the ICP-OES measurements, and an increase in the MnO/Fe<sub>2</sub>O<sub>3</sub> ratio (Fig. 3A). The varved sediments also contain elevated U, Th and K concentrations in relation to the underlying non-varved sediment (Supplementary Table 1), resulting in a factor of ~2 increase in the ED<sub>R</sub> which, when applied to the ED<sub>e</sub> values in Fig. 3, aligns the first-order age approximations of the varved and non-varved sediment, supporting the thesis that the observed variation in ED<sub>e</sub> is one driven by dose rate. It is possible that the change in redox conditions at this transition resulted in this enrichment of radiogenic elements, however, further assessment of decay series disequilibria and the time-dependency of chemical alterations (including U-enrichment) is required to better characterise this transition.

#### 4.4. Time Period 4, Termination II

The POSLnet and PIRSLnet profiles for Termination II were broadly similar in shape, and both measures showed an overall increase with depth (Fig. 4A). There were some small anomalies in the blue depletion index and the PIRSL/POSL ratio (Fig. 4B) corresponding to some of the more extreme net values, which suggests that such values could be driven by different bleaching histories or mineralogical variations (changing quartz contents). It was not possible to determine sensitivity and ED<sub>e</sub> values for all samples due to low mineral abundances and sensitivities. Where it was achievable, the values were shown to be highly variable between aliquots, between measurement techniques, and through time (Fig. 4C and D).

Termination II covers the broadest time range in this study and thus variability was anticipated, given the multiple high-amplitude environmental and sedimentological variations occurring during this transition from cold to warm temperatures. Suigetsu itself was non-static during this period, and sedimentological evidence suggests that it transitioned from fluvio-lacustrine in MIS 6 to lacustrine (and brackish) during MIS 5e, representing a dynamic environment both physically and geochemically. Another possible contributor to the lack of distinct trends is the implementation of spot sampling at low resolution over a large age range, which can result in additional noise (as samples capture extremes of environmental conditions without context from adjacent material). Despite it being difficult to isolate individual influences without relevant complementary data from sedimentological analysis, these observations suggest that the luminescence characteristics of this sediment are sensitive to a variety of competing environmental factors which could include lake depth, catchment drainage patterns, lake geochemistry, sediment source, flood events and climatic factors.

#### 4.5. Estimated dose rates

The ED<sub>R</sub> values showed down-core variations as a result of changing elemental concentrations, estimated water content and cosmic dose rate (Supplementary Table 1). The values were on the order of ~1–3 mGy/yr (Supplementary Table 2). When the ED<sub>R</sub> values are considered alongside the ED<sub>e</sub> values from the lab profiling, differences between chronometers are apparent; both the QF-blue and the PMF-blue ED<sub>e</sub> values yield first order approximate ages which are broadly consistent (within an order of magnitude) with the existing Suigetsu ages across Time Periods 2–4, with the former underestimating age for ED<sub>R</sub> values approaching the upper bound (~3 mGy/yr) and the latter typically overestimating age for the ED<sub>R</sub> values approaching the lower bound (~1 mGy/yr). The ED<sub>e</sub> values derived from the PMF-IR measurements consistently overestimate the existing Suigetsu ages, and the signals from all three fractions overestimate the true age of the sediment from Time Period 1. Constraining ages beyond these tentative observations would be erroneous, given the uncertainties in ED<sub>R</sub> calculation (namely assumptions

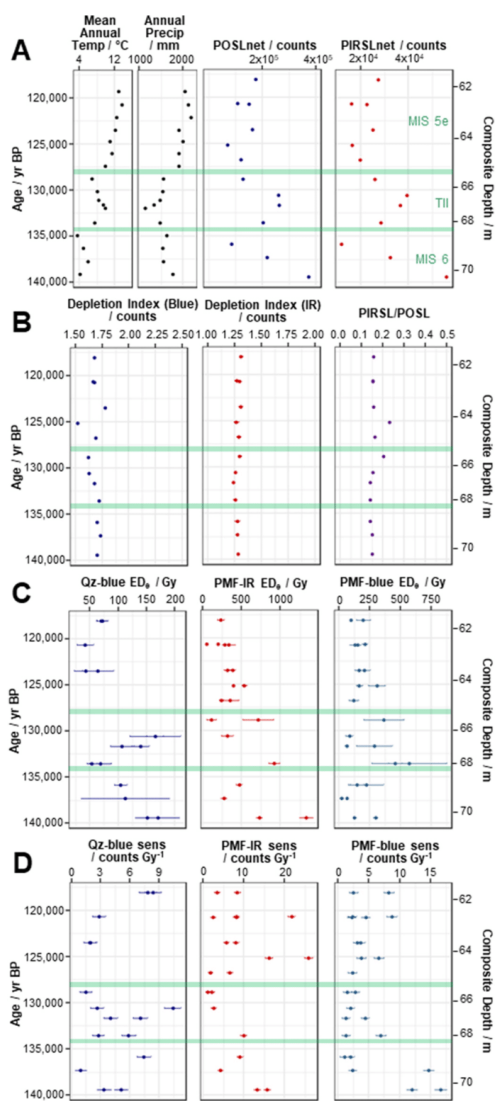


Fig. 4. Results of the POSL (Panels A and B) and lab profiling (Panels C and D) analysis for the 13 samples in Time Period 4. Panel A also shows contextual data (pollen-reconstructed mean annual temperature and pollen-reconstructed total annual precipitation from Suigetsu. Green horizontal bars indicate approximate boundaries between MIS 6, TII and MIS 5e, based on the pollen-reconstructed average annual temperature.

relating to the estimation of alpha efficiency, grain size and internal grain activity) and ED<sub>e</sub> calculation (given that the samples are not mineralogically pure and only two aliquots were measured per fraction). However, these estimations do suggest that the PMF-IR signal is better suited as an environmental tracer, and that the QF-blue and PMF-blue

signals show greater chronometric accuracy.

## 5. Discussion

### 5.1. Luminescence characteristics and environmental change

Throughout all four time periods it was possible to quantify a range of luminescence characteristics from the Suigetsu sediments. In most cases, the trends detected by the POSL and lab profiling approaches were very similar, and both techniques identified the same key environmental shifts in each of the four periods. The differences between the POSLnet and PIRSLnet profiles and the ED<sub>e</sub> profiles can be attributed to variations in sensitivity, and as such, it could be argued that by removing the sensitivity component, the lab profiling approach provided a more accurate representation of down-core luminescence characteristics and should be the principal methodology for future studies. Moreover, the lab profiling analysis was conducted on chemically treated fractions with better (albeit not perfect) mineralogical constraint, which, by virtue, provides more accurate ED<sub>e</sub> values. However, the POSL approach provided a more comprehensive suite of measurements (including depletion indices and PIRSL/POSL) which have the potential to capture a broader range of environmental shifts (albeit that they did not serve this function within the context of the present study). Additionally, the trends were clearer when a more intense, contiguous sampling approach (such as that used for Time Periods 1 and 3) was used, as this provided key contextual information and continuous data across transitions. The POSL approach is more suited to this type of sampling because it allows for rapid, non-destructive measurement of samples without a requirement for chemical preparation. Furthermore, the POSL analysis was conducted on larger samples (reducing geostatistical scatter). As a result, using both methods in a paired approach has advantages, as this offers both a more accurate determination of luminescence characteristics and a breadth of proxies for consideration. However, if large quantities of samples are necessary to clearly isolate trends, then the POSL approach is demonstrably sufficient for this purpose, especially in conjunction with complementary data. Calibrating the sensitivity of the POSL using an external radiation source could offer a means to ascertain sensitivity-corrected approximations of estimated equivalent dose whilst minimising processing time for large sample quantities (Munyikwa and Brown, 2014; Stone et al., 2015).

The principal signals seen in the key variables: POSLnet; PIRSLnet and ED<sub>e</sub> were interpreted as relating to the different predominant environmental factors in each of the four time periods, allowing us to well-characterise the effects (and non-effects) of a range of distinctive perturbations. Hence, any common drivers between the time periods were masked by high amplitude variations of a single driver in each case. Differences in sampling approaches also preclude common interpretation of the variables as a result of different intervals between samples (and hence probing the variables on different timescales), amounts of integrated time within each sample (providing different weightings to single event layers) and the proficiency of contiguous versus spot-sampling approaches to identify trends on different scales, as discussed above. Not all of the luminescence variables could be attributed to a specific environmental change, however this could be due to our incomplete understanding of past catchment changes. Further “ground-truthing” of these proxies is required in other lacustrine settings (building on the work of Písková et al. (2019)) to extend the applicability of this technique elsewhere. Nonetheless, it is highly promising that some of the selected variables were sensitive to known catchment changes, and that drivers could be hypothesised for other variables. This shows that by using POSL and lab profiling analysis, it was possible to gain further insight into environmental change at Suigetsu.

### 5.2. Assessment of dating potential

Future luminescence dating of the Suigetsu cores is feasible based on

the approximations of  $ED_2$  and  $ED_4$  shown above. All the samples from Time Periods 3 and 4 (which are older than the limit of radiocarbon dating, and hence targets for future dating) produced quantifiable natural signals. Responses were consistently measurable for large doses (50 Gy) but not small (5 Gy), suggesting that the grains are low in sensitivity, but not insufficiently sensitive so as to preclude future construction of dose response curves. A comparison of quartz and polymineral chronometric accuracy tentatively suggested that the QF-blue and PMF-blue signals were consistent with the existing Suigetsu chronology. Hence, blue light OSL dating of quartz is one possible future dating method (because the QF-blue fraction was highly dominated by quartz), however, the QF-blue fraction showed lower sensitivities and the quantity of quartz within the sediment was lower than other mineralogies. A key consideration for sampling will be how this (alongside the availability of core material) will direct sampling. Another possible method is blue light OSL dating of feldspar. The luminescence signal of feldspars dominates the PMF-blue signals (which showed good chronometric accuracy) from Suigetsu because of the low abundance and sensitivity of quartz within the PMF-blue fraction (which therefore contributes very small amounts of signal). The PMF-IR signals consistently overestimated the age of the material and hence will not be suitable for dating (however, these signals are valuable contributors of information regarding catchment environmental change).

Additional considerations for dating are a better appraisal of quartz saturation via the construction of dose response curves, and an assessment of the feldspar fraction for evidence of incomplete bleaching to avoid an over-estimate of age. Further to this, it will be important to refine any calculations of dose rate; particularly by quantifying decay series disequilibrium (through alpha spectrometry) and developing a model of water content variability in order to reduce age uncertainty. Additionally, in light of the other key finding of this study (that luminescence signals from this material are influenced by environmental change), it would be incorrect to interpret any calculations of age as if this were not the case. Careful sampling (e.g., by avoiding the sampling of flood layers) will be vital when looking to determine full OSL ages for the Suigetsu cores, as will making use of further luminescence profiling to characterise these effects around target horizons for dating. Despite these complexities, the evidence suggests that luminescence dating can contribute accurate, meaningful age information to the current Suigetsu age-depth model.

## 6. Conclusions

A combined approach of POSL analysis and lab profiling provided a complementary suite of variables which detected a range of environmental changes at Lake Suigetsu, Japan. Across the four time periods, the luminescence characteristics of the sediment showed a clear response to flood events (Time Period 1) and the initiation of varving (Time Period 3), and broad fluctuations which coincided with variations in magnetic palaeointensity (Time Period 2) and a complex response to environmental changes during Termination II (Time Period 4). There was no response of the luminescence proxies to the connection of Suigetsu to the Sea of Japan (Time Period 1). Local environmental perturbations which caused a sedimentological change across decadal to centennial timescales showed the clearest trends in the luminescence profiles when probed with contiguous, high-resolution sampling. The value of these techniques in a lacustrine setting was demonstrated across a ~140,000-year age range. POSL analysis and lab profiling provide a practical solution to the time- and core material-constraints of traditional luminescence analysis, whilst allowing the detection of catchment-sensitive signals. The core material produced quantifiable luminescence signals and hence future luminescence dating is feasible. First order approximate ages from the PMF-IR signals suggest that these produce an overestimation of age, and hence future dating will target the QF-blue signal (which equates to blue light OSL dating of quartz) and PMF-blue signal (which equates to blue light OSL dating of feldspar),

alongside a more accurate assessment of dose rate. The contribution of this work to our understanding of past dynamics at Lake Suigetsu demonstrates the applicability of rapid luminescence profiling of lake sediment cores for characterising past environmental change.

## Research Data

Accompanying data from the POSL analysis, laboratory profiling analysis and dose rate estimates can be found at <https://doi.org/10.5525/gla.researchdata.1263>.

## Declaration of competing interest

The authors declare that they have no known competing financial interests or personal relationships that could have appeared to influence the work reported in this paper.

## Acknowledgements

This research did not receive any specific grant from funding agencies in the public, commercial, or not-for-profit sectors. CLR received funding from the NERC IAPETUS2 Doctoral Training Partnership. The SG06 core was recovered under NERC grant NE/D000289/1 awarded to TN. The authors would like to thank Dr Valerie Olive for performing the ICP-MS and ICP-OES analysis.

## Appendix A. Supplementary information

Supplementary information relating to this article can be found online at <https://doi.org/10.1016/j.quageo.2022.101319>.

## References

- Albert, P.G., Smith, V.C., Suzuki, T., McLean, D., Tomlinson, E.L., Miyabuchi, Y., Kitaba, I., Mark, D.F., Moriwaki, H., , SG06 Project Members, Nakagawa, T., 2019. Geochemical characterisation of the Late Quaternary widespread Japanese tephrostratigraphic markers and correlations to the Lake Suigetsu sedimentary archive (SG06 core). *Quat. Geochronol.* 52, 103–131. <https://doi.org/10.1016/j.quageo.2019.01.005>.
- Armitage, S.J., Pinder, R.C., 2017. Testing the applicability of optically stimulated luminescence dating to Ocean Drilling Program cores. *Quat. Geochronol.* 39, 124–130. <https://doi.org/10.1016/j.quageo.2017.02.008>.
- Bateman, M.D., Catt, J.A., 1996. An absolute chronology for the raised beach and associated deposits at Sewerby, East Yorkshire, England. *J. Quat. Sci.* 11 (5), 389–395. [https://doi.org/10.1002/\(SICI\)1099-1417\(199609/10\)11:5<389:aid-jqs260>3.0.co;2-k](https://doi.org/10.1002/(SICI)1099-1417(199609/10)11:5<389:aid-jqs260>3.0.co;2-k).
- Bronk Ramsey, C., Heaton, T.J., Scholout, G., Staff, R.A., Bryant, C.L., Brauer, A., Lamb, H.F., Marshall, M.H., Nakagawa, T., 2020. Reanalysis of the atmospheric radiocarbon calibration record from Lake Suigetsu, Japan. *Radiocarbon* 62 (4), 989–999. <https://doi.org/10.1017/RDC.2020.18>.
- Bronk Ramsey, C., Staff, R.A., Bryant, C.L., Brock, F., Kitagawa, H., Van Der Plicht, J., Scholout, G., Marshall, M.H., Brauer, A., Lamb, H.F., Payne, R.L., Tarasov, P.E., Haraguchi, T., Gotanda, K., Yonenobu, H., Yokoyama, Y., Tada, R., Nakagawa, T., 2012. A complete terrestrial radiocarbon record for 11.2 to 52.8 kyr B.P. *Science* 338 (6105), 370–374. <https://doi.org/10.1126/science.1226660>.
- Burbridge, C.I., Sanderson, D.C.W., Housley, R.A., Allsworth Jones, P., 2007. Survey of Palaeolithic sites by luminescence profiling, a case study from Eastern Europe. *Quat. Geochronol.* 2 (1–4), 296–302. <https://doi.org/10.1016/j.quageo.2006.05.024>.
- Duan, W., Cheng, H., Tan, M., Li, X., Lawrence Edwards, R., 2019. Timing and structure of Termination II in north China constrained by a precisely dated stalagmite record. *Earth Planet. Sci. Lett.* 512, 1–7. <https://doi.org/10.1016/j.epsl.2019.01.043>.
- Gao, L., Gao, L., Yin, Y., Yu, G., Liao, M., 2017. Optical dating of Holocene tidal deposits from the southwestern coast of the South Yellow Sea using different grain-size quartz fractions. *J. Asian Earth Sci.* 135, 155–165. <https://doi.org/10.1016/j.jseas.2016.12.036>.
- Ghilardi, M., Sanderson, D., Kinnaird, T., Bicket, A., Balossino, S., Parisot, J.C., Hermitte, D., Guibal, F., Fleury, J.T., 2015. Dating the bridge at Avignon (south France) and reconstructing the Rhone River fluvial palaeo-landscape in Provence from medieval to modern times. *J. Archaeol. Sci. Report* 4, 336–354. <https://doi.org/10.1016/j.jasrep.2015.10.002>.
- Hu, G., Yi, C., Zhang, J., Cao, G., Pan, B., Liu, J., Jiang, T., Yi, S., Li, D., Huang, J., 2018. Chronology of a lacustrine core from Lake Lingco Co using a combination of OSL,  $^{14}C$  and  $^{210}Pb$  dating: implications for the dating of lacustrine sediments from the Tibetan Plateau. *Boreas* 47 (2), 656–670. <https://doi.org/10.1111/bor.12291>.
- Hyodo, M., Nakagawa, T., Matsushita, H., Kitaba, I., Yamada, K., Tanabe, S., Bradak, B., Miki, M., McLean, D., Staff, R.A., Smith, V.C., Albert, P.G., Bronk Ramsey, C.,

- Yamasaki, A., Kitagawa, J., Suigetsu 2014 Project Members, 2022. Intermittent non-axial dipolar-field dominance of twin Laschamp excursions. *Commun. Earth Environ.* <https://doi.org/10.1038/s43247-022-00401-0>.
- Kadereit, A., DeWitt, R., Johnson, T.C., 2012. Luminescence properties and optically (post-IR blue-light) stimulated luminescence dating of limnic sediments from northern Lake Malawi - chances and limitations. *Quat. Geochronol.* 10, 160–166. <https://doi.org/10.1016/j.quageo.2012.02.021>.
- Kinnaird, T.C., Sanderson, D.C.W., Bigelow, G.F., 2015. Feldspar SARA IRSL dating of very low dose rate aeolian sediments from Sandwick South, Unst, Shetland. *Quat. Geochronol.* 30, 168–174. <https://doi.org/10.1016/j.quageo.2015.02.019>.
- Li, J., Yang, S., Shu, J., Li, R., Chen, X., Meng, Y., Ye, S., He, L., 2020. Vegetation history and environment changes since MIS 5 recorded by pollen assemblages in sediments from the western Bohai Sea, Northern China. *J. Asian Earth Sci.* 187 (October 2019), 104085. <https://doi.org/10.1016/j.jseas.2019.104085>.
- Long, H., 2012. High-resolution OSL chronology of a sediment core from Lake Nam Co on the southern Tibetan Plateau: implication for lake evolution since the late Glacial. *Quat. Int.* 279–280, 287–288. <https://doi.org/10.1016/j.quaint.2012.08.762>, 2012.
- Marshall, M.H., Scholout, G., Nakagawa, T., Lamb, H.F., Brauer, A., Staff, R.A., Bronk Ramsey, C., Tarasov, P.E., Gotanda, K., Haraguchi, T., Yokoyama, Y., Yonenobu, H., Tada, R., 2012. A novel approach to varve counting using  $\mu$ XRF and X-radiography in combination with thin-section microscopy, applied to the Late Glacial chronology from Lake Suigetsu, Japan. *Quat. Geochronol.* 13, 70–80. <https://doi.org/10.1016/j.quageo.2012.06.002>.
- McLean, D., Albert, P.G., Nakagawa, T., Suzuki, T., Staff, R.A., Yamada, K., Kitaba, I., Haraguchi, T., Kitagawa, J., Smith, V.C., 2018. Integrating the Holocene tephrostratigraphy for East Asia using a high-resolution cryptophyta study from Lake Suigetsu (SG14 core), central Japan. *Quat. Sci. Rev.* 183, 36–58. <https://doi.org/10.1016/j.quascirev.2017.12.013>.
- Munyikwa, K., Brown, S., 2014. Rapid equivalent dose estimation for eolian dune sands using a portable OSL reader and polyminerally standardised luminescence growth curves: expedited sample screening for OSL dating. *Quat. Geochronol.* 22, 116–125. <https://doi.org/10.1016/j.quageo.2014.04.002>.
- Munyikwa, K., Kinnaird, T.C., Sanderson, D.C., 2021. The potential of portable luminescence readers in geomorphological investigations: a review. *Earth Surf. Process. Landforms* 46 (1), 131–150. <https://doi.org/10.1002/esp.4975>.
- Nakagawa, T., Gotanda, K., Haraguchi, T., Danbara, T., Yonenobu, H., Brauer, A., Yokoyama, Y., Tada, R., Takemura, K., Staff, R.A., Payne, R.L., Bronk Ramsey, C., Bryant, C.L., Brock, F., Scholout, G., Marshall, M.H., Tarasov, P.E., Lamb, H.F., 2012. SG06, a fully continuous and varved sediment core from Lake Suigetsu, Japan: stratigraphy and potential for improving the radiocarbon calibration model and understanding of late Quaternary climate changes. *Quat. Sci. Rev.* 36, 164–176. <https://doi.org/10.1016/j.quascirev.2010.12.013>.
- Nelson, M., Rittenour, T., Cornachione, H., 2019. Sampling methods for luminescence dating of subsurface deposits from cores. *Methods Protoc.* 2 (4), 88. <https://doi.org/10.3390/mps2040088>.
- Olive, V., Ellam, R.M., Wilson, L., 2001. A protocol for the determination of the rare earth elements at picomole level in rocks by ICP-MS: results on geological reference materials USGS PCC-1 and DTS-1. *Geostand. Newsl.* 25 (2-3), 219–228. <https://doi.org/10.1111/j.1751-908X.2001.tb00597.x>.
- Pears, B., Brown, A.G., Toms, P.S., Wood, J., Sanderson, D., Jones, R., 2020. A sub-centennial-scale optically stimulated luminescence chronostratigraphy and late Holocene flood history from a temperate river confluence. *Geology* 48 (8), 819–825. <https://doi.org/10.1130/G47079.1>.
- Písková, A., Roman, M., Bulínová, M., Pokorný, M., Sanderson, D., Cresswell, A., Lirio, J. M., Coria, S.H., Nedbalová, L., Lami, A., Musazzi, S., 2019. Late-Holocene palaeoenvironmental changes at Lake Esmeralda (Vega Island, Antarctic Peninsula) based on a multi-proxy analysis of laminated lake sediment. *Holocene* 29 (7), 1155–1175. <https://doi.org/10.1177/0959683619838033>.
- Porat, N., López, G.I., Lensky, N., Elinson, R., Avni, Y., Elgart-Sharon, Y., Faershtein, G., Gadot, Y., 2019. Using portable OSL reader to obtain a time scale for soil accumulation and erosion in archaeological terraces, the Judean Highlands, Israel. *Quat. Geochronol.* 49 (April 2018), 65–70. <https://doi.org/10.1016/j.quageo.2018.04.001>.
- Rasmussen, S.O., Bigler, M., Blockley, S.P., Blunier, T., Buchardt, S.L., Clausen, H.B., Cvijanovic, I., Dahl-Jensen, D., Johnsen, S.J., Fischer, H., Gkinis, V., Guillemin, M., Hoek, W.Z., Lowe, J., Pedro, J.B., Popp, T., Seierstad, I.K., Steffensen, J.-P., Svensson, A.M., Winstrup, M., 2014. A stratigraphic framework for abrupt climatic changes during the Last Glacial period based on three synchronized Greenland ice-core records: refining and extending the INTIMATE event stratigraphy. *Quat. Sci. Rev.* 106, 14–28. <https://doi.org/10.1016/j.quascirev.2014.09.007>.
- Saito-Kato, M., Yamada, K., Staff, R.A., Nakagawa, T., Yonenobu, H., Haraguchi, T., Takemura, K., Bronk Ramsey, C., 2013. An assessment of the magnitude of the AD 1586 Tensho tsunami inferred from Lake Suigetsu sediment cores. *J. Geogr.* 122, 493–501. <https://doi.org/10.5026/jgeography.122.493> (in Japanese, with English abstract).
- Sanderson, D.C., Kinnaird, T.C., 2019. Optically stimulated luminescence dating as a geochronological tool for late quaternary sediments in the red sea region. In: Rasul, N.M.A., Stewart, I.C.F. (Eds.), *Geological Setting, Palaeoenvironment and Archaeology of the Red Sea*. Springer, Cham, pp. 685–707. [https://doi.org/10.1007/978-3-319-99408-6\\_31](https://doi.org/10.1007/978-3-319-99408-6_31).
- Sanderson, D.C.W., Murphy, S., 2010. Using simple portable OSL measurements and laboratory characterisation to help understand complex and heterogeneous sediment sequences for luminescence dating. *Quat. Geochronol.* 5 (2–3), 299–305. <https://doi.org/10.1016/j.quageo.2009.02.001>.
- Scholout, G., Staff, R.A., Brauer, A., Lamb, H.F., Marshall, M.H., Bronk Ramsey, C., Nakagawa, T., 2018. An extended and revised Lake Suigetsu varve chronology from ~50 to ~10 ka BP based on detailed sediment micro-facies analyses. *Quat. Sci. Rev.* 200, 351–366. <https://doi.org/10.1016/j.quascirev.2018.09.021>.
- Staff, R.A., Ramsey, C.B., Bryant, C.L., Brock, F., Payne, R.L., Scholout, G., Marshall, M. H., Brauer, A., Lamb, H.F., Tarasov, P.E., Yokoyama, Y., Haraguchi, T., Gotanda, K., Yonenobu, H., Nakagawa, T., 2011. New 14C determinations from Lake Suigetsu, Japan: 12,000 to 0 cal BP. *Radiocarbon* 53 (3), 511–528. <https://doi.org/10.1017/S003822200034627>.
- Stone, A.E.C., Bateman, M.D., Thomas, D.S.G., 2015. Rapid age assessment in the Namib Sand Sea using a portable luminescence reader. *Quat. Geochronol.* 30, 134–140. <https://doi.org/10.1016/j.quageo.2015.02.002>.
- Zhao, G., Ye, S., Laws, E.A., He, L., Yuan, H., Ding, X., Wang, J., 2019. Carbon burial records during the last ~40,000 years in sediments of the Liaohhe Delta wetland, China. *Estuarine. Coast. Shelf Sci.* 226 (July 2018), 106291. <https://doi.org/10.1016/j.eccs.2019.106291>.

## References

Adolphi, F. and Muscheler, R. (2016) 'Synchronizing the Greenland ice core and radiocarbon timescales over the Holocene – Bayesian wiggle–matching of cosmogenic radionuclide records', *Climate of the Past*, 12, pp. 15–30. Available at: <https://doi.org/10.5194/cp-12-15-2016>.

Adolphi, F., Ramsey, C.B., Erhardt, T., Edwards, R.L., Cheng, H., Turney, C.S.M., Cooper, A., Svensson, A., Rasmussen, S.O., Fischer, H. and Muscheler, R. (2018) 'Connecting the Greenland ice–core and U / Th timescales via cosmogenic radionuclides: testing the synchronicity of Dansgaard–Oeschger events', *Climate of the Past*, 14, pp. 1755–1781. Available at: <https://doi.org/10.5194/cp-14-1755-2018>.

Aichner, B., Feakins, S.J., Lee, J.E., Herzschuh, U. and Liu, X. (2015) 'High–resolution leaf wax carbon and hydrogen isotopic record of the late Holocene paleoclimate in arid Central Asia', *Climate of the Past*, 11, pp. 619–633. Available at: <https://doi.org/10.5194/cp-11-619-2015>.

Aichner, B., Ott, F., Slowinski, M., Norýskiewicz, A.M., Brauer, A. and Sachse, D. (2018) 'Leaf wax n–alkane distributions record ecological changes during the Younger Dryas at Trzechowskie paleolake (northern Poland) without temporal delay', *Climate of the Past*, 14, pp. 1607–1624. Available at: <https://doi.org/10.5194/cp-14-1607-2018>.

Albert, P. G., Smith, V. C., Suzuki, T., McLean, D., Tomlinson, E. L., Miyabuchi, Y., Kitaba, I., Mark, D. F., Moriwaki, H., SG06 Project Members and Nakagawa, T. (2019) 'Geochemical characterisation of the Late Quaternary widespread Japanese tephrostratigraphic markers and correlations to the Lake Suigetsu sedimentary archive (SG06 core)', *Quaternary Geochronology*, 52, pp. 103–131. Available at: <https://doi.org/10.1016/j.quageo.2019.01.005>.

Albert, P.G., Smith, V.C., Suzuki, T., Tomlinson, E.L., Nakagawa, T., McLean, D., Yamada, M., Staff, R.A., Schlolaut, G., Takemura, K., Nagahashi, Y., Kimura, J. and SG06 Project Members (2018) 'Constraints on the frequency and dispersal of explosive eruptions at Sambe and Daisen volcanoes (South–West Japan Arc)

from the distal Lake Suigetsu record (SG06 core)', *Earth–Science Reviews*, 185, pp. 1004–1028. Available at: <https://doi.org/10.1016/j.earscirev.2018.07.003>.

Amekawa, S., Kashiwagi, K., Hori, M., Sone, T., Kato, H., Okumura, T., Yu, T.L., Shen, C.C. and Kano, A. (2021) 'Stalagmite evidence for East Asian winter monsoon variability and  $^{18}\text{O}$ -depleted surface water in the Japan Sea during the last glacial period', *Progress in Earth and Planetary Science*, 8, article 18. Available at: <https://doi.org/10.1186/s40645-021-00409-8>.

Araguás–Araguás, L., Froehlich, K. and Rozanski, K. (1998) 'Stable isotope composition of precipitation over southeast Asia', *Journal of Geophysical Research Atmospheres*, 103(D22), pp. 28721–28742. Available at: <https://doi.org/10.1029/98JD02582>.

Armitage, S. J. and Pinder, R. C. (2017) 'Testing the applicability of optically stimulated luminescence dating to Ocean Drilling Program cores', *Quaternary Geochronology*, 39, pp. 124–130. Available at: <https://doi.org/10.1016/j.quageo.2017.02.008>.

Barker, S. and Knorr, G. (2021) 'Millennial scale feedbacks determine the shape and rapidity of glacial termination', *Nature Communications*, 12, article 2273. Available at: <https://doi.org/10.1038/s41467-021-22388-6>.

Barker, S., Knorr, G., Edwards, R.L., Parrenin, F., Putnam, A.E., Skinner, L.C., Wolff, E. and Ziegler, M. (2011) '800,000 Years of abrupt climate variability', *Science*, 334, pp. 347–351. Available at: <https://doi.org/10.1126/science.1203580>.

Bateman, M. D. and Catt, J. A. (1996) 'An absolute chronology for the raised beach and associated deposits at Sewerby, East Yorkshire, England', *Journal of Quaternary Science*, 11(5), pp. 389–395. Available at: [https://doi.org/10.1002/\(SICI\)1099-1417\(199609/10\)11:5<389::AID-JQS260>3.0.CO;2-K](https://doi.org/10.1002/(SICI)1099-1417(199609/10)11:5<389::AID-JQS260>3.0.CO;2-K)

Bateman, M.D., McHale, K., Bayntun, H.J. and Williams, N. (2020) 'Understanding historical coastal spit evolution: A case study from Spurn, East

Yorkshire, UK', *Earth Surface Processes and Landforms*, 45, pp. 3670–3686.

Available at: <https://doi.org/10.1002/esp.4991>.

Bateman, M.D., Stein, S., Ashurst, R.A. and Selby, K. (2015) 'Instant luminescence chronologies? High resolution luminescence profiles using a portable luminescence reader', *Quaternary Geochronology*, 30, pp. 141–146.

Available at: <https://doi.org/10.1016/j.quageo.2014.12.007>.

Bell, W.T. (1980) 'Alpha dose attenuation in quartz grains for thermoluminescence dating', *Ancient TL*, 12(8), pp. 4–8.

Benson, L. V. and White, J.W.C. (1994) 'Stable isotopes of oxygen and hydrogen in the Truckee River-Pyramid Lake surface-water system. 3. Source of water vapor overlying Pyramid Lake', *Limnology and Oceanography*, 39(8), pp. 1945–1958.

Available at: <https://doi.org/10.4319/lo.1994.39.8.1945>.

Berkelhammer, M., Sinha, A., Mudelsee, M., Cheng, H., Edwards, R.L. and Cannariato, K. (2010) 'Persistent multidecadal power of the Indian Summer Monsoon', *Earth and Planetary Science Letters*, 290(1–2), pp. 166–172. Available at: <https://doi.org/10.1016/j.epsl.2009.12.017>.

Bershaw, J. (2018) 'Controls on deuterium excess across Asia', *Geosciences*, 8(7). Available at: <https://doi.org/10.3390/geosciences8070257>.

Bowen, G.J., Cai, Z., Fiorella, R.P. and Putman, A.L. (2019) 'Isotopes in the water cycle: Regional- to global-scale patterns and applications', *Annual Review of Earth and Planetary Sciences*, 47, pp. 453–479. Available at:

<https://doi.org/10.1146/annurev-earth-053018-060220>.

Brand, W.A., Coplen, T.B., Vogl, J., Rosner, M. and Prohaska, T. (2014) *Assessment of international reference materials for isotope-ratio analysis (IUPAC technical report)*, *Pure and Applied Chemistry*. Available at:

<https://doi.org/10.1515/pac-2013-1023>.

Brewer, T.S., LENG, M.J., Mackay, A.W., Lamb, A.L., Tyler, J.J. and Marsh, N.G. (2008) 'Unravelling contamination signals in biogenic silica oxygen isotope

composition: the role of major and trace element geochemistry', *Journal of Quaternary Science*, 23(4), pp. 311–320. Available at: <https://doi.org/10.1002/jqs>.

Broecker, W.S. and Henderson, G.M. (1998) 'The sequence of events surrounding Termination II and their implications for the cause of glacial–interglacial CO<sub>2</sub> changes', *Paleoceanography*, 13(4), pp. 352–364. Available at: <https://doi.org/10.1029/98PA00920>.

Bronk Ramsey, C. (2009) 'Bayesian Analysis of Radiocarbon Dates', *Radiocarbon*, 51(1), pp. 337–360. Available at: <https://doi.org/10.1017/S0033822200033865>.

Bronk Ramsey, C. and Lee, S. (2013) 'Recent and Planned Developments of the Program OxCal', *Radiocarbon*, 55(2), pp. 720–730. Available at: <https://doi.org/10.1017/s0033822200057878>.

Bronk Ramsey, C., Heaton, T. J., Scholaut, G., Staff, R. A., Bryant, C. L., Brauer, A., Lamb, H. F., Marshall, M. H. and Nakagawa, T. (2020) 'Reanalysis of the Atmospheric Radiocarbon Calibration Record from Lake Suigetsu, Japan', *Radiocarbon*, 62(4), pp. 989–999. Available at: <https://doi.org/10.1017/RDC.2020.18>.

Bronk Ramsey, C., Staff, R. A., Bryant, C. L., Brock, F., Kitagawa, H., Van Der Plicht, J., Scholaut, G., Marshall, M. H., Brauer, A., Lamb, H. F., Payne, R. L., Tarasov, P. E., Haraguchi, T., Gotanda, K., Yonenobu, H., Yokoyama, Y., Tada, R. and Nakagawa, T. (2012) 'A complete terrestrial radiocarbon record for 11.2 to 52.8 kyr B.P.', *Science*, 338(6105), pp. 370–374. Available at: <https://doi.org/10.1126/science.1226660>.

Burbidge, C. I., Sanderson, D. C. W., Housley, R. A. and Allsworth Jones, P. (2007) 'Survey of Palaeolithic sites by luminescence profiling, a case study from Eastern Europe', *Quaternary Geochronology*, 2(1–4), pp. 296–302. Available at: <https://doi.org/10.1016/j.quageo.2006.05.024>

Cai, Y., Fung, I.Y., Edwards, R.L., An, Z., Cheng, H., Lee, J.E., Tan, L., Shen, C.C., Wang, X., Day, J.A., Zhou, W., Kelly, M.J. and Chiang, J.C.H. (2015)

'Variability of stalagmite-inferred Indian monsoon precipitation over the past 252,000 y', *Proceedings of the National Academy of Sciences of the United States of America*, 112(10), pp. 2954–2959. Available at:

<https://doi.org/10.1073/pnas.1424035112>.

Cai, Z. and Tian, L. (2016) 'Atmospheric controls on seasonal and interannual variations in the precipitation isotope in the East Asian Monsoon region', *Journal of Climate*, 29(4), pp. 1339–1352. Available at:

<https://doi.org/10.1175/JCLI-D-15-0363.1>.

Caley, T., Malaizé, B., Kageyama, M., Landais, A. and Masson-Delmotte, V. (2013) 'Bi-hemispheric forcing for Indo-Asian monsoon during glacial terminations', *Quaternary Science Reviews*, 59, pp. 1–4. Available at:

<https://doi.org/10.1016/j.quascirev.2012.10.008>.

Cartier, R., Sylvestre, F., Paillès, C., Sonzogni, C., Couapel, M., Alexandre, A., Mazur, J.C., Brisset, E., Miramont, C. and Guiter, F. (2019) 'Diatom-oxygen isotope record from high-altitude Lake Petit (2200 m a.s.l.) in the Mediterranean Alps: Shedding light on a climatic pulse at 4.2 ka', *Climate of the Past*, 15, pp. 253–263. Available at: <https://doi.org/10.5194/cp-15-253-2019>.

Castañeda, I.S. and Schouten, S. (2011) 'A review of molecular organic proxies for examining modern and ancient lacustrine environments', *Quaternary Science Reviews*, 30(21–22), pp. 2851–2891. Available at:

<https://doi.org/10.1016/j.quascirev.2011.07.009>.

Chacko, T., Cole, D.R. and Horita, J. (2001) 'Equilibrium oxygen, hydrogen and carbon isotope fractionation factors applicable to geologic systems', *Reviews in Mineralogy and Geochemistry*, 43(1), pp. 1–81. Available at:

<https://doi.org/10.1515/9781501508745-004>.

Chapligin, B., Leng, M.J., Webb, E., Alexandre, A., Dodd, J.P., Ijiri, A., Lücke, A., Shemesh, A., Abelmann, A., Herzsuh, U., Longstaffe, F.J., Meyer, H., Moschen, R., Okazaki, Y., Rees, N.H., Sharp, Z.D., Sloane, H.J., Sonzogni, C., Swann, G.E.A., Sylvestre, F., Tyler, J.J. and Yam, R. (2011) 'Inter-laboratory comparison of oxygen isotope compositions from biogenic silica', *Geochimica et*

*Cosmochimica Acta*, 75, pp. 7242–7256. Available at:

<https://doi.org/10.1016/j.gca.2011.08.011>.

Chen, W., Wang, L., Feng, J., Wen, Z., Ma, T., Yang, X. and Wang, C. (2019) ‘Recent Progress in Studies of the Variabilities and Mechanisms of the East Asian Monsoon in a Changing Climate’, *Advances in Atmospheric Sciences*, 36, pp. 887–901. Available at: <https://doi.org/10.1007/s00376-019-8230-y>.

Cheng, H., Edwards, R.L., Sinha, A., Spötl, C., Yi, L., Chen, S., Kelly, M., Kathayat, G., Wang, X., Li, X., Kong, X., Wang, Y., Ning, Y. and Zhang, H. (2016) ‘The Asian monsoon over the past 640,000 years and ice age terminations’, *Nature*, 534, pp. 640–646. Available at: <https://doi.org/10.1038/nature18591>.

Cheng, H., Edwards, R.L., Wang, Y., Kong, X., Ming, Y., Kelly, M.J., Wang, X., Gallup, C.D. and Liu, W. (2006) ‘A penultimate glacial monsoon record from Hulu Cave and two-phase glacial terminations’, *Geology*, 34(3), pp. 217–220. Available at: <https://doi.org/10.1130/G22289.1>.

Cheng, H., Zhang, H., Zhao, J., Li, H., Ning, Y. and Kathayat, G. (2019) ‘Chinese stalagmite paleoclimate researches: A review and perspective’, *Science China Earth Sciences*, 62(10), pp. 1489–1513. Available at: <https://doi.org/10.1007/s11430-019-9478-3>.

Chiang, J.C.H., Fung, I.Y., Wu, C.H., Cai, Y., Edman, J.P., Liu, Y., Day, J.A., Bhattacharya, T., Mondal, Y. and Labrousse, C.A. (2015) ‘Role of seasonal transitions and westerly jets in East Asian paleoclimate’, *Quaternary Science Reviews*, 108, pp. 111–129. Available at: <https://doi.org/10.1016/j.quascirev.2014.11.009>.

Chivall, D., Berstan, R., Bull, I.D. and Evershed, R.P. (2012) ‘Isotope effects associated with the preparation and methylation of fatty acids by boron trifluoride in methanol for compound-specific stable hydrogen isotope analysis via gas chromatography/thermal conversion/isotope ratio mass spectrometry’, *Rapid Communications in Mass Spectrometry*, 26, pp. 1232–1240. Available at: <https://doi.org/10.1002/rcm.6188>.

- Chowdary, J.S., Hu, K., Srinivas, G., Kosaka, Y., Wang, L. and Rao, K.K. (2019) 'The Eurasian Jet Streams as Conduits for East Asian Monsoon Variability', *Current Climate Change Reports*, 5, pp. 233–244. Available at: <https://doi.org/10.1007/s40641-019-00134-x>.
- Clayton, R.N. and Mayeda, T.K. (1963) 'The use of bromine pentafluoride in the extraction of oxygen from oxides and silicates for isotopic analysis', *Geochimica et Cosmochimica Acta*, 27(1), pp. 43–52. Available at: [https://doi.org/10.1016/0016-7037\(63\)90071-1](https://doi.org/10.1016/0016-7037(63)90071-1).
- Clemens, S.C., Holbourn, A., Kubota, Y., Lee, K.E., Liu, Z., Chen, G., Nelson, A. and Fox-Kemper, B. (2018) 'Precession-band variance missing from East Asian monsoon runoff', *Nature Communications*, 9(1), article 3364. Available at: <https://doi.org/10.1038/s41467-018-05814-0>.
- Cong, L., Wang, Y., Zhang, X., Chen, T., Gao, D. and An, F. (2021) 'Radiocarbon and Luminescence Dating of Lacustrine Sediments in Zhari Namco, Southern Tibetan Plateau', *Frontiers in Earth Science*, 9, pp. 1–13. Available at: <https://doi.org/10.3389/feart.2021.640172>.
- Coplen, T.B., Kendall, C. and Hopple, J. (1983) 'Comparison of stable isotope reference samples', *Nature*, 302, pp. 236–238. Available at: <https://doi.org/10.1038/302236a0>.
- Craig, H. (1961) 'Isotopic variations in meteoric waters', *Science*, 133, pp. 1702–1703. Available at: <https://doi.org/10.1126/science.133.3465.1702>.
- Dansgaard, W. (1964) 'Stable isotopes in precipitation', *Tellus A: Dynamic Meteorology and Oceanography*, 16(4), pp. 436–468. Available at: <https://doi.org/10.3402/tellusa.v16i4.8993>.
- Darling, W.G. (2004) 'Hydrological factors in the interpretation of stable isotopic proxy data present and past: A European perspective', *Quaternary Science Reviews*, 23, pp. 743–770. Available at: <https://doi.org/10.1016/j.quascirev.2003.06.016>.

- Dean, J.R., Jones, M.D., Leng, M.J., Metcalfe, S.E., Sloane, H.J., Eastwood, W.J. and Roberts, C.N. (2018) 'Seasonality of Holocene hydroclimate in the Eastern Mediterranean reconstructed using the oxygen isotope composition of carbonates and diatoms from Lake Nar, central Turkey', *Holocene*, 28(2), pp. 267–276. Available at: <https://doi.org/10.1177/0959683617721326>.
- Delaygue, G. (2009) 'Oxygen Isotopes', in V. Gornitz (ed.) *Encyclopedia of Paleoclimatology and Ancient Environments*. Encyclopedia of Earth Sciences Series. Dordrecht: Springer. Available at: [https://doi.org/10.1007/978-1-4020-4411-3\\_163](https://doi.org/10.1007/978-1-4020-4411-3_163).
- Denton, G.H., Anderson, R.F., Toggweiler, J.R., Edwards, R.L., Schaefer, J.M. and Putnam, A.E. (2010) 'The last glacial termination', *Science*, 328(5986), pp. 1652–1656. Available at: <https://doi.org/10.1126/science.1184119>.
- Dominguez, F., Cuxart, J. and Van Oevelen, P. (2020) 'The Intersection between Global Monsoons and Regional Hydroclimate Projects', *GEWEX Quarterly*, 30(4).
- Duan, W., Cheng, H., Tan, M., Li, X. and Lawrence Edwards, R. (2019) 'Timing and structure of Termination II in north China constrained by a precisely dated stalagmite record', *Earth and Planetary Science Letters*, 512, pp. 1–7. Available at: <https://doi.org/10.1016/j.epsl.2019.01.043>.
- Duan, W., Wang, Xu, Tan, M., Cui, L., Wang, Xuefeng and Xiao, Z. (2022) 'Variable Phase Relationship Between Monsoon and Temperature in East Asia During Termination II Revealed by Oxygen and Clumped Isotopes of a Northern Chinese Stalagmite', *Geophysical Research Letters*, 49, article e2022GL098296. Available at: <https://doi.org/10.1029/2022GL098296>.
- Duller, G.A.T. (2008) 'Single-grain optical dating of Quaternary sediments: Why aliquot size matters in luminescence dating', *Boreas*, 37, pp. 589–612. Available at: <https://doi.org/10.1111/j.1502-3885.2008.00051.x>.
- EPICA Community Members (2006) 'One-to-one coupling of glacial climate variability in Greenland and Antarctica', *Nature*, 444, pp. 195–198. Available at: <https://doi.org/10.1038/nature05301>.

Esri (2022a). “World Dark Grey Base” [basemap] 1:10,000,000 (panel A), 1:400,000 (panel B), 1:67,946 (panel C).

<https://www.arcgis.com/home/item.html?id=a284a9b99b3446a3910d4144a50990f6> (accessed 12/09/2022).

Esri (2022b). “World Hillshade” [basemap] 1:10,000,000 (panel A), 1:400,000 (panel B), 1:67,946 (panel C).

<https://www.arcgis.com/home/item.html?id=1b243539f4514b6ba35e7d995890db1d> (accessed 12/09/2022).

Esri (2022c). “World Dark Gray Base” [basemap]. 1:60,000 (main), 1:40,000,000 (insert).

[https://services.arcgisonline.com/arcgis/rest/services/Canvas/World\\_Dark\\_Gray\\_Base/MapServer](https://services.arcgisonline.com/arcgis/rest/services/Canvas/World_Dark_Gray_Base/MapServer) (accessed 26/10/2021).

Esri (2022d). “World Hillshade” [basemap]. 1:60,000 (main), 1:40,000,000 (insert).

<https://doc.arcgis.com/en/data-appliance/7.2/maps/world-hillshade.htm> (accessed 26/10/2021).

Esri (2023a). “World Imagery” [basemap]. 1:81,435,618.

<https://www.arcgis.com/home/item.html?id=10df2279f9684e4a9f6a7f08febac2a9> (accessed 27/02/2023).

Esri (2023b). “World Imagery” [basemap]. 1:45,567,224.

<https://www.arcgis.com/home/item.html?id=10df2279f9684e4a9f6a7f08febac2a9> (accessed 27/02/2023).

Esri (2023c). “World Imagery” [basemap]. 1:7,851,046.

<https://www.arcgis.com/home/item.html?id=10df2279f9684e4a9f6a7f08febac2a9> (accessed 27/02/2023).

Esri (2023d). “World Imagery” [basemap]. 1:439,079.

<https://www.arcgis.com/home/item.html?id=10df2279f9684e4a9f6a7f08febac2a9> (accessed 27/02/2023).

- Esri (2023e). “World Imagery (WGS84)” [basemap]. 1:37,314,123 (panel a), 1:7,851,046 (panel b), 1:530,430 (panel c).  
<https://www.arcgis.com/home/item.html?id=898f58f2ee824b3c97bae0698563a4b3> (accessed 12/01/2023).
- Esri (2023f). “Light Grey Canvas” [basemap] 1:66,623,747 (upper panel), 1:43,517 (lower panel).  
<https://www.arcgis.com/home/item.html?id=979c6cc89af9449cbeb5342a439c6a76> (accessed 20/03/2023).
- Esri (2023g). “World Hillshade” [basemap] 1:66,623,747 (upper panel), 1:43,517 (lower panel).  
<https://www.arcgis.com/home/item.html?id=1b243539f4514b6ba35e7d995890db1d> (accessed 20/03/2023).
- Fu, W., Shu, Y., Yi, Z., Su, Y., Pan, Y., Zhang, F. and Brynjolfsson, S. (2022) ‘Diatom morphology and adaptation: Current progress and potentials for sustainable development’, *Sustainable Horizons*, 2, article 100015. Available at: <https://doi.org/10.1016/j.horiz.2022.100015>.
- Fuchs, M. and Owen, L.A. (2008) ‘Luminescence dating of glacial and associated sediments: review, recommendations and future directions’, *Boreas*, 37, pp. 636–659. Available at: <https://doi.org/10.1111/j.1502-3885.2008.00052.x>.
- Fuchs, M., Kreutzer, S., Fischer, M., Sauer, D. and Sørensen, R. (2012) ‘OSL and IRSL dating of raised beach sand deposits along the southeastern coast of Norway’, *Quaternary Geochronology*, 10, pp. 195–200. Available at: <https://doi.org/10.1016/j.quageo.2011.11.009>.
- Fudeyasu, H., Ichiyanagi, K., Sugimoto, A., Yoshimura, K., Ueta, A., Yamanaka, M.D. and Ozawa, K. (2008) ‘Isotope ratios of precipitation and water vapor observed in Typhoon Shanshan’, *Journal of Geophysical Research Atmospheres*, 113, article D112113. Available at: <https://doi.org/10.1029/2007JD009313>.
- Gallagher, S.J., Kitamura, A., Iryu, Y., Itaki, T., Koizumi, I. and Hoiles, P.W. (2015) ‘The Pliocene to recent history of the Kuroshio and Tsushima Currents: a

multi-proxy approach', *Progress in Earth and Planetary Science*, 2, article 17. Available at: <https://doi.org/10.1186/s40645-015-0045-6>.

Gallagher, S.J., Sagawa, T., Henderson, A.C.G., Saavedra-Pellitero, M., De Vleeschouwer, D., Black, H., Itaki, T., Toucanne, S., Bassetti, M.A., Clemens, S., Anderson, W., Alvarez-Zarikian, C. and Tada, R. (2018) 'East Asian Monsoon History and Paleoceanography of the Japan Sea Over the Last 460,000 Years', *Paleoceanography and Paleoclimatology*, 33(7), pp. 683–702. Available at: <https://doi.org/10.1029/2018PA003331>.

Gao, L., Gao, L., Yin, Y., Yu, G., and Liao, M. (2017) 'Optical dating of Holocene tidal deposits from the southwestern coast of the South Yellow Sea using different grain-size quartz fractions', *Journal of Asian Earth Sciences*, 135, pp. 155–165. Available at: <https://doi.org/10.1016/j.jseaes.2016.12.036>.

García-Alix, A., Camuera, J., Ramos-Román, M.J., Toney, J.L., Sachse, D., Schefuß, E., Jiménez-Moreno, G., Jiménez-Espejo, F.J., López-Avilés, A., Anderson, R.S. and Yanes, Y. (2021) 'Paleohydrological dynamics in the Western Mediterranean during the last glacial cycle', *Global and Planetary Change*, 202, article 103527. Available at: <https://doi.org/10.1016/j.gloplacha.2021.103527>.

Geen, R., Bordoni, S., Battisti, D.S. and Hui, K. (2020) 'Monsoons, ITCZs, and the Concept of the Global Monsoon', *Reviews of Geophysics*, 58(4), article e2020RG000700. Available at: <https://doi.org/10.1029/2020RG000700>.

Ghilardi, M., Sanderson, D., Kinnaird, T., Bicket, A., Balossino, S., Parisot, J.C., Hermitte, D., Guibal, F. and Fleury, J.T. (2015) 'Dating the bridge at Avignon (south France) and reconstructing the Rhone River fluvial palaeo-landscape in Provence from medieval to modern times', *Journal of Archaeological Science: Reports*, 4, pp. 336–354. Available at: <http://dx.doi.org/10.1016/j.jasrep.2015.10.002>.

Gibson, J.J., Birks, S.J. and Yi, Y. (2016) 'Stable isotope mass balance of lakes: A contemporary perspective', *Quaternary Science Reviews*, 131, pp. 316–328. Available at: <https://doi.org/10.1016/j.quascirev.2015.04.013>.

Gonfiantini, R. (1986) 'Environmental isotopes in lake studies', in Fritz, P. and Fontes, J.C. (eds), *Handbook of environmental isotope geochemistry volume two, the terrestrial environment*, B. Elsevier, Netherlands, pp. 113–168.

Available at: <https://doi.org/10.1016/B978-0-444-42225-5.50008-5>.

Gorbarenko, S.A., Malakhova, G.Y., Artemova, A. V., Bosin, A.A., Yanchenko, E.A. and Vasilenko, Y.P. (2019) 'Millennial scale cycles in the Bering Sea during penultimate and last glacials; their similarities and differences', *Quaternary International*, 525, pp. 151–158. Available at:

<https://doi.org/10.1016/j.quaint.2019.07.016>.

Grant, K.M., Rohling, E.J., Bronk Ramsey, C., Cheng, H., Edwards, R.L., Florindo, F., Heslop, D., Marra, F., Roberts, A.P., Tamisiea, M.E. and Williams, F. (2014) 'Sea-level variability over five glacial cycles', *Nature Communications*, 5, article 5076. Available at: <https://doi.org/10.1038/ncomms6076>.

Gröning, M., Dargie, M., Winckler, G. (2007) *Reference sheet for reference materials: NBS28 & NBS30*, IAEA, Vienna. Available at:

[https://nucleus.iaea.org/sites/ReferenceMaterials/Shared%20Documents/ReferenceMaterials/StableIsotopes/NBS-28/NBS28\\_NBS30.pdf](https://nucleus.iaea.org/sites/ReferenceMaterials/Shared%20Documents/ReferenceMaterials/StableIsotopes/NBS-28/NBS28_NBS30.pdf)

Han, L.Y., Li, T.Y., Cheng, H., Edwards, R.L., Shen, C.C., Li, H.C., Huang, C.X., Li, J.Y., Yuan, N., Wang, H.B., Zhang, T.T. and Zhao, X. (2016) 'Potential influence of temperature changes in the Southern Hemisphere on the evolution of the Asian summer monsoon during the last glacial period', *Quaternary International*, 392, pp. 239–250. Available at:

<https://doi.org/10.1016/j.quaint.2015.05.068>.

Hasegawa, H., Akata, N., Kawabata, H., Sato, T., Chikuchi, Y. and Hisamatsu, S. (2014) 'Characteristics of hydrogen and oxygen stable isotope ratios in precipitation collected in a snowfall region, Aomori Prefecture, Japan', *Geochemical Journal*, 48(1), pp. 9–18. Available at:

<https://doi.org/10.2343/geochemj.2.0279>.

Hayashi, R., Takahara, H., Hayashida, A. and Takemura, K. (2010) 'Millennial-scale vegetation changes during the last 40,000yr based on a pollen

record from Lake Biwa, Japan', *Quaternary Research*, 74(1), pp. 91–99.

Available at: <https://doi.org/10.1016/j.yqres.2010.04.008>.

He, J., Jia, G., Li, L. and Wang, P. (2017a) 'Differential timing of C4 plant decline and grassland retreat during the penultimate deglaciation', *Global and Planetary Change*, 156, pp. 26–33. Available at:

<https://doi.org/10.1016/j.gloplacha.2017.08.001>.

He, S., Gao, Y., Li, F., Wang, H. and He, Y. (2017b) 'Impact of Arctic Oscillation on the East Asian climate: A review', *Earth–Science Reviews*, 164, pp. 48–62.

Available at: <https://doi.org/10.1016/j.earscirev.2016.10.014>.

Heaton, T.J., Blaauw, M., Blackwell, P.G., Bronk Ramsey, C., Reimer, P.J. and Scott, E.M. (2020) 'The IntCal20 Approach to Radiocarbon Calibration Curve Construction: A New Methodology Using Bayesian Splines and Errors-in-Variables', *Radiocarbon*, 62(4), pp. 821–863. Available at:

<https://doi.org/10.1017/RDC.2020.46>.

Herzschuh, U. (2006) 'Palaeo-moisture evolution in monsoonal Central Asia during the last 50,000 years', *Quaternary Science Reviews*, 25, pp. 163–178.

Available at: <https://doi.org/10.1016/j.quascirev.2005.02.006>.

Holtvoeth, J., Whiteside, J.H., Engels, S., Freitas, F.S., Grice, K., Greenwood, P., Johnson, S., Kendall, I., Lengger, S.K., Lücke, A., Mayr, C., Naafs, B.D.A., Rohrsen, M. and Sepúlveda, J. (2019) 'The paleolimnologist's guide to compound-specific stable isotope analysis – An introduction to principles and applications of CSIA for Quaternary lake sediments', *Quaternary Science Reviews*, 207, pp. 101–133. Available at:

<https://doi.org/10.1016/j.quascirev.2019.01.001>.

Hu, G., Yi, C., Zhang, J., Cao, G., Pan, B., Liu, J., Jiang, T., Yi, S., Li, D. and Huang, J. (2018) 'Chronology of a lacustrine core from Lake Linggo Co using a combination of OSL,  $^{14}\text{C}$  and  $^{210}\text{Pb}$  dating: implications for the dating of lacustrine sediments from the Tibetan Plateau', *Boreas*, 47(2), pp. 656–670.

Available at: <https://doi.org/10.1111/bor.12291>.

Hut, G. (1987) *Stable Isotope Reference Samples for Geochemical and Hydrological Investigations*, Rep. Consultants Group Meeting, Vienna, 1985.

Available at:

[https://inis.iaea.org/collection/NCLCollectionStore/\\_Public/18/075/18075746.pdf](https://inis.iaea.org/collection/NCLCollectionStore/_Public/18/075/18075746.pdf).

Hyodo, M., Nakagawa, T., Matsushita, H., Kitaba, I., Yamada, K., Tanabe, S., Bradák, B., Miki, M., McLean, D., Staff, R.A., Smith, V.C., Albert, P.G., Bronk Ramsey, C., Yamasaki, A., Kitagawa, J. and Suigetsu 2014 Project Members (2022) 'Intermittent non-axial dipolar-field dominance of twin Laschamp excursions', *Communications Earth & Environment*, 3, article 79. Available at: <https://doi.org/10.1038/s43247-022-00401-0>.

IAEA (2023) 'Stable Isotopes' Available at:

<https://www.iaea.org/topics/nuclear-science/isotopes/stable-isotopes>

(accessed 02/01/2024).

Ichiyanagi, K. and Tanoue, M. (2016) 'Stable isotopes in precipitation across Japan during an intensive observation period throughout 2013', *Journal of Japanese Association of Hydrological Sciences*, 46(2), pp. 123–138. Available at: <https://doi.org/10.4145/jahs.46.123>.

Ichiyanagi, K., Tanoue, M. and on behalf of the Isotope Mapping Working Group of the Japanese Society of Hydrological Science (IMWG/JAHS) (2016) 'Spatial analysis of annual mean stable isotopes in precipitation across Japan based on an intensive observation period throughout 2013', *Isotopes in Environmental and Health Studies*, 52(4–5), pp. 353–362. Available at: <https://doi.org/10.1080/10256016.2015.1132215>.

Ishiwatari, R., Negishi, K., Yoshikawa, H. and Yamamoto, S. (2009) 'Glacial-interglacial productivity and environmental changes in Lake Biwa, Japan: A sediment core study of organic carbon, chlorins and biomarkers', *Organic Geochemistry*, 40(4), pp. 520–530. Available at: <https://doi.org/10.1016/j.orggeochem.2009.01.002>.

Japanese Meteorological Agency (2022). Japanese Meteorological Agency Weather Station Dataset for Mihama, Fukui Prefecture. <https://www.data.jma.go.jp/risk/obsdl/index.php> (accessed 10/02/2022).

Japanese Meteorological Agency (2023). Japanese Meteorological Agency Weather Station Dataset for Tsuruga, Fukui Prefecture. <https://www.data.jma.go.jp/risk/obsdl/index.php> (accessed 23/06/2023).

Jasechko, S., Birks, S.J., Gleeson, T., Wada, Y., Fawcett, P.J., Sharp, Z.D., McDonnell, J.J. and Welker, J.M. (2014) 'The pronounced seasonality of global groundwater recharge', *Water Resources Research*, 50(11), pp. 8845–8867. Available at: <https://doi.org/10.1002/2014WR015809>.

Jiang, X., Wang, Y., Kong, X., Wu, J., Shao, X., Xia, Z. and Cheng, H. (2005) 'Abrupt climate change of East Asian Monsoon at 130 ka BP inferred from a high resolution stalagmite  $\delta^{18}\text{O}$  record', *Chinese Science Bulletin*, 50(23), pp. 2765–2769. Available at: <https://doi.org/10.1360/982004-819>.

Jin, L., Schneider, B., Park, W., Latif, M., Khon, V. and Zhang, X. (2014) 'The spatial-temporal patterns of Asian summer monsoon precipitation in response to Holocene insolation change: A model-data synthesis', *Quaternary Science Reviews*, 85, pp. 47–62. Available at: <https://doi.org/10.1016/j.quascirev.2013.11.004>.

Johnsen, S., Clausen, H.B., Dansgaard, W., Gundestrup, N.S., Hammer, C.U., Andersen, U., Andersen, K.K., Hvidberg, C.S., Steffensen, P., White, J., Jouzel, J. and Fisher, D. (1997) 'The  $\delta^{18}\text{O}$  record along the Greenland Ice Core Project deep ice core and the problem of possible Eemian climatic instability', *Journal of Geophysical Research*, 102(C12), pp. 26397–26410. Available at: <https://doi.org/10.1029/97JC00167>.

Jouzel, J. (2003) 'Water Stable Isotopes: Atmospheric Composition and Applications in Polar Ice Core Studies', in *Treatise on Geochemistry*. Elsevier Ltd, pp. 213–243. Available at: <https://doi.org/10.1016/B0-08-043751-6/04040-8>.

- Jun–Mei, L., Jian–Hua, J. and Shi–Yan, T. (2013) ‘Re–Discussion on East Asian Meiyu Rainy Season’, *Atmospheric and Oceanic Science Letters*, 6, pp. 279–283. Available at: <https://doi.org/10.3878/j.issn.1674-2834.13.0024>.
- Kadereit, A., DeWitt, R. and Johnson, T. C. (2012) ‘Luminescence properties and optically (post–IR blue–light) stimulated luminescence dating of limnic sediments from northern Lake Malawi – Chances and limitations’, *Quaternary Geochronology*, 10, pp. 160–166. Available at: <https://doi.org/10.1016/j.quageo.2012.02.021>.
- Kawakami, S., Fukusawa, H. and Kanaori, Y. (1996) ‘A new opportunity to detect paleo–earthquake events dating back to the past 10 millennia: a record from lacustrine sediment’, *Engineering Geology*, 43, pp. 177–188. Available at: [https://doi.org/10.1016/0013-7952\(96\)00059-2](https://doi.org/10.1016/0013-7952(96)00059-2).
- Kawamura, K., Parrenin, F., Lisiecki, L., Uemura, R., Vimeux, F., Severinghaus, J.P., Hutterli, M.A., Nakazawa, T., Aoki, S., Jouzel, J., Raymo, M.E., Matsumoto, K., Nakata, H., Motoyama, H., Fujita, S., Goto–Azuma, K., Fujii, Y. and Watanabe, O. (2007) ‘Northern Hemisphere forcing of climatic cycles in Antarctica over the past 360,000 years’, *Nature*, 448, pp. 912–916. Available at: <https://doi.org/10.1038/nature06015>.
- Kelly, M.J., Edwards, R.L., Cheng, H., Yuan, D., Cai, Y., Zhang, M., Lin, Y. and An, Z. (2006) ‘High resolution characterization of the Asian Monsoon between 146,000 and 99,000 years B.P. from Dongge Cave, China and global correlation of events surrounding Termination II’, *Palaeogeography, Palaeoclimatology, Palaeoecology*, 236, pp. 20–38. Available at: <https://doi.org/10.1016/j.palaeo.2005.11.042>.
- Kendall, C. and Caldwell, E.A. (1998) ‘Fundamentals of Isotope Geochemistry’, in C. Kendall and J.J. McDonnell (eds) *Isotope Tracers in Catchment Hydrology*. Amsterdam: Elsevier Science B.V., pp. 51–86. Available at: <https://wwwrcamnl.wr.usgs.gov/isoig/isopubs/itchch2.html>.
- Kinnaird, T. C., Sanderson, D. C. W. and Bigelow, G. F. (2015) ‘Feldspar SARA IRSL dating of very low dose rate aeolian sediments from Sandwick South, Unst,

Shetland', *Quaternary Geochronology*, 30(B), pp. 168–174. Available at: <https://doi.org/10.1016/j.quageo.2015.02.019>.

Kinnaird, T.C., Sanderson, D.C.W. and Woodward, N.L. (2011) 'Applying luminescence methods to geoarchaeology: A case study from Stronsay, Orkney', *Earth and Environmental Science Transactions of the Royal Society of Edinburgh*, 102, pp. 191–199. Available at: <https://doi.org/10.1017/S1755691012011115>.

Kitagawa, H. and van der Plicht, J. (1998) 'A 40,000-year varve chronology from Lake Suigetsu, Japan: Extension of the  $^{14}\text{C}$  calibration curve', *Radiocarbon*, 40(1), pp. 505–515. Available at: <https://doi.org/10.1017/S0033822200018385>.

Kitagawa, H. and van der Plicht, J. (2000) 'Atmospheric Radiocarbon Calibration Beyond 11,900 cal BP from Lake Suigetsu Laminated Sediments', *Radiocarbon*, 42(3), pp. 370–381. Available at: <https://doi.org/10.1017/s0033822200030319>.

Kitoh, A. (2017) 'The Asian monsoon and its future change in climate models: A review', *Journal of the Meteorological Society of Japan*, 95(1), pp. 7–33. Available at: <https://doi.org/10.2151/jmsj.2017-002>.

Kondo, R. and Butani, J. (2007) 'Comparison of the diversity of sulfate-reducing bacterial communities in the water column and the surface sediments of a Japanese meromictic lake', *Limnology*, 8, pp. 131–141. Available at: <https://doi.org/10.1007/s10201-007-0201-9>.

Kondo, R., Kasashima, N., Matsuda, H. and Hata, Y. (2000) 'Determination of thiosulfate in a meromictic lake', *Fisheries Science*, 66(6), pp. 1076–1081. Available at: <https://doi.org/10.1046/j.1444-2906.2000.00171.x>.

Kondo, R., Kodera, M., Mori, Y., Okamura, T., Yoshikawa, S. and Ohki, K. (2014) 'Spatiotemporal distribution of bacteriochlorophylls in the meromictic Lake Suigetsu, Japan', *Limnology*, 15, pp. 77–83. Available at: <https://doi.org/10.1007/s10201-013-0415-y>.

Kossler, A., Tarasov, P.E., Schlolaut, G., Nakagawa, T., Marshall, M.H., Brauer, A., Staff, R.A., Bronk Ramsey, C., Bryant, C.L., Lamb, H.F., Demske, D., Gotanda, K., Haraguchi, T., Yokoyama, Y., Yonenobu, H. and Tada, R. (2011) 'Onset and termination of the late-glacial climate reversal in the high-resolution diatom and sedimentary records from the annually laminated SG06 core from Lake Suigetsu, Japan', *Palaeogeography, Palaeoclimatology, Palaeoecology*, 306(3–4), pp. 103–115. Available at:

<https://doi.org/10.1016/j.palaeo.2011.04.004>.

Kubota, Y., Kimoto, K., Tada, R., Uchida, M. and Ikehara, K. (2019) 'Millennial-scale variability of East Asian summer monsoon inferred from sea surface salinity in the northern East China Sea (ECS) and its impact on the Japan Sea during Marine Isotope Stage (MIS) 3', *Progress in Earth and Planetary Science*, 6(1), article 39. Available at:

<https://doi.org/10.1186/s40645-019-0283-0>.

Kurita, N., Fujiyoshi, Y., Nakayama, T., Matsumi, Y. and Kitagawa, H. (2015) 'East Asian Monsoon controls on the inter-annual variability in precipitation isotope ratio in Japan', *Climate of the Past*, 11, pp. 339–353. Available at:

<https://doi.org/10.5194/cp-11-339-2015>.

Lacey, J.H. and Jones, M.D. (2018) 'Quantitative reconstruction of early Holocene and last glacial climate on the Balkan Peninsula using coupled hydrological and isotope mass balance modelling', *Quaternary Science Reviews*, 202, pp. 109–121. Available at:

<https://doi.org/10.1016/j.quascirev.2018.09.007>.

Landais, A., Dreyfus, G., Capron, E., Jouzel, J., Masson-Delmotte, V., Roche, D.M., Prié, F., Caillon, N., Chappellaz, J., Leuenberger, M., Lourantou, A., Parrenin, F., Raynaud, D. and Teste, G. (2013) 'Two-phase change in CO<sub>2</sub>, Antarctic temperature and global climate during Termination II', *Nature Geoscience*, 6, pp. 1062–1065. Available at: <https://doi.org/10.1038/ngeo1985>.

Laskar, J., Robutel, P., Joutel, F., Gastineau, M., Correia, A.C.M. and Levrard, B. (2004) 'A long-term numerical solution for the insolation quantities of the

Earth', *Astronomy and Astrophysics*, 428, pp. 261–285. Available at:

<https://doi.org/10.1051/0004-6361:20041335>.

Lau, K. and Li, M. (1984) 'The Monsoon of East Asia and its Global Associations—A Survey', *Bulletin of the American Meteorological Society*, 65(2), pp. 114–125.

Available at:

[https://doi.org/10.1175/1520-0477\(1984\)065<0114:tmoeaa>2.0.co;2](https://doi.org/10.1175/1520-0477(1984)065<0114:tmoeaa>2.0.co;2).

Lawrence, R.J. and Gedzelman, D.S., (1996) 'Low stable isotope ratios of tropical cyclone rains', *Geophysical Research Letters*, 23(5), pp. 527–530.

Available at: <https://doi.org/10.1029/96GL00425>.

Lécuyer, C., Bojar, A.V., Daux, V. and Legendre, S. (2021) 'Geographic variations in the slope of the  $\delta^2\text{H}$ – $\delta^{18}\text{O}$  meteoric water line over Europe: a record of increasing continentality', in A.-V. Bojar, A. Pelc, and C. Lécuyer (eds) *Stable Isotope Studies of the Water Cycle and Terrestrial Environments*. London: Geological Society, pp. 5–17.

Available at: <https://doi.org/10.1144/SP507-2020-68>.

Leipe, C., Nakagawa, T., Gotanda, K., Müller, S. and Tarasov, P.E. (2015) 'Late Quaternary vegetation and climate dynamics at the northern limit of the East Asian summer monsoon and its regional and global-scale controls', *Quaternary Science Reviews*, 116, pp. 57–71.

Available at: <https://doi.org/10.1016/j.quascirev.2015.03.012>.

Leng, M.J. and Barker, P.A. (2006) 'A review of the oxygen isotope composition of lacustrine diatom silica for palaeoclimate reconstruction', *Earth-Science Reviews*, 75, pp. 5–27.

Available at: <https://doi.org/10.1016/j.earscirev.2005.10.001>.

Leng, M.J. and Marshall, J.D. (2004) 'Palaeoclimate interpretation of stable isotope data from lake sediment archives', *Quaternary Science Reviews*, 23, pp. 811–831.

Available at: <https://doi.org/10.1016/j.quascirev.2003.06.012>.

Leng, M.J. and Sloane, H.J. (2008) 'Combined oxygen and silicon isotope analysis of biogenic silica', *Journal of Quaternary Science*, 23(4), pp. 313–319. Available at: <https://doi.org/10.1002/jqs>.

Li, C., Kano, N., Ueno, Y., Hanabusa, M., Jiao, Y., Imaizumi, H. and Watanabe, N. (2010) 'Characteristics of Oxygen Stable Isotopic Ratio in Precipitations in Niigata Prefecture, Japan', *Radioisotopes*, 59(2), pp. 93–102. Available at: <https://doi.org/10.3769/radioisotopes.59.93>.

Li, J., Yang, S., Shu, J., Li, R., Chen, X., Meng, Y., Ye, S. and He, L. (2020) 'Vegetation history and environment changes since MIS 5 recorded by pollen assemblages in sediments from the western Bohai Sea, Northern China', *Journal of Asian Earth Sciences*, 187(October 2019), article 104085. Available at: <https://doi.org/10.1016/j.jseaes.2019.104085>.

Li, T.Y., Shen, C.C., Huang, L.J., Jiang, X.Y., Yang, X.L., Mii, H.S., Lee, S.Y. and Lo, L. (2014) 'Stalagmite-inferred variability of the Asian summer monsoon during the penultimate glacial–interglacial period', *Climate of the Past*, 10(3), pp. 1211–1219. Available at: <https://doi.org/10.5194/cp-10-1211-2014>.

Lian, O.B. and Roberts, R.G. (2006) 'Dating the Quaternary: progress in luminescence dating of sediments', *Quaternary Science Reviews*, 25(19–20), pp. 2449–2468. Available at: <https://doi.org/10.1016/j.quascirev.2005.11.013>.

Liang, Y., Zhao, K., Edwards, R.L., Wang, Y., Shao, Q., Zhang, Z., Zhao, B., Wang, Q., Cheng, H. and Kong, X. (2020) 'East Asian monsoon changes early in the last deglaciation and insights into the interpretation of oxygen isotope changes in the Chinese stalagmite record', *Quaternary Science Reviews*, 250, article 106699. Available at: <https://doi.org/10.1016/j.quascirev.2020.106699>.

Lisiecki, L.E. and Raymo, M.E. (2005) 'A Pliocene–Pleistocene stack of 57 globally distributed benthic  $\delta^{18}\text{O}$  records', *Paleoceanography*, 20, article PA1003. Available at: <https://doi.org/10.1029/2004PA001071>.

- Lisiecki, L.E. and Stern, J. V (2016) 'Regional and global benthic  $\delta^{18}\text{O}$  stacks for the last glacial cycle', *Paleoceanography*, 31, pp. 1368–1394. Available at: <https://doi.org/10.1002/2016PA003002>.
- Liu, D., Wang, Y., Cheng, H., Kong, X. and Chen, S. (2013) 'Centennial-scale Asian monsoon variability during the mid-Younger Dryas from Qingtian Cave, central China', *Quaternary Research (United States)*, 80(2), pp. 199–206. Available at: <https://doi.org/10.1016/j.yqres.2013.06.009>.
- Long, H. (2012) 'High-resolution OSL chronology of a sediment core from Lake Nam Co on the southern Tibetan Plateau: Implication for lake evolution since the late Glacial', *Quaternary International*, 279–280, pp. 287–288. Available at: <https://doi.org/10.1016/j.quaint.2012.08.762>.
- Loulergue, L., Schilt, A., Spahni, R., Masson-Delmotte, V., Blunier, T., Lemieux, B., Barnola, J.M., Raynaud, D., Stocker, T.F. and Chappellaz, J. (2008) 'Orbital and millennial-scale features of atmospheric  $\text{CH}_4$  over the past 800,000 years', *Nature*, 453, pp. 383–386. Available at: <https://doi.org/10.1038/nature06950>.
- Lupien, R.L., Russell, J.M., Pearson, E.J., Castañeda, I.S., Asrat, A., Foerster, V., Lamb, H.F., Roberts, H.M., Schäbitz, F., Trauth, M.H., Beck, C.C., Feibel, C.S. and Cohen, A.S. (2022) 'Orbital controls on eastern African hydroclimate in the Pleistocene', *Scientific Reports*, 12, article 3170. Available at: <https://doi.org/10.1038/s41598-022-06826-z>.
- Ma, T. and Chen, W. (2021) 'Climate variability of the East Asian winter monsoon and associated extratropical-tropical interaction: a review', *Annals of the New York Academy of Sciences*, 1504(1), pp. 44–62. Available at: <https://doi.org/10.1111/nyas.14620>.
- Ma, T., Chen, W., Graf, H.F., Ding, S., Xu, P., Song, L. and Lan, X. (2020) 'Different impacts of the East Asian Winter Monsoon on the surface air temperature in North America during ENSO and neutral ENSO years', *Journal of Climate*, 33(24), pp. 10671–10690. Available at: <https://doi.org/10.1175/JCLI-D-18-0760.1>.

Machavaram, M. V. and Krishnamurthy, R. V. (1995) 'Earth surface evaporative process: A case study from the Great Lakes region of the United States based on deuterium excess in precipitation', *Geochimica et Cosmochimica Acta*, 59(20), pp. 4279–4283. Available at: [https://doi.org/10.1016/0016-7037\(95\)00256-Y](https://doi.org/10.1016/0016-7037(95)00256-Y).

Mackay, A.W., Swann, G.E.A., Brewer, T.S., Leng, M.J., Morley, D.W., Piotrowska, N., Rioual, P. and White, D. (2011) 'A reassessment of late glacial – Holocene diatom oxygen isotope record from Lake Baikal using a geochemical mass–balance approach', *Journal of Quaternary Science*, 26(6), pp. 627–634. Available at: <https://doi.org/10.1002/jqs.1484>.

Mann, D.G. and Vanormelingen, P. (2013) 'An inordinate fondness? the number, distributions, and origins of diatom species', *Journal of Eukaryotic Microbiology*, 60, pp. 414–420. Available at: <https://doi.org/10.1111/jeu.12047>.

Marcott, S.A., Bauska, T.K., Buizert, C., Steig, E.J., Rosen, J.L., Cuffey, K.M., Fudge, T.J., Severinghaus, J.P., Ahn, J., Kalk, M.L., McConnell, J.R., Sowers, T., Taylor, K.C., White, J.W.C. and Brook, E.J. (2014) 'Centennial–scale changes in the global carbon cycle during the last deglaciation', *Nature*, 514, pp. 616–619. Available at: <https://doi.org/10.1038/nature13799>.

Marshall, M. H., Schlolaut, G., Nakagawa, T., Lamb, H. F., Brauer, A., Staff, R. A., Bronk Ramsey, C., Tarasov, P. E., Gotanda, K., Haraguchi, T., Yokoyama, Y., Yonenobu, H. and Tada, R. (2012) 'A novel approach to varve counting using  $\mu$ XRF and X–radiography in combination with thin–section microscopy, applied to the Late Glacial chronology from Lake Suigetsu, Japan', *Quaternary Geochronology*, 13, pp. 70–80. Available at: <https://doi.org/10.1016/j.quageo.2012.06.002>.

Masson–Delmotte, V., Stenni, B., Blunier, T., Cattani, O., Chappellaz, J., Cheng, H., Dreyfus, G., Edwards, R.L., Falourd, S., Govin, A., Kawamura, K., Johnsen, S.J., Jouzel, J., Landais, A., Lemieux–Dudon, B., Lourantou, A., Marshall, G., Minster, B., Mudelsee, M., Pol, K., Röthlisberger, R., Selmo, E. and Waelbroeck, C. (2010) 'Abrupt change of Antarctic moisture origin at the end of termination II', *Proceedings of the National Academy of Sciences of the United States of*

*America*, 107(27), pp. 12091–12094. Available at:

<https://doi.org/10.1073/pnas.0914536107>.

Masuzawa, T. and Kitano, Y. (1982a) 'Diagenetic deposition of manganese in sediment of a historically meromictic lake, Lake Suigetsu, Japan', *Journal of the Oceanographical Society of Japan*, 38, pp. 73–80. Available at:

<https://doi.org/10.1007/BF02110293>.

Masuzawa, T. and Kitano, Y. (1982b) 'Sulfate reduction and sulfur fixation in sediment of a historically meromictic lake, Lake Suigetsu, Japan', *Journal of the Oceanographical Society of Japan*, 38, pp. 21–27. Available at:

<https://doi.org/10.1007/BF02113818>.

Matsuyama, M. (1973) 'Changes in the limnological features of a meromictic Lake Suigetsu during the years, 1926–1967', *Journal of the Oceanographical Society of Japan*, 29, pp. 131–139. Available at:

<https://doi.org/10.1007/BF02109088>.

Matsuyama, M. (1974) 'Vertical distributions of some chemical substances in surface sediments of a meromictic Lake Suigetsu', *Journal of Quaternary Science*, 30, pp. 209–215. Available at: <https://doi.org/10.1007/BF02111046>.

McLean, D., Albert, P. G., Nakagawa, T., Suzuki, T., Staff, R. A., Yamada, K., Kitaba, I., Haraguchi, T., Kitagawa, J. and Smith, V. C. (2018) 'Integrating the Holocene tephrostratigraphy for East Asia using a high-resolution cryptotephra study from Lake Suigetsu (SG14 core), central Japan', *Quaternary Science Reviews*, 183, pp. 36–58. Available at:

<https://doi.org/10.1016/j.quascirev.2017.12.013>.

McLean, D., Albert, P.G., Nakagawa, T., Staff, R.A., Suzuki, T. and Smith, V.C. (2016) 'Identification of the Changbaishan "Millennium" (B-Tm) eruption deposit in the Lake Suigetsu (SG06) sedimentary archive, Japan: Synchronisation of hemispheric-wide palaeoclimate archives', *Quaternary Science Reviews*, 150, pp. 301–307. Available at: <https://doi.org/10.1016/j.quascirev.2016.08.022>.

McClean, D., Albert, P.G., Suzuki, T., Nakagawa, T., Kimura, J. and Chang, Q. (2020) 'Constraints on the timing of explosive volcanism at Aso and Aira calderas (Japan) between 50 and 30 ka: New insights from the Lake Suigetsu sedimentary record', *Geochemistry, Geophysics, Geosystems*, 21(8), article e2019GC008874. Available at: <https://doi.org/10.1029/2019GC008874>.

McClean, D., Albert, P.G., Suzuki, T., Nakagawa, T., Kimura, J., Chang, Q., Macleod, A., Blockley, S.P., Staff, R.A., Yamada, K., Kitaba, I., Haraguchi, T., Kitagawa, J. and Smith, V.C. (2019) 'Refining the eruptive history of Ulleungdo and Changbaishan volcanoes (East Asia) over the last 86 kyrs using distal sedimentary records', *Journal of Volcanology and Geothermal Research*, 389, article 106669. Available at: <https://doi.org/10.1016/j.jvolgeores.2019.106669>.

Mejdahl, V. (1979) 'Thermoluminescence dating: beta-dose attenuation in quartz grains', *Archaeometry*, 21(1), pp. 61–72. Available at: <https://doi.org/10.1111/j.1475-4754.1979.tb00241.x>.

Meyers, P.A. and Ishiwatari, R. (1993) 'Lacustrine organic geochemistry—an overview of indicators of organic matter sources and diagenesis in lake sediments', *Organic Geochemistry*, 20(7), pp. 867–900. Available at: [https://doi.org/10.1016/0146-6380\(93\)90100-P](https://doi.org/10.1016/0146-6380(93)90100-P).

Mohtadi, M., Prange, M. and Steinke, S. (2016) 'Palaeoclimatic insights into forcing and response of monsoon rainfall', *Nature*, 533, pp. 191–199. Available at: <https://doi.org/10.1038/nature17450>.

Mori, T., Kashiwagi, K., Amekawa, S., Kato, H., Okumura, T., Takashima, C., Wu, C.C., Shen, C.C., Quade, J. and Kano, A. (2018) 'Temperature and seawater isotopic controls on two stalagmite records since 83 ka from maritime Japan', *Quaternary Science Reviews*, 192, pp. 47–58. Available at: <https://doi.org/10.1016/j.quascirev.2018.05.024>.

Morley, D.W., Leng, M.J., Mackay, A.W., Sloane, H.J., Rioual, P. and Battarbee, R.W. (2004) 'Cleaning of lake sediment samples for diatom oxygen isotope analysis', *Journal of Paleolimnology*, 31, pp. 391–401. Available at: <https://doi.org/10.1023/B:JOPL.0000021854.70714.6b>

Munyikwa, K. and Brown, S. (2014) 'Rapid equivalent dose estimation for aeolian dune sands using a portable OSL reader and polymineralic standardised luminescence growth curves: Expedited sample screening for OSL dating', *Quaternary Geochronology*, 22, pp. 116–125. Available at: <https://doi.org/10.1016/j.quageo.2014.04.002>.

Munyikwa, K., Kinnaird, T.C. and Sanderson, D.C. (2021) 'The potential of portable luminescence readers in geomorphological investigations: a review', *Earth Surface Processes and Landforms*, 46(1), pp. 131–150. Available at: <https://doi.org/10.1002/esp.4975>.

Nakagawa, T., Gotanda, K., Haraguchi, T., Danhara, T., Yonenobu, H., Brauer, A., Yokoyama, Y., Tada, R., Takemura, K., Staff, R.A., Payne, R.L., Bronk Ramsey, C., Bryant, C.L., Brock, F., Scholout, G., Marshall, M.H., Tarasov, P.E. and Lamb, H.F. (2012) 'SG06, a fully continuous and varved sediment core from Lake Suigetsu, Japan: Stratigraphy and potential for improving the radiocarbon calibration model and understanding of late Quaternary climate changes', *Quaternary Science Reviews*, 36, pp. 164–176. Available at: <https://doi.org/10.1016/j.quascirev.2010.12.013>.

Nakagawa, T., Kitagawa, H., Yasuda, Y., Tarasov, P.E., Nishida, K., Gotanda, K. and Sawai, Y. (2003) 'Asynchronous climate changes in the North Atlantic and Japan during the last termination', *Science*, 299(5607), pp. 688–691. Available at: <https://doi.org/10.1126/science.1078235>.

Nakagawa, T., Tarasov, P., Staff, R., Bronk Ramsey, C., Marshall, M., Scholout, G., Bryant, C., Brauer, A., Lamb, H., Haraguchi, T., Gotanda, K., Kitaba, I., Kitagawa, H., van der Plicht, J., Yonenobu, H., Omori, T., Yokoyama, Y., Tada, R. and Yasuda, Y. (2021) 'The spatio-temporal structure of the Lateglacial to early Holocene transition reconstructed from the pollen record of Lake Suigetsu and its precise correlation with other key global archives: Implications for palaeoclimatology and archaeology', *Global and Planetary Change*, 202, article 103493. Available at: <https://doi.org/10.1016/j.gloplacha.2021.103493>.

Nakagawa, T., Tarasov, P.E., Kitagawa, H., Yasuda, Y. and Gotanda, K. (2006) 'Seasonally specific responses of the East Asian monsoon to deglacial climate

changes', *Geology*, 34(7), pp. 521–524. Available at:

<https://doi.org/10.1130/G21764.1>.

Nakagawa, T., Tarasov, P.E., Nishida, K., Gotanda, K. and Yasuda, Y. (2002) 'Quantitative pollen-based climate reconstruction in central Japan: Application to surface and Late Quaternary spectra', *Quaternary Science Reviews*, 21(18–19), pp. 2099–2113. Available at:

[https://doi.org/10.1016/S0277-3791\(02\)00014-8](https://doi.org/10.1016/S0277-3791(02)00014-8).

Nelson, M., Rittenour, T. and Cornachione, H. (2019) 'Sampling Methods for Luminescence Dating of Subsurface Deposits from Cores', *Methods and Protocols*, 2(4), article 88. Available at: <https://doi.org/10.3390/mps2040088>.

Nilsson-Kerr, K., Anand, P., Sexton, P.F., Leng, M.J., Misra, S., Clemens, S.C. and Hammond, S.J. (2019) 'Role of Asian summer monsoon subsystems in the inter-hemispheric progression of deglaciation', *Nature Geoscience*, 12, pp. 290–295. Available at: <https://doi.org/10.1038/s41561-019-0319-5>.

Oba, T. and Murayama, M. (2004) 'Sea-surface temperature and salinity changes in the northwest Pacific since the last glacial maximum', *Journal of Quaternary Science*, 19(4), pp. 335–346. Available at: <https://doi.org/10.1002/jqs.843>.

Oba, T., Irino, T., Yamamoto, M., Murayama, M., Takamura, A. and Aoki, K. (2006) 'Paleoceanographic change off central Japan since the last 144,000 years based on high-resolution oxygen and carbon isotope records', *Global and Planetary Change*, 53(1–2), pp. 5–20. Available at:

<https://doi.org/10.1016/j.gloplacha.2006.05.002>.

Olive, V., Ellam, R.M. and Wilson, L. (2001) 'A protocol for the determination of the rare earth elements at picomole level in rocks by ICP-MS: Results on geological reference materials USGS PCC-1 and DTS-1', *Geostandards Newsletter*, 25(2–3), pp. 219–228. Available at:

<https://doi.org/10.1111/j.1751-908X.2001.tb00597.x>.

Oppo, D.W. and Sun, Y. (2005) 'Amplitude and timing of sea-surface temperature change in the northern South China Sea: Dynamic link to the East

Asian monsoon', *Geology*, 33(10), pp. 785–788. Available at:

<https://doi.org/10.1130/G21867.1>.

Overpeck, J., Anderson, D., Trumbore, S. and Prell, W. (1996) 'The southwest Indian Monsoon over the last 18000 years', *Climate Dynamics*, 12, pp. 213–225.

Available at: <https://doi.org/10.1007/BF00211619>.

Park, Jungjae, Park, Jinheum, Yi, S., Cheul Kim, J., Lee, E. and Choi, J. (2019) 'Abrupt Holocene climate shifts in coastal East Asia, including the 8.2 ka, 4.2 ka, and 2.8 ka BP events, and societal responses on the Korean peninsula', *Scientific Reports*, 9, article 10806. Available at:

<https://doi.org/10.1038/s41598-019-47264-8>.

Pears, B., Brown, A.G., Toms, P.S., Wood, J., Sanderson, D. and Jones, R. (2020) 'A sub-centennial-scale optically stimulated luminescence chronostratigraphy and late Holocene flood history from a temperate river confluence', *Geology*, 48(8), pp. 819–825. Available at:

<https://doi.org/10.1130/G47079.1>.

Pearson, E.J., Juggins, S. and Tyler, J.J. (2014) 'Ultra-high resolution total organic carbon analysis using Fourier Transform Near Infrared Reflectance Spectroscopy (FT-NIRS)', *Geochemistry, Geophysics, Geosystems*, 15(1), pp. 292–301. Available at: <https://doi.org/10.1002/2013GC004928>.

Pířková, A., Roman, M., Bulínová, M., Pokorný, M., Sanderson, D., Cresswell, A., Lirio, J.M., Coria, S.H., Nedbalová, L., Lami, A. and Musazzi, S. (2019) 'Late-Holocene palaeoenvironmental changes at Lake Esmeralda (Vega Island, Antarctic Peninsula) based on a multi-proxy analysis of laminated lake sediment', *The Holocene*, 29(7), pp. 1155–1175. Available at:

<https://doi.org/10.1177%2F0959683619838033>.

Plancq, J., Cavazzin, B., Juggins, S., Haig, H.A., Leavitt, P.R. and Toney, J.L. (2018) 'Assessing environmental controls on the distribution of long-chain alkenones in the Canadian Prairies', *Organic Geochemistry*, 117, pp. 43–55.

Available at: <https://doi.org/10.1016/j.orggeochem.2017.12.005>.

Porat, N., López, G. I., Lensky, N., Elinson, R., Avni, Y., Elgart–Sharon, Y., Faershtein, G. and Gadot, Y. (2019) ‘Using portable OSL reader to obtain a time scale for soil accumulation and erosion in archaeological terraces, the Judean Highlands, Israel’, *Quaternary Geochronology*, 49, pp. 65–70. Available at: <https://doi.org/10.1016/j.quageo.2018.04.001>.

Putman, A.L., Fiorella, R.P., Bowen, G.J. and Cai, Z. (2019) ‘A Global Perspective on Local Meteoric Water Lines: Meta-analytic Insight Into Fundamental Controls and Practical Constraints’, *Water Resources Research*, 55, pp. 6896–6910. Available at: <https://doi.org/10.1029/2019WR025181>.

Rasmussen, S. O., Bigler, M., Blockley, S. P., Blunier, T., Buchardt, S. L., Clausen, H. B., Cvijanovic, I., Dahl–Jensen, D., Johnsen, S. J., Fischer, H., Gkinis, V., Guillevic, M., Hoek, W. Z., Lowe, J., Pedro, J. B., Popp, T., Seierstad, I. K., Steffensen, J., Svensson, A. M. and Winstrup, M. (2014) ‘A stratigraphic framework for abrupt climatic changes during the Last Glacial period based on three synchronized Greenland ice–core records: Refining and extending the INTIMATE event stratigraphy’, *Quaternary Science Reviews*, 106, pp. 14–28. Available at: <https://doi.org/10.1016/j.quascirev.2014.09.007>.

Reimer, P.J., Austin, W.E.N., Bard, E., Bayliss, A., Blackwell, P.G., Bronk Ramsey, C., Butzin, M., Cheng, H., Edwards, R.L., Friedrich, M., Grootes, P.M., Guilderson, T.P., Hajdas, I., Heaton, T.J., Hogg, A.G., Hughen, K.A., Kromer, B., Manning, S.W., Muscheler, R., Palmer, J.G., Pearson, C., Van Der Plicht, J., Reimer, R.W., Richards, D.A., Scott, E.M., Southon, J.R., Turney, C.S.M., Wacker, L., Adolphi, F., Büntgen, U., Capano, M., Fahrni, S.M., Fogtmann–Schulz, A., Friedrich, R., Köhler, P., Kudsk, S., Miyake, F., Olsen, J., Reinig, F., Sakamoto, M., Sookdeo, A. and Talamo, S. (2020) ‘The IntCal20 Northern Hemisphere Radiocarbon Age Calibration Curve (0–55 cal kBP)’, *Radiocarbon*, 62(4), pp. 725–757. Available at: <https://doi.org/10.1017/RDC.2020.41>.

Reimer, P.J., Bard, E., Bayliss, A., Beck, J.W., Blackwell, P.G., Bronk Ramsey, C., Buck, C.E., Cheng, H., Edwards, R.L., Friedrich, M., Grootes, P.M., Guilderson, T.P., Haflidason, H., Hajdas, I., Hattt, C., Heaton, T.J., Hoffmann, D.L., Hogg, A.G., Hughen, K.A., Kaiser, K.F., Kromer, B., Manning, S.W., Niu,

M., Reimer, R.W., Richards, D.A., Scott, E.M., Southon, J.R., Staff, R.A., Turney, C.S.M. and van der Plicht, J. (2014) 'IntCal13 and Marine13 radiocarbon age calibration curves 0–50,000 years cal BP', *Radiocarbon*, 55(4), pp. 1869–1887. Available at: [https://doi.org/10.2458/azu\\_js\\_rc.55.16947](https://doi.org/10.2458/azu_js_rc.55.16947).

Rex, C.L., Staff, R.A., Sanderson, D.C.W., Cresswell, A.J., Marshall, M.H., Hyodo, M., Horiuchi, D., Tada, R. and Nakagawa, T. (2022) 'Controls on luminescence signals in lake sediment cores: A study from Lake Suigetsu, Japan', *Quaternary Geochronology*, 71, article 101319. Available at: <https://doi.org/10.1016/j.quageo.2022.101319>.

Rex, C.L., Tyler, J.J., Nagaya, K., Staff, R.A., Leng, M.J., Yamada, K., Kitaba, I., Kitagawa, J., Kojima, H. and Nakagawa, T. (2024) 'The contemporary stable isotope hydrology of Lake Suigetsu and surrounding catchment (Japan) and its implications for sediment-derived palaeoclimate records', *Quaternary Science Advances*, 13, article 100145. Available at: <https://doi.org/10.1016/j.qsa.2023.100145>.

Rolph, G., Stein, A. and Stunder, B. (2017) 'Real-time Environmental Applications and Display sYstem: READY', *Environmental Modelling and Software*, 95, pp. 210–228. Available at: <https://doi.org/10.1016/j.envsoft.2017.06.025>.

Rosman, K.J.R. and Taylor P.D.P. (1998) '1997 report of the IUPAC Subcommittee for Isotopic Abundance Measurements', *Pure and Applied Chemistry*, 70, pp. 217–235. Available at: <https://doi.org/10.1351/pac199870010217>.

Rozanski, K., Araguás–Araguás, L. and Gonfiantini, R. (2013) 'Isotopic Patterns in Modern Global Precipitation', *Climate Change in Continental Isotopic Records*, 78. Available at: <https://doi.org/10.1029/gm078p0001>.

Rozanski, K., Klisch, M.A., Wachniew, P., Gorczyca, Z., Goslar, T., Edwards, T.W.D. and Shemesh, A. (2010) 'Oxygen–isotope geothermometers in lacustrine sediments: New insights through combined  $\delta^{18}\text{O}$  analyses of aquatic cellulose, authigenic calcite and biogenic silica in Lake Gościaz, central Poland',

*Geochimica et Cosmochimica Acta*, 74, pp. 2957–2969. Available at:

<https://doi.org/10.1016/j.gca.2010.02.026>.

Russell, J.M. and Johnson, T.C. (2006) ‘The water balance and stable isotope hydrology of Lake Edward, Uganda–Congo’, *Journal of Great Lakes Research*, 32(1), pp. 77–90. Available at:

[https://doi.org/10.3394/0380-1330\(2006\)32\[77:TWBASI\]2.0.CO;2](https://doi.org/10.3394/0380-1330(2006)32[77:TWBASI]2.0.CO;2).

Sachse, D., Billault, I., Bowen, G.J., Chikaraishi, Y., Dawson, T.E., Feakins, S.J., Freeman, K.H., Magill, C.R., McInerney, F.A., van der Meer, M.T.J., Polissar, P., Robins, R.J., Sachs, J.P., Schmidt, H.–L., Sessions, A.L., White, J.W.C., West, J.B. and Kahmen, A. (2012) ‘Molecular Paleohydrology: Interpreting the Hydrogen–Isotopic Composition of Lipid Biomarkers from Photosynthesizing Organisms’, *Annual Review of Earth and Planetary Sciences*, 40, pp. 221–249. Available at: <https://doi.org/10.1146/annurev-earth-042711-105535>.

Sachse, D., Radke, J. and Gleixner, G. (2006) ‘ $\delta D$  values of individual n–alkanes from terrestrial plants along a climatic gradient – Implications for the sedimentary biomarker record’, *Organic Geochemistry*, 37, pp. 469–483.

Available at: <https://doi.org/10.1016/j.orggeochem.2005.12.003>.

Saito–Kato, M., Yamada, K., Staff, R.A., Nakagawa, T., Yonenobu, H., Haraguchi, T., Takemura, K. and Bronk Ramsey, C. (2013) ‘An Assessment of the Magnitude of the AD1586 Tensho Tsunami Inferred from Lake Suigetsu Sediment Cores’, *Journal of Geography (Chigaku Zasshi)*, 122(3), pp. 493–501. Available at: <https://doi.org/10.5026/jgeography.122.493>.

Sandeep, K., Shankar, R., Warriar, A.K., Yadava, M.G., Ramesh, R., Jani, R.A., Weijian, Z. and Xuefeng, L. (2017) ‘A multi–proxy lake sediment record of Indian summer monsoon variability during the Holocene in southern India’, *Palaeogeography, Palaeoclimatology, Palaeoecology*, 476, pp. 1–14. Available at: <https://doi.org/10.1016/j.palaeo.2017.03.021>.

Sanderson, D. C. W. and Murphy, S. (2010) ‘Using simple portable OSL measurements and laboratory characterisation to help understand complex and heterogeneous sediment sequences for luminescence dating’, *Quaternary*

*Geochronology*, 5(2–3), pp. 299–305. Available at:

<https://doi.org/10.1016/j.quageo.2009.02.001>.

Sanderson, D.C. and Kinnaird, T.C. (2019) ‘Optically Stimulated Luminescence Dating as a Geochronological Tool for Late Quaternary Sediments in the Red Sea Region’, in: Rasul, N.M.A., Stewart, I.C.F. (Eds.), *Geological Setting, Palaeoenvironment and Archaeology of the Red Sea*. Springer, Cham, pp. 685–707. Available at: [https://doi.org/10.1007/978-3-319-99408-6\\_31](https://doi.org/10.1007/978-3-319-99408-6_31).

Sanyal, P. and Sinha, R. (2010) ‘Evolution of the Indian summer monsoon: Synthesis of continental records’, *Geological Society, London, Special Publication*, 342, pp. 153–183. Available at: <https://doi.org/10.1144/SP342.11>.

Sauer, P.E., Eglinton, T.I., Hayes, J.M., Schimmelmann, A. and Sessions, A.L. (2001) ‘Compound-specific D/H ratios of lipid biomarkers from sediments as a proxy for environmental and climatic conditions’, *Geochimica et Cosmochimica Acta*, 65(2), pp. 213–222. Available at: [https://doi.org/10.1016/S0016-7037\(00\)00520-2](https://doi.org/10.1016/S0016-7037(00)00520-2).

Schlolaut, G. (2018) ‘The Varve Interpolation Program 3.0.0 – A unique and easy to use tool for incompletely varved sediments’, *Quaternary Geochronology*, 48, pp. 17–24. Available at: <https://doi.org/10.1016/j.quageo.2018.07.014>.

Schlolaut, G., Brauer, A., Marshall, M.H., Nakagawa, T., Staff, R.A., Bronk Ramsey, C., Lamb, H.F., Bryant, C.L., Naumann, R., Dulski, P., Brock, F., Yokoyama, Y., Tada, R. and Haraguchi, T. (2014) ‘Event layers in the Japanese Lake Suigetsu “SG06” sediment core: Description, interpretation and climatic implications’, *Quaternary Science Reviews*, 83, pp. 157–170. Available at: <https://doi.org/10.1016/j.quascirev.2013.10.026>.

Schlolaut, G., Brauer, A., Nakagawa, T., Lamb, H.F., Tyler, J.J., Staff, R.A., Marshall, M.H., Bronk Ramsey, C., Bryant, C.L. and Tarasov, P.E. (2017) ‘Evidence for a bi-partition of the Younger Dryas Stadial in East Asia associated with inversed climate characteristics compared to Europe’, *Scientific Reports*, 7, article 44983. Available at: <https://doi.org/10.1038/srep44983>.

Schlolaut, G., Marshall, M.H., Brauer, A., Nakagawa, T., Lamb, H.F., Staff, R.A., Bronk Ramsey, C., Bryant, C.L., Brock, F., Kossler, A., Tarasov, P.E., Yokoyama, Y., Tada, R. and Haraguchi, T. (2012) 'An automated method for varve interpolation and its application to the Late Glacial chronology from Lake Suigetsu, Japan', *Quaternary Geochronology*, 13, pp. 52–69. Available at: <https://doi.org/10.1016/j.quageo.2012.07.005>.

Schlolaut, G., Staff, R. A., Brauer, A., Lamb, H. F., Marshall, M. H., Bronk Ramsey, C. and Nakagawa, T. (2018) 'An extended and revised Lake Suigetsu varve chronology from ~50 to ~10 ka BP based on detailed sediment micro-facies analyses', *Quaternary Science Reviews*, 200, pp. 351–366. Available at: <https://doi.org/10.1016/j.quascirev.2018.09.021>.

Schmidt, M., Leipe, C., Becker, F., Goslar, T., Hoelzmann, P., Mingram, J., Müller, S., Tjallingii, R., Wagner, M. and Tarasov, P.E. (2019) 'A multi-proxy palaeolimnological record of the last 16,600 years from coastal Lake Kushu in northern Japan', *Palaeogeography, Palaeoclimatology, Palaeoecology*, 514, pp. 613–626. Available at: <https://doi.org/10.1016/j.palaeo.2018.11.010>.

Seal, R.R. and Shanks, W.C. (1998) 'Oxygen and hydrogen isotope systematics of Lake Baikal, Siberia: Implications for paleoclimate studies', *Limnology and Oceanography*, 43(6), pp. 1251–1261. Available at: <https://doi.org/10.4319/lo.1998.43.6.1251>.

Shen, C.C., Kano, A., Hori, M., Lin, K., Chiu, T.C. and Burr, G.S. (2010) 'East Asian monsoon evolution and reconciliation of climate records from Japan and Greenland during the last deglaciation', *Quaternary Science Reviews*, 29(23–24), pp. 3327–3335. Available at: <https://doi.org/10.1016/j.quascirev.2010.08.012>.

Shi, Z. (2016) 'Response of Asian summer monsoon duration to orbital forcing under glacial and interglacial conditions: Implication for precipitation variability in geological records', *Quaternary Science Reviews*, 139, pp. 30–42. Available at: <https://doi.org/10.1016/j.quascirev.2016.03.008>.

Shigematsu, T., Tabushi, M., Nishikawa, Y., Muroga, T. and Matsunaga, Y. (1961) 'Geochemical Study on Lakes Mikata', *Bulletin of the Institute for Chemical*

*Research, Kyoto University*, 39, pp. 43–56. Available at:

<http://hdl.handle.net/2433/75785>.

Sigl, M., Fudge, T.J., Winstrup, M., Cole-dai, J., Ferris, D., McConnell, J.R., Taylor, K.C., Welten, K.C., Woodruff, T.E., Adolphi, F., Bisiaux, M., Brook, E.J., Buizert, C., Caffee, M.W., Dunbar, N.W., Edwards, R., Geng, L., Iverson, N., Koffman, B., Layman, L., Maselli, O.J., Mcgwire, K., Muscheler, R., Nishiizumi, K., Pasteris, D.R., Rhodes, R.H. and Sowers, T.A. (2016) 'The WAIS Divide deep ice core WD2014 chronology – Part 2: Annual-layer counting (0–31 ka BP)', *Climate of the Past*, 12, pp. 769–786. Available at:

<https://doi.org/10.5194/cp-12-769-2016>.

Sinnl, G., Adolphi, F., Christl, M., Welten, K.C., Woodruff, T., Caffee, M., Svensson, A., Muscheler, R. and Rasmussen, S.O. (2023) 'Synchronizing ice-core and U/Th timescales in the Last Glacial Maximum using Hulu Cave  $^{14}\text{C}$  and new  $^{10}\text{Be}$  measurements from Greenland and Antarctica', *Climate of the Past*, 19(6), pp. 1153–1175. Available at: <https://doi.org/10.5194/cp-19-1153-2023>.

Smedley, R.K. (2018) 'Telling the time with dust, sand and rocks', *Elements*, 14, pp. 9–14. Available at: <https://doi.org/10.2138/gselements.14.1.9>.

Smith, A.C., Leng, M.J., Swann, G.E.A., Barker, P.A., Mackay, A.W., Ryves, D.B., Sloane, H.J., Chenery, S.R.N. and Hems, M. (2016) 'An experiment to assess the effects of diatom dissolution on oxygen isotope ratios', *Rapid Communications in Mass Spectrometry*, 30, pp. 293–300. Available at:

<https://doi.org/10.1002/rcm.7446>.

Smith, V.C., Mark, D.F., Staff, R.A., Blockley, S.P., Bronk Ramsey, C., Bryant, C.L., Nakagawa, T., Han, K.K., Weh, A., Takemura, K. and Danhara, T. (2011) 'Toward establishing precise  $^{40}\text{Ar}/^{39}\text{Ar}$  chronologies for Late Pleistocene palaeoclimate archives: An example from the Lake Suigetsu (Japan) sedimentary record', *Quaternary Science Reviews*, 30(21–22), pp. 2845–2850. Available at:

<https://doi.org/10.1016/j.quascirev.2011.06.020>.

Smith, V.C., Staff, R.A., Blockley, S.P.E., Bronk Ramsey, C., Nakagawa, T., Mark, D.F., Takemura, K. and Danhara, T. (2013) 'Identification and correlation

of visible tephras in the Lake Suigetsu SG06 sedimentary archive, Japan: Chronostratigraphic markers for synchronising of east Asian/west Pacific palaeoclimatic records across the last 150 ka', *Quaternary Science Reviews*, 67, pp. 121–137. Available at: <https://doi.org/10.1016/j.quascirev.2013.01.026>.

Sone, T., Kano, A., Okumura, T., Kashiwagi, K., Hori, M., Jiang, X. and Shen, C.C. (2013) 'Holocene stalagmite oxygen isotopic record from the Japan Sea side of the Japanese Islands, as a new proxy of the East Asian winter monsoon', *Quaternary Science Reviews*, 75, pp. 150–160. Available at: <https://doi.org/10.1016/j.quascirev.2013.06.019>.

Spratt, R.M. and Lisiecki, L.E. (2016) 'A Late Pleistocene sea level stack', *Climate of the Past*, 12, pp. 1079–1092. Available at: <https://doi.org/10.5194/cp-12-1079-2016>.

Staff, R. A. (2011) *Research on Radiocarbon Calibration Records, Focussing on New Measurements from Lake Suigetsu, Japan*, PhD thesis, University of Oxford. Available at: <https://ora.ox.ac.uk/objects/uuid:c0e1fb81-bb25-487f-b85c-0d006ba4680d>

Staff, R. A., Ramsey, C. B., Bryant, C. L., Brock, F., Payne, R. L., Scholaut, G., Marshall, M. H., Brauer, A., Lamb, H. F., Tarasov, P. E., Yokoyama, Y., Haraguchi, T., Gotanda, K., Yonenobu, H. and Nakagawa, T. (2011) 'New <sup>14</sup>C determinations from Lake Suigetsu, Japan: 12,000 to 0 cal BP', *Radiocarbon*, 53(3), pp. 511–528. Available at: <https://doi.org/10.1017/S0033822200034627>.

Staff, R.A., Bronk Ramsey, C., Nakagawa, T. and Suigetsu 2006 Project Members (2010) 'A re-analysis of the Lake Suigetsu terrestrial radiocarbon calibration dataset', *Nuclear Instruments and Methods in Physics Research, Section B: Beam Interactions with Materials and Atoms*, 268(7–8), pp. 960–965. Available at: <https://doi.org/10.1016/j.nimb.2009.10.074>.

Staff, R.A., Scholaut, G., Bronk Ramsey, C., Brock, F., Bryant, C.L., Kitagawa, H., van der Plicht, J., Marshall, M.H., Brauer, A., Lamb, H.F., Payne, R.L., Tarasov, P.E., Haraguchi, T., Gotanda, K., Yonenobu, H., Yokoyama, Y. and Nakagawa, T. (2013) 'Integration of the Old and New Lake Suigetsu (Japan)

Terrestrial Radiocarbon Calibration Data Sets', *Radiocarbon*, 55(4), pp. 2049–2058. Available at: [https://doi.org/10.2458/azu\\_js\\_rc.v55i2.16339](https://doi.org/10.2458/azu_js_rc.v55i2.16339).

Stein, A.F., Draxler, R.R., Rolph, G.D., Stunder, B.J.B., Cohen, M.D. and Ngan, F. (2015) 'NOAA's HYSPLIT atmospheric transport and dispersion modelling system', *Bulletin of the American Meteorological Society*, 96(12), pp. 2059–2077. Available at: <https://doi.org/10.1175/BAMS-D-14-00110.1>.

Stone, A. E. C., Bateman, M. D. and Thomas, D. S. G. (2015) 'Rapid age assessment in the Namib Sand Sea using a portable luminescence reader', *Quaternary Geochronology*, 30(B), pp. 134–140. Available at: <https://doi.org/10.1016/j.quageo.2015.02.002>.

Stone, A., Bateman, M.D., Burrough, S.L., Garzanti, E., Limonta, M., Radeff, G. and Telfer, M.W. (2019) 'Using a portable luminescence reader for rapid age assessment of aeolian sediments for reconstructing dunefield landscape evolution in southern Africa', *Quaternary Geochronology*, 49, pp. 57–64. Available at: <https://doi.org/10.1016/j.quageo.2018.03.002>.

Suzuki, Y., Tada, R., Yamada, K., Irino, T., Nagashima, K., Nakagawa, T. and Omori, T. (2016) 'Mass accumulation rate of detrital materials in Lake Suigetsu as a potential proxy for heavy precipitation: a comparison of the observational precipitation and sedimentary record', *Progress in Earth and Planetary Science*, 3, article 5. Available at: <https://doi.org/10.1186/s40645-016-0081-x>.

Swann, G.E.A. & Snelling, A. (2023) *Isotope sample preparation of diatoms for paleoenvironmental research V.2*, PLoS ONE. Available at: <https://dx.doi.org/10.17504/protocols.io.36wgg4knovk5/v2>.

Swann, G.E.A., Leng, M.J., Sloane, H.J., Maslin, M.A. and Onodera, J. (2007) 'Diatom oxygen isotopes: Evidence of a species effect in the sediment record', *Geochemistry, Geophysics, Geosystems*, 8, article 6. Available at: <https://doi.org/10.1029/2006GC001535>.

Swann, G.E.A., Mackay, A.W., Vologina, E., Jones, M.D., Panizzo, V.N., Leng, M.J., Sloane, H.J., Snelling, A.M. and Sturm, M. (2018) 'Lake Baikal isotope

records of Holocene Central Asian precipitation', *Quaternary Science Reviews*, 189, pp. 210–222. Available at:

<https://doi.org/10.1016/j.quascirev.2018.04.013>.

Tan, L., Cai, Y., An, Z., Edwards, R.L., Cheng, H., Shen, C.C. and Zhang, H. (2011) 'Centennial- to decadal-scale monsoon precipitation variability in the semi-humid region, northern China during the last 1860 years: Records from stalagmites in Huangye cave', *Holocene*, 21(2), pp. 287–296. Available at:

<https://doi.org/10.1177/0959683610378880>.

Taniguchi, M., Nakayama, T., Tase, N. and Shimada, J. (2000) 'Stable isotope studies of precipitation and river water in the Lake Biwa basin, Japan', *Hydrological Processes*, 14(3), pp. 539–556. Available at:

[https://doi.org/10.1002/\(SICI\)1099-1085\(20000228\)14:3<539::AID-HYP953>3.0.CO;2-L](https://doi.org/10.1002/(SICI)1099-1085(20000228)14:3<539::AID-HYP953>3.0.CO;2-L).

Thomas, E.K., Clemens, S.C., Prell, W.L., Herbert, T.D., Huang, Y., Liu, Z., Sinninghe Damsté, J.S., Sun, Y. and Wen, X. (2014) 'Temperature and leaf wax  $\delta^2\text{H}$  records demonstrate seasonal and regional controls on Asian monsoon proxies', *Geology*, 42(12), pp. 1075–1078. Available at:

<https://doi.org/10.1130/G36289.1>.

Thomas, Z.A., Kwasniok, F., Boulton, C.A., Cox, P.M., Jones, R.T., Lenton, T.M. and Turney, C.S.M. (2015) 'Early warnings and missed alarms for abrupt monsoon transitions', *Climate of the Past*, 11(12), pp. 1621–1633. Available at:

<https://doi.org/10.5194/cp-11-1621-2015>.

Tierney, J.E., Russell, J.M. and Huang, Y. (2010) 'A molecular perspective on Late Quaternary climate and vegetation change in the Lake Tanganyika basin, East Africa', *Quaternary Science Reviews*, 29, pp. 787–800. Available at:

<https://doi.org/10.1016/j.quascirev.2009.11.030>.

Tierney, J.E., Russell, J.M., Huang, Y., Sinninghe Damsté, J.S., Hopmans, E.C. and Cohen, A.S. (2008) 'Northern hemisphere controls on tropical southeast African climate during the past 60,000 years', *Science*, 322, pp. 252–255.

Available at: <https://doi.org/10.1126/science.1160485>.

Tierney, J.E., Torfstein, A. and Bhattacharya, T. (2022) 'Late Quaternary hydroclimate of the Levant: The leaf wax record from the Dead Sea', *Quaternary Science Reviews*, 289, article 107613. Available at: <https://doi.org/10.1016/j.quascirev.2022.107613>.

Tiwari, M., Singh, A.K. and Sinha, D.K. (2015) 'Stable Isotopes: Tools for Understanding Past Climatic Conditions and Their Applications in Chemostratigraphy', in M. Ramkumar (ed.) *Chemostratigraphy: Concepts, Techniques, and Applications*. Elsevier Inc., pp. 65-92. Available at: <https://doi.org/10.1016/B978-0-12-419968-2.00003-0>.

Tyler, J.J., Kashiya, Y., Ohkouchi, N., Ogawa, N., Yokoyama, Y., Chikaraishi, Y., Staff, R.A., Ikehara, M., Bronk Ramsey, C., Bryant, C.L., Brock, F., Gotanda, K., Haraguchi, T., Yonenobu, H. and Nakagawa, T. (2010) 'Tracking aquatic change using chlorine-specific carbon and nitrogen isotopes: The last glacial-interglacial transition at Lake Suigetsu, Japan', *Geochemistry, Geophysics, Geosystems*, 11(9), article Q09010. Available at: <https://doi.org/10.1029/2010GC003186>.

Uemura, R., Yonezawa, N., Yoshimura, K., Asami, R., Kadena, H., Yamada, K. and Yoshida, N. (2012) 'Factors controlling isotopic composition of precipitation on Okinawa Island, Japan: Implications for paleoclimate reconstruction in the East Asian Monsoon region', *Journal of Hydrology*, 475, pp. 314-322. Available at: <https://doi.org/10.1016/j.jhydrol.2012.10.014>.

Urabe, T., Kuriyama, M., Matsumoto, R. and Kumon, F. (2014) 'Late Quaternary climates of East Asia deduced from the total organic carbon contents of cored sediments (MD179-3304, 3312) off Joetsu City, Japan Sea', *Journal of Asian Earth Sciences*, 90, pp. 209-217. Available at: <https://doi.org/10.1016/j.jseaes.2013.07.036>.

van Bree, L.G.J., Peterse, F., van der Meer, M.T.J., Middelburg, J.J., Negash, A.M.D., De Crop, W., Cocquyt, C., Wieringa, J.J., Verschuren, D. and Sinninghe Damsté, J.S. (2018) 'Seasonal variability in the abundance and stable carbon-isotopic composition of lipid biomarkers in suspended particulate matter from a stratified equatorial lake (Lake Chala, Kenya/Tanzania): Implications for

the sedimentary record', *Quaternary Science Reviews*, 192, pp. 208–224.

Available at: <https://doi.org/10.1016/j.quascirev.2018.05.023>.

van Hardenbroek, M., Chakraborty, A., Davies, K.L., Harding, P., Heiri, O., Henderson, A.C.G., Holmes, J.A., Lasher, G.E., Leng, M.J., Panizzo, V.N., Roberts, L., Schilder, J., Trueman, C.N. and Wooller, M.J. (2018) 'The stable isotope composition of organic and inorganic fossils in lake sediment records: Current understanding, challenges, and future directions', *Quaternary Science Reviews*, 196, pp. 154–176. Available at:

<https://doi.org/10.1016/j.quascirev.2018.08.003>.

Voelker, S.L., Brooks, J.R., Meinzer, F.C., Roden, J., Pazdur, A., Pawelczyk, S., Hartsough, P., Snyder, K., Plavcová, L. and Šantrůček, J. (2014) 'Reconstructing relative humidity from plant  $\delta^{18}\text{O}$  and  $\delta\text{D}$  as deuterium deviations from the global meteoric water line', *Ecological Applications*, 24(5), pp. 960–975.

Available at: <https://doi.org/10.1890/13-0988.1>.

Vuille, M., Werner, M., Bradley, R.S. and Keimig, F. (2005) 'Stable isotopes in precipitation in the Asian monsoon region', *Journal of Geophysical Research Atmospheres*, 110(D23). Available at: <https://doi.org/10.1029/2005JD006022>.

Vystavna, Y., Harjung, A., Monteiro, L.R., Matiatos, I. and Wassenaar, L.I. (2021) 'Stable isotopes in global lakes integrate catchment and climatic controls on evaporation', *Nature Communications*, 12, pp. 1–7. Available at:

<https://doi.org/10.1038/s41467-021-27569-x>.

WAIS Divide Project Members, Fudge, T.J., Steig, E.J., Markle, B.R., Schoenemann, S.W., Ding, Q., Taylor, K.C., McConnell, J.R., Brook, E.J., Sowers, T., White, J.W.C., Alley, R.B., Cheng, H., Clow, G.D., Cole-Dai, J., Conway, H., Cuffey, K.M., Edwards, J.S., Lawrence Edwards, R., Edwards, R., Fegyveresi, J.M., Ferris, D., Fitzpatrick, J.J., Johnson, J., Hargreaves, G., Lee, J.E., Maselli, O.J., Mason, W., McGwire, K.C., Mitchell, L.E., Mortensen, N., Neff, P., Orsi, A.J., Popp, T.J., Schauer, A.J., Severinghaus, J.P., Sigl, M., Spencer, M.K., Vaughn, B.H., Voigt, D.E., Waddington, E.D., Wang, X. and Wong, G.J. (2013) 'Onset of deglacial warming in West Antarctica driven by local

orbital forcing', *Nature*, 500, pp. 440–444. Available at:

<https://doi.org/10.1038/nature12376>.

Walker, M.J., Johnsen, S.J., Rasmussen, S.O., Popp, T., Steffensen, J., Gibbard, P., Hoek, W.Z., Lowe, J., Andrews, J., Bjo, S., Cwynar, L.C., Hughen, K.A., Kershaw, P., Kromer, B., Litt, T., Lowe, D.J., Nakagawa, T., Newnham, R., Schwander, J. and Rck, B. (2009) 'Formal definition and dating of the GSSP (Global Stratotype Section and Point) for the base of the Holocene using the Greenland NGRIP ice core, and selected auxiliary records', *Journal of Quaternary Science*, 24(1), pp. 3–17. Available at:

<https://doi.org/10.1002/jqs.1227>.

Wang, H. and Fan, K. (2005) 'Central–north China precipitation as reconstructed from the Qing dynasty: Signal of the Antarctic Atmospheric Oscillation', *Geophysical Research Letters*, 32(24), article L24705. Available at:

<https://doi.org/10.1029/2005GL024562>.

Wang, L., Li, J., Lu, H., Gu, Z., Rioual, P., Hao, Q., Mackay, A.W., Jiang, W., Cai, B., Xu, B., Han, J. and Chu, G. (2012) 'The East Asian winter monsoon over the last 15,000 years: Its links to high–latitudes and tropical climate systems and complex correlation to the summer monsoon', *Quaternary Science Reviews*, 32, pp. 131–142. Available at: <https://doi.org/10.1016/j.quascirev.2011.11.003>.

Wang, L., Sarnthein, M., Erlenkeuser, H., Grimalt, J., Grootes, P., Heilig, S., Ivanova, E., Kienast, M., Pelejero, C. and Pflaumann, U. (1999) 'East Asian monsoon climate during the Late Pleistocene: High–resolution sediment records from the South China Sea', *Marine Geology*, 156(1–4), pp. 245–284. Available at: [https://doi.org/10.1016/S0025-3227\(98\)00182-0](https://doi.org/10.1016/S0025-3227(98)00182-0).

Wang, Y., Cheng, H., Edwards, R.L., He, Y., Kong, X., An, Z., Wu, J., Kelly, M.J., Dykoski, C.A. and Li, X. (2005) 'The Holocene Asian monsoon: Links to solar changes and North Atlantic climate', *Science*, 308(5723), pp. 854–857. Available at: <https://doi.org/10.1126/science.1106296>.

Wang, Y., Cheng, H., Edwards, R.L., Kong, X., Shao, X., Chen, S., Wu, J., Jiang, X., Wang, X. and An, Z. (2008) 'Millennial– and orbital–scale changes in the East

Asian monsoon over the past 224,000 years', *Nature*, 451, pp. 1090–1093.

Available at: <https://doi.org/10.1038/nature06692>.

Wang, Y., Liu, X. and Herzschuh, U. (2010) 'Asynchronous evolution of the Indian and East Asian Summer Monsoon indicated by Holocene moisture patterns in monsoonal central Asia', *Earth–Science Reviews*, 103(3–4), pp. 135–153.

Available at: <https://doi.org/10.1016/j.earscirev.2010.09.004>.

Wang, Y.J., Cheng, H., Edwards, R.L., An, Z.S., Wu, J.Y., Shen, C.C. and Dorale, J.A. (2001) 'A high-resolution absolute-dated late Pleistocene monsoon record from Hulu Cave, China', *Science*, 294(5550), pp. 2345–2348. Available at:

<https://doi.org/10.1126/science.1064618>.

Wassenaar, L.I., Athanasopoulos, P. and Hendry, M.J. (2011) 'Isotope hydrology of precipitation, surface and ground waters in the Okanagan Valley, British Columbia, Canada', *Journal of Hydrology*, 411(1–2), pp. 37–48. Available at:

<https://doi.org/10.1016/j.jhydrol.2011.09.032>.

Webster, P.J., Magaña, V.O., Palmer, T.N., Shukla, J., Tomas, R.A., Yanai, M. and Yasunari, T. (1998) 'Monsoons: processes, predictability, and the prospects for prediction', *Journal of Geophysical Research: Oceans*, 103(C7), pp. 14451–14510. Available at:

<https://doi.org/10.1029/97jc02719>.

Wen, X., Liu, Z., Wang, S., Cheng, J. and Zhu, J. (2016) 'Correlation and anti-correlation of the East Asian summer and winter monsoons during the last 21,000 years', *Nature Communications*, 7, article 11999. Available at:

<https://doi.org/10.1038/ncomms11999>.

Wintle, A.G. (2008) 'Luminescence dating: Where it has been and where it is going', *Boreas*, 37, pp. 471–482. Available at:

<https://doi.org/10.1111/j.1502-3885.2008.00059.x>.

Wintle, A.G. and Adamiec, G. (2017) 'Optically stimulated luminescence signals from quartz: A review', *Radiation Measurements*, 98, pp. 10–33. Available at:

<https://doi.org/10.1016/j.radmeas.2017.02.003>.

Wu, Y., Shi, X., Gong, X., Jian, Z., Zou, J., Liu, Y., Lohmann, G., Gorbarenko, S.A., Tiedemann, R. and Lembke-Jene, L. (2020) 'Evolution of the Upper Ocean Stratification in the Japan Sea Since the Last Glacial', *Geophysical Research Letters*, 47(16), article e2020GL088255. Available at:

<https://doi.org/10.1029/2020GL088255>.

Xia, C., Liu, G., Hu, Y. and Meng, Y. (2018) 'Precipitation Stable Isotope Variability in Tropical Monsoon Climatic Zone of Asia', *IOP Conference Series: Materials Science and Engineering*, 392(4). Available at:

<https://doi.org/10.1088/1757-899X/392/4/042028>.

Xia, Z., Welker, J.M. and Winnick, M.J. (2022) 'The Seasonality of Deuterium Excess in Non-Polar Precipitation', *Global Biogeochemical Cycles*, 36(10), article e2021GB007245. Available at: <https://doi.org/10.1029/2021GB007245>.

Xu, D., Lu, H., Wu, N., Liu, Z., Li, T., Shen, C. and Wang, L. (2013) 'Asynchronous marine-terrestrial signals of the last deglacial warming in East Asia associated with low- and high-latitude climate changes', *Proceedings of the National Academy of Sciences of the United States of America*, 110(24), pp. 9657-9662. Available at: <https://doi.org/10.1073/pnas.1300025110>.

Xu, H., Goldsmith, Y., Lan, J., Tan, L., Wang, X., Zhou, X., Cheng, J., Lang, Y. and Liu, C. (2020) 'Juxtaposition of Western Pacific Subtropical High on Asian Summer Monsoon Shapes Subtropical East Asian Precipitation', *Geophysical Research Letters*, 47(3), article e2019GL084705. Available at: <https://doi.org/10.1029/2019GL084705>.

Xue, G., Cai, Y., Ma, L., Cheng, X., Cheng, H., Edwards, R.L., Li, D. and Tan, L. (2019) 'A new speleothem record of the penultimate deglacial: Insights into spatial variability and centennial-scale instabilities of East Asian monsoon', *Quaternary Science Reviews*, 210, pp. 113-124. Available at: <https://doi.org/10.1016/j.quascirev.2019.02.023>.

Yamada, K., Omori, T., Kitaba, I., Hori, T. and Nakagawa, T. (2021) 'Extraction method for fossil pollen grains using a cell sorter suitable for routine  $^{14}\text{C}$  dating',

Quaternary Science Reviews, 272, article 107236. Available at:

<https://doi.org/10.1016/j.quascirev.2021.107236>.

Yan, M., Liu, Z.Y., Ning, L. and Liu, J. (2020) 'Holocene EASM–EAWM Relationship Across Different Timescales in CCSM3', *Geophysical Research Letters*, 47, article e2020GL088451. Available at:

<https://doi.org/10.1029/2020GL088451>.

Yancheva, G., Nowaczyk, N.R., Mingram, J., Dulski, P., Schettler, G., Nengendank, J.F.W., Liu, J., Sigman, D.M., Peterson, L.C. and Haug, G.H. (2007) 'Influence of the intertropical convergence zone on the East Asian monsoon', *Nature*, 445(7123), pp. 74–77. Available at:

<https://doi.org/10.1038/nature05431>.

Yang, K., Cai, W., Huang, G., Hu, K., Ng, B. and Wang, G. (2022) 'Increased variability of the western Pacific subtropical high under greenhouse warming', *Proceedings of the National Academy of Sciences of the United States of America*, 119(23), article e2120335119. Available at:

<https://doi.org/10.1073/pnas.2120335119>.

Yaskawa, K., Nakajima, T., Kawai, N., Torii, M., Natsuhara, N. and Horie, S. (1973) 'Palaeomagnetism of a Core from Lake Biwa (I)', *Journal of Geomagnetism and Geoelectricity*, 25(4), pp. 447–474. Available at:

<https://doi.org/10.5636/jgg.25.447>.

Yasuda, Y., Yamaguchi, K., Nakagawa, T., Fukusawa, H., Kitagawa, J. and Okamura, M. (2004) 'Environmental variability and human adaptation during the Lateglacial/Holocene transition in Japan with reference to pollen analysis of the SG4 core from Lake Suigetsu', *Quaternary International*, 123–125, pp. 11–19.

Available at: <https://doi.org/10.1016/j.quaint.2004.02.003>.

Yihui, D. and Chan, J.C.L. (2005) 'The East Asian summer monsoon: An overview', *Meteorology and Atmospheric Physics*, 89(1–4), pp. 117–142.

Available at: <https://doi.org/10.1007/s00703-005-0125-z>.

Yoshida, A. and Takeuti, S. (2009) 'Quantitative reconstruction of palaeoclimate from pollen profiles in northeastern Japan and the timing of a cold reversal event during the Last Termination', *Journal of Quaternary Science*, 24(8), pp. 1006–1015. Available at: <https://doi.org/10.1002/jqs.1284>.

Yoshimura, K. (2015) 'Stable water isotopes in climatology, meteorology, and hydrology: A review', *Journal of the Meteorological Society of Japan*, 93(5), pp. 513–533. Available at: <https://doi.org/10.2151/jmsj.2015-036>.

Yuan, D., Cheng, H., Edwards, R.L., Dykoski, C.A., Kelly, M.J., Zhang, M., Qing, J., Lin, Y., Wang, Y., Wu, J., Dorale, J.A., An, Z. and Cai, Y. (2004) 'Timing, Duration, and Transitions of the Last Interglacial Asian Monsoon', *Science*, 304(5670), pp. 575–578. Available at: <https://doi.org/10.1126/science.1091220>.

Zhang, H., Brahim, Y.A., Li, H., Zhao, J., Kathayat, G., Tian, Y., Baker, J., Wang, J., Zhang, F., Ning, Y., Edwards, R.L. and Cheng, H. (2019) 'The Asian Summer Monsoon: Teleconnections and Forcing Mechanisms—A Review from Chinese Speleothem  $\delta^{18}\text{O}$  Records', *Quaternary*, 2(3), article 26. Available at: <https://doi.org/10.3390/quat2030026>.

Zhang, H., Griffiths, M.L., Chiang, J.C.H., Kong, W., Wu, S., Atwood, A., Huang, J., Cheng, H., Ning, Y. and Xie, S. (2018) 'East Asian hydroclimate modulated by the position of the westerlies during Termination I', *Science*, 362, pp. 580–583. Available at: <https://doi.org/10.1126/science.aat9393>.

Zhang, H., Griffiths, M.L., Huang, J., Cai, Y., Wang, C., Zhang, F., Cheng, H., Ning, Y., Hu, C. and Xie, S. (2016) 'Antarctic link with East Asian summer monsoon variability during the Heinrich Stadial–Bølling interstadial transition', *Earth and Planetary Science Letters*, 453, pp. 243–251. Available at: <https://doi.org/10.1016/j.epsl.2016.08.008>.

Zhang, P., Cheng, H., Edwards, R.L., Chen, F., Wang, Y., Yang, X., Liu, Jian, Tan, M., Wang, X., Liu, Jinghua, An, C., Dai, Z., Zhou, J., Zhang, D., Jia, J., Jin, L. and Johnson, K.R. (2008) 'A test of climate, sun, and culture relationships from an 1810–year Chinese cave record', *Science*, 322(5903), pp. 940–942. Available at: <https://doi.org/10.1126/science.1163965>.

Zhang, R., Yan, Q., Zhang, Z.S., Jiang, D., Otto-Bliesner, B.L., Haywood, A.M., Hill, D.J., Dolan, A.M., Stepanek, C., Lohmann, G., Contoux, C., Bragg, F., Chan, C.L., Chandler, M.A., Jost, A., Kamae, Y., Abe-Ouchi, A., Ramstein, G., Rosenbloom, N.A., Sohl, L. and Ueda, H. (2013) 'Mid-Pliocene East Asian monsoon climate simulated in the PlioMIP', *Climate of the Past*, 9(5), pp. 2085–2099. Available at: <https://doi.org/10.5194/cp-9-2085-2013>.

Zhang, Y., Yu, J., Su, Y., Du, Y. and Liu, Z. (2020) 'A comparison of n-alkane contents in sediments of five lakes from contrasting environments', *Organic Geochemistry*, 139, p. article 103943. Available at: <https://doi.org/10.1016/j.orggeochem.2019.103943>.

Zhao, G., Ye, S., Laws, E. A., He, L., Yuan, H., Ding, X. and Wang, J. (2019) 'Carbon burial records during the last ~40,000 years in sediments of the Liaohe Delta wetland, China', *Estuarine, Coastal and Shelf Science*, 226, article 106291. Available at: <https://doi.org/10.1016/j.ecss.2019.106291>.

Zhong, W., Ma, Q., Xue, J., Zheng, Y., Cai, Y., Ouyang, Y. and Yu, X. (2011) 'Humification degree as a proxy climatic record since the last deglaciation derived from a limnological sequence in South China', *Geochemistry International*, 49, pp. 407–414. Available at: <https://doi.org/10.1134/S0016702911040094>.